

---

**Solid Freeform and  
Additive Fabrication—2000**

**DTIC QUALITY INSPECTED 4**

**20001019 009**

**MATERIALS RESEARCH SOCIETY  
SYMPOSIUM PROCEEDINGS VOLUME 625**

---

# **Solid Freeform and Additive Fabrication—2000**

Symposium held April 24-26, 2000, San Francisco, California, U.S.A.

**EDITORS:**

**Stephen C. Danforth**

Rutgers University  
Piscataway, New Jersey, U.S.A.

**Duane Dimos**

Sandia National Laboratories  
Albuquerque, New Mexico, U.S.A.

**Fritz B. Prinz**

Stanford University  
Stanford, California, U.S.A.

**DISTRIBUTION STATEMENT A**  
Approved for Public Release  
Distribution Unlimited



**Materials Research Society**  
Warrendale, Pennsylvania

This work was supported in part by the Office of Naval Research under Grant Number ONR: N00014-99-1-0931. The United States Government has a royalty-free license throughout the world in all copyrightable material contained herein.

Single article reprints from this publication are available through  
University Microfilms Inc., 300 North Zeeb Road, Ann Arbor, Michigan 48106

CODEN: MRSPDH

Copyright 2000 by Materials Research Society.  
All rights reserved.

This book has been registered with Copyright Clearance Center, Inc. For further information, please contact the Copyright Clearance Center, Salem, Massachusetts.

Published by:

Materials Research Society  
506 Keystone Drive  
Warrendale, PA 15086  
Telephone (724) 779-3003  
Fax (724) 779-8313  
Web site: <http://www.mrs.org/>

#### Library of Congress Cataloging-in-Publication Data

Solid freeform and additive fabrication—2000 : symposium held April 24–26, 2000, San Francisco, California, U.S.A. / editors, Stephen C. Danforth, Duane Dimos, Fritz B. Prinz

p.cm.—(Materials Research Society symposium proceedings,  
ISSN 0272-9172 ; v. 625)

Includes bibliographical references and indexes.

ISBN 1-55899-533-1

1. Manufacturing processes—Congresses. 2. Solid freeform fabrication—Congresses.

3. Composite materials—Congresses. 4. Ceramic materials—Congresses. 5. Lasers—Industrial applications—Congresses. I. Danforth, Stephen C. II. Dimos, Duane III. Prinz, Fritz B.

IV. Materials Research Society symposium proceedings ; v. 625

TS183. S658 2000

670.42'7—dc21

00-061664

Manufactured in the United States of America

## CONTENTS

Preface .....	ix
Materials Research Society Symposium Proceedings .....	x

### *DIRECT METAL FABRICATION*

Microstructural Study of Laser Formed Ti-6Al-4V .....	3
S.M. Kelly, S.L. Kampe, and C.R. Crowe	
<b>*Understanding the Microstructure and Properties of Components Fabricated by Laser Engineered Net Shaping (LENS) .....</b>	<b>9</b>
M.L. Griffith, M.T. Ensz, J.D. Puskar, C.V. Robino, J.A. Brooks, J.A. Philliber, J.E. Smugeresky, and W.H. Hofmeister	
Microstructures of Laser Deposited 304L Austenitic Stainless Steel .....	21
John A. Brooks, Thomas J. Headley, and Charles V. Robino	
Characterization of Laser Deposited Niobium and Molybdenum Silicides .....	31
C.A. Brice, K.I. Schwendner, S. Amancherla, H.L. Fraser, and X.D. Zhang	
Investigation into Freeform Fabrication of Multi-Material Parts by 3D Welding and Milling Process .....	37
Yong-Ak Song and Sehyung Park	

### *TOOLING AND PHOTO PROCESSING*

Dimensionally Accurate Mold Inserts and Metal Components by Direct Metal Laser Sintering .....	45
Jan-Erik Lind, Juha Kotila, Tatu Syvänen, and Olli Nyrhilä	
Conformal Cooling Versus Conventional Cooling: An Injection Molding Case Study With P-20 and 3DP™-Processed Tooling .....	51
Wayde R. Schmidt, Ronald D. White, Connie E. Bird, and Joseph V. Bak	

\*Invited Paper

<b>*Rapid Electroforming Tooling</b> .....	<b>57</b>
Bo Yang and Ming C. Leu	
<b>*Selective Laser Sintering of Zirconia</b> .....	<b>67</b>
Nicole R. Harlan, David Bourell, Seok-Min Park, and Joseph J. Beaman, Jr.	
<b>Processing-Structure-Property Relations of Polymer-Polymer Composites Formed by Cryogenic Mechanical Alloying for Selective Laser Sintering Applications</b> .....	<b>75</b>
J.P. Schultz, J.P. Martin, R.G. Kander, and C.T.A. Suchicital	
<b>Freeform Fabrication of Functional Silicon Nitride Components by Direct Photo Shaping</b> .....	<b>81</b>
S. Ventura, S. Narang, P. Guerit, S. Liu, D. Twait, P. Khandelwal, E. Cohen, and R. Fish	
<b>Refrigerative Stereolithography Using Sol-Gel Transformable Photopolymer Resin and Direct Masking</b> .....	<b>91</b>
T. Murakami, A. Kamimura, and N. Nakajima	

***DIRECT PATTERNING***

<b>*Matrix Assisted Pulsed Laser Evaporation Direct Write (MAPLE DW): A New Method to Rapidly Prototype Active and Passive Electronic Circuit Elements</b> .....	<b>99</b>
J.M. Fitz-Gerald, D.B. Chrisey, A. Piqu, R.C.Y. Auyeung, R. Mohdi, H.D. Young, H.D. Wu, S. Lakeou, and R. Chung	
<b>Pattern Writing by Implantation in a Large-Scale PSII System With Planar Inductively Coupled Plasma Source</b> .....	<b>111</b>
Lingling Wu, Hongjun Gao, and Dennis M. Manos	
<b>Ink Jet Deposition of Ceramic Suspensions: Modeling and Experiments of Droplet Formation</b> .....	<b>117</b>
N. Reis and B. Derby	
<b>Lateral Dye Distribution With Ink-Jet Dye Doping of Polymer Organic Light Emitting Diodes</b> .....	<b>123</b>
Conor F. Madigan, Thomas R. Hebner, J.C. Sturm, Richard A. Register, and Sandra Troian	

\*Invited Paper

<b>Calculation of Hamaker Constants in Nonaqueous Fluid Media</b> .....	129
Nelson Bell and Duane Dimos	
<b>All-Printed Inorganic Logic Elements Fabricated by Liquid Embossing</b> .....	135
Colin Bulthaupt, Eric Wilhelm, Brian Hubert, Brent Ridley, and Joe Jacobson	
<b>*Rapid Prototyping of Patterned Multifunctional Nanostructures</b> .....	141
Hongyou Fan, Gabriel P. López, and C. Jeffrey Brinker	
<b>Electrostatic Printing: A Versatile Manufacturing Process for the Electronics Industries</b> .....	151
Robert H. Detig	

**COMPOSITES AND CERAMICS**

<b>Modeling and Optimization of Novel Actuators Produced by Solid Freeform Fabrication</b> .....	159
B.A. Cheeseman, X.P. Ruan, A. Safari, S.C. Danforth, and T.W. Chou	
<b>*Processing of Organic/Inorganic Composites by Stereolithography</b> .....	165
J.H. Lee, R.K. Prud'homme, and I.A. Aksay	
<b>Automated Fabrication of Ceramic Electronic Packages by Stereo-Photolithography</b> .....	173
W.R. Zimbeck, J.H. Jang, W. Schulze, and R.W. Rice	
<b>Using Layered Manufacturing to Create Textured Microstructures in Si<sub>3</sub>N<sub>4</sub> Ceramics</b> .....	179
S. Rangarajan, B. Harper, R. McCuiston, A. Safari, Z. Kalman, W. Mayo, S.C. Danforth, and C. Gasdaska	
<b>μ-Mold Shape Deposition Manufacturing of Ceramic Parts</b> .....	187
S.W. Nam, J. Stampfl, H.C. Liu, S. Kang, and F.B. Prinz	

**CERAMICS AND SOLUTION PROCESSES**

<b>*Freeform Fabrication of Ceramics by Hot-Melt Ink-Jet Printing</b> .....	195
B. Derby, N. Reis, K.A.M. Seerden, P.S. Grant, and J.R.G. Evans	

\*Invited Paper

---

<b>Process-Property-Performance Relationship for Fused Deposition of Ceramics (FDC) Feedstock Materials</b> .....	<b>203</b>
N. Venkataraman, S. Rangarajan, B. Harper, M.J. Matthewson, A. Safari, and S.C. Danforth	
<b>*Gas Phase Solid Freeform Fabrication of SALDVI of SiC Cermets</b> .....	<b>211</b>
J.E. Crocker, L. Shaw, and H.L. Marcus	
<b>Author Index</b> .....	<b>217</b>
<b>Subject Index</b> .....	<b>219</b>

\*Invited Paper

## PREFACE

Solid freeform (SFF) and additive fabrication processes are defining a revolutionary new approach for materials manufacturing that is leading to a capability for producing parts quicker, cheaper and with more functionality than previously thought possible. The key aspect of these direct fabrication techniques is the ability to deposit or build up material only where it is required to produce finished parts. The additive nature of these processes leads to tremendous flexibility in the shape and complexity of parts that can be fabricated.

While excellent engineering progress has been made in this field, significant work on materials issues associated with these layer-wise additive processes remains to be done. For example, material microstructure can be strongly influenced by the specific deposition process. Many techniques also produce unique microstructures that dramatically impact materials performance. In addition, important processing issues exist not only for fabricating the final materials (e.g., binder burnout, densification and polymerization), but also for preparing the starting materials (e.g., powders, slurries, inks and fibers). Furthermore, the ability to do point-wise deposition of one or more materials provides the opportunity for fabricating materials with novel microstructural and macrostructural features, such as micro-engineered porosity, graded interfaces, and complex multi-material constructions. In particular, the materials compatibility issues associated with multi-material, multi-functional components are just beginning to be addressed.

This symposium, "Solid Freeform and Additive Fabrication," held April 24–26 at the 2000 MRS Spring Meeting in San Francisco, California, is the third in a series. The first was held at the 1997 MRS Spring Meeting. The second was held at the 1998 MRS Fall Meeting and was published as MRS Symposium Proceedings Volume 542. This symposium brought together experts in the SFF field to discuss recent developments in SFF and additive methods for fabricating metals, ceramics, polymers, and composites. The symposium focused on processing-structure-property relationships and relevant materials modeling approaches. Various presentations covered methods ranging from laser chemical vapor deposition (LCVD) to ink-jet based processes. The entire range of materials, i.e., polymeric, metallic and ceramic components for structural, biological, and electronic applications were covered in the various papers. Contributions also discussed applications of these advanced processing techniques. A joint session with Symposium V, "Materials Development for Direct Write Technologies," was held and the joint papers are being published in both proceedings. The joint session with Symposium V covered various materials approaches that are currently being developed for fabricating mesoscopic integrated conformal electronics (MICE). These talks described materials and methods to fabricate passive electronic devices (such as conductors, insulators and capacitors) on conformal surfaces at temperatures below 400°C.

This symposium was financially supported by the Office of Naval Research (ONR) and Sandia National Laboratories, for which the editors are extremely grateful. The editors would also like to thank Kyriakos Labropoulos, Simona Turcu, and Bryan W. McEnerney for their assistance in compiling the symposium proceedings.

Stephen C. Danforth  
Duane Dimos  
Fritz B. Prinz

June 2000



## MATERIALS RESEARCH SOCIETY SYMPOSIUM PROCEEDINGS

- Volume 578— Multiscale Phenomena in Materials—Experiments and Modeling, I.M. Robertson, D.H. Lassila, R. Phillips, B. Devincere, 2000, ISBN: 1-55899-486-6
- Volume 579— The Optical Properties of Materials, J.R. Chelikowsky, S.G. Louie, G. Martinez, E.L. Shirley, 2000, ISBN: 1-55899-487-4
- Volume 580— Nucleation and Growth Processes in Materials, A. Gonis, P.E.A. Turchi, A.J. Ardell, 2000, ISBN: 1-55899-488-2
- Volume 581— Nanophase and Nanocomposite Materials III, S. Komameni, J.C. Parker, H. Hahn, 2000, ISBN: 1-55899-489-0
- Volume 582— Molecular Electronics, S.T. Pantelides, M.A. Reed, J. Murday, A. Aviram, 2000, ISBN: 1-55899-490-4
- Volume 583— Self-Organized Processes in Semiconductor Alloys, A. Mascarenhas, D. Follstaedt, T. Suzuki, B. Joyce, 2000, ISBN: 1-55899-491-2
- Volume 584— Materials Issues and Modeling for Device Nanofabrication, L. Merhari, L.T. Wille, K.E. Gonsalves, M.F. Gyure, S. Matsui, L.J. Whitman, 2000, ISBN: 1-55899-492-0
- Volume 585— Fundamental Mechanisms of Low-Energy-Beam-Modified Surface Growth and Processing, S. Moss, E.H. Chason, B.H. Cooper, T. Diaz de la Rubia, J.M.E. Harper, R. Murti, 2000, ISBN: 1-55899-493-9
- Volume 586— Interfacial Engineering for Optimized Properties II, C.B. Carter, E.L. Hall, S.R. Nutt, C.L. Briant, 2000, ISBN: 1-55899-494-7
- Volume 587— Substrate Engineering—Paving the Way to Epitaxy, D. Norton, D. Schlom, N. Newman, D. Matthiesen, 2000, ISBN: 1-55899-495-5
- Volume 588— Optical Microstructural Characterization of Semiconductors, M.S. Unlu, J. Piqueras, N.M. Kalkhoran, T. Sekiguchi, 2000, ISBN: 1-55899-496-3
- Volume 589— Advances in Materials Problem Solving with the Electron Microscope, J. Bentley, U. Dahmen, C. Allen, I. Petrov, 2000, ISBN: 1-55899-497-1
- Volume 590— Applications of Synchrotron Radiation Techniques to Materials Science V, S.R. Stock, S.M. Mini, D.L. Perry, 2000, ISBN: 1-55899-498-X
- Volume 591— Nondestructive Methods for Materials Characterization, G.Y. Baaklini, N. Meyendorf, T.E. Matikas, R.S. Gilmore, 2000, ISBN: 1-55899-499-8
- Volume 592— Structure and Electronic Properties of Ultrathin Dielectric Films on Silicon and Related Structures, D.A. Buchanan, A.H. Edwards, H.J. von Bardeleben, T. Hattori, 2000, ISBN: 1-55899-500-5
- Volume 593— Amorphous and Nanostructured Carbon, J.P. Sullivan, J. Robertson, O. Zhou, T.B. Allen, B.F. Coll, 2000, ISBN: 1-55899-501-3
- Volume 594— Thin Films—Stresses and Mechanical Properties VIII, R. Vinci, O. Kraft, N. Moody, P. Besser, E. Shaffer II, 2000, ISBN: 1-55899-502-1
- Volume 595— GaN and Related Alloys—1999, T.H. Myers, R.M. Feenstra, M.S. Shur, H. Amano, 2000, ISBN: 1-55899-503-X
- Volume 596— Ferroelectric Thin Films VIII, R.W. Schwartz, P.C. McIntyre, Y. Miyasaka, S.R. Summerfelt, D. Wouters, 2000, ISBN: 1-55899-504-8
- Volume 597— Thin Films for Optical Waveguide Devices and Materials for Optical Limiting, K. Nashimoto, R. Pachter, B.W. Wessels, J. Shmulovich, A.K.-Y. Jen, K. Lewis, R. Sutherland, J.W. Perry, 2000, ISBN: 1-55899-505-6
- Volume 598— Electrical, Optical, and Magnetic Properties of Organic Solid-State Materials V, S. Ermer, J.R. Reynolds, J.W. Perry, A.K.-Y. Jen, Z. Bao, 2000, ISBN: 1-55899-506-4
- Volume 599— Mineralization in Natural and Synthetic Biomaterials, P. Li, P. Calvert, T. Kokubo, R.J. Levy, C. Scheid, 2000, ISBN: 1-55899-507-2
- Volume 600— Electroactive Polymers (EAP), Q.M. Zhang, T. Furukawa, Y. Bar-Cohen, J. Scheinbeim, 2000, ISBN: 1-55899-508-0
- Volume 601— Superplasticity—Current Status and Future Potential, P.B. Berbon, M.Z. Berbon, T. Sakuma, T.G. Langdon, 2000, ISBN: 1-55899-509-9
- Volume 602— Magnetoresistive Oxides and Related Materials, M. Rzechowski, M. Kawasaki, A.J. Millis, M. Rajeswari, S. von Molnár, 2000, ISBN: 1-55899-510-2
- Volume 603— Materials Issues for Tunable RF and Microwave Devices, Q. Jia, F.A. Miranda, D.E. Oates, X. Xi, 2000, ISBN: 1-55899-511-0
- Volume 604— Materials for Smart Systems III, M. Wun-Fogle, K. Uchino, Y. Ito, R. Gotthardt, 2000, ISBN: 1-55899-512-9

---

## MATERIALS RESEARCH SOCIETY SYMPOSIUM PROCEEDINGS

- Volume 605— Materials Science of Microelectromechanical Systems (MEMS) Devices II, M.P. deBoer, A.H. Heuer, S.J. Jacobs, E. Peeters, 2000, ISBN: 1-55899-513-7
- Volume 606— Chemical Processing of Dielectrics, Insulators and Electronic Ceramics, A.C. Jones, J. Veteran, D. Mullin, R. Cooper, S. Kaushal, 2000, ISBN: 1-55899-514-5
- Volume 607— Infrared Applications of Semiconductors III, M.O. Manasreh, B.J.H. Stadler, I. Ferguson, Y-H. Zhang, 2000, ISBN: 1-55899-515-3
- Volume 608— Scientific Basis for Nuclear Waste Management XXIII, R.W. Smith, D.W. Shoesmith, 2000, ISBN: 1-55899-516-1
- Volume 609— Amorphous and Heterogeneous Silicon Thin Films—2000, R.W. Collins, H.M. Branz, S. Guha, H. Okamoto, M. Stutzmann, 2000, ISBN: 1-55899-517-X
- Volume 610— Si Front-End Processing—Physics and Technology of Dopant-Defect Interactions II, A. Agarwal, L. Pelaz, H-H. Vuong, P. Packan, M. Kase, 2000, ISBN: 1-55899-518-8
- Volume 611— Gate Stack and Silicide Issues in Silicon Processing, L. Clevenger, S.A. Campbell, B. Herner, J. Kittl, P.R. Besser, 2000, ISBN: 1-55899-519-6
- Volume 612— Materials, Technology and Reliability for Advanced Interconnects and Low-k Dielectrics, K. Maex, Y-C. Joo, G.S. Oehrlein, S. Ogawa, J.T. Wetzel, 2000, ISBN: 1-55899-520-X
- Volume 613— Chemical-Mechanical Polishing 2000—Fundamentals and Materials Issues, R.K. Singh, R. Bajaj, M. Meuris, M. Moinpour, 2000, ISBN: 1-55899-521-8
- Volume 614— Magnetic Materials, Structures and Processing for Information Storage, B.J. Daniels, M.A. Seigler, T.P. Nolan, S.X. Wang, C.B. Murray, 2000, ISBN: 1-55899-522-6
- Volume 615— Polycrystalline Metal and Magnetic Thin Films—2000, L. Gignac, O. Thomas, J. MacLaren, B. Clemens, 2000, ISBN: 1-55899-523-4
- Volume 616— New Methods, Mechanisms and Models of Vapor Deposition, H.N.G. Wadley, G.H. Gilmer, W.G. Barker, 2000, ISBN: 1-55899-524-2
- Volume 617— Laser-Solid Interactions for Materials Processing, D. Kumar, D.P. Norton, C.B. Lee, K. Ebihara, X. Xi, 2000, ISBN: 1-55899-525-0
- Volume 618— Morphological and Compositional Evolution of Heteroepitaxial Semiconductor Thin Films, J.M. Millunchick, A-L. Barabasi, E.D. Jones, N. Modine, 2000, ISBN: 1-55899-526-9
- Volume 619— Recent Developments in Oxide and Metal Epitaxy—Theory and Experiment, M. Yeadon, S. Chiang, R.F.C. Farrow, J.W. Evans, O. Auciello, 2000, ISBN: 1-55899-527-7
- Volume 620— Morphology and Dynamics of Crystal Surfaces in Complex Molecular Systems, J. DeYoreo, W. Casey, A. Malkin, E. Vlieg, M. Ward, 2000, ISBN: 1-55899-528-5
- Volume 621— Electron-Emissive Materials, Vacuum Microelectronics and Flat-Panel Displays, K.L. Jensen, W. Mackie, D. Temple, J. Itoh, R. Nemanich, T. Trottier, P. Holloway, 2000, ISBN: 1-55899-529-3
- Volume 622— Wide-Bandgap Electronic Devices, R.J. Shul, F. Ren, M. Murakami, W. Pletschen, 2000, ISBN: 1-55899-530-7
- Volume 623— Materials Science of Novel Oxide-Based Electronics, D.S. Ginley, D.M. Newns, H. Kawazoe, A.B. Kozyrev, J.D. Perkins, 2000, ISBN: 1-55899-531-5
- Volume 624— Materials Development for Direct Write Technologies, D.B. Chrisey, D.R. Gamota, H. Helvajian, D.P. Taylor, 2000, ISBN: 1-55899-532-3
- Volume 625— Solid Freeform and Additive Fabrication—2000, S.C. Danforth, D. Dimos, F.B. Prinz, 2000, ISBN: 1-55899-533-1
- Volume 626— Thermoelectric Materials 2000—The Next Generation Materials for Small-Scale Refrigeration and Power Generation Applications, T.M. Tritt, G.S. Nolas, G. Mahan, M.G. Kanatzidis, D. Mandrus, 2000, ISBN: 1-55899-534-X
- Volume 627— The Granular State, S. Sen, M. Hunt, 2000, ISBN: 1-55899-535-8
- Volume 628— Organic/Inorganic Hybrid Materials—2000, R.M. Laine, C. Sanchez, E. Giannelis, C.J. Brinker, 2000, ISBN: 1-55899-536-6
- Volume 629— Interfaces, Adhesion and Processing in Polymer Systems, S.H. Anastasiadis, A. Karim, G.S. Ferguson, 2000, ISBN: 1-55899-537-4
- Volume 630— When Materials Matter—Analyzing, Predicting and Preventing Disasters, M. Ausloos, A.J. Hurd, M.P. Marder, 2000, ISBN: 1-55899-538-2

Prior Materials Research Society Symposium Proceedings available by contacting Materials Research Society

---

**Direct Metal Fabrication**

## MICROSTRUCTURAL STUDY OF LASER FORMED Ti-6Al-4V

S.M. KELLY, S.L. KAMPE, C.R. CROWE\*

Materials Science and Engineering Department, Virginia Tech, Blacksburg, VA 24061-0237

\*Virginia Tech Alexandria Research Institute, Alexandria, VA 22314

### ABSTRACT

A microstructural evaluation of as-deposited Lasformed<sup>SM</sup> Ti-6Al-4V, a Laser Additive Manufacturing (LAM) process, is the subject of the current work. Distinct features of the macrostructure include: large columnar prior- $\beta$  grains (the initial solid to form upon cooling from the melt) have grown through multiple deposited layers due to epitaxial growth from previously solidified layers; a well defined heat affected zone; the presence of "layer bands," which are speculated to be a result of macrosegregation in the solidifying melt puddle and/or the complex thermal history that the part received as it was built, layer by layer. The microstructure of the layer band consists of larger colonies of acicular  $\alpha$  outlined in transformed  $\beta$ , whereas the adjacent material consists of smaller colonies having the same type of structure.

### INTRODUCTION

Lasforming<sup>SM</sup> is a Laser Additive Manufacturing (LAM) process developed by AeroMet Corporation, which combines high power laser cladding technologies with the advanced methodologies of rapid prototyping to manufacture complex, near-net shape metal parts.<sup>1,2</sup> Figure 1 is a schematic of the LasForm<sup>SM</sup> process. Gas atomized or pre-alloyed powders are introduced into the focal point of a high power laser (18 kW CO<sub>2</sub>) and a layer of molten material is deposited onto the substrate (or previously deposited layer). The part is rastered in the x-y plane to build an individual layer, and then stepped down in the z direction to start a new layer. Oxygen levels are controlled during the fabrication of the part by purging of the chamber with argon, allowing for production of titanium parts having less than 0.10 wt% dissolved oxygen. Fully dense, near-net shape structures (Figure 2) can be built at a rate of 2 to 15 pounds per hour. AeroMet has produced parts having various geometries from Ti-6Al-4V, Ti-6242, and commercially pure (CP) titanium using the LasForm<sup>SM</sup> process.

The current work is a microstructural investigation of as-deposited Ti-6Al-4V parts built

### The AeroMet<sup>SM</sup> Laser Additive Manufacturing Process

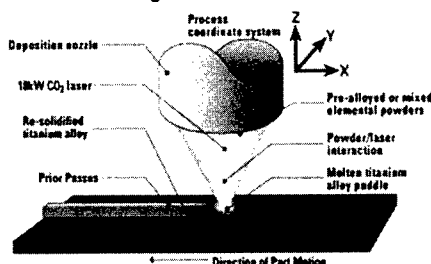


Figure 1: The AeroMet Lasforming<sup>SM</sup> process.<sup>3</sup>

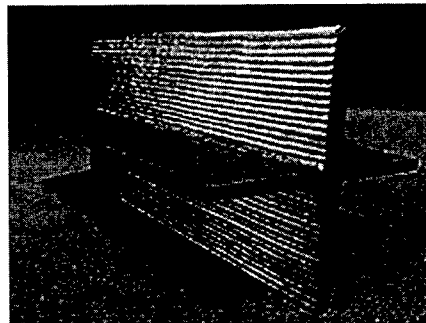


Figure 2: A "rib-on-web" Lasformed<sup>SM</sup> part where linear Ti-6Al-4V ribs (7.6 cm high, 1.3 cm wide) have been deposited on a Ti-6Al-4V plate. The part shown is 33 cm long, 15.2 cm high, and 15.2 cm wide.<sup>3</sup>

using the LasForm<sup>SM</sup> process. Understanding of the microstructure formed as a result of the complex thermal history experienced during the building of a part is the primary step in using LAM as a tool to build functionally gradient materials. Work has been completed at Sandia National Labs on understanding the microstructural development using the Laser Engineered Net Shaping (LENS<sup>TM</sup>) process to build H13 tool steel parts.<sup>4,5</sup> In the Sandia study, a thermocouple was used to measure the in-situ temperature excursions as a function of time resulting from layers being deposited to build the H13 tool steel part. Currently, experimental thermal history data from the manufacturing of Ti-6Al-4V parts is not available to the authors of this paper; therefore, one possible thermal excursion “scenario” will be presented in order to explain the formation of particular microstructures and to show the importance of such data.

## EXPERIMENT

Lasformed<sup>SM</sup> Ti-6Al-4V test coupons, similar to the one shown in Figure 3, were received from AeroMet to undergo microstructural evaluation. Each deposited layer was about 6 mm thick; however, each ripple seen in the photograph below is about 3 mm thick. The substrate is 6 mm thick Ti-6Al-4V plate, mill annealed at 700-730 °C for 2 hours.

### Sample Preparation

Micrographic specimens were excised from the as-deposited coupons using a non-intrusive sectioning saw. A height-width profile (y-z plane in Figure 1) was polished and etched to reveal the microstructure. The etchant was a solution containing 100 ml of deionized water and 5 ml of hydrofluoric acid and was applied for 10 seconds.

### Hardness Measurements

Vickers macrohardness and microhardness measurements were taken from the bottom to the top of the as-deposited part in order to determine if there was a hardness profile as a result of the temperature excursions experienced during the part build. Each indentation was measured 3 times in order to minimize error. Vickers macrohardness measurements were made using a load of 20 kgf applied for 10 seconds. For the microhardness measurements, a load of 300 gf was applied for 10 seconds.

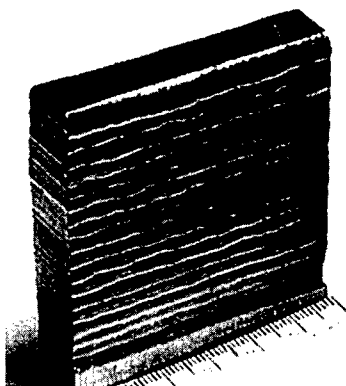


**Figure 3:** As-deposited Ti-6Al-4V Lasformed<sup>SM</sup> coupons.

## RESULTS

The as-deposited macrostructure along the height and width of the part is shown in Figure 4. There are several distinct features shown in this photograph, including the heat-affected zone (HAZ) in the substrate (Region A), large columnar prior- $\beta$  grains, and the presence of equally spaced horizontal bands near the cusps of joining layers (layer bands, Region B). The layer bands appear as a thin strip of darker material running along the width of the part. Each of these areas is examined in greater detail in Figures 5 through 10. Region C is an area containing the last three layers deposited, which are absent of layer bands.

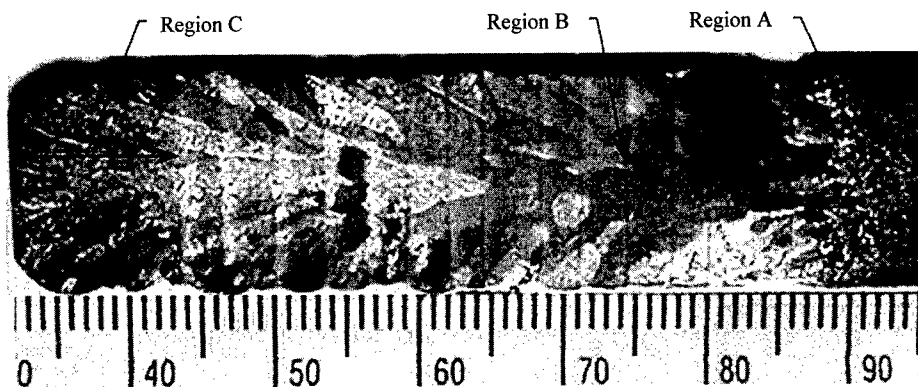


**Figure 4:** Photograph of the as-deposited macrostructure showing the heat-affected zone (A), large columnar prior- $\beta$  grains (entire part), layer bands (B), and a region absent of layer banding (C).

In Figure 5, we see the heat affected zone (HAZ) of the substrate and the transition from equiaxed to columnar prior- $\beta$  grains for the first 3 layers deposited. The HAZ is characterized by smaller, equiaxed prior- $\beta$  grains nearest to the bottom of the substrate (i.e. base metal) which become larger at the top of the substrate. The prior- $\beta$  grains change from an equiaxed to a columnar shape in the area where the first deposited layer is located. Initial solidification of the columnar grains occurs epitaxially from the grains in the base metal, or previously deposited layers, due to similarities in the composition and surface energies of the metal. This allows for the columnar grains to continue growing across layers as shown in Figure 4 and 6. In Figures 4 and 5 it is shown that the large columnar prior- $\beta$  grains are oriented towards the substrate. The cause of this aligned orientation is that during high-energy processes, such as welding and laser deposition of thick layers, the growing grains align themselves with the steepest temperature

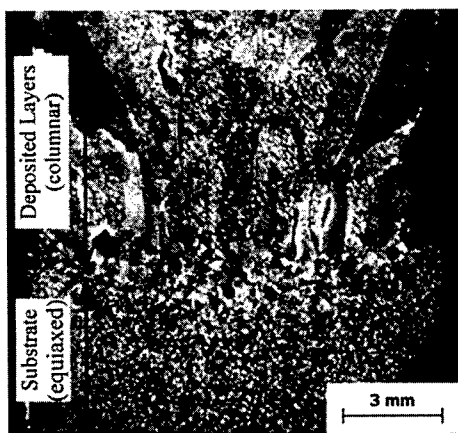


**Figure 5:** Enlarged area of the heat affected zone in the as-deposited material showing the transition from equiaxed to columnar prior- $\beta$  grains.

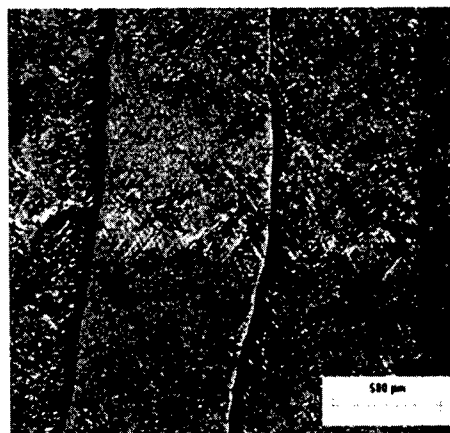


**Figure 6:** Micrograph showing large columnar prior- $\beta$  grains that have grown through a layer in the as-deposited material. A layer band runs horizontally through the micrograph.

gradients.<sup>6</sup>

Figure 7 shows a layer band in relation to the cusp of two joining layers. Typically, these horizontal layer bands form about 500  $\mu\text{m}$  above the cusp. Bands were visible as regions of darker color on all of the as-deposited coupons. A line appeared at every layer; with the exception of the top two layers as shown in Figure 4 (Region C). The microstructure of the as-deposited material (Figure 8) consists of a Widmanstätten structure: acicular  $\alpha$  outlined in  $\beta$  with discontinuous  $\alpha$  at prior- $\beta$  grain boundaries. A layer band can be described as coarse colonies of acicular  $\alpha$  (transformed  $\beta$ ) Widmanstätten structure. A colony is defined here as several parallel needles (grains) of acicular  $\alpha$  aligned along the same  $[110]$  direction. The colonies in the adjacent material are smaller than those that define a layer band. Representative micrographs taken from the layer band and in the adjacent material show the difference in colony size (Figures 9 and 10). Theories for this banding effect will be presented later in the paper.

Vickers microhardness measurements were made horizontally along width of the as-deposited material on a layer band and in the adjacent layer. Vickers macrohardness was measured along the vertical profile of the part (substrate to the top of the part). There was no distinguishable difference in hardness in the as-deposited material as shown in Table I.

Initially, three theories for the appearance of the layer bands were proposed, including, oxidation, segregation of solute, and thermal cycling effects. It was thought the surface of each freshly deposited layer would oxidize, forming an  $\alpha$ -case (the  $\alpha$  phase is stabilized by oxygen

**Table I:** Vickers hardness measurements for as-deposited Ti-6Al-4V.

<i>Measurement</i>	<i>Average Vickers Hardness</i>
Horizontal, On Layer Band	$351 \pm 21 \text{ HV}_{30\text{gf}}$
Horizontal, In Layer	$347 \pm 13 \text{ HV}_{30\text{gf}}$
Vertical, All Data	$344 \pm 7 \text{ HV}_{20\text{kgf}}$
Vertical, On Layer Band	$346 \pm 4 \text{ HV}_{20\text{kgf}}$
Vertical, In Layer	$346 \pm 6 \text{ HV}_{20\text{kgf}}$

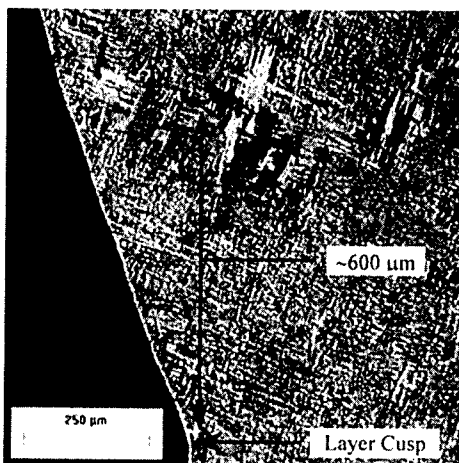


**Figure 7:** Micrograph showing position of layer band in relation to a layer cusp. The distance is approximately 600  $\mu\text{m}$ .

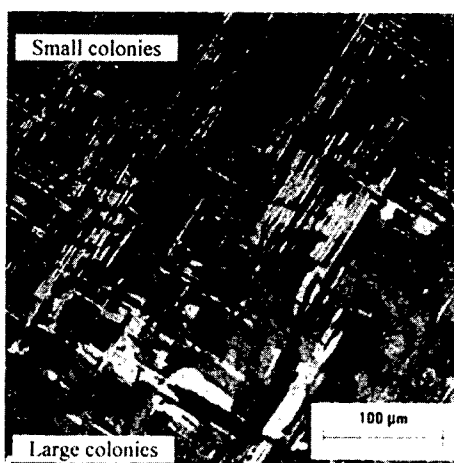


**Figure 8:** Difference in the size of acicular  $\alpha$  colonies in the layer band and surrounding material.

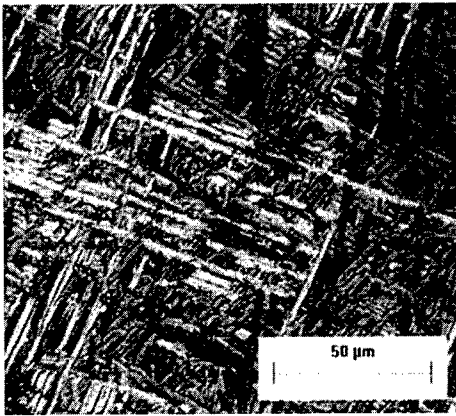


**Figure 9:** As-deposited microstructure of the material adjacent to a layer band showing smaller colonies of acicular  $\alpha$ .  $\beta$  is found between the  $\alpha$  grains.



**Figure 10:** Microstructure of a layer band in the as-deposited material consisting of coarse colonies of acicular  $\alpha$  outlined in  $\beta$ .

interstitials). As the next layer is deposited, the  $\alpha$ -case of the previous layer would be “buried” in the microstructure. Oxidation effects were ruled out as a cause of the layer band for several reasons. First, the hardness both on and off of the layer band were very similar, whereas an  $\alpha$  case is described as hard and brittle.<sup>7</sup> Secondly, an  $\alpha$ -case is not observed on the free surface of the part under the microscope, nullifying the likelihood of the  $\alpha$ -case forming on the interior. Lastly, the Lasforming<sup>SM</sup> process is done in a relatively inert atmosphere, suggesting that little or no oxidation should occur.

The second hypothesis for the formation of the layer band is macrosegregation of solute in the solidifying material. Macrosegregation is defined as segregation that extends over several grain diameters. The type of macrosegregation that is described most often in literature on fusion welding is termed transverse solute banding.<sup>8-12</sup> The bands normally appear as curvilinear contours on the polished and etched surfaces of fusion weldments. These bands are attributed to thermal variations in the weld pool, which periodically change the solid-liquid interface velocity.<sup>8,9,11</sup> Electron microprobe studies have shown that in titanium alloys, transverse solute banding is a result of vanadium and aluminum segregation.<sup>9</sup> The bands seen as a result of the Lasforming<sup>SM</sup> process are linear along the width of the part, not curvilinear as in fusion welding processes. The bands are oriented normal to the direction of heat flow<sup>9</sup>, which is one dimensional in the build of the Lasformed<sup>SM</sup> part (free convection and radiation effects are ignored). In fusion welding the heat is conducted in two or three dimensions (curvilinear isotherms) due to the close proximity of the substrate to the fusion zone.

The third hypothesis for the presence of layer bands in the Lasformed<sup>SM</sup> material is due to the multiple thermal cycles that a fixed point sees during the build of the part. One could imagine several thermal excursions to different regions in the Ti-6Al-4V phase diagram. The cooling rate in similar LAM processes<sup>4</sup> and fusion welding<sup>12</sup> can range from 10 to 10,000 °C/s. In Ti-6Al-4V, subsequent reheating of the build into different phase fields coupled with rapid cooling rates could lead to a variety of microstructures over a short distance. For instance, if a narrow region of the part was heated into the  $\beta$  phase field and cooled rapidly, the structure would most likely transform to  $\alpha'$  or  $\alpha''$  (martensite) +  $\beta$  as opposed to nucleation and growth of  $\alpha$  +  $\beta$  at slower cooling rates. As the build height increases, the heat source is further from a



fixed point in the build, thereby decreasing the magnitude of the temperature excursions. This allows for decomposition of the  $\alpha'$  or  $\alpha''$  to an  $\alpha+\beta$  structure. This is a logical series of events that could lead to the formation of layer bands in a LAM process.

## CONCLUSION

An initial investigation of the as-deposited microstructure in Lasformed<sup>SM</sup> Ti-6Al-4V is currently underway. The as-deposited macrostructure of the polished and etched material exhibited large columnar prior- $\beta$  grains, a well-defined heat-affected zone, and the presence of horizontal layer bands located just above the cusps of each layer. The microstructure of the layer bands revealed larger colonies of acicular  $\alpha$  outlined in transformed  $\beta$ , whereas in the adjacent material, smaller colonies were found. Vickers hardness measurements proved that the layer bands and adjacent material had the same hardness. It is speculated that the layer bands are a result of macrosegregation of aluminum and vanadium in the solidifying metal and/or the complex thermal history each layer receives as subsequent layers are deposited. Further analytical work needs to be completed to justify these theories. Heat treatment of the as-deposited material as well as a computer model of the Lasforming<sup>SM</sup> process is currently underway.

## ACKNOWLEDGEMENTS

The authors would like to thank Dr. Kevin Slattery of Boeing-Phantom Works and Dr. Frank Arcella at AeroMet for their assistance. We would also like to thank Mr. Ben Hailer and Mr. Jeffrey Schultz for their informative discussions and Mr. David Berry for his technical assistance. This research is sponsored by Boeing and ONR under contract number N00014-98-3-0022.

## REFERENCES

1. F.G. Arcella, D.H. Abbott, and M.A. House, Presented in the Rapid Prototyping Session of the 1998 Powder Metallurgy World Conference and Exposition, Granada, Spain, October 18-22, 1998.
2. F.G. Arcella, D.H. Abbott, and M.A. House, AIAA Paper 2000-1465, Presented at the 41st AIAA Structures, Structural Dynamics & Materials Conference, Atlanta, GA, April 11, 2000.
3. AeroMet Corporation web site: <http://www.aerometcorp.com>
4. J. Brooks, C. Robino, T. Headley, S. Goods, M. Griffith, in *Proceedings of the Solid Freeform Fabrication Symposium*, edited by D.L. Bourell, J.L. Beaman, R.H. Crawford, H.L. Marcus, and J.W. Barlow (Austin, TX, 1999) pp. 375-382.
5. M.L. Griffith, M.E. Schlienger, L.D. Harwell, M.S. Oliver, M.D. Baldwin, M.T. Ensz, M. Essien, J. Brooks, C.V. Robino, J.E. Smugeresky, W.H. Hofmeister, M.J. Wert, and D.V. Nelson, *Materials and Design* **20**, pp. 107-113 (1999).
6. K.E. Easterling, *Introduction to the Physical Metallurgy of Welding*, 1<sup>st</sup> ed. (Butterworths, Boston, 1983), pp. 52-59.
7. Boyer, Rodney R., in *Metals Handbook: Metallography and Microstructures*, 9<sup>th</sup> ed., vol.9, (American Society for Materials, Materials Park, OH, 1985) pp. 458-475.
8. W.A. Baeslack III, *Mat. Sci. Letters*, **1**, pp. 229-231 (1982).
9. A.T. D'Annessa, *Weld. J.* **45**, pp. 569s-576s (1966).
10. G.J. Davies, J.G. Garland, *Int. Metallurgical Reviews* **20**, pp. 83-106 (1975).
11. W.A. Baeslack III, D.W. Becker, and F.H. Froes, *JOM* **36** (5), pp. 46-58 (1984).
12. W.A. Baeslack III, J.R. Davis, and C.E. Cross, in *ASM Handbook: Welding, Brazing, and Soldering* 9<sup>th</sup> ed., vol. 6, (ASM Intl., Materials Park, OH, 1993) pp. 507-523.

## UNDERSTANDING THE MICROSTRUCTURE AND PROPERTIES OF COMPONENTS FABRICATED BY LASER ENGINEERED NET SHAPING (LENS)

M. L. Griffith\*, M. T. Ensz\*, J. D. Puskar\*, C. V. Robino\*, J. A. Brooks\*\*, J. A. Philliber\*\*, J. E. Smugeresky\*\*, †W. H. Hofmeister

\*Sandia National Laboratories, Albuquerque, NM 87185

\*\*Sandia National Laboratories, Livermore, CA 94551

†Vanderbilt University, Department of Chemical Engineering, Nashville, TN 37235

### ABSTRACT

Laser Engineered Net Shaping (LENS) is a novel manufacturing process for fabricating metal parts directly from Computer Aided Design (CAD) solid models. The process is similar to rapid prototyping technologies in its approach to fabricate a solid component by layer additive methods. However, the LENS technology is unique in that fully dense metal components with material properties similar to wrought materials can be fabricated. The LENS process has the potential to dramatically reduce the time and cost required realizing functional metal parts. In addition, the process can fabricate complex internal features not possible using existing manufacturing processes. The real promise of the technology is the potential to manipulate the material fabrication and properties through precision deposition of the material, which includes thermal behavior control, layered or graded deposition of multi-materials, and process parameter selection.

### INTRODUCTION

Direct laser metal deposition processing is a promising manufacturing technology, which could significantly reduce the length of time between initial concept and finished part. To facilitate adoption of this technology in the manufacturing environment, further understanding is required to ensure routine fabrication of robust components with desired material properties. This requires understanding and control of the material behavior during part fabrication. This paper describes our research to understand solidification aspects, thermal behavior, and material properties for laser metal deposition technologies.

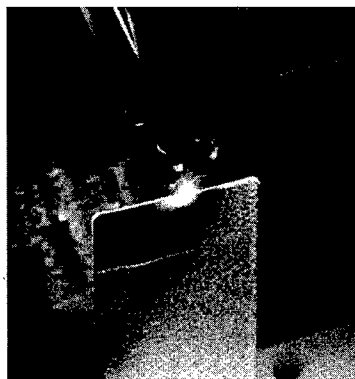
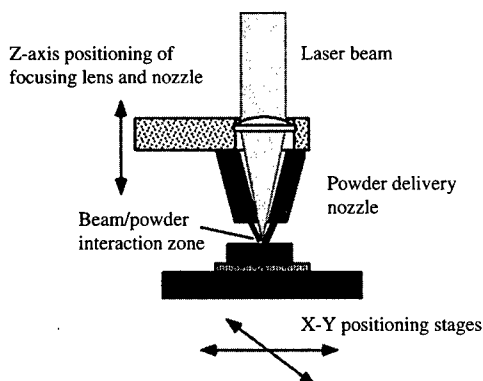


Figure 1: (a) Schematic of LENS process.

(b) In-situ wall fabrication.

---

The specific laser metal deposition technique used for this study is the Laser Engineered Net Shaping (LENS) process [1-5]. Figure 1a shows a schematic of the LENS process. A component is fabricated by focusing a laser beam onto a substrate while simultaneously injecting metal powder particles to create a molten pool. The substrate is moved beneath the laser beam in the X-Y plane to deposit a thin cross section, thereby creating the desired geometry for each layer. After deposition of each layer, the powder delivery nozzle and focusing lens assembly are incremented in the positive Z-direction, thereby building a three dimensional component layer additively. Figure 1b shows the deposition of a single pass wall in 316 stainless steel. LENS components have been fabricated from various alloys including stainless steel, tool steel, nickel-based super alloys, and titanium.

Any LENS fabricated component has a complex thermal history. It is important to understand the bulk and transient thermal behavior to reproducibly fabricate parts. The ultimate intent is to monitor the thermal signatures and to incorporate sensors and feedback algorithms to control part fabrication. With appropriate sensors and feedback, the geometric properties (accuracy, surface finish) as well as the materials' properties (e.g. strength, ductility) of a component can be designed into the part through the fabrication parameters.

To advance direct fabrication capabilities, the LENS process must be able to accommodate a wide range of materials and deposition styles. Over the past few years, we have built up an extensive material database to understand the range of materials processable by LENS. However, because LENS is a precision, point by point, fabrication process, we have expanded the deposition capability to include composites and graded structures [6]. Therefore, the designer can tailor physical properties critical to component performance. Examples include graded deposition for matching coefficient of thermal expansion between dissimilar materials, layered fabrication for novel mechanical properties, and new alloy design where elemental constituents and/or alloys are blended to create new materials.

In this paper, we will discuss our efforts to understand, model, and control microstructural evolution and material properties. We will also show advanced capabilities that are possible with a precision deposition process to tailor and enhance performance.

## **MATERIAL PROPERTIES**

### Material Database

As stated in the introduction, many alloys have been used to fabricate parts by LENS. Table I is a partial list of the room temperature mechanical properties for alloys ranging from stainless steel to titanium to nickel-based alloys. In most cases, the LENS properties are as good as if not better than the traditionally fabricated material. For stainless steel 316 (SS316), the yield strength is double that of wrought, while retaining a ductility of nearly 50%. This is most likely due to Hall-Petch grain size refinement, where finer grain sizes results in higher yield strengths. Typical LENS-processed grain sizes range from 1-10 microns, where traditional wrought material is around 40 microns. At 40 microns, this translates to a yield strength of 30 ksi, versus a 1 micron grain size should be equivalent to a yield strength 67 ksi [7]. As-process LENS SS316 has a yield strength of 63 ksi, indicating that grain size refinement is controlling strength properties.

**Table I:** Room temperature mechanical properties for various alloys fabricated by LENS. LENS properties are from as-process parts except where noted (\*annealed, \*\* solution treated + annealed). LENS properties are compared to wrought material except when heat treated (HT), and properties are compared to same HT for traditional processing.

MATERIAL	UTS (KSI)		YTS (KSI)		EI (%)	
	Wrought	LENS™	Wrought	LENS™	Wrought	LENS™
SS 316	85	110	34	63	50	46
SS 304L	---	95	40	47	55	70
H-13	250	247	210	212	12	1-3
Ti-6Al-4V*	135	130-145	124	120-140	10	1-16
IN718**	200	203	168	162	20	16
IN 625	121	135	58	89	37	38
IN 600	---	106	---	62	---	40



#### Effect of Layered Deposition

For LENS components that will be used in the as-processed state, it is important to understand the effect of layered deposition and the many layer interfaces on the resulting mechanical properties. In the worst case, the layers are not well fused during fabrication, forming large pores, resulting in poor mechanical properties. But for fully dense material, it is necessary to determine the effect of the layered deposition on resulting performance. This will be important as more complex schemes are used to deposit material (e.g. multi-axis).

Simple sample geometries were chosen where the tensile direction is either parallel (H) or perpendicular (V) to the layers. Table II shows the results for two stainless steel alloys and two nickel superalloys. The stainless steel alloys show the greatest effect of the layered deposition, where the strengths are lower for the vertical samples. This is most likely due to stress state condition where the layers are perpendicular to the pull direction and any imperfections will initiate fracture. Inspection of the fracture surfaces shows fracture initiation occurs at a layer interface [8]. However, microstructural inspection does not reveal any defects or other features at the interface that would result in this behavior. The yield strengths are much higher for the horizontal samples, with a tradeoff in ductility. The horizontal specimens do show secondary cracks forming at the interface, further indicating that there is some sort of weak microstructure at the interface. Further microstructural analysis is required to understand the effect of the interfaces on resulting properties.

The nickel superalloys show little effect of the layered deposition, and variations in properties are more likely a result due to the small sampling of parts. It should be noted that many LENS parts are post-heat treated, and after a solution heat treat, the layered deposition structure completely disappears.

**Table II:** A comparison of build direction on as-processed room temperature tensile properties for two stainless steel and two nickel alloys.

	<b>MATERIAL</b>	<b>UTS (KSI)</b>	<b>YTS (KSI)</b>	<b>EI (%)</b>	
<b>V</b> 	SS 316-V	115	65	66	
	SS 316-H	117	86	30	
	SS 304L-V	95	47	70	
	SS 304L-H	103	65	59	
	IN 625-V	135	89	38	
	IN 625-H	136	75	37	
	IN 690-V	88	56	45	
	IN 690-H	108	63	48	
	<b>H</b> 				

#### Effect of Process Parameters

One of the main goals of this research is to determine the effect of various process parameters on resulting material properties. With an understanding of their effect, we hope to predict and tailor the final performance behavior. An initial set of experiments was performed using H13 tool steel. Simple hollow boxes (shell build), one line wide, were fabricated with the following dimensions and deposition parameters:

Size: 101.6 mm x 101.6 mm x 152.4 mm

Layer increment = 250  $\mu$ m

Power: 200, 250 and 300 Watts

Velocity: 5.92, 7.62, and 9.31 mm/s

By changing the power and velocity values, the deposition energy or thermal input is varied which could have an effect on final strength and ductility properties. Figure 2 shows the room temperature tensile results for nine power and velocity combinations. By modifying the deposition energy, one can tailor the strength and ductility values. For low energy input, through low power or high traverse velocity, the molten bead will solidify quickly resulting in high yield and ultimate tensile strength values. If the performance requires significant ductility or strain capability, parts should be fabricated at high energy input using high power and/or slow traverse velocity. As with many fabrication technologies, and in the case of H13 tool steel, one cannot achieve the highest strength and ductility values simultaneously. The designer must consider what are the performance priorities and match the processing conditions to achieve those properties.

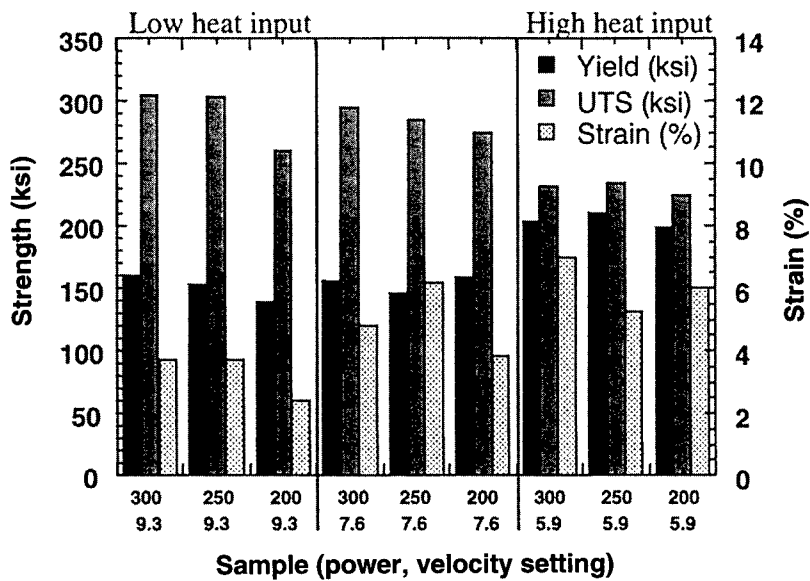


Figure 2: Comparison of room temperature tensile properties for H13 tool steel shell build samples fabricated at various power and velocity values.

## MATERIAL UNDERSTANDING AND CONTROL

In order to understand the development of structure and properties in the solidified material, it is important to know the thermal gradients and cooling rates in and around the molten pool. These gradients control the morphology and size of the first solid to form, and are a primary factor in determining the properties of the sample. Thermal measurements, microstructural studies, and modeling can be combined to develop process parameters to control microstructural development and tailor the properties of samples for particular applications.

### Thermal Imaging

It is known intuitively that a thermal gradient exists across the molten pool and into the bulk material created by the LENS process. The nature and extent of this gradient has not been fully characterized. Since mechanical properties are dependent upon the microstructure of the material, which in turn is a function of the thermal history of solidification, an understanding of the temperature gradient induced by LENS processing is of special interest. It would be particularly beneficial to use non-invasive thermal imaging to measure the temperature profile and gradients and to use these thermal profiles in feedback control.

Preliminary experiments were conducted using ultra high speed digital imaging techniques [9-11] during LENS processing to provide insight as to the size of the molten pool and the thermal gradients in 316 stainless steel (SS316) samples fabricated using the LENS process. Figure 3 shows a typical view of the molten pool seen from the top. The image has

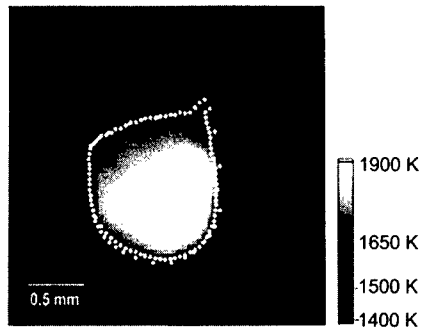


**Figure 3:** Image of molten pool during LENS processing. Dotted outline represents the solidification interface temperature, 1650 K, for stainless steel 316.

been converted to temperature and colorized according to the adjacent scale. In the figure, the bead motion is from top to bottom, as signified by the thermal tail. The solidification interface, or pool area, at 1650 K is outlined and this is monitored in real time. Note there is an abundance of extra energy or superheat within the molten pool (greater than 250 K), which will effect the thermal gradients and solidification microstructures.

The thermal profiles of the build reveal interesting non-linearities in the build process. Profiles were compiled for wall geometry builds as a function of laser power. These are presented in Figure 4 for SS316 alloy. The laser power for each profile is shown in the legend. The molten pool size increases with power up to 275W. Above 275W the energy of the laser drives the pool temperature up without significant change in the length of the molten zone. Note also that the slopes of the temperature profiles outside the molten zone generally increase as the power decreases. Higher power results in more bulk heating of the sample away from the molten zone. This results in a lower cooling rate in the sample after solidification. For example, the cooling rate of the 275W sample 0.5 mm from the solid-liquid interface is twice that of the 410W sample. The initial scale of the microstructure, however, should be determined by the cooling rate at the solid-liquid interface.

A complete series of line builds was analyzed to determine the cooling rate at the solid-liquid interface. These determinations are shown in Figure 5. At the interface the cooling rates are substantially higher at the low power levels and remain fairly constant at the higher powers. Thus, the highest quench rates are available at the lowest power, when the molten zone is small. As the laser power is increased, the quench rate at the interface settles at 1000-1500 K/s. All these results are for thin-walled features which show a great change in thermal gradients for changes in power. In contrast, for bulk solid fabrication, the cooling rates are not so varied. At the highest powers, the cooling rate is much lower, about 500 K/s, so that one may expect a more coarsened microstructure due to grain growth. With information about temperatures in and around the molten pool, pool size, and thermal gradients, we hope to utilize in-situ control to improve the capabilities of parts fabricated by LENS.

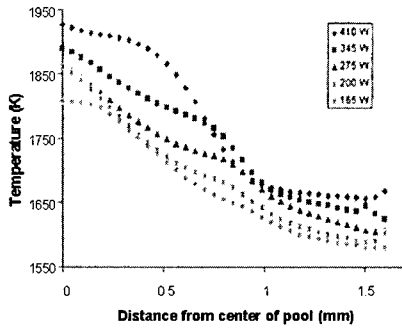


**Figure 4:** Thermal profiles from the center of the molten pool along the direction of translation for several different laser power settings.

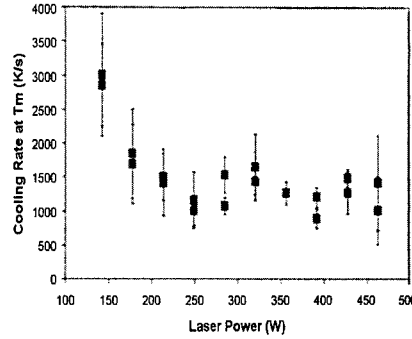


**Figure 5:** Cooling rates calculated from a large series of images as a function of laser power.

In-situ Control of Thermal Signature using Visible Imaging

With an understanding of the molten pool temperatures, thermal gradients, and steady state pool sizes, this information can be utilized to control the process. By matching the pool area to the specific thermal condition, one can extend the overhang capability in a 3-axis LENS system. Figure 6 shows a thin-walled hollow tube, two lines wide, with a 40° overhang. Without any control over the thermal behavior or molten pool area, only a 20° overhang is possible. Now, the pool area is matched to the geometric condition, in this case supported versus partially supported sections, to maintain a consistent, reliable build at 40°.

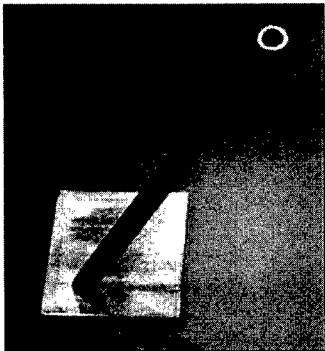


**Figure 6:** Photo showing advanced capability using closed loop control to fabricate double thick wall tube with 40° angle.

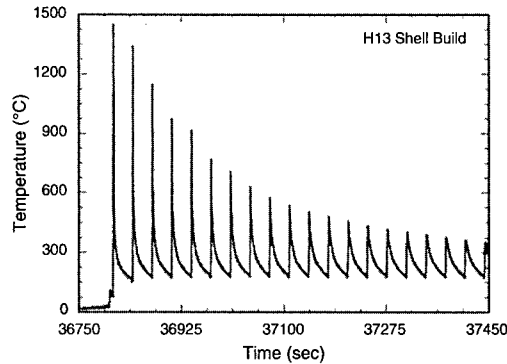


**Figure 7:** Temperature traces at one position as twenty layers are deposited on top of thermocouple inserted into H13 LENS shell build.



---

### Thermocouple measurements to determine macro-thermal transients

A relatively easy way to obtain the thermal history during LENS processing is by inserting a thermocouple (TC) directly into the sample during fabrication [9]. Fine diameter (10  $\mu\text{m}$ ) Type C thermocouple wire is used for measurements to ensure no reaction during deposition, and care was taken to insert the TC bead into the deposition zone for accurate temperature measurements. Figure 7 shows the in-situ temperature readings for twenty deposition layers from a representative thermocouple inserted during fabrication of H13 tool steel. Each peak represents the thermocouple response as the laser passes over or near the thermocouple, from initial insertion to subsequent layer depositions. The thermal excursions dampen out when either the energy source moves away from the thermocouple during fabrication of a layer or subsequent layers are deposited. After the initial peak in temperature, approximately 1500 °C, the heat is quickly conducted away in about 15 seconds to a nominal value of 150 °C for the first layer. This initial thermal signature should result in a solidification process producing a high strength microstructure. Yet, for LENS processing, each subsequent pass reheats the previous layers, such that after the fifth layer is deposited, the initial layer still receives thermal excursions to 900 °C. Following thirteen deposition layers, the thermocouple nominally reads 500 °C. This complicated thermal cycling affects the material properties including residual stress and mechanical strength due to tempering or aging effects. This thermal behavior and effect on final properties is discussed in the next section.

### Microstructure Evolution in LENS Fabrication

The characteristics of microstructural evolution in LENS fabrication can be complex due to the thermal transients and are dependent on the alloy system. However, some general considerations can be illustrated by discussion of a specific alloy system and the models which must be developed to describe the response of the alloy to processing. H13 tool steel provides a good example of an alloy system where there are several mechanisms for microstructural changes during processing. The LENS processing of this system has recently been described in more detail [12]. This is a commercially available secondary hardening alloy that is of significant industrial importance that, when conventionally heat treated, exhibits a martensitic structure strengthened by the formation of Mo and Cr containing alloy carbides.

Due to the layer additive nature of the LENS process, the thermal cycles associated with the LENS process can involve numerous reheating cycles. Thus, the goal of any assessment of microstructural evolution is to determine the response of the alloy to these cycles. For a shell build of H13, the peak temperature of the cycle provides a convenient means to classify the cycle and the response of the material. As shown in Figure 8, the build microstructure can be related to the H13 phase diagram, although it must be noted that, given the rapid heating and cooling rates, non-equilibrium conditions exist and the diagram can only be used as a general guide. The microstructure shown was taken from the final portion of the build, and can be separated into three different regions corresponding to peak temperature. Also shown is the height of the individual build passes.

Region I is composed of as-solidified H13 (last pass) and supercritically reheated (fully reaustenitized) material. Some segregation of alloying elements occurs as a result of partitioning during solidification, and little alloy element homogenization occurs due to the slow diffusion rates of substitutional alloying elements in austenite [13]. The exception is carbon for which the diffusivity is much more rapid and a uniform distribution is expected [13]. The supercritical region extends from the liquidus temperature to the ferrite + carbide two-phase region, which on

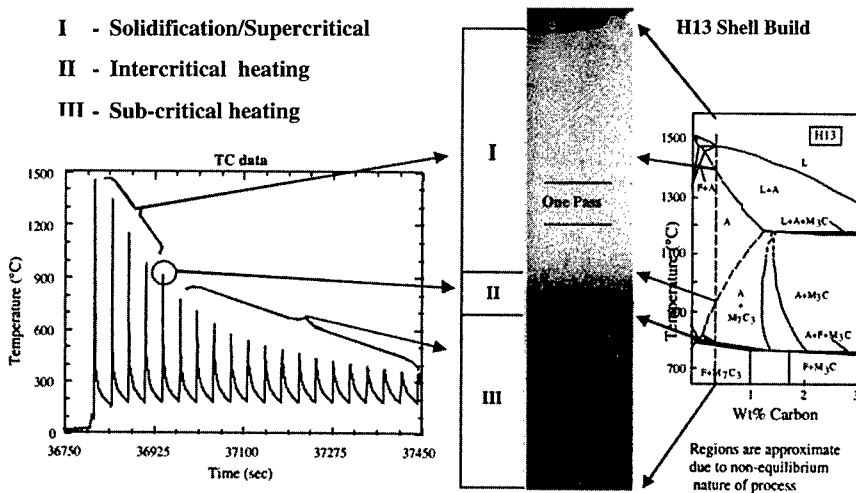


**Figure 8:** Correlation between measured thermal cycles, microstructure, and the phase diagram for H13 (0.04 wt% C) shell build. Three thermal regions are used to describe the behavior. The pass height for these conditions is approximately 0.25 mm.

the equilibrium diagram is approximately 925°C. The light etching material of the supercritical region is untempered martensite (hardness of 59 HRC) in which no carbides were detected using transmission electron microscopy (TEM).

Region II corresponds to material cycled into the intercritical two-phase and narrow three-phase regions shown on the diagram and corresponds to the fifth layer from the top of the build. This material had been previously cycled into the supercritical region, and is the uppermost dark etching region in Figure 8. It is interesting that the height of this region is close to that of a single pass height, and based on the phase diagram, would have contained a thermal gradient of roughly 150°/0.25 mm (~600°C/mm). For the thermal cycles shown, only the peak temperature of the fifth thermal cycle lies within this region. The region therefore consists of a mixture of carbides and martensite (formed from the austenite present at the peak temperature).

Region III contains the material that in addition to having experienced thermal cycles in the upper two regions, also experienced subcritical thermal cycles. For H13, the subcritical cycles can result in additional alloy carbide precipitation and/or carbide coarsening. The final microstructure (in the bulk of the build) therefore consists of martensite containing several types of alloy carbides. In this region, the hardness initially drops to a value of 54 HRC and can further reduce depending on the processing and thermal history [12].

#### Model Descriptions

Given the qualitative descriptions for the microstructural changes which occur in each build region, it remains to develop kinetic models for the various mechanisms. Here again, it is important to recognize that these models are necessarily alloy dependent, and must reflect the principal strengthening mechanisms operative in the alloy. For H13, the supercritically heated region (Region I) is relatively simple because the hardenability and cooling rates during the

---

cycles are both high. Thus the microstructure after the supercritical cycles is essentially single phase fresh (untempered) martensite, although there may be some residual inhomogeneity in the alloy element distributions through the martensite. The solidification segregation of alloy elements can be estimated with knowledge of the solidification partition coefficients and conventional solidification models. The extent to which alloy element concentrations are homogenized during the supercritical passes can be estimated by using conventional diffusion calculations, but it is important to note that the diffusion equations must be solved over the thermal cycle(s) and therefore generally require numerical methods.

The microstructural changes occurring in Region II are perhaps the most severe and difficult to describe from a model perspective. During the intercritical cycles, the martensite present after the supercritical cycles transforms into ferrite, austenite, and carbides. At the temperatures involved (above 800 °C), the rate of this transformation is very high and difficult to analyze experimentally. Efforts are underway to develop kinetics models for these types of transformations (see, for example 14), but for the present overview it is sufficient to note that these models must describe the nucleation and growth of the austenite and carbides as well as the fractions of each constituent (austenite, ferrite and carbide) as they evolve during the temperature transient. Here again, the athermal nature of the process generally necessitates a numerical approach. It is important to note here that steels (and titanium alloys) are the only common commercial alloys that undergo these types of solid state phase transformations. As a result, other alloys, such as Ni-based superalloys, are therefore significantly less complex in terms of microstructural evolution.

Although the influence of the subcritical cycles is less pronounced than that of the intercritical cycles, the effects of these cycles can still be significant in terms of the microstructural evolution and resultant properties. For H13, the principal effects are those related to the precipitation and coarsening of alloy carbides. There are a number of approaches to describing these changes, and an example of one such approach is given in Ref. 12. In that work, hardness was selected as the property of interest, and a simple kinetic model describing the evolution of hardness during the subcritical cycling was developed. Inasmuch as many alloys of commercial interest are precipitation hardenable, models of this type are generally applicable to a wide range of alloys.

## **EXPANDING MATERIAL DEPOSITION CAPABILITY**

One of the unique aspects to LENS is the point by point deposition style. With this type of deposition, it is possible to optimize the build parameters in order to improve fabrication. Software has been developed to allow the designer to choose or correlate the build parameters- such as layer thickness, hatch spacing, power, velocity, material, etc.- to part position. This is useful in many aspects: 1) deposition rate is tailored to feature size, 2) surface finish is controlled through outside border parameters, 3) feature size is correlated to deposition parameters to improve accuracy, and 4) multiple materials can be selected to tailor properties in particular part sections. Figure 9 is a simple example of tailoring the parameters for fabrication of a gear. Finer parameters (layer thickness and hatch) and a hardfacing alloy are used in the tooth section for good surface finish, feature definition, and wear properties. The inside section is an example of bulk deposition with a different alloy where the deposition rate is doubled and the alloy has more ductile properties. Therefore, the choices in deposition parameters and materials open a whole new capability in part fabrication. Results for layered and graded fabrication have been shown elsewhere for LENS [6].



**Figure 9:** An example of tailored parameter and material fabrication for a gear section.

## SUMMARY

In general, the evolution of microstructure and properties during LENS processing can be very complex. We are currently using visible and thermocouple techniques to determine the micro (molten pool) and macro (part) thermal history to gain an understanding of the LENS process. With in-situ monitoring, we have initiated process control through maintaining a setpoint for the molten pool area to extend the overhang capability. This control is coupled with new software to select deposition parameters that are tailored to the part geometry as well as the material performance through multi-material deposition. As we gain more knowledge of the process and resulting properties, we will further develop our models to predict and control the microstructural evolution.

## ACKNOWLEDGMENTS

This work supported by the U. S. Department of Energy under contract DE-AC04-94AL85000. Sandia is a multiprogram laboratory operated by Sandia Corporation, a Lockheed Martin Company, for the United States Department of Energy.

## REFERENCES

1. M. L. Griffith, D. M. Keicher, C. L. Atwood, J. A. Romero, J. E. Smugeresky, L. D. Harwell, D. L. Greene, "Free Form Fabrication of Metallic Components using Laser Engineered Net Shaping (LENS)", *Proceedings of the Solid Freeform Fabrication Symposium*, August 12-14, 1996, Austin, TX, p. 125.
2. D. M. Keicher, J. A. Romero, M. L. Griffith, C. L. Atwood, "Laser Metal Deposition of Alloy 625 for Free Form Fabrication", *Proceedings of the World Congress on Powder Metallurgy and Particulate Materials*, June 16-21, 1996, Washington, D.C.
3. John E. Smugeresky, Dave M. Keicher, Joseph A. Romero, Michelle L. Griffith, Lane D. Harwell, "Using the Laser Engineered Net Shaping (LENS) Process to Produce Complex Components from a CAD Solid Model", *Photonics West SPIE Proceedings - Lasers as Tools for Manufacturing*, Volume 2993, 1997, p. 91.

- 
4. E. Schlienger, D. Dimos, M. Griffith, J. Michael, M. Oliver, T. Romero, J. Smugeresky, "Near Net Shape Production of Metal Components using LENS", *Proceedings of the Third Pacific Rim International Conference on Advanced Materials and Processing*, July 12-16, 1998, Honolulu, HI, p. 1581.
  5. C. L. Atwood, M. L. Griffith, M. E. Schlienger, L. D. Harwell, M. T. Ensz, D. M. Keicher, M. E. Schlienger, J. A. Romero, J. E. Smugeresky, "Laser Engineered Net Shaping (LENS): A Tool for Direct Fabrication of Metal Parts", *Proceedings of ICALEO '98*, November 16-19, 1998, Orlando, FL, p. E-1.
  6. M. L. Griffith, L. D. Harwell, J. A. Romero, E. Schlienger, C. L. Atwood, J. E. Smugeresky, "Multi-Material Processing by LENS", *Proceedings of the Solid Freeform Fabrication Symposium*, August, 1997, Austin, TX, p.387.
  7. B.P. Kashyap, K. Tangri, *Acta metall. mater.*, Vol. 43, No. 11 pp. 3971-3981, (1995).
  8. J. Philliber, J. Smugeresky, B. Somerday, M. Griffith, "Microstructure and Properties of LENS processed 304L Stainless Steel", Presented at the Annual meeting of TMS, Nashville, TN, March 13-15, 2000.
  9. M. L. Griffith, M. E. Schlienger, L. D. Harwell, M. S. Oliver, M. D. Baldwin, M. T. Ensz, J. E. Smugeresky, M. Essien, J. Brooks, C. V. Robino, W. H. Hofmeister, M. J. Wert, D. V. Nelson, "Thermal Behavior in the LENS Process", *Proceedings of the Solid Freeform Fabrication Symposium*, August, 1998, Austin, TX, p. 89.
  10. M. L. Griffith, M. E. Schlienger, L. D. Harwell, M. S. Oliver, M. D. Baldwin, M. T. Ensz, J. E. Smugeresky, M. Essien, J. Brooks, C. V. Robino, W. H. Hofmeister, M. J. Wert, D. V. Nelson, *Journal of Materials Design*, volume 20 number 2/3, June 1999, p 107-114.
  11. W. Hofmeister, M. Wert, J. Smugeresky, J.A. Philliber, M. Griffith, and M Ensz, *JOM*, Vol. 51, No. 7, available from JOM-e online at [www.tms.org/pubs/journals/JOM/9907/Hofmeister/Hofmeister-9907.html](http://www.tms.org/pubs/journals/JOM/9907/Hofmeister/Hofmeister-9907.html).
  12. J. Brooks, C. Robino, T. Headley, S. Goods, and M. Griffith, "Microstructure and Property Optimization of LENS Deposited H13 Tool Steel", *Proceedings of the Solid Freeform Fabrication Symposium*, August, 1999, Austin, TX, p.375-382.
  13. J. A. Brooks, M. I. Baskes, and F. A. Greulich, *Metall. Trans. A*, 22A, (1991), pp. 915-925.
  14. R. C. Dykhuizen, C. V. Robino, and G. A. Knorovsky, *Metall. and Mat. Trans. B*, 30B, (1999), pp. 107-117.

## Microstructures of Laser Deposited 304L Austenitic Stainless Steel

John A. Brooks<sup>1</sup>, Thomas J. Headley<sup>2</sup> and Charles V. Robino<sup>2</sup>  
Sandia National Laboratories, Livermore, CA<sup>1</sup>/Albuquerque, NM<sup>2</sup>

### ABSTRACT

Laser deposits fabricated from two different compositions of 304L stainless steel powder were characterized to determine the nature of the solidification and solid state transformations. One of the goals of this work was to determine to what extent novel microstructures consisting of single-phase austenite could be achieved with the thermal conditions of the LENS process. Although ferrite-free deposits were not obtained, structures with very low ferrite content were achieved. It appeared that, with slight changes in alloy composition, this goal could be met via two different solidification and transformation mechanisms.

### INTRODUCTION

Near net shape fabrication using the LENS (Laser Engineered Net Shape) process has matured to the point that complex three-dimensional shapes can be reliably processed from a CAD file. However, relatively little work has been conducted to determine to what extent the processing conditions, especially the relatively rapid cooling rates, can be utilized to produce unique or novel microstructures. The austenitic stainless steels are often used for their elevated temperature and corrosion properties, and sometimes for their non-ferromagnetic characteristics. However, in cast or welded materials the properties can be degraded for a number of reasons. These materials often exhibit a two-phase structure of austenite with several percent ferrite (0-10%) and in the absence of ferrite, exhibit a considerable amount of microsegregation. At elevated service temperature the ferrite can transform to sigma phase greatly reducing toughness. Ferrite can also affect corrosion behavior and its magnetic characteristics can limit the use of cast material in critical applications. In the absence of ferrite, the high degree of segregation can also degrade corrosion resistance. However, it must be noted that cast, welded and wrought materials containing several percent ferrite are acceptable for many engineering applications. A large amount of work has been conducted on high-energy-density (HED) welding of the 300 series stainless steels and this work has shown that alloy composition can have a large effect on weld structure and the development of unique microstructures [1-9]. In this study, the ability to develop unique structures, i.e. fully austenitic, in LENS built material of 304L alloy was investigated by varying: (1) the  $Cr_{eq}/Ni_{eq}$  ratio of the starting powders within the commercial composition range, (2) the solidification velocity via the travel speed of deposition, and (3) the cooling rate via block build (faster) and shell build (slower) deposition geometries.

### MATERIALS

Thermodynamic programs can be used both to predict the alloy phase diagram and to provide input into solidification models for predicting solidification behavior and microstructures [5,10,11,12]. Using these concepts, two alloys were designed with different  $Cr_{eq}/Ni_{eq}$  ratios [13] within the commercial 304L composition range. The heat compositions and  $Cr_{eq}/Ni_{eq}$  ratios are given in Table I. The specific  $Cr_{eq}/Ni_{eq}$  ratios were chosen based on their potential to produce single-phase austenite structures via two different solidification/transformation mechanisms when subjected to the high solidification velocity and cooling rates of pulsed laser welding. Under these conditions, it was expected that heat #2 would solidify as primary austenite with no residual ferrite, and that heat #3 would solidify as ferrite but then completely transform to austenite, possibly by a massive transformation. This expected behavior can be understood using a schematic of the Fe-Ni-Cr pseudo-binary in figure 1. A casting or conventional weld of heat #2, with  $Cr_{eq}/Ni_{eq}=1.55$ , should solidify as primary ferrite with secondary solidification of peritectic or eutectic austenite. Upon cooling through the two-phase  $\delta + \gamma$  field, much of the

ferrite transforms to austenite by a diffusion-controlled transformation leaving several percent retained ferrite at room temperature [14-17].

**Table I.** Heat compositions and  $Cr_{eq}/Ni_{eq}$  ratios

Heat#	Cr	Ni	Mn	Si	C	$Cr_{eq}/Ni_{eq}$
2	19.7	11.9	1.74	0.59	0.04	1.53
3	20.3	10.5	1.74	0.54	0.03	1.78

Hammer and Svensson equivalents:  
 $Cr_{eq} = Cr + 1.37Mo + 1.5Si + 2Nb + 3Ti$   
 $Ni_{eq} = Ni + 0.31Mn + 22C + 14.2N + Cu$   
 Bal Fe

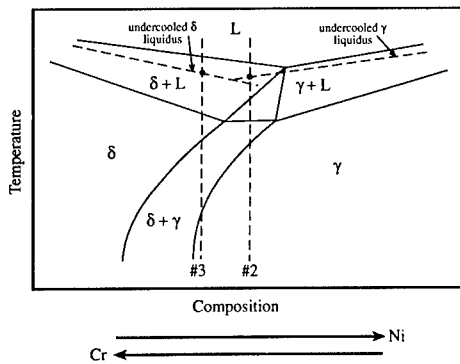


**Figure 1.** Schematic of Fe-Ni-Cr pseudo binary showing how solidification and transformation behavior can be affected by changing  $Cr_{eq}/Ni_{eq}$  ratio and cooling rate.

The faster solidification and cooling conditions of laser processing were expected to produce sufficient undercooling for heat #2 to solidify as single-phase austenite [11,12,18]. It can be seen from the schematic in figure 1 that solidification at the dendrite tip would occur as austenite at a temperature where the heat #2 composition intersects the undercooled austenite liquidus. This occurs at a higher temperature than required for solidification as undercooled ferrite. Likewise a casting or conventional weld of heat #3, with  $Cr_{eq}/Ni_{eq} = 1.78$ , should solidify as primary ferrite. Then during cooling through the  $\delta + \gamma$  field, most of the ferrite would transform to austenite, again by a diffusion-controlled transformation, but at a lower temperature and with more retained ferrite than heat #2 [15,17]. However, laser processing was expected to cause this heat to solidify as fully single-phase ferrite, and if the cooling rate through the  $\delta + \gamma$  field is sufficiently fast to suppress the diffusion-controlled transformation to austenite, then upon reaching the single-phase austenite field the ferrite will transform massively to austenite.

Single-phase austenite structures were predicted for the two heat compositions under laser welding conditions in which cooling rates are  $\sim 10^5$  °C/s. Thus one goal of this work was to investigate whether powders of these compositions could also be fabricated in LENS deposits to yield unique single-phase austenite structures. LENS deposits of both heats were fabricated using three different travel speeds, 8.5, 17, and 34 mm/sec to vary the solidification velocity, and two different configurations, shells and blocks, to vary the cooling rates. The shells were box-like structures 6.35 cm on a side and were made with a single-width line deposit  $\sim 0.5$  mm wide. Multiple passes approximately 0.254 mm high were used to produce the several-cm high shells.

The wall thickness of ~0.5 mm varied with travel speed, with higher velocities resulting in slightly thinner wall thickness. Blocks 7.6 cm long and 9.5 mm wide were built using alternating layers, each made of overlapping passes with ~0.4 mm spacing. The alternating layers were deposited with a 90° orientation between layers. The height of each layer of the several-cm high deposit was approximately 0.254 mm. Cooling rates for the shell builds were measured at ~3500°C/s. Although cooling rates for the block builds were not measured, they are estimated to be a factor of 1.5-2 greater in the interior of the builds than for the shell builds. After the LENS deposits were fabricated, pulsed YAG laser welds were made on some deposits to verify the predictions of the thermodynamic programs and solidification models that single-phase austenite structures would be produced in these specific compositions under very fast cooling rates.

## RESULTS

The microstructures of the pulsed YAG laser welds made on the LENS deposits of both heats are shown in figure 2. Figure 2a shows the single-phase austenite microstructure of heat #2 as predicted for this alloy composition under rapid cooling rates. This microstructure is characteristic of primary austenite solidification. The fine columnar dendritic solidification structure resulting from a small degree of microsegregation, even under the rapid solidification and cooling rates, is clearly visible. Figure 2b shows the microstructure of heat #3 that also appears to be single-phase austenite. It is likely that, as predicted, this weld solidified as single-phase ferrite and transformed completely to austenite during the rapid cooling conditions leaving a fine-grained, single-phase structure. It can be seen that, although both microstructures are single-phase austenite, they differ considerably due to their different solidification and transformation histories.

By contrast, all LENS deposits of both heats contained varying amounts of residual ferrite. The microstructure of a block build LENS deposit of heat #2 is shown in figure 3. The lower magnification of figure 3a shows the two 90°-orientations of the individual LENS deposits. Figure 3b at higher magnification shows a region of overlapping passes resulting in two different growth directions. Unlike the laser weld microstructure, the LENS deposit consists of two phases, ferrite and austenite, resulting from primary ferrite solidification and subsequent transformation on cooling. TEM studies were conducted on the heat #2 block to determine the nature of the ferrite and the degree of microsegregation. A low magnification STEM image is shown in figure 4a. The ferrite (dark phase) is distributed along the center of the original dendrite cores. Evidence of microsegregation is also visible due to the differences in polishing rate resulting from the changes in composition. STEM traces were made in two locations: from ferrite in one cell core to ferrite in the adjacent cell core, and also across several solidification

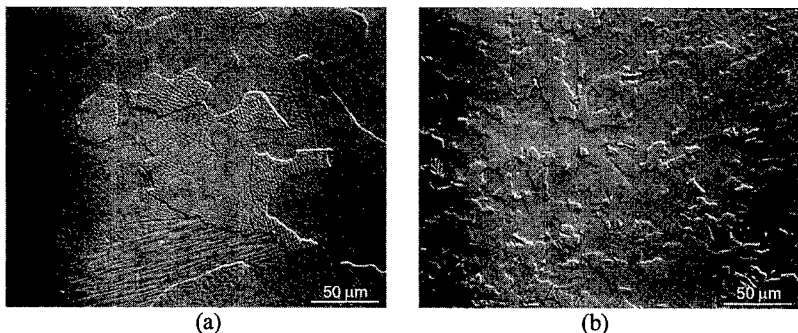


**Figure 2.** Optical microstructures of laser welds made on LENS deposits from (a) heat #2 (note dendrites evident at A), and (b) heat #3.



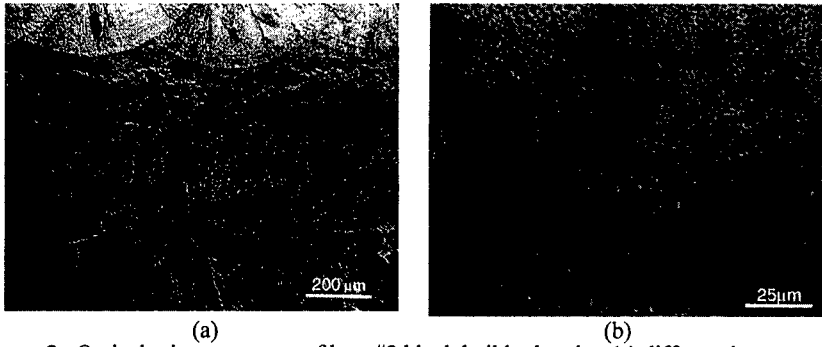
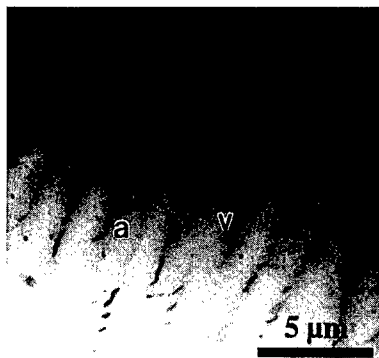
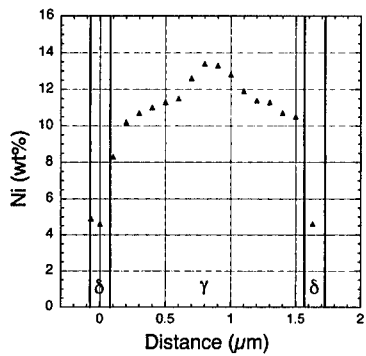


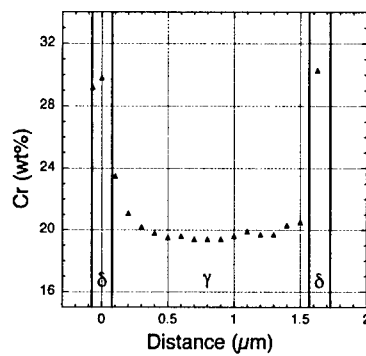
**Figure 3.** Optical microstructures of heat #2 block builds showing (a) different layers and LENS passes. (b) Higher magnification showing region of pass boundary and different solidification growth direction. Dark phase is ferrite along dendrite cores.



(a)



(b)



(c)

**Figure 4.** (a) STEM image from heat #2 block build showing ferrite along dendrite cores. Note both vermicular (v) and acicular (a) morphologies. (b) and (c) Profiles for Ni and Cr between the two ferrite particles (arrows) in (a)

cells free of ferrite. The resulting concentration profiles for Ni and Cr between two ferrite particles within adjacent dendrite cores are shown in figures 4 b and c. It can be seen that the cell boundary located between the ferrite is enriched in Ni and depleted in Cr, while the ferrite is enriched in Cr and depleted in Ni. This segregation behavior is a result of partitioning both during solidification, where Ni partitions to the liquid, and also during the subsequent solid state transformation of ferrite to austenite where Ni partitions to the austenite and Cr to the ferrite. Figure 5a shows a region of the same sample in which the cell boundaries are free of ferrite. The profiles in figures 5 b and c show the Ni and Cr concentrations across the cellular structure where the solidified ferrite transformed completely to austenite. Considerable residual segregation exists as a variation in Ni of ~3wt% and Cr of ~2wt%. These profiles are also characteristic of primary ferrite solidification.

It was difficult to identify individual austenite grains in the STEM and TEM bright field images in heat #2 since much of the grain boundary is coincident within ferrite-austenite boundaries. However, elongated grains ~10  $\mu\text{m}$  wide were clearly visible in TEM dark field and have aspect ratios of ~2-4 to one, with solidification cells oriented parallel to the long direction. TEM results showed there were two general morphologies of the ferrite, both of which can be seen in the STEM image in figure 4a. In some grains an elongated vermicular ferrite structure nearly parallel to the cells existed, while in other grains a more acicular ferrite structure existed at an angle to the cell core. All the ferrite within one grain had the same crystallographic orientation. It was found that the acicular structure exhibited a Nishiyama-Wassermann (N-W) orientation relationship [19, 20] between the ferrite and austenite. The microstructures of the

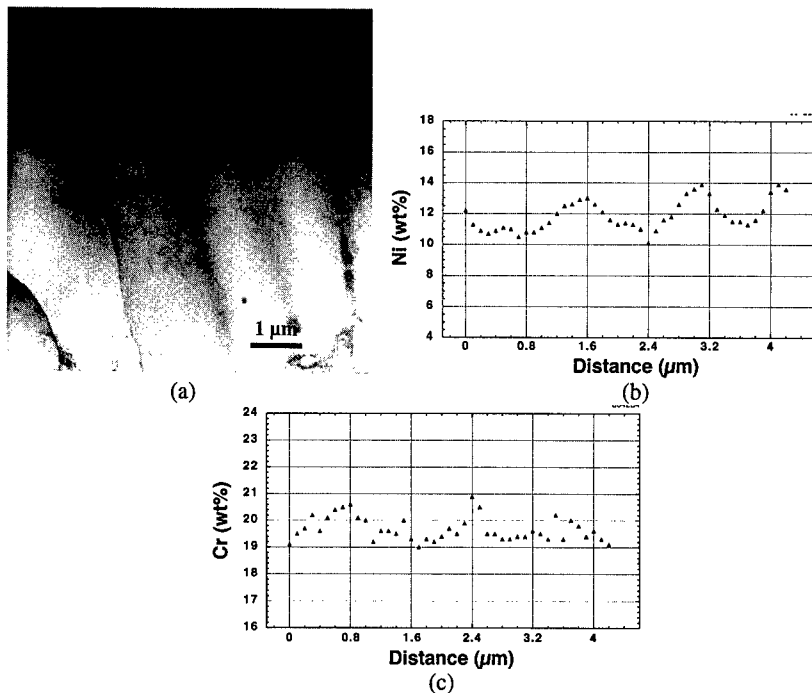


**Figure 5.** (a) STEM image of ferrite-free cellular structure in block build of heat #2 showing location of trace across several cells free of ferrite. (b) and (c) Resulting concentration profiles for Ni and Cr.

shell builds of heat #2 were similar to those of the block builds shown in figures 3 and 4. Also, there was little observable microstructural difference resulting from change in travel speed (i.e. solidification velocity) for both the shell and block builds.

In contrast to heat #2, the microstructures of the shell and block builds of heat #3 were visually quite different, but again changes in travel speed had no apparent microstructural effect. The microstructure of the shell build is shown in figure 6. In the low magnification micrograph in figure 6a the individual passes are clearly visible. A region at the interpass boundary is shown in figure 6b. A fairly complex structure exists with a mixture of grain sizes and internal twins. The dark phase in the microstructure is ferrite, primarily of a lathy morphology [1]. TEM showed that this ferrite was of similar composition to that in heat #2 shown in figure 4, i.e. enriched in Cr and depleted in Ni.

On the other hand, the microstructure of the block build of heat #3 more closely resembled the laser weld in this material shown in figure 2b. The optical microstructure of the heat #3 block build is shown in figure 7. The lower magnification in Figure 7a shows what appears to be a fine-grain, single-phase structure except for a band in the heat-affected-zone (HAZ) at the interpass region apparent near the top of the micrograph. This band contains some second-phase ferrite. A higher magnification image taken near the center of a pass is shown in figure 7b where a more duplex structure exists with large grains near the center of the micrograph and regions of smaller grains at the right side. At this magnification some ferrite is observable as small dark spots, especially in the fine-grain regions.

TEM was also conducted on the block build of heat #3. The solidification cell structure was not as evident as it was in the ferrite-free regions in the build of heat #2. However, there were a few regions where a faint network of slightly denser-appearing material existed that may correspond to solidification cells. Also, there was much less ferrite present than in the block build of heat #2. The austenite grains exhibited a duplex structure, either roughly equiaxed, large grains 10s of  $\mu\text{m}$  in size and often internally twinned, or groups of smaller grains, 2-4  $\mu\text{m}$  in size. This grain structure is consistent with the optical micrograph shown in figure 7b. The groups of small grains tended to have a common crystallographic direction, i.e. texture, although their boundaries were wide-angle boundaries. These smaller grains tended to be elongated and associated with more ferrite particles than the large equiaxed grains. Ferrite particles tended to be located at grain boundaries in the small-grain regions, although some intragranular ferrite was also observed. The ferrite at the grain boundaries tended to be along the elongated boundaries which were roughly parallel from grain to grain. This morphology may mimic the solidification cell morphology, although this has not been verified. If so, the cells would be  $\sim 2 \mu\text{m}$  wide.

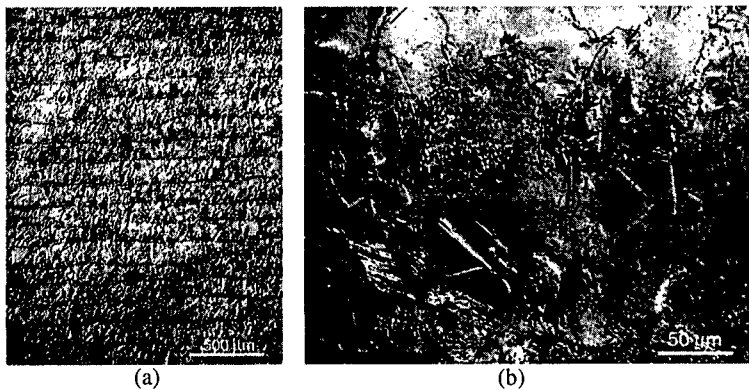


**Figure 6.** Optical micrographs of shell build in heat #3 showing (a) different LENS passes, and (b) higher magnification of interpass region showing ferrite morphology.

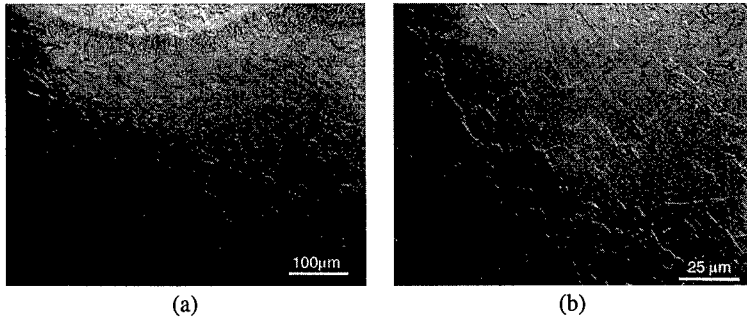


**Figure 7.** Optical micrographs of block build of heat #3. Note in (a) ferrite in HAZ at interpass boundary near top of micrograph and remaining apparent single-phase structure. (b) Note some residual ferrite more highly concentrated in the finer-grain region.

The larger equiaxed grains usually contained a few ferrite particles per grain within the thin foil section, and all particles within a given grain were elongated in the same direction suggesting a prior solidification cell structure. A cellular dislocation structure with tangled walls and cell size typically 0.5-1  $\mu\text{m}$  was also present within the large grains, figure 8a. There was also a prevalence of long, thin ( $\leq 0.1 \mu\text{m}$  wide) ferrite particles on the grain boundaries of the large equiaxed grains, figure 8b. In the limited regions examined it appeared that as much as 10-20% of the grain boundary area contained ferrite. This is significantly more than was found on the grain boundaries in heat #2. Also observed were a few isolated regions of ferrite in long, thin parallel laths, i.e. lathy (or acicular) ferrite, similar to that shown in the optical micrograph of the shell builds in figure 6. Such regions are thought to be associated with the interpass boundaries shown in figure 7a.

STEM EDS analysis was conducted on the heat #3 block build to determine both the composition of the ferrite and to what extent, if any, microsegregation resulting from solidification or solid state transformations existed. In all cases the ferrite was highly enriched in Cr and depleted in Ni compared to the austenite, similar to that shown in figure 4. Results of an analysis for Ni and Cr conducted across austenite in the large grain region are shown in figure 9. Figure 9a shows the trace where the analysis was taken. The profiles in figures 9b and c show

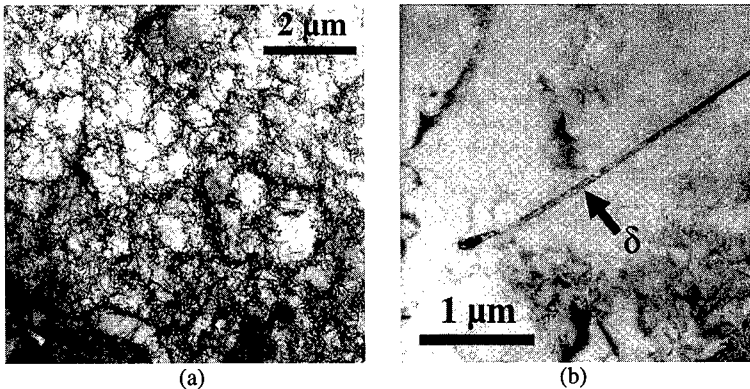
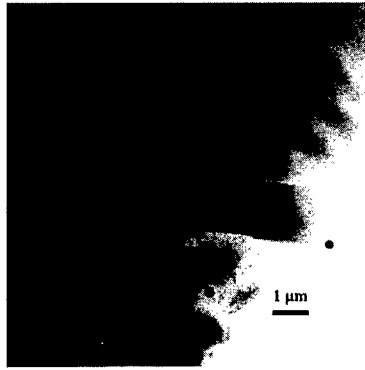
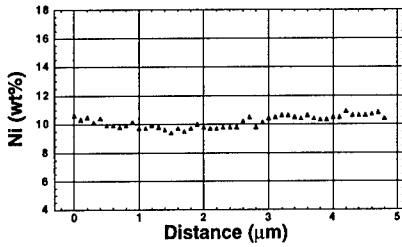


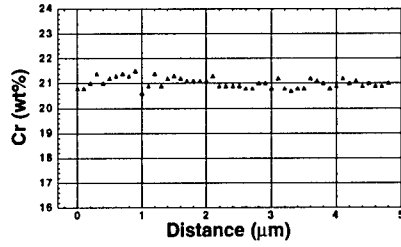
**Figure 8.** (a) Dislocation cell structure in large austenite grain in heat #3 block build. (b) Thin ferrite layer (arrow) on austenite grain boundary.



(a)



(b)



(c)

**Figure 9.** STEM image in center of large grain of heat #3 block build showing trace where EDS analysis was made. (b) and (c) Concentration profiles for Ni and Cr.

that the Ni and Cr concentrations are fairly homogeneous with no clear evidence of microsegregation, suggesting a massive transformation from ferrite to austenite may have occurred. The measured value of both elements varies by only ~1wt%, compared to the ~3wt% variation observed in the heat #2 block build, figures 5 b and c.

## DISCUSSION

There are several mechanisms by which single-phase austenite can be obtained in rapidly solidified 304L deposited material. One is for solidification to occur completely as austenite. Another is for solidification to occur as ferrite, which becomes homogenized during both solidification and cooling in the single-phase ferrite region, and then transforms to austenite during rapid cooling where the transformation occurs massively without any long-range diffusion. If cooling is not sufficiently rapid, partitioning of alloying elements between the two phases occurs during the transformation of ferrite to austenite in the two-phase field, see figure 1. A third possible mechanism exists in lean alloys in which the two-phase field is fairly narrow and the transformation is completed at sufficiently high temperature [21]. In this case the diffusion-controlled transformation of ferrite to austenite may go to completion and leave no retained ferrite.

In heat #2 it was clear that the solidification conditions were not sufficiently rapid to provide the necessary undercooling for solidification to occur as austenite. It was clear from the ferrite morphology and STEM analysis that solidification occurred as primary ferrite. However,

there were some regions of cell boundaries where residual microsegregation of Cr and Ni was detected, figure 5, but the cell cores were free of ferrite. It is likely that these are regions in which the transformation of ferrite to austenite went to completion as discussed above. Grains containing the vermicular ferrite likely solidified in a peritectic reaction with secondary austenite growing from the melt [22], whereas grains containing the acicular ferrite solidified completely as ferrite. In the latter case, austenite then nucleated in the Ni-enriched cell boundaries with the low-energy N-W orientation relationship. Thus heat #2 did not solidify as primary austenite as predicted for the high solidification rates, but this may possibly be achieved by adjusting the  $Cr_{eq}/Ni_{eq}$  ratio to a slightly lower value [17].

With the composition of heat #3, it appeared that the cooling rates of the pulsed YAG laser welds were sufficiently fast to suppress the diffusion-controlled transformation of ferrite to austenite. Instead, the solidified ferrite likely transformed massively to single-phase austenite. However this was not the case for the LENS deposits. In the shell builds, although there were internally twinned large-grain regions, ferrite was distributed throughout the deposit.

The cooling rates of block builds of alloy #3 did produce a structure that was very low in ferrite content. The exception was in some HAZ regions at the interpass boundaries, where more ferrite appeared to form by re-heating during subsequent passes into the ferrite phase field, or two-phase ferrite + austenite field, and did not completely re-transform during cooling. In the remainder of the microstructure almost all the ferrite transformed to austenite during cooling. However, unlike some HED welds [1,5], the residual ferrite and austenite were of much different composition, whereas a massive transformation would occur with little change in composition. Also, in many cases thin regions of ferrite were observed along grain boundaries although no evidence of microsegregation could be detected with STEM EDS in the ferrite-free regions. This lack of segregation was also noted in the massively transformed HED welds.

There was a large difference in grain structure of the block builds made from the two heats. The grains in heat #3 were finer, more equiaxed, faceted, and more internally twinned than those in heat #2. These grain-structure features, lack of microsegregation, and large regions free of ferrite in the block builds are consistent with a massive transformation [23]. However, the large difference in composition between the residual ferrite and austenite shows that those regions of the microstructure containing residual ferrite transformed by long-range diffusion. It is also possible that in the ferrite-free regions, the diffusion-controlled transformation went to completion similar to some of the regions observed in heat #2, figure 4. Thus it is possible that both types of transformation, diffusion-controlled and massive, occurred in heat #3 which would help explain the reduced amount of ferrite in the block builds. It can be expected that the differences in solidification mode, ferrite/austenite vs. fully ferrite, will also affect (reduce) the final degree of microsegregation.

Although a totally single-phase austenitic microstructure was not obtained in this study, it should be noted that this goal can likely be met with further slight adjustments in alloy composition. Nonetheless, the deposits exhibited very good tensile properties. The 0.2% yield strengths of the shell and block builds were ~310 Mpa and ~380 Mpa, respectively. These values are considerably higher than the yield strength of wrought, annealed 304L which is 240 Mpa.

## SUMMARY

Two alloy variations were designed within the commercial composition range of 304L stainless steel to determine to what extent single-phase austenite structures could be fabricated in LENS deposits. Pulsed YAG laser welds on LENS deposits of the two heats did produce single-phase austenite structures, one a direct product of solidification and the other a product of massive transformation of ferrite to austenite. It was found that the LENS fabricated heat of lower  $Cr_{eq}/Ni_{eq}$  ratio, unlike the laser weld, solidified as primary ferrite, likely with some grains solidifying completely as ferrite and others with some secondary solidification of austenite. This was concluded from differences in retained ferrite morphology. However, with a slightly lower  $Cr_{eq}/Ni_{eq}$  ratio, a single-phase austenite structure may be achieved directly as the solidification product. In this case a certain degree of microsegregation would exist.

LENS fabricated heat #3 with the higher Cr<sub>eq</sub>/Ni<sub>eq</sub> ratio solidified completely as primary ferrite. However, unlike the laser weld, not all the ferrite transformed to austenite upon cooling. The amount of ferrite retained was much less in the more rapidly cooled block builds than in the slower cooled shell builds. It was unclear if some of the structure transformed massively, although large differences between ferrite and austenite compositions showed that some, if not all the structure transformed by a long-range diffusion transformation. It is possible that, with slight modifications in composition, the LENS cooling rates of the block builds may be sufficiently rapid to produce a massively transformed, homogeneous single-phase austenite structure.

#### ACKNOWLEDGMENTS

M. S. Oliver fabricated the LENS deposit specimens. A. D. Gardea performed the metallographic preparation. This work was performed at Sandia National Laboratories, a Lockheed Martin Company, for the U.S. Department of Energy under contract number DE-AC04-94AL85000.

#### REFERENCES

1. J. A. Brooks and A. W. Thompson, *International Materials Reviews* **36** (1), 16 (1991).
2. S. A. David and J. M. Vitek, in *Lasers in Metallurgy*, edited by K. Mukherjee and J. Mazumder (TMS-AIME, Warrendale, PA, 1981), p. 247.
3. J. M. Vitek, A. Dasgupta, and S. A. David, *Metall. Trans. A* **14A**, 1833 (1983).
4. S. Katayama and A. Matsunawa, in *Proc. ICALEO*, San Francisco, pp.19-25 (1985).
5. J. A. Brooks, M. I. Baskes and F. A. Greulich, *Metall. Trans. A* **22A**, 915 (1991).
6. J. W. Elmer, S. M. Allen and T. W. Eagar, *Metall. Trans. A* **20A**, 2117 (1989).
7. S. A. David, J. M. Vitek and T. L. Hubble, *Weld. J.* **66** (10), 289-s (1987).
8. Y. Nakao, K. Nishimoto, and W. Zhang, *Trans. JWJ* **119**, 101 (1988).
9. H. Inoue, T. Koseki, S. Ohkita, *ISIJ* **1977**, 1248.
10. W. Kurz and D. J. Fisher, *Fundamentals of Solidification*, (Trans Tech Publications Ltd., Switzerland, 1989).
11. S. Fukumoto and W. Kurz, *ISIJ International* **37** (7), 677 (1997).
12. J. W. Elmer, in *The Metals Science of Joining*, edited by M. J. Cieslak, Perepezko, Kang and Glicksman, (TMS, Warrendale, PA, 1992) pp.123-133.
13. O. Hammer and U. Svensson, in *Solidification and Casting of Metals* (The Metals Society, London, 1979), p. 401.
14. T. Takalo, N. Suutula and T. Moisio, *Metall. Trans. A* **10** (4), 1173 (1979).
15. N. Suutula, Effect of solidification conditions on the solidification mode in austenitic stainless steels, *Acta Universitatis Ouluensis, Series C Technica* **23**, (University of Oulu, Oulu, Finland 1982).
16. N. Suutula, T. Takalo and T. Moisio, *Metall. Trans. A* **10** (4), 512 (1979).
17. C. J. Long and W. T. DeLong, *Weld. J.* **52**, 281-s (1973).
18. B. Laursen, F. Olsen, J. Yardy and T. Funder-Kristensen, in *International Conference on Welding and Joining Science and Technology*, Madrid, Spain, (ASM, 1997) pp. 571-580.
19. S. Nishiyama, *Sci. Rept.*, Tokyo Univ. **23**, 369 (1993).
20. G. Wasserman, *Ach. Eisenhüttenwesen* **16**, 647 (1933).
21. J. W. Pugh and J. D. Nisbet, *Trans. TMS-AIME* **188**, 268 (1950).
22. J. A. Brooks, N. Yang and J. Krafcik, in *Recent Trends In Welding Science and Technology*, edited by S. A. David and J. M. Vitek, (ASM International, 1992).
23. D. A. Porter and K. E. Easterling, in *Phase Transformations in Metals and Alloys*, (Chapman and Hall, 1992), pp.349-358.

## CHARACTERIZATION OF LASER DEPOSITED NIOBIUM AND MOLYBDENUM SILICIDES

C. A. BRICE\*, K. I. SCHWENDNER\*, S. AMANCHERLA\*, H. L. FRASER\*,  
X. D. ZHANG†

\*Department of Materials Science and Engineering, The Ohio State University, Columbus,  
OH 43210, brice.12@osu.edu

†Reynolds Metal Company, Richmond, VA

### ABSTRACT

Recent advances in laser deposition technology have made the production of advanced composite materials more technically feasible. By utilizing the unique characteristics of the laser deposition process, materials can be made that are difficult to produce by conventional methods. Structural silicide materials hold promise for high temperature applications, unfortunately, their low toughness has prevented their practical use [1-4]. The introduction of a second phase can greatly increase their low temperature mechanical properties. Laser direct deposition can be used to deposit these materials near net shape and produce an *in-situ* alloy that has the desired structure for improving properties. *In-situ* alloying was accomplished by using an Optomec LENS™ (Laser Engineered Net Shaping) machine to deposit elemental niobium-silicon and molybdenum-silicon-boron powder blends. The resultant microstructures showed a homogeneous structure with a primary silicide phase surrounded by a continuous eutectic phase. These deposits were characterized using scanning and transmission electron microscopy, x-ray diffraction, and by energy dispersive spectroscopy.

### INTRODUCTION

Laser engineered net shaping (LENS™) is a manufacturing processes developed at Sandia National Laboratory in the early 90's. This technology utilizes a Nd:YAG laser to fuse metallic powders into fully dense parts. Computerized motion controls allows extremely complex shapes to be deposited directly from a CAD computer file. Prealloyed or elemental blended powders can be used for feedstock. Prealloyed powders have the benefit of having a constant composition, thus producing a very homogeneous deposit. These powders, however, are not readily available and can be very expensive to make. Elemental powders, while being easier to procure, can produce segregated deposits that are not fully alloyed. The goal of this work is to produce *in-situ* alloys of structural silicide composites from elemental powder blends utilizing LENS™ technology.

### EXPERIMENTAL

Several cylinders of each composition were deposited using the Optomec LENS machine. One alloy was an elemental powder blend consisting of 70 atomic percent molybdenum, 10 atomic percent silicon, and 20 atomic percent boron. The second alloy was an elemental powder blend consisting of 65 atomic percent niobium and 35 atomic percent



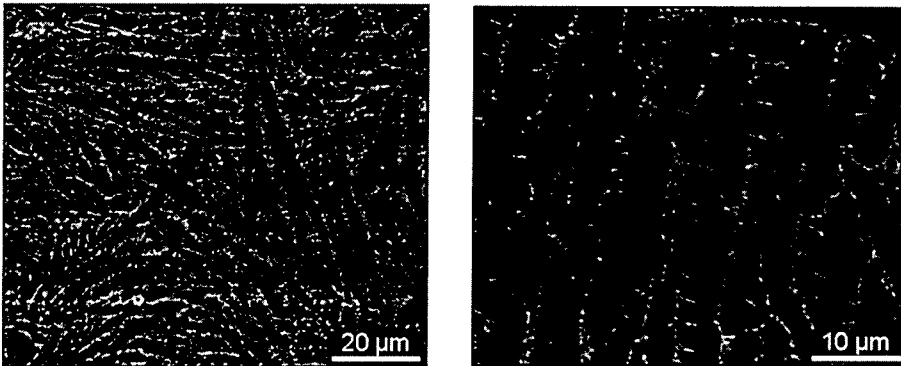


**Figure 1:** Backscattered electron micrographs of laser deposited molybdenum-boron-silicon.

silicon. These powders were obtained from Alfa Aesar and had a size distribution of -60 to +325 mesh. The powders were combined in a plastic bottle and mixed thoroughly before being loaded into the powder feeder. The LENS™ unit was then used to fuse these powders into small samples, roughly 1/2 inch in diameter and 3/8 inch high. Approximately 400 watts output power from the laser was used to achieve full density in the samples.

The deposited cylinders were then cross-sectioned and samples were mounted in conductive resin for examination in the scanning electron microscope (SEM). A Philips XL-30 FEG SEM was used to perform the analysis. Transmission electron microscope (TEM) foils were made by EDM core drilling through the cross-section of the sample. These cross-sectional cores were then sliced into thin sections, dimple ground and thinned using an ion mill. The analysis was done on a Philips CM200 microscope with an EDAX energy dispersive spectroscopic (EDS) attachment. X-ray diffraction (XRD) analysis was performed on a Scintag-PAD-V X-ray diffraction unit.

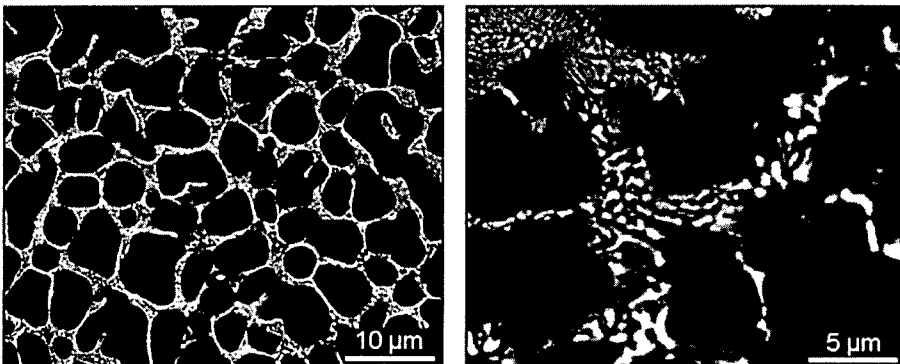


**Figure 2:** Backscattered electron micrographs of laser deposited niobium-silicon.

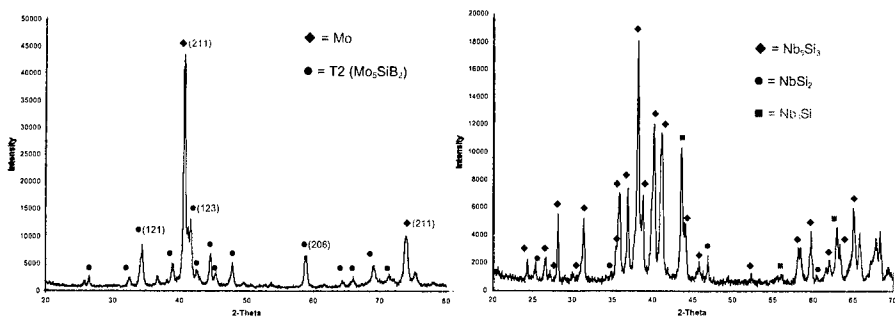


**Figure 3:** X-ray diffraction scans of niobium-silicon alloy (left) and molybdenum-boron silicon alloy (right).

## RESULTS AND DISCUSSION

The equilibrium ternary phase diagram for the Mo-Si-B system predicts three phases should be present, Mo, Mo<sub>3</sub>SiB<sub>2</sub>, and Mo<sub>2</sub>B, at the given composition [5]. Cross-sectional backscattered electron SEM images of the as-deposited Mo-Si-B samples (Figure 1) show that only two phases appear to be present. This contradiction can be explained by considering that (a) the composition lies very close to phase boundary of the Mo<sub>2</sub>B phase, hence little or none of this phase can be expected, and (b) equilibrium structures are not expected in the as-deposited material due to rapid solidification rates ( $\approx 10^4$  K/sec). These SEM images show that the molybdenum concentrations are highest in the eutectic-like structure found between the dark regions. Using EDS analysis, the dark regions were found to have a Mo:Si:B ratio of approximately 5:1:2. The eutectic structure was much too fine to accurately conduct EDS analysis. Based on these observations, it would appear that the dark phase is Mo<sub>3</sub>SiB<sub>2</sub> (also known as T2) and the eutectic structure consists of a mixture of molybdenum and T2. X-ray diffraction patterns were taken to confirm the phases present in the alloy. The results are shown in Figure 3. This scan confirms that the alloy is two phase, consisting of pure molybdenum and Mo<sub>3</sub>SiB<sub>2</sub>.

TEM examination of the Mo-Si-B alloy was done to confirm the results seen through SEM and XRD analysis and to determine exactly where each phase exists in the microstructure. Figure 4 shows a TEM micrograph of the Mo-Si-B alloy in the eutectic region of the sample. The electron diffraction spot patterns correspond to the [001] and  $[\bar{1}\bar{1}0]$  zone axes in the tetragonal T2 phase, confirming that the primary phase is T2 and the eutectic structure is a mixture of molybdenum and T2. These results agree well with what is expected from the equilibrium phase diagram suggesting that this is a stable microstructure and heat treatment should have little effect on it.

The Nb-Si binary phase diagram predicts a mixture of Nb<sub>3</sub>Si<sub>3</sub> and niobium. Backscattered electron SEM images (Figure 2) of the Nb-Si alloy shows a structure similar to that of the Mo-Si-B alloy, with a primary phase surrounded by a continuous eutectic structure. A closer look at the samples in the SEM images, however, shows that at least three phases are present. An x-ray diffraction scan was done to determine the phase compo-

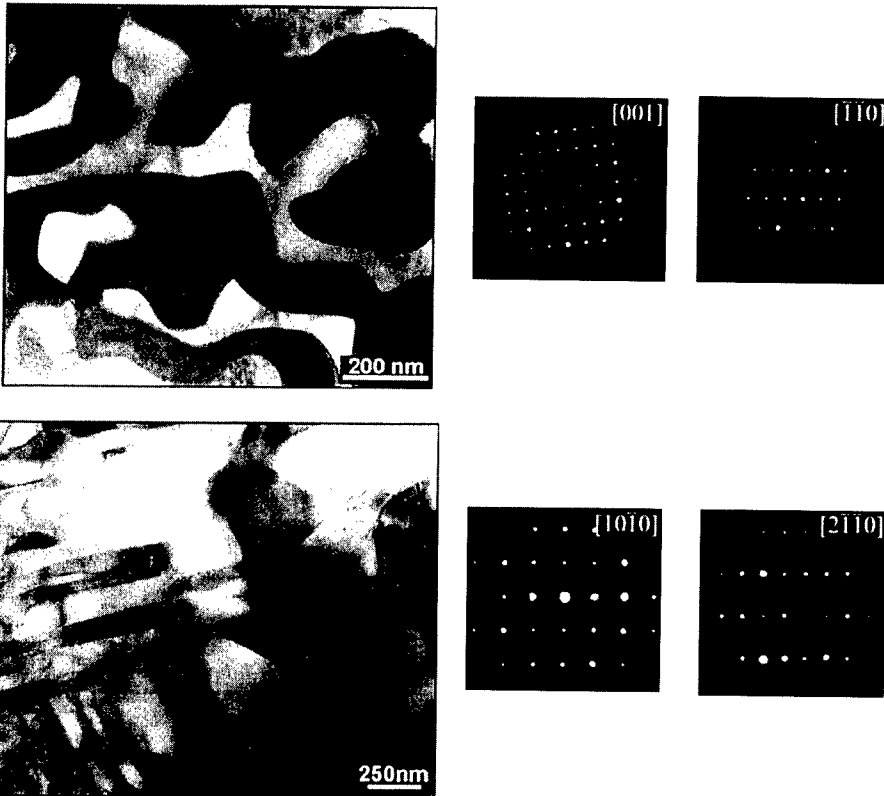


**Figure 4:** Top: Transmission electron micrograph of Mo-Si-B alloy in the eutectic region. Spot patterns correspond to the specified zone axes in the tetragonal T2 phase. Bottom: TEM micrograph of Nb-Si alloy showing Nb rich area. Spot patterns correspond to the specified zone axes in the hexagonal NbSi<sub>2</sub> phase.

sition of the alloy. The scan (Figure 3) shows two niobium-rich phases are present, Nb<sub>5</sub>Si<sub>3</sub> and Nb<sub>3</sub>Si, and one silicon rich phase, NbSi<sub>2</sub>. The appearance of a silicon rich phase is not predicted according to the equilibrium phase diagram. As with the Mo-Si-B alloy, the composition lies near a phase boundary so that it is possible for local chemical variations (i.e. higher silicon concentrations) to produce NbSi<sub>2</sub>, the silicon-rich phase.

TEM evaluation of the Nb-Si alloy confirmed the existence of NbSi<sub>2</sub> phase. Figure 4 shows a TEM micrograph and the spot patterns associated with the hexagonal compound NbSi<sub>2</sub>. Unlike the Mo-Si-B alloy, the Nb-Si alloy contains metastable phases that are not predicted by the given composition at equilibrium. This suggests that the microstructure is metastable and susceptible to phase changes upon heat treatment.

---

## CONCLUSIONS

Two different silicon alloys were deposited using direct laser deposition technology. One alloy consisted of Mo with 10 at% Si and 20 at% B and the other alloy had a composition of Nb with 35 at% Si. In both alloys an *in-situ* composite structure was homogeneously formed from elemental blends of powders. The Mo-Si-B alloy produced a primary phase of T2 with a continuous eutectic comprised of Mo and T2. These phases correspond well with the predicted equilibrium ternary phase diagram. The Nb-Si alloy showed a structure with three phases present, including a metastable silicon-rich phase NbSi<sub>2</sub>. Similar to the Mo-Si-B alloy, the primary phase is a silicide compound, Nb<sub>3</sub>Si<sub>3</sub>, which is surrounded by a continuous eutectic of Nb<sub>5</sub>Si<sub>3</sub> and Nb<sub>3</sub>Si. The non-equilibrium NbSi<sub>2</sub> phase is likely due to local composition fluctuations in the powder feed stream.

## REFERENCES

- 1 A. K. Vasudevan and J. J Petrovic, *Mater. Sci. Eng.*, A155, (1992) 1-17
- 2 D. M. Dimiduk, D. B Miracle, Y. W. Kim and M. G. Mendiratta, *ISIJ International*, v. 31 (1991), 1223-1234
- 3 P. J. Meschter and D. S. Schwartz, *JOM*, 41, (1989) 52-55
- 4 D. M. Shah, D. Berczik, D. L. Anton and R. Hecht, *Mater. Sci. Eng.*, A155, (1992) 45-57
- 5 A. Costa e Silva and M. J. Kaufman, *Intermetallics*, 5, (1997) 1-15

## INVESTIGATION INTO FREEFORM FABRICATION OF MULTI-MATERIAL PARTS BY 3D WELDING AND MILLING PROCESS

Yong-Ak Song, Sehyung Park

Korea Institute of Science and Technology KIST, CAD/CAM Research Center  
P.O.Box 131, Cheongryang, Seoul, Korea, yongak@kist.re.kr

### ABSTRACT

Solid Freeform Fabrication (SFF) gives engineers a new freedom to build parts which have proved impossible to manufacture using conventional techniques. However, the surface finish and accuracy of SFF parts are still lower than those of parts which have been machined in conventional operations. A process combination of additive and subtractive techniques is currently being developed in order to overcome this problem. The hybrid approach called "3D Welding and Milling" uses welding as an additive and conventional milling as a subtractive technique, thereby exploiting the advantages of both processes. In this paper, the attempt was made to build multi-material parts, especially molds, by using two different deposition strategies. The results show that it is a feasible approach to build multi-material metal parts directly.

### INTRODUCTION

With an increasing demand for metallic prototypes and tools [1], several direct SFF techniques such as 3D Welding [1], Selective Laser Sintering (SLS) [3] and Laser-Engineered Net Shaping (LENS) [4], Controlled Metal Buildup (CMB) [5] and Shape Deposition Manufacturing (SDM) [6] have been developed. The feature common to all of these approaches is that metals supplied either in the form of powder or wire, are melted directly in most cases with the laser beam. Due to the complete melting, however, the accuracy and surface quality of the parts are generally lower than those of machined parts.

To overcome this process-inherent problem, a combination of additive and subtractive techniques offers a possible means. In the past, this approach has been already implemented in Shape Deposition Manufacturing (SDM) of Stanford University and in Controlled Material Buildup (CMB) developed at the IPT Aachen. In these processes, each layer is deposited as a near-net shape using thermal deposition, mainly laser cladding. The layer is then shaped in a CNC milling operation to net shape before proceeding with the next layer. In SDM processes, the top as well as the side faces of each layer are machined and then protected by a support structure made of copper. This support structure is then removed in an etching process when the part is completely fabricated.

As contribution to this process development, a process combination of conventional metal inert gas arc welding with subsequent milling called 3D Welding and Milling [7, 8] discussed in this paper. First, welding is used to build a layer by depositing single beads side by side, Fig. 1. Depending on the welding parameters such as welding speed and power, the bead thickness varies in a range of 0.5mm ~ 1.5 mm. When the deposition of a layer is finished, its top surface is machined in order to obtain a smooth surface with an exact thickness for further deposition. The combination with face milling offers a distinct advantage to set any layer thickness between 0.1 mm ~ 1 mm. When the sequence of deposition and face milling is finished, surface finishing is applied in the same setup to remove remaining stair steps on the surface and to increase the accuracy of the near-net shape metal part.

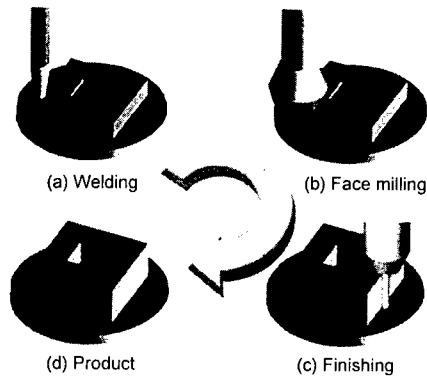
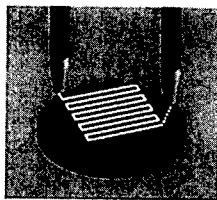


Fig. 1: Process principle of 3D Welding and Milling

**EXPERIMENT**

Starting from the single bead experiment, the influence exerted by the main process parameters, voltage, current and welding speed on the formation of single beads was investigated. Then, multiple layers were built to examine the microstructure and the hardness of the layers. The focus was also on the feasibility study of direct fabrication of multi-material parts. Principally, there are two approaches available when it comes to deposit multi-materials, Fig. 2. The first approach is to adapt the number of welding guns to the number of materials to be deposited. However, the different thermal expansion coefficients have to be considered when selecting the material combination. The second approach consists in building only the shell without filling the inner area. When the build-up process is completed, these areas are then filled with low-melting alloys. This allows a short deposition time at lower warpage.

1. Use of two welding guns



2. Building shell structure and subsequent filling

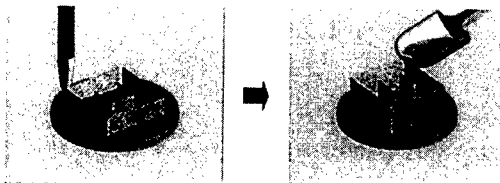


Fig. 2: Two different approaches for depositing multi-material parts

To realize these approaches, the “HybridRP” machine was developed in cooperation with Korea Institute of Machinery and Materials KIMM. It consists of a 3-axis vertical milling machine and two straight MIG welding guns attached to the machine spindle. These two welding guns allow depositing either two different sorts of wire material or two different sizes of the same wire sort in a layer. The single beads are deposited on a substrate plate which is preheated up to 200 ° C. This preheating is necessary to reduce the thermal stress build-up during welding. This kind of machine configuration has a considerable advantage over other SFF machines in that only a simple retrofitting of an existing 3-axis milling machine is required in order to carry out the process, thus eliminating any need to purchase special equipment.

## RESULTS

Optimizing the parameters in the ranges of 16V-36V and 60A-140A at a welding speed between 200 mm/min and 1400 mm/min, permitted the deposition of single, connected beads instead of loose spheres. The suitable welding parameters for the deposition of mild steel AWS 5.18 E70S-6 with a wire diameter of 0.9 mm were found to be 19 V and 120 A at a welding speed of 1.2 m/min.

Fig. 3 shows a thin wall made of 8 layers with and without finishing. In case of the part without machining, the instability of the arc welding process caused a defect in the middle of the bead deposited. Initially small in size, the defect in the layer influenced the height of the next bead deposited, thereby increasing the size of the defect, until no further deposition was possible. This result shows that face milling is necessary not only to increase geometrical accuracy in z direction, but also to stabilize the deposition process. In case of thin walls, the minimum wall thickness is 4 mm with a surface roughness of  $R_a = 200 \mu\text{m}$  along the height. After machining, a minimum wall thickness of 1 mm with a surface quality of  $10 \mu\text{m}$  is achievable.

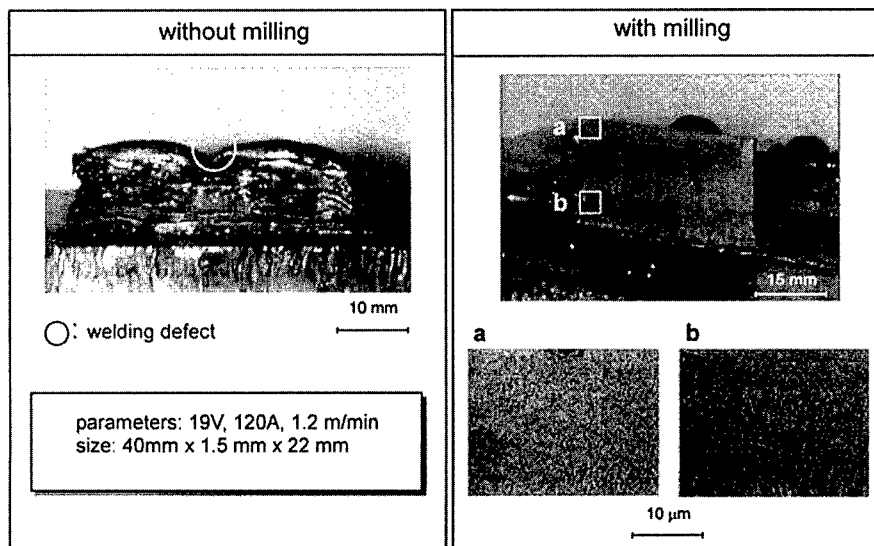
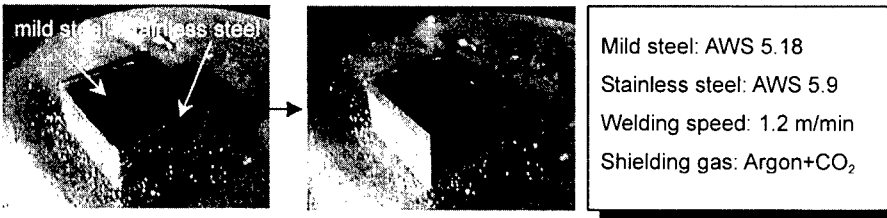


Fig. 3: Thin walls with and without milling

The microstructure analysis shows an almost completely dense structure. Only a small number of process-inherent pores are recognizable in the microstructure. This dense structure is due to the fact that most of the pores, normally existing in the overlapping zone between the beads, are completely removed during the face milling. Analysis of the cross-section in the wall reveals different microstructures depending on the height. The microstructure in the upper area of the wall contains enlarged grains with a spherical shape (see a in Fig. 3). In each grain, a second phase can be observed due to the low cooling rate. Compared to that, the microstructure of the lower area contains relatively small grains as well as some dendrites (see b in Fig. 3). This microstructure of the bottom area is the result of rapid heat conduction into the substrate plate at the beginning of the deposition process. The hardness measurement also proves the difference in microstructure along the height. Starting from a hardness value of 331.8 HV at the bottom, the hardness decreases to 280.5 HV with increasing height.

To investigate the potential of the 3D Welding and Milling process for building multi-material parts, two square test parts were built, as shown in Fig. 4. The first part was built using two different steel sorts. The inner area of each layer was filled with mild steel AWS 5.18 ER 70S-6 while the boundary was deposited with stainless steel AWS 5.9 ER 308. The total layer number was 30 at a layer thickness of 1.0 mm. As a result, a part made of mild steel in the inside and stainless steel on the outside was fabricated. Due to the low difference in the thermal expansion coefficients,  $11 \cdot 10^{-6}/K$  of mild steel and  $16 \cdot 10^{-6}/K$  of stainless steel, no cracks were found in the interface region. In case of a large difference in thermal expansion coefficients, however, a gradual deposition method is recommendable [9]. The second test part in Fig. 4 was built only by depositing the shell of the square and the inside was then filled with tin-bismuth alloy after completion of the build-up process. The tin alloy has a melting point of 120 °C and is therefore only appropriate for applications at low temperature. Another possible alloy for filling the shell structure is zinc-aluminum-copper alloy with a melting point of 420 °C.

#### Approach 1



#### Approach 2

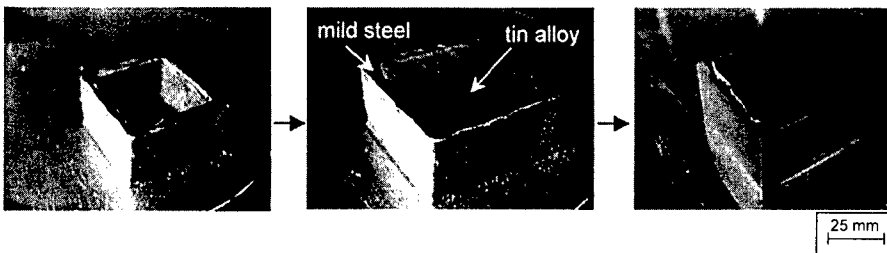


Fig. 4: Test parts built with two different filling techniques



Further test examples of the second filling approach are shown in Fig. 5. In case of the core insert consisting of 63 layers with a layer thickness of 1.0 mm, tin-bismuth was used to fill the shell, while the cavity was filled with a zinc alloy. The cavity consists of 68 layers with a layer thickness of 1.0 mm. This successful fabrication proves the feasibility of this approach for building multi-material metal parts, especially prototype tools. However, it has to be found out in injection molding test whether these inserts can withstand the injection molding conditions.

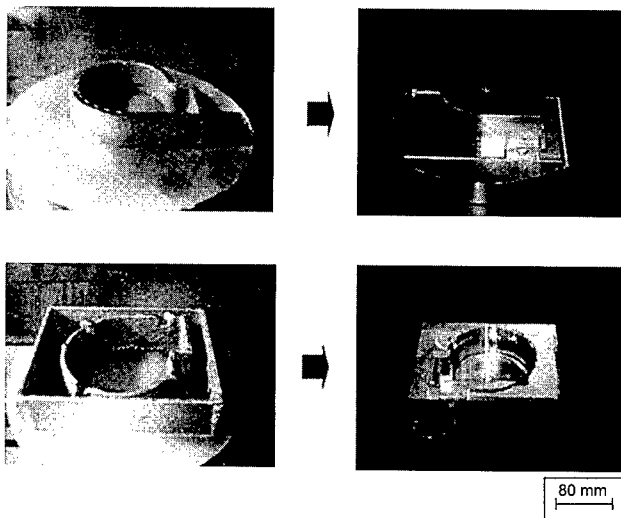


Fig. 5: Mold core and cavity built with filling technique

## CONCLUSIONS

At present, the dimensional accuracy as well as the surface quality of metallic parts and tools manufactured using SFF techniques, still lag far behind those of conventionally machined workpieces. To increase accuracy and surface roughness, a hybrid approach has been developed which exploits an additive and subtractive technique called 3D Welding and Milling.

The main advantage of the process combination is the ability to use different materials when building parts. Two approaches have been developed for this purpose: use of two welding guns for depositing the inner and the boundary of layer separately or filling the shell with low-melting alloys. The second approach is useful when it comes to building of metal parts with large areas to fill, especially large injection molds. It reduces the fabrication time as well as the thermal warpage. In future, the prototype molds fabricated by 3D Welding and Milling have to be tested in injection molding to see whether they can withstand the molding conditions.

## REFERENCES

- [1] S. Ashley, From CAD art to rapid metal tools, Mechanical Engineering, ASME International, 3, p. 82-87 (1997)
- [2] P. Dickens, M. Pridham, M. Cobb, I. Gibson, G. Dixon, 3D welding, Proceedings of the First European Conference on Rapid Prototyping, University of Nottingham, England, pp.

81-93 (1992)

- [3] F. Klocke, T. Celiker, Y.-A. Song, Rapid metal tooling, Proceedings of the 4th European Conference on Rapid Prototyping, University of Nottingham, England, pp. 225-245 (1995)
- [4] M. Griffith, D. M. Keicher, C. L. Atwood, Freeform fabrication of metallic components using laser engineered net shaping (LENS), Proceedings of the Solid Freeform Fabrication Symposium, University of Texas at Austin, pp. 125-131 (1996)
- [5] F. Klocke, H. Wirtz, W. Meiners, Direct Manufacturing of Metal Prototypes and Prototype Tools, Proceedings of the Solid Freeform Fabrication Symposium, University of Texas at Austin, pp. 141-148 (1996)
- [6] J. R. Fessler, R. Merz, A. h. Nickel, F.B Prinz, Laser deposition of metals for shape deposition manufacturing, Proceedings of the Solid Freeform Fabrication Symposium, University of Texas at Austin, pp. 117-124 (1996)
- [7] Y.-A. Song, S. Park, K. Hwang, D. Choi, H. Jee, 3D Welding and Milling for Direct Prototyping of Metallic Parts, Proceedings of the Solid Freeform Fabrication Symposium, University of Texas at Austin, pp. 495-501 (1998)
- [8] Y.-A. Song, S. Park, H. Jee, D. Choi, B. Shin, 3D Welding and Milling – A Direct Approach for Fabrication of Injection Molds, Proceedings of the Solid Freeform Fabrication Symposium, University of Texas at Austin, pp. 793-800 (1999)
- [9] M. Griffith, L. Harwell, J. Romero, Multi-Material Processing by LENS, Proceedings of the Solid Freeform Fabrication Symposium, University of Texas at Austin, pp. 387-393 (1997)

---

## **Tooling and Photo Processing**

## **DIMENSIONALLY ACCURATE MOLD INSERTS AND METAL COMPONENTS BY DIRECT METAL LASER SINTERING**

JAN-ERIK LIND\*, JUHA KOTILA, TATU SYVÄNEN, OLLI NYRHILÄ  
Rapid Product Innovations, Aholantie 17, 21290 Rusko, FINLAND  
jan-erik.lind@rapid-product-innovations.fi

### **ABSTRACT**

One of the main deficiencies in today's rapid tooling techniques is the capability of producing only near net-shape parts. Direct Metal Laser Sintering (DMLS) is a technique that enables the fabrication of true net-shape parts in just a few hours with only minimum post-processing. The DMLS is a laser-based rapid tooling process developed in Europe by Rapid Product Innovations (formerly Electrolux Rapid Development Finland) and EOS GmbH Germany. Rapid Product Innovations was also the first to implement this technology to functional prototyping by using two proprietary bronze-based powders and a new steel-based powder. The technique enables the fabrication of tailored microstructures from porous matrix to near full density. Thus, functionally gradient structures can be fabricated, i.e. material is sintered to full density only where it is needed. This paper describes the philosophy of fabricating true net-shape mold inserts and metal components, but also concentrates on how to maintain the dimensional accuracy even after the post-processing. The study shows that even  $\pm 0.05$  mm accuracy can be obtained. The results of the study also illustrate the beneficial effects of reduced layer thickness and post-processing on the surface roughness and mechanical properties as well as the suitability of various conventional and non-conventional coatings. With reduced layer thickness, the step-shaped effect of the layers was no longer visible. The surface was even further improved by shot peening and coating. In addition, case studies from injection molding, pressure die-casting and direct metal component fabrication are presented.

### **INTRODUCTION**

Rapid Prototyping (RP) and Rapid Tooling (RT) technologies have been developing for over a decade now and a variety of techniques have been presented. Recently the RT concept has been expanded to cover also rapid manufacturing of components and therefore the term Rapid Tooling and Manufacturing (RTM) can be used. Most of the techniques are based on layered manufacturing, which is an effective way of building parts, but has also some limitations. The step-shaped effect is almost always visible and freestanding geometries could be difficult to fabricate without complex support structures.

The overall performance evaluation of an RTM system focuses on four critical factors: 1) speed, 2) accuracy, 3) surface quality and 4) mechanical properties. Speed has to be considered as duration from the start of the whole project to a finished mold or molded parts. This way the cost efficiency of an RTM technique can be compared with conventional methods provided of course that the geometry can be fabricated with conventional methods at all. Dimensional accuracy can still be considered as the most important criterion: The fabricated part should be net-shape in order to use an RTM technique rationally. The cost efficiency is best achieved when the surfaces need no additional machining after the fabrication. This goes hand-in-hand with surface quality: If the surfaces require extensive finishing, the dimensional accuracy is lost. Therefore, only minor finishing or post-processing is acceptable, if any. The fourth factor influencing on the performance is the mechanical properties of the fabricated structure.

Conventionally the structure is built to be as strong as possible which is not the optimal way: The mechanical requirements of the mold depend on the size of the series to be produced as well as on the material to be molded or cast. Therefore, in order to save time and energy, the material properties of the mold should be tailored to withstand only as much strain as necessary. In addition, the strongest material should be deposited only where it is needed based on known stresses inside the mold.

Material research started at Rapid Product Innovations already in the late eighties. The research was first focused on pressureless furnace sintering of metal powders [1]. The objective was to produce net-shape metal molds for injection molding with the assistance of a negative mold pattern. Using a special powder mixture that did not shrink during furnace sintering proved to be the best solution for the process. After finding a suitable mixture [2] the need for a more flexible process was evident and a European RP machine manufacturer EOS GmbH was contacted. The result was a co-operation agreement and the first generation bronze-based powder was developed especially for the Direct Metal Laser Sintering (DMLS) process in 1995 [3,4]. In 1996 the powder as well as the machine were released to commercial use. The next step was to develop new powders. In addition to bronze-based powder with smaller layer thickness (50 µm), a completely new steel-based powder was introduced in 1998 [5]. This was also the first time when direct laser sintering of steel powder was possible. The properties of these materials can be seen in Table I.

Combining process control with the non-shrinking behavior of the powder mixture [6,7] has one remarkable outcome: the sintered parts are net-shape. The surfaces require minor post-processing after the sintering and with special precautions the dimensional accuracy is retained even with the post-processing. The mechanical properties are sufficient for injection molding, direct component manufacturing and based on several tests, also for die casting.

**Table I.** Selected material properties of commercially available DMLS-materials. \*DirectMetal and DirectSteel are trademarks of EOS GmbH, Germany.

	DirectMetal™100-V3	DirectMetal™50-V2*	DirectSteel™50-V1*
Layer thickness	100 µm	50 µm	50 µm
Main constituent	Bronze	Bronze	Steel
UTS	≤ 200 N/mm <sup>2</sup>	≤ 200 N/mm <sup>2</sup>	≤ 500 N/mm <sup>2</sup>
Brinell hardness	90-120 HB	90-120 HB	150-220 HB
Typical porosity	20 %	20 %	5 %
Max operating temperature	600°C	400°C	850°C

## EXPERIMENT

### Operating Principle of the DMLS Machine

The EOSINT M 250 machine consists of a high-power CO<sub>2</sub> laser, beam guiding optics, galvo-scanners, flat-field optics, platform and powder dispenser mechanics, powder recoating system and PC-control (Fig. 1.). There is also an atmosphere unit for creating an inert nitrogen atmosphere when steel powders are laser sintered. Furthermore, the building platform is

equipped with a heater for compensating possible stresses and for removing possible moisture from the powders.

The actual sintering sequence is the following: First a powder layer of predetermined thickness is spread on the surface of the building plate with the recoater arm. Then the laser scans the slice file geometry on the powder layer and bonds it metallurgically to the building plate. After the layer is completed, the building platform moves downward

exactly the distance of the prevailing layer thickness. After this the recoater moves over the platform and spreads a new layer of powder on the previously sintered layer. This sequence continues until the part is finished. Finally, unsintered powder is sieved back to the powder dispenser for reuse and the part is removed from the machine.

Layered manufacturing principle enables the fabrication of very complex shapes. The loose powder around the sintered structure acts as a support for the subsequent layers. Thus, the fabrication of surfaces with negative drafting angle is possible up to  $-45^\circ$  without support structures. For fabricating metal components the supports are necessary for fastening the component to the building plate. After the fabrication the supports are removed with conventional techniques.

### Dimensional Accuracy and Post-Processing

Dimensional accuracy and post-processing experiments can be divided into two areas: effect of reduced layer thickness and dimensional changes due to shot peening. The reduced layer thickness was enabled by the development of a new proprietary steel powder which can be laser sintered with as thin as  $20\ \mu\text{m}$  layers [9]. Presumably the step-shaped effect could be reduced dramatically with  $20\ \mu\text{m}$  layers.

The actual experiments were made by laser sintering test parts ( $100 \times 20 \times 30\ \text{mm}$ ) from steel- and bronze-based powders. X, Y and Z dimensions were measured and the parts were shot peened. The resulting surfaces of the  $20\ \mu\text{m}$  layer steel parts were compared visually with  $50\ \mu\text{m}$  layer parts. In addition, the surface roughness was measured for comparison with coated parts and dimensions were measured again. Mechanical properties of the  $20\ \mu\text{m}$  and  $50\ \mu\text{m}$  steel parts were compared by sintering UTS test bars.

### Coatings

The suitability of various conventional and non-conventional coatings was studied in order to increase the surface quality and at the same time retain the dimensional accuracy. Only restrictions were that the coating should be done below  $400^\circ\text{C}$  for bronze and  $850^\circ\text{C}$  for steel, because of the swelling of the sintered matrix above these temperatures. A common definition for all tested coatings was that they were all slurries. The solid media in the slurries was either

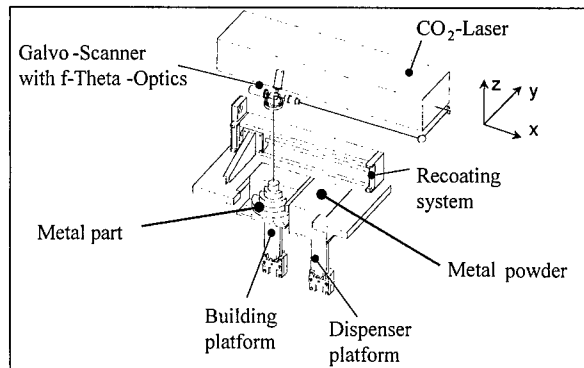


*Figure 1. Schematic presentation of the DMLS machine assembly [8].*

metallic or ceramic and the binder was either organic or inorganic. The solid media would flow with the binder, as it is drawn inside the matrix by capillary forces, filling the pores on the surface.

The solid media tested were metal (copper, bronze, aluminum, nickel) or ceramic (boron nitride, iron and zinc oxides) powders. From these the metal powders outperformed the ceramic ones, because of their ductility. During finishing the ceramic powders usually flaked off leaving open pores on the surface. Especially during shot peening the metal powder particles were squeezed deeper inside the pores thus sealing the surface.

The binders were the hardest to find. A high-temperature epoxy resin was used for bronze, but it could not be used for steel especially in die casting applications, because of a quite low temperature resistance. Therefore an inorganic alternative had to be found. Aluminum phosphate was finally selected due to its beneficial behavior with the laser-sintered materials.

Copper/epoxy and aluminum/aluminum phosphate were selected for the powder/binder experiments. The coatings were brushed on the surface of the test parts and subsequently the coating was cured. The epoxy resin was cured at 125°C for 1,5 hours and the aluminum phosphate based coating was cured at 340°C for 30 minutes. After this the resulting surface was shot peened with 0,2-0,4 mm spherical steel shot until visual saturation was reached.

## RESULTS

### Dimensional Accuracy and Post-Processing

The experiments with the 20 µm layer thickness for the new steel-based powder were successful. The dimensions of the parts were found to be within the ± 0,05 mm margin and with shot peening the surface roughness was reduced from  $R_a$  14 µm to  $R_a$  5,2 µm (Table II.). The new steel-based powder enables complete melting of horizontal surfaces during sintering to 0 % porosity resulting in  $R_a$  values of even 3 µm as sintered. In fact, for the first time in laser sintering of metals the layered structure was no longer visible. The detail accuracy on the curved surfaces was so good that the individual triangles from the original STL-files could be clearly distinguished. In order to obtain higher quality sintered surfaces, higher resolution has to be used in file preparation, which increases the size of the files. This imposes more strict requirements on the file preparation and the software.

After shot peening it was found that the surfaces had compressed between 0,05 and 0,1 mm (Table II.), which was mainly due to the densification of the surface. The same values were found for the 50 µm bronze material also.

*Table II. Results of the post-process experiments for bronze- and steel-based DMLS powders.*

Therefore, the phenomenon is not a function of the material properties, but instead a function of the surface porosity. The compressibility can be compensated by filling the surface pores with a slurry. After this the densifying media is already present and the

	Bronze 50 µm layers	Steel 50 µm layers	Steel 20 µm layers
Length as-sintered [mm]	100.02	100.04	100.04
Change in dimension due to shot peening [mm]	-0.09	-0.07	-0.06
$R_a$ before [µm]	13.22	18.10	14.19
$R_a$ after shot peening [µm]	4.85	6.84	5.20
$R_y$ before [µm]	81.90	128.00	92.14
$R_y$ after shot peening [µm]	23.30	44.80	37.44

surface cannot compress so much. The surface quality and dimensional accuracy enable the use of DMLS inserts directly in injection molding applications with only shot peening as post-process treatment. The surfaces can be further polished, if necessary, to even  $R_a$  0,5  $\mu\text{m}$  with only minor effort.

The average UTS value of the 20  $\mu\text{m}$  steel bars was 604 MPa, which corresponds to a 20 percent increase in tensile strength when compared to the standard 50  $\mu\text{m}$  layer powder. This is an additional benefit since the mold geometries are more and more complex and thin pins etc. have to be as strong as possible.

### Coatings

Coating experiments proved that by filling the surface pores the dimensions could be retained net-shape even with shot peening. Table III shows that the actual change in dimension is smaller than 0.05 mm for both bronze- and steel-based materials. The results were the same for both copper/epoxy and aluminum/aluminum phosphate systems and therefore only results of the aluminum/aluminum phosphate system are presented. The surface roughness decreased also slightly thus enabling even shorter turnaround of the laser sintered mold inserts. This was remarkable because with slurry coating and shot peening the surface quality of the mold inserts could be significantly improved in just a few hours while still retaining the dimensional accuracy. In practice this means shortening of the finishing stage from days to hours.

*Table III. Results of the coating experiments for bronze- and steel-based DMLS powders.*

	Bronze 50 $\mu\text{m}$ layers	Steel 20 $\mu\text{m}$ layers
Length as-sintered [mm]	100.02	100.04
Length after coating and shot peening [mm]	100.01	100.02
$R_a$ before [ $\mu\text{m}$ ]	13.74	14.35
$R_a$ after [ $\mu\text{m}$ ]	3.77	4.44

### Cases

The DMLS process is a standard tool for production of injection molding inserts at Rapid Product Innovations. At the moment about 200 projects have been carried out and a lot of experience has been gained. In addition to injection molding, pressure die casting for magnesium and aluminum has been tested and 720 chainsaw components die cast in aluminum in a steel-based DMLS mold. The latest application area however has been the direct fabrication of metal components. Components such as belt pulleys for an automobile engine, liquid sampling nozzles and inlet tubes with complex internal channels have been fabricated and all components are in functional testing. A few examples are shown in Figure 2. From left to right the figures present examples of injection molding, die-casting and component fabrication. The injection molding example is a double injection molding of thermoplastic elastomer and polypropylene. The mold halves were constructed from four inserts and the total size of one mold half was 300 x 400 mm. The die casting example is a chainsaw component called "cutting arm". The component was cast both in aluminum and magnesium. The DMLS component examples are an engine belt pulley and a transmission component both used in a test engine. The lead-time of the components was 2 days for the pulley and 1 day for the transmission component.



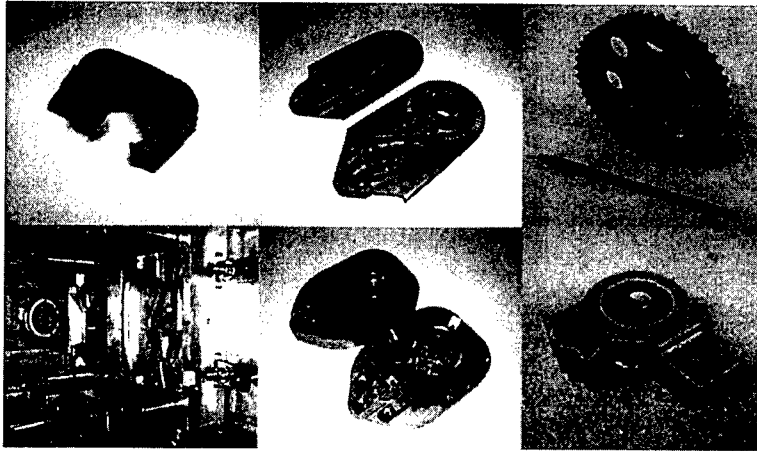


*Figure 2. Case examples of injection molding, pressure die-casting and component fabrication with the DMLS technology.*

## CONCLUSIONS

It has been presented that with special precautions and optimized material properties net-shape mold inserts and components can be fabricated and the dimensions retained even with post-processing. The dimensional accuracy was retained with slurry coating and shot peening. The DMLS technology enables the fabrication of high quality surfaces with the new steel-based powder and 20  $\mu\text{m}$  layer thickness resulting in very short lead times compared to conventional techniques. Furthermore, fully functional metal components can be fabricated with very complex geometries.

## REFERENCES

1. O.Nyrhilä, *Pressureless Sintering of Metal Powders*, M.Sc Thesis, University of Turku, 1993.
2. O. Nyrhilä, S. Syrjälä, U.S. Patent No. 5 061 439 (29 October 1991).
3. T. Syvänen, *Direct Laser Sintering of Metals – Material and Process Development*, M.Sc. Thesis, Tampere University of Technology, 1996.
4. O. Nyrhilä, U.S. Patent No. 5 732 323 (24 March 1998).
5. J. Kotila, *Development of Steel Based Metal Powder for DMLS-Process*, M.Sc.Thesis, Tampere University of Technology, 1998.
6. R. M. German, *Sintering Theory and Practice*, John Wiley & Sons, New York, NY, 1996, p. 225.
7. W.-F. Wang, *Effect of Tin Addition on the Microstructure Development and Corrosion Resistance of Sintered 304L Stainless Steels*, J. Mater. Eng. and Perform., Vol. 8(6), pp. 649-652, (1999).
8. EOS GmbH, presentation graphics, 1999.
9. T. Syvänen, O. Nyrhilä, J. Kotila, J-E. Lind, *New Innovations in Direct Metal Laser Sintering Process - A Step Forward in Rapid Prototyping and Manufacturing*, Proc. of 1999 ICALEO conference: Laser Materials Processing, San Diego, CA. (to be published).

## **CONFORMAL COOLING VERSUS CONVENTIONAL COOLING: AN INJECTION MOLDING CASE STUDY WITH P-20 AND 3DP™-PROCESSED TOOLING**

Wayde R. Schmidt, Ronald D. White\*, Connie E. Bird and Joseph V. Bak, United Technologies Research Center, East Hartford, CT, USA; \*currently at GE Appliances, Louisville, KY, USA.

### **ABSTRACT**

A series of designed experiments was performed in an attempt to evaluate and quantify the historically "anecdotal" benefits of conformal cooling for injection molding tooling. The study considered different generic part geometries, gating schemes, mold materials, plastic resins and cooling approaches. This paper provides an overview of the mold design approach, cooling simulation, tool fabrication via the 3DP™ process, as well as part molding and inspection results.

### **INTRODUCTION**

Proper thermal management of metal injection molding tooling is critical for increasing overall part quality, as well as reducing molding cycle time and thereby increasing production rates<sup>1,2</sup>. The incorporation of cooling lines into a tool provides one mechanism to control heat build-up within that tool, and offers a means to manage the process of removing heat from the injected plastic. In general practice, the cooling system is the last area to be considered when designing and building an injection mold. Conventional methods for adding cooling lines to the tool inserts are generally applied after the insert is fabricated, often placing severe limitations on the possible configuration of the cooling channels, and typically providing for sub-optimal control of heat flow. As a result, the cooling channels must be routed around the core or cavity as space permits, and the number and size of the cooling circuits are generally limited by the ejector system for the part. It is often not possible to place cooling channels directly within the mold inserts; cooling passages must be placed in the bolsters or support blocks.

Mold temperature is known to strongly influence the amount and distribution of residual stress in molded parts. Uneven cavity temperatures result in parts with molded-in stresses, warped sections, sink marks, poor surface appearance, and varying part dimensions from cycle-to-cycle and even from cavity-to-cavity. Therefore, in order to produce parts to correct (and increasingly tight) dimensions and tolerances, the core and cavity temperatures must be controlled during the molding process.

Solid freeform fabrication (SFF) methods, and in particular, MIT's Three-Dimensional Printing (3DP™) process allows for the manufacture of internal geometries such as complex cooling passages with non-circular cross-sections, which can be designed to be conformal to the molding cavity. Conformal passages created with the 3DP™ process provide the ability to control more accurately the temperature of the molding cavity throughout the process cycle. Such temperature control has the potential to produce parts with lower residual stresses and to shorten cycle time, ultimately reducing part cost and increasing profits. The ability to create conformal cooling channels using the 3DP™ process offers design flexibility and challenges the mold designer to consider cooling circuit schemes that were previously impossible to manufacture.

## EXPERIMENTAL METHODS

### Test Part Design

Two test geometries were created. The first part geometry was a simple box 83 mm long by 42 mm wide by 20 mm high. A full height slit was added to the long sidewalls to reduce stiffness. A second box geometry was created to challenge conformal cooling channels to follow the part surface and penetrate into very narrow core features. This new geometry included ribs to create additional loads. Two gating schemes were also selected; a center gate with a large sprue which would likely increase cooling time, and an edge gate with a narrow gate that would break easily from the runner. The gate locations were independent of the box geometry. Figure 1 illustrates the geometries for the test box and the gating schemes.

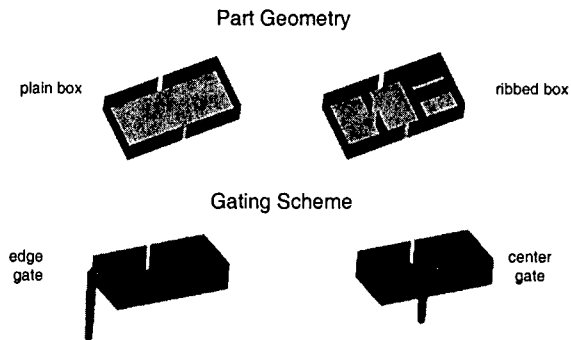


Figure 1. Test Part and Gating Geometries Investigated in this Study.

### Simulation and Analysis

A  $2^{k-n}$  fractional factorial Design of Experiments (DOE) was performed using JMP Statistical Discovery Software (Version 3, SAS Institute, Inc., Cary, NC). Seven parameters were evaluated at two levels according to Table 1, providing an ideal case of 32 separate experimental runs. Four of these runs called for conformal cooling in P-20 tool inserts, which were not fabricated. A modified experimental design consisted of three  $2^{5-1}$  tests, requiring that two of the seven factors be held constant in each of the three tests, with 16 runs for each test. Omitting duplicate runs, the total number of experimental runs was 40, with 20 replicate parts molded for each run.

Table 1. Design of Experiment (DOE) Parameters Evaluated in this Study.

Factor	Low Value	High Value
Polymer	Celcon M90 polyacetal	Minlon 10B40 polyamide
Pack/Hold Pressure	Low (50% peak)	High (75% peak)
Coolant Temperature	50°C (Celcon); 50°C (Minlon)	95°C (Celcon); 95°C (Minlon)
Gating Scheme	Center Sprue/Gate	Edge Sprue/Gate
Part Geometry	Plain Box	Ribbed Box
Mold Material	P-20 steel	3DP™ 420SS/bronze
Cooling Method	Conventional Gun Drilled	Conformal

Thermal analysis of cooling line geometries was performed using MARC Finite Element Analysis Code. Cooling lines were designed and located nominally 1.5 channel diameters away from the tool surface, with every attempt to position the line conformal to the part geometry. Cooling passage diameters were 6.35 mm for conventional cooling and ranged from 1.7 to 6.35 mm for conformal configurations. Injection molding simulations on select part/cooling configurations were performed with C-MOLD (release 99.1) and replicated the cycle times and process parameters of the molding trials. C-MOLD filling, cooling and warp/shrink analyses were also used to optimize the box geometry and cooling channel configurations, as well as to predict pressure drop and minimum flow requirements. The final designs were based on iterative cooling and heat flow analysis. Simulations relied on the Fast Cool 2-Domain pvT Tait Model Constants for Celcon M90 and Minlon 10B40.

Tooling Insert Fabrication, Molding Experiments and Inspection

Ten mold inserts were fabricated as described in Table 2. 3DP™ processed inserts were fabricated in the 3DP™ Laboratory at MIT or at ExtrudeHone (Irwin, PA) using the ProMetal commercial tooling system. P-20 and 3DP™ processed tool inserts were machined or finished as needed by Anglo Precision Mold, Inc. (Milford, CT) using conventional technology. Although no P-20 mold inserts with conformal cooling were fabricated, the DOE test results could be extrapolated to predict the performance of such molds.

Table 2. Summary of the Tooling Inserts Fabricated and Evaluated During this Study.

Tooling Configurations						
Number	Mold Material	Gate Location	Box Geometry	Cooling Method	Cavity Code	Core Code
1	P20	Center	Plain	Conventional	P20-2	P20-1
2	P20	Edge	Plain	Conventional	P20-1	P20-1
3	P20	Center	Ribbed	Conventional	P20-2	P20-2
4	P20	Edge	Ribbed	Conventional	P20-1	P20-2
5	3DP™	Center	Ribbed	Conventional	3DP™-2	3DP™-2
6	3DP™	Center	Plain	Conformal	3DP™-2	3DP™-3
7	3DP™	Center	Ribbed	Conformal	3DP™-2	3DP™-4
8	3DP™	Edge	Ribbed	Conventional	3DP™-1	3DP™-2
9	3DP™	Edge	Plain	Conformal	3DP™-3	3DP™-3
10	3DP™	Edge	Ribbed	Conformal	3DP™-3	3DP™-4

Two resin systems were used. Celcon polyacetal (Hoechst Celanese Corporation) is a commonly used polymer that is very prone to warpage. Its relatively low thermal conductivity (1.6 Btu-in/hr/ft<sup>2</sup>/F) was expected to result in longer cooling times. Minlon polyamide (DuPont Engineering Polymers) has a relatively high thermal conductivity (3.0 Btu-in/hr/ft<sup>2</sup>/F) and mineral filler that was expected to reduce the relative shrinkage. All plastic injection molding experiments were performed using a Toyo Plastar Ti-90G2 90-ton injection molding machine and dried resins. Tooling inserts were incorporated into standard MUD frames for molding runs. Molded parts were allowed to stabilize at ambient conditions for at least 48 hours prior to inspection and comparison to mold dimensions. Cycle time, cooling time, length and width shrinkage of the molded part, and the distance of the gaps in the walls of the parts were tracked. Part inspection on critical dimensions was achieved using vernier calipers or an electronic jig which captured data directly to a computer.

## RESULTS

Simulation and analysis indicated that the largest impediments to heat removal from the plastic part are the air gap between the molded part and the tool (upon shrinkage) and the low conduction of heat through the plastic. Iterative design and analysis provided promising cooling configurations for the plain and ribbed box part geometries. Figure 2 illustrates a comparison of cooling schemes for the ribbed box part. The conformal approach allowed local cooling within the otherwise inaccessible pockets of the ribbed box. Total fluid flow was kept constant between the two cooling designs; higher pressure drops in conformal cooling passages were not considered detrimental to overall cooling performance.

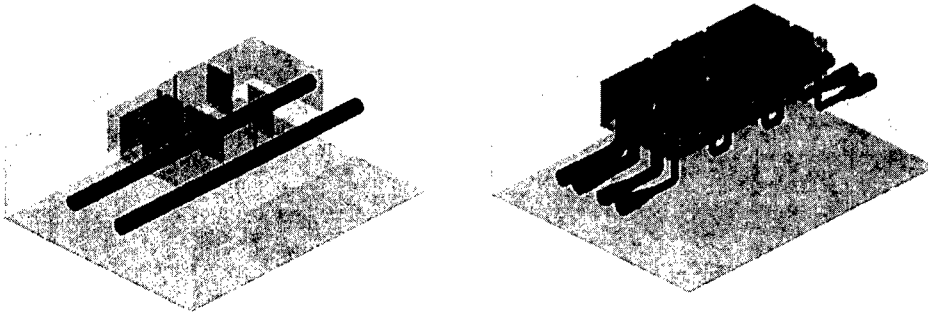


Figure 2. Solid model representations of the core tools for creating the ribbed box test geometry, incorporating conventional (left) and conformal (right) cooling approaches.

The DOE results indicated that next to polymer type, cooling method had the greatest effect on part shrinkage. In separate molding trials specific to cooling type, the “best possible” conventionally-cooled P-20-molded parts were compared to the “best possible” conformally-cooled 3DP™-molded parts (using center gate and ribbed box test geometries). One set of simulations is seen in Figure 3.

The upper left quadrant of Figure 3 demonstrates the cooling scheme geometry and indicates a maximum temperature difference of nearly 4 °F between the core and cavity tool inserts. This compares favorably to a value of 21 °F obtained for the conventionally cooled case (not shown). The lower left quadrant of Figure 3 shows a reasonably uniform temperature distribution at a part ejection time of 24.6 s, especially within the separate pockets. Note also the higher temperature in the center sprue region. The conventionally-cooled analog shows a 10 °F higher maximum temperature, local hot spots within the smaller pockets, and disproportionately cooler part edges. Shrinkage and warpage are also relatively more uniform and have lower magnitude for the conformally-cooled case (upper and lower right quadrants of Figure 3).

Assessment of the entire data set obtained during this study indicates that conformal cooling in a 3DP™ mold insert will reduce cycle time, cooling time and shrinkage relative to the baseline conventionally cooled P-20 mold insert (Tables 3 and 4). Furthermore, the gap dimensions of the molded part will more closely match the tool dimensions when conformal cooling is used. Notably, although conformally cooled P-20 molds were not built in this study, the simulation

models also predict that conformal cooling in the P-20 mold inserts would further reduce cycle time, cooling time and shrinkage. This interesting result is due to the relatively higher thermal conductivity of P-20 (253 Btu-in/hr/ft<sup>2</sup>/F) versus the 3DP<sup>TM</sup> processed composite (197 Btu-in/hr/ft<sup>2</sup>/F), an indication that P-20 is more effective at removing heat from the molded part.

### Celcon M90 Conformal Cooling 3DP Mold

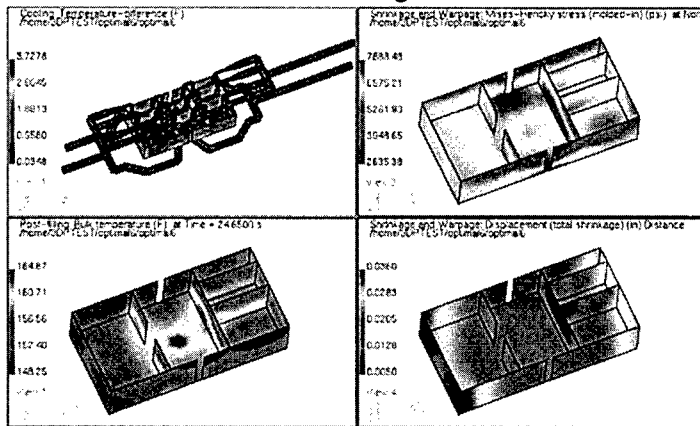


Figure 3. C-MOLD Simulations for “best case” conditions using conformally-cooled 3DP<sup>TM</sup> insert mold material, the ribbed box test part geometry, and Celcon M90 resin.

Inspection of Table 3 shows that 3DP<sup>TM</sup>-processed molds with conventional cooling perform poorer than a comparable P-20 mold, primarily because of the higher thermal conductivity of P-20. In contrast, 3DP<sup>TM</sup> processed inserts with conformal cooling reduced cycle and cooling times by nominally 19-20% relative to “baseline”.

Table 3. Quantitative Results Comparing Cycle and Cooling Times for Cooled P-20 and 3DP<sup>TM</sup> Mold Inserts Relative to a Baseline Condition of Conventionally Cooled P-20.

Cooling Method	Cycle Time (seconds)		Cooling Time (seconds)	
	Mold Material		Mold Material	
	P-20	3DP <sup>TM</sup>	P-20	3DP <sup>TM</sup>
Conventional	33.3 baseline	35.1 +5.4%	25.7 baseline	29.0 +12.8%
Conformal	25.2 -24.3% (predicted)	27.0 -18.9%	17.3 -32.7% (predicted)	20.6 -19.8%

Table 4 shows similar trends for shrinkage data. Although measured gap dimensions are not shown, the results were consistent with reduced shrinkage for parts molded with conformally cooled tool inserts. Further inspection of the data indicates that with conventional cooling, parts molded with 3DP<sup>TM</sup> tooling had greater shrinkage than the complementary P-20 case. Conformal

cooling provided 13.5% less shrinkage in length and 16.7% less shrinkage in width than the baseline conditions. Further reduction in dimensional shrinkage would be expected with conformally-cooled P-20 tooling.

Table 4. Quantitative Results Comparing Part Shrinkage for Cooled P-20 and 3DP™ Mold Inserts Relative to a Baseline Condition of Conventionally Cooled P-20.

Cooling Method	Part Shrinkage (inches)			
	Length		Width	
	Mold Material		Mold Material	
	P-20	3DP™	P-20	3DP™
Conventional	0.074 baseline	0.086 +16.2%	0.060 baseline	0.066 +10.0%
Conformal	0.052 -29.7% (predicted)	0.064 -13.5%	0.044 -26.7% (predicted)	0.050 -16.7%

This study quantitatively showed the benefits of conformal cooling, with respect to reductions in both cycle and cooling times, and in part dimensional shrinkages. In an ideal situation, the preferred mold would incorporate conformal cooling, have an inherently high thermal conductivity, and be comprised of conventional mold material. The latter two items may be mutually exclusive or limiting, but it is critical that the mold provides a path for efficient heat flow and that the mechanical properties of the tool provide the required lifetime for high volume molding operations. Additional cooling benefits could be achieved if a resin system with a high thermal conductivity was available for the molding application.

#### ACKNOWLEDGEMENTS

The authors wish to acknowledge the technical support provided at UTRC by Lee Hoffman (design, solid modeling), Glenn Allen (injection molding, part inspection) and Allen Murray (part inspection), as well as the guidance provided by Jim Irish (UTRC) and Bill Cline (UTAutomotive). The participation of United Technologies Corporation as a member of the 3DP™ Tooling Consortium, funded in part by NSF Cooperative Agreement No. DMI-9420964 (Dr. Kesh Narayanan, program monitor), provided the basis for this work. Solid freeform metal tooling inserts were fabricated at the MIT 3DP™ Laboratory (Dave Brancazio) and ExtrudeHone (Mike Rynerson).

#### REFERENCES

1. E. Sachs, S. Allen, M. Cima, E. Wylonis and H. Guo, "Production of Injection Molding Tooling with Conformal Cooling Channels using the Three Dimensional Printing Process", *Solid Freeform Fabrication Proceedings*, eds. H. L. Marcus, J. J. Beaman, D. L. Bourell, J. W. Barlow and R. H Crawford, The University of Texas at Austin (1995) pp. 448-467 and references therein.
2. X. Xu, E. Sachs, S. Allen, and M. Cima, "Designing Conformal Cooling Channels for Tooling", *Solid Freeform Fabrication Proceedings*, eds. H. L. Marcus, J. J. Beaman, D. L. Bourell, J. W. Barlow and R. H Crawford, The University of Texas at Austin (1998) pp. 131-146 and references therein.

## RAPID ELECTROFORMING TOOLING

Bo Yang\* Ming C. Leu\*\*

\* Department of Mechanical Engineering, New Jersey Institute of Technology, Newark, NJ 07102, yangbo@pb.com

\*\* Department of Mechanical and Aerospace Engineering and Engineering Mechanics, University of Missouri-Rolla, Rolla, MO 65409

### ABSTRACT

A method of rapid electroforming tooling for the production of metal tools including molds, dies, and electrical discharge machining electrodes is developed. Geometry and material of the solid freeform fabricated part, properties of the electroformed metal, and process parameters are significant factors that cause inaccuracy in the manufactured tools. Thermomechanical modeling and numerical simulation are used to simulate thermal stresses induced during the burnout process that removes the rapid prototyping part from the electroform. The analysis demonstrates that appropriate design of the rapid prototyping part geometry and selection of electroform thickness not only reduce thermal stress, thus improving tooling accuracy, but also minimize manufacturing time and cost.

### INTRODUCTION

Electroforming is the use of electrodeposition of metal onto a part that is subsequently separated from the deposit to produce a metal shell. This can be used to make molds and dies for replicating the part [1]. The metalized part, which has the required shape, dimensions, accuracy and roughness, is sunked into an electrolyte bath as the cathode and deposited a layer of metal, normally copper or nickel, for a specified thickness. The part is then separated from the metal shell. The shell is then backed with other materials to form a mold cavity or an EDM (electric discharge machining) electrode. A nickel electroformed part can be used for a prototyping tool or even a production tool [2], and a copper electroformed part can be used as an EDM electrode [3]. Metals deposited by electroforming have distinct properties [4]. Dimensional tolerances can be very good, often up to 0.0025 mm, and surface finishes of 0.05  $\mu\text{m}$  can be obtained quite readily if the master part is adequately smooth [5].

Solid freeform fabrication (SFF), or rapid prototyping (RP), is being increasingly used in industry for prototyping, tooling and manufacturing applications [6, 7]. Rapid tooling is the process of directly or indirectly employing RP technologies to fabricate castings, dies, molds and EDM electrodes. Currently used rapid hard tooling processes such as 3D Keltool [8], 3-dimensional printing (3DP) [9] and RapidTool [10], first bind metal powders by various techniques to generate a green part. Afterwards the part is debinded, sintered, and infiltrated with copper or other metals to produce functional metal parts. The powder metallurgy approaches involve random noise shrinkage during the sintering process and thus the generated metal parts suffer dimensional uncertainty and they usually have rough surface finish. The emergence of SFF has brought about new opportunities for electroforming in rapid tooling [11]. Since electroforming can closely copy the geometry and surface quality of an RP part, the accuracy and



surface finish of the produced tool is largely determined by the accuracy and surface finish of the RP part.

This paper first describes the tooling process and case studies on electroforming of stereolithography (SL) parts to generate EDM electrodes and mold cavities. The investigation on the tooling generation demonstrates that the main sources of tooling inaccuracy are thermal deformations caused by burnout of the SL part and by backfilling of the electroformed metal shell with a molten metal. At the process of separating the metal shell from the SL part, the part is incinerated at about 560 °C. The thermal expansion of the SL part deforms the metal shell because the coefficient of thermal expansion of the SL part material is much larger than that of nickel or copper. In the backfilling process, the molten metal is cast into a metal box and solidified, which also generates thermal deformation. Only low melting alloy with the melting point below 135 °C is used in the case studies so the backfilling caused deformation is not serious. Thus the study on backfilling deformation is not included in this paper.

A thermomechanical model is established to analyze the thermally induced stress during the burnout of the SL part. The model is implemented in ANSYS software to numerically simulate the thermal stress based on finite element method (FEM). The presented study demonstrates that the integration of electroforming with solid freeform fabrication is a viable way for the making of metal dies, molds, and EDM electrodes.

## PRINCIPLE OF RAPID TOOLING PROCESS AND CASE STUDIES

### Tooling Process

The process for making EDM electrodes by electroforming of SL parts is illustrated in Fig. 1. Compared with making EDM electrodes by direct electroplating of copper on positive SL parts [12], this method has the advantage of not requiring uniform thickness of the plated copper. The negative (complementary) geometry of the EDM electrode is prototyped by stereolithography for use as the RP part. The part must be rigid enough to withstand the electroforming stress [13] induced during the metal layer deposition process. Before electroforming of the SL part, metalization of the SL part surface is needed to make the part electrically conductive. Several techniques for metalization of nonconductive materials are available [14]. Electroless plating, a process involving autocatalytic or chemical reduction of aqueous metal ions onto a base substrate, is used in our study to metalize the SL part. The metalized SL parts are then electroplated with copper to a desired thickness. In the process of separating the SL part from the metal shell, prevention of the electroform deformation is extremely important. The RP part built with ceramic and other difficult-to-melt materials are preferred to be separated by mechanical extraction. Melting, burning out, or heat softening can be applied to wax and thermoplastic RP parts. SL resin is a thermosetting material, and burning out of the SL part is the preferred separation method. Complete incineration of the SL part is observed at the temperature of about 560 °C. During the burnout process, the heat results in expansion of the part. This may crack or deform the electroformed metal shell. The geometry of the RP part and the thickness of the electroformed metal shell are important considerations in order to reduce the manufacturing time and cost, while the stresses exerted on the metal shell due

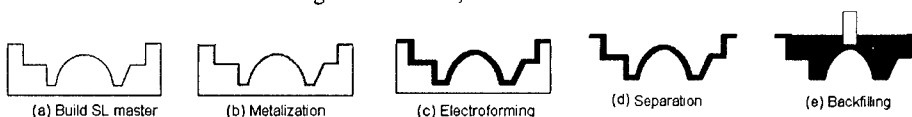


Figure 1. EDM electrode making process



Figure 2. Mold making process.

to the thermal expansion of the part do not crack the copper shell or generate unacceptable deformation. Because the EDM electrode does not contact the workpiece during the electrical discharge machining process, the strength of the electrode is not critical. A low melting alloy with good electrical and thermal conductivity is good for backfilling the shell to form an EDM electrode.

The rapid mold making process is very similar to the process of making EDM electrodes. This is illustrated in Fig. 2. A layer of metal, which is thick enough to resist the deformation caused by the separation and backfilling, is electroformed upon an SL part metalized by nickel electroless plating. The deformation of the metal shell generated during the burnout process is largely affected by the electroforming thickness, material properties, and geometry of the part. Backfilling of the electroform is more critical in manufacturing a mold cavity compared with manufacturing an electrode due to the high strength required in the subsequent injection molding process. The harder the backfilled metal, the higher the strength of the mold cavity. However, a harder metal usually has a higher melting temperature. Casting with a high melting temperature metal tends to generate larger thermal stresses, which may cause larger deformation in the electroformed metal shell. To reduce the injection molding cycle time, conformal cooling lines may be laid around the nickel shell before the backfilling process [15].

### Case Studies

Two SL parts of the same geometry, as illustrated in Fig. 3(b), are used to make EDM electrodes using the tooling process with the copper layer thickness of 2 mm and 4 mm. The cavity of the SL part is 12 mm deep. The SL cavities are polished to the surface finish of 1.24  $\mu\text{m}$ . After polishing, key dimensions as shown in Fig. 3(a) are measured three times and the average is recorded in Table 1. The electroforms on the SL electrodes show that the corners with zero radius can be electroformed, although the copper layer thickness is always the smallest in these positions. Both SL parts are electroformed at room temperature to avoid thermal expansion. After burnout of the SL resin at the oven temperature of 560  $^{\circ}\text{C}$ , the corresponding dimensions are measured and compared with those measured on the SL parts. The results are also recorded in Table 1. As shown, the dimensional deviation of the electrode with 4 mm thick copper shell is smaller than that of the electrode with 2 mm thick copper shell. The largest

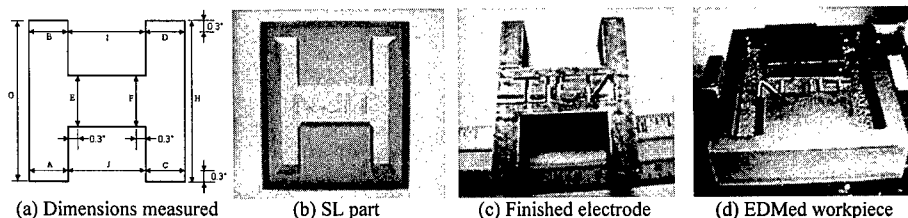


Figure 3. Electroformed electrode and EDM generated workpiece.

deviation is 0.26% for the 2 mm thick copper layer electrode, and 0.14% for the 4 mm thick one. This means that the thicker the electroform, the stronger of the electroform to resist the thermal expansion of the SL part during the burnout process. The surface finish of the two finished EDM electrodes is measured, and the average surface roughness is about 1.26  $\mu\text{m}$  for both electrodes. The copper shell is backed with a tin-lead alloy whose melting point is 103  $^{\circ}\text{C}$ . The finished electrodes are then used to machine a hard steel workpiece using the machining settings typically used for EDM roughing. The burned cavity with a depth of 10 mm shown in Fig. 3(d) is generated by electrode 2.

Table 1: Dimensional data of SL parts vs. those of electroformed electrodes (unit: mm)

	A	B	C	D	E	F	G	H	I	J
Master 1	11.562	11.595	11.585	11.575	17.996	17.983	61.107	61.132	38.095	38.085
Electrode 1	11.552	11.580	11.572	11.562	17.978	17.960	61.074	61.095	38.181	38.176
Deviation 1	0.010	0.015	0.013	0.013	0.018	0.023	0.033	0.037	0.086	0.093
% Deviation	0.09	0.13	0.11	0.11	0.10	0.13	0.05	0.06	0.24	0.26
Master 2	11.639	11.638	11.618	11.610	17.886	17.902	61.229	61.212	38.120	38.090
Electrode 2	11.632	11.628	11.603	11.600	17.871	17.888	61.201	61.180	38.173	38.142
Deviation 2	0.009	0.010	0.015	0.010	0.015	0.014	0.028	0.031	0.054	0.052
% Deviation	0.08	0.09	0.10	0.09	0.08	0.08	0.05	0.05	0.14	0.13

Two SL parts shown in Fig. 4(a) are used to produce two nickel electroforms shown in Fig. 4(b). Nickel is used for electroforming because its mechanical properties are about the same as those of stainless steel and nickel is highly wear and corrosion resistant. The electroforms are then backed with a tin-lead alloy and copper to generate the mold cavities shown in Fig. 4(c) and Fig. 4(d), respectively. The geometry of the SL part is difficult to create by machining due to the sharp corners and fine features. The parts are polished to a surface finish of 1.22  $\mu\text{m}$ . Each dimension (see Fig. 5) of the polished parts SL 1 and SL 2 is measured three times using a coordinate measuring machine (CMM), and the average is recorded as listed in Table 2. After metalizing the parts with nickel to a thickness of about 0.005 mm by electroless plating, the parts are nickel-electroformed with the sulfamate electrolyte to form a nickel shell with the thickness of 2 mm. The nickel electroformed shell (2 mm thick) from SL 2 is then backed with copper (whose melting temperature is 1083  $^{\circ}\text{C}$ ) to a thickness of 2 mm also by electrodeposition. The nickel shell 1 is put into a metal box and backfilled with a molten tin-lead alloy whose melting temperature is 138.5  $^{\circ}\text{C}$ . The electroformed SL parts are then put into an incinerator to burn out the resin at 560  $^{\circ}\text{C}$ . After burnout, each corresponding dimension of the mold cavity is measured three times using the CMM, and the average is recorded as listed in Table 2. The dimensional deviation of the mold 1 is larger than that of the mold 2 (see Table 2) because the nickel shell 2 is backed with copper and is more rigid than the nickel shell 1 backed with the tin-lead alloy in resisting thermal expansion of the SL part during the resin burnout process. The surface finish of both mold cavities is measured 1.27  $\mu\text{m}$ , which is about the same as that of the SL parts.

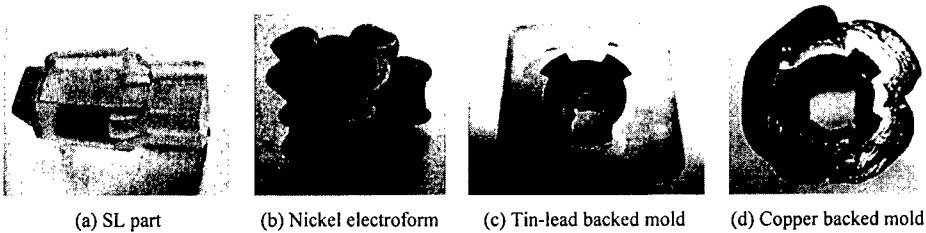


Figure 4. Nickel electroformed mold cavities with fine features.

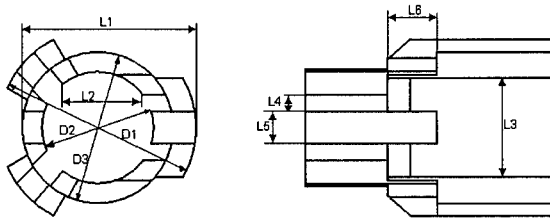


Figure 5. Measured dimensions.

Table 2. Dimensional data of SL parts vs. electroformed mold cavities (unit: mm)

	D1	D2	D3	L1	L2	L3	L4	L5	L6
Part 1	30.503	23.421	16.828	27.033	10.932	15.225	2.578	5.108	7.661
Mold 1	30.579	23.477	16.868	27.089	10.947	15.245	2.583	5.113	7.666
Deviation 1	0.076	0.056	0.040	0.066	0.015	0.020	0.005	0.005	0.005
% deviation	0.25	0.24	0.24	0.21	0.14	0.13	0.20	0.10	0.07
Part 2	30.490	23.365	16.982	28.021	11.059	15.254	2.497	5.09	7.686
Mold 2	30.533	23.396	16.998	28.053	11.069	15.266	2.499	5.095	7.688
Deviation 2	0.039	0.031	0.018	0.032	0.010	0.012	0.002	0.005	0.002
% deviation	0.12	0.13	0.11	0.11	0.09	0.08	0.10	0.10	0.03

### **Factors Affecting Tooling Accuracy**

The factors that affect accuracy in the described tooling process include the accuracy of the RP part, deformation caused by electroforming stress, and deformations generated during the separation and backfilling processes. We have been able to achieve deviation between the master part and the electroformed tool as small as 0.0025 mm in electroforming. Thermal deformations caused by burning out the SFF part and by backfilling the electroformed shell with a molten metal are important sources of inaccuracy. Low melting point alloys with good electrical and thermal conductivity can be used to backfill the shell to form an EDM electrode with small thermal deformation. An electroformed mold cavity backed with a high-strength metal can significantly improve the durability of the electroformed mold and increase the ability of the mold to resist deformation during the injection molding process. However, a high strength metal always has a high melting point, which may generate large deformation in the mold cavity when the molten metal is solidifying. Our experiment shows that when a copper shell is backfilled with aluminum (whose melting temperature is 667 °C), the copper shell deforms severely. Backfilling with an alloy of low melting temperature, such as the tin-lead alloy used in the case studies, will generate little thermal deformation.

### **MODELING AND ANALYSIS OF THE BURNOUT PROCESS**

#### **Thermomechanical Modeling of the Burnout Process**

The problem of thermal stresses induced during the burnout of an SL part is a multi-material, non-linear, transient, thermal-mechanical coupling problem. Boley and Weiner [16] proved that the solution to this problem is independent of thermally-induced stresses under the condition that the time history of displacement closely follows the variation in temperature and

vice versa. We assume that the burnout process satisfies this condition because the thermal expansion during this process closely follows the temperature variation. Then the thermomechanical coupling problem can be simplified as an uncoupled, transient thermal stress problem. With this assumption the modeling of the thermal stress can be divided into two steps: thermal modeling and structural modeling.

Thermal modeling is used to compute the transient temperature field  $T(x,y,z,t)$  during the burnout process. The governing heat conduction equation is

$$\alpha \nabla^2 T = \frac{\partial T}{\partial t} \quad (1)$$

where  $\alpha = \frac{k}{c\rho}$ ;  $k$ ,  $c$ , and  $\rho$  are heat conductivity, specific heat, and material density, respectively.

The two initial conditions are that both the metal shell and the SL pattern are at the room temperature,  $T_r$ . The air inside the oven chamber has perfect thermal contact with the outer surface of the electroformed object. Our analysis shows that the maximum thermal stress when heat convection is considered is essentially the same as the maximum thermal stress when heat convection is ignored. Thus the first boundary condition is:

$$T(p,t) = f(t) \quad (2)$$

where  $p$  is a point on the surface of the metal, and  $f(t)$  represents the oven temperature. There are two cases for  $f(t)$ . One is that the oven is preheated to the burnout temperature, and the other is that the electroformed SL part is put into the oven before heating up the oven. The first situation is referred to as a step thermal load and the second a ramp thermal load.

Because the metal shell is in perfect contact with the rapid prototyping part, the heat transfer at the boundary of the RP part and the metal shell is dominated by conduction. The temperatures of the RP part and metal shell at the boundary surfaces are the same. In addition, the heat flux leaving the metal shell through the contact surface equals to that entering the rapid prototyping part. Thus for a point  $P$  on the contact surface of the metal shell and the RPpart, the boundary conditions are:

$$T_m(P_b,t) = T_r(P_b,t) \quad (3)$$

$$k_m \frac{\partial T_m}{\partial n}(P_b,t) = k_r \frac{\partial T_r}{\partial n}(P_b,t) \quad (4)$$

where the subscripts  $m$  and  $r$  refer to the metal shell and the RP part, respectively, and  $n$  is the normal to the boundary surface at point  $P_b$ .

Structure modeling is used to calculate the thermally induced stress exerted on the metal shell. From the mechanics of material, stresses are related to strains by

$$\{\sigma\} = [D] \{\varepsilon^e\} \quad (5)$$

where  $\{\sigma\}$  is the stress vector,  $[D]$  is the elasticity matrix,  $\{\varepsilon^e\}$  equals  $\{\varepsilon\} - \{\varepsilon^h\}$ ,  $\{\varepsilon\}$  is the total strain vector, and  $\{\varepsilon^h\}$  is the thermal strain vector.  $\{\varepsilon^h\}$  is

$$\{\varepsilon^h\} = \Delta T [\alpha_x \alpha_y \alpha_z 0 0 0]^T \quad (6)$$

where  $\alpha$  is the coefficient of thermal expansion,  $\Delta T$  is the temperature rise, which can be obtained from the thermal analysis. The strains are related to the nodal displacements by

$$\{\epsilon\} = [B] \{u\} \quad (7)$$

where  $[B]$  is the strain-displacement matrix and  $\{u\}$  is the nodal displacement vector. Therefore, the following equations can be solved:

$$\{\epsilon^t\} = [B] \{u\} - \{\epsilon^{th}\} \quad (8)$$

### Thermal Stress Simulation for a Cylindrical SL Part

The above thermomechanical model is applied to an SL cylinder with outer radius of 50 mm and length of 100 mm, which is nickel electroformed and then burned. The radius  $A$  of the inner hole of the cylinder and the electroform thickness  $t$  are variables. We assume that the oven is preheated to the burnout temperature (560 °C) and the temperature is constant during the burning process. To solve this problem, ANSYS 5.4, a finite element analysis software package, is used to simulate the thermal stress resulted from the burnout process. Fig. 6 shows the simulation results with four different sets of variables. For solid SL parts, when the electroform thickness increases from 2 mm to 4 mm, the maximum thermal stress decreases from 144 MPa to 81.3 MPa (see Fig. 6(a) and 6(b)). When  $A=25$  mm, compared with the solid SL parts the

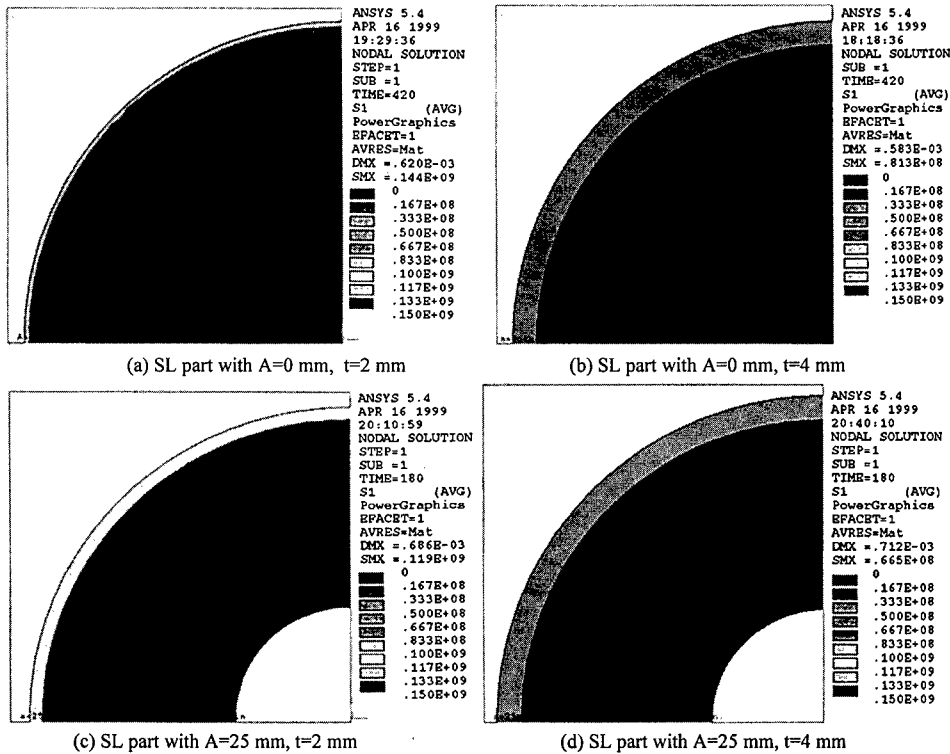


Figure 6. Simulation of thermal stresses with different SL parts and electroform thickness

maximum thermal stress for 2 mm electroform thickness reduces from 144 MPa to 119 MPa (see Fig. 6(a) and 6(c)), and the maximum thermal stress for 4 mm electroform thickness reduces from 81.3 MPa to 66.5 MPa (see Fig. 6(b) and 6(d)). During the burnout process, the maximum thermal stress changes over time, as illustrated in Fig. 7. Fig. 8 illustrates that with the same SL part, the maximum thermal stress decreases when the electroform thickness increases. Also, the larger the inner hole, the smaller the thermal stress. This demonstrates that thermal stress induced by the burnout process can be reduced when a rapid prototyping part is built with appropriate design of its geometric structure. The structure needs to be strong enough to resist the electroforming stress, which is determined by electroforming process parameters. In our case if the electroforming stress exerted on the electroformed nickel shell is 10 MPa, the deformation caused by the electroforming stress has values listed in Table 3. From the table, we can see that solid SL cylinders always have smaller electroforming deformations than those with internal holes. When A increases, the electroforming deformation increases. Table 4 lists the build time and material costs for different SL parts. It shows how much the inner hole can save the build time and material cost.

Table 3. Electroforming deformation for different sets of parameters A and t

	t=1 mm	t=2 mm	t=3 mm	t=4 mm	t=5 mm	t=6 mm
A=0 mm	0.0024	0.0046	0.0067	0.0078	0.0109	0.0128
A=25 mm	0.0043	0.0085	0.0142	0.0187	0.0231	0.0275
A=35 mm	0.0096	0.0194	0.0282	0.0372	0.0461	0.0547

Table 4. Comparison of build time and material cost for different SL parts

	Build Time (hour)	SL 5170 Material Cost
Solid	35.27	\$ 161.63
A=25mm	26.46	\$ 121.25
A=35mm	17.98	\$ 82.43

### Thermal Stress Simulation for a Complex SL Part

The mold cavities generated previously are used to perform thermal stress analysis for a complex SL pattern. Solid and shelled SL parts are used in performing the analysis, and their shapes are shown in Fig. 9. The wall thickness for the shelled SL part is about 6 mm. The maximum thermal stress reduces from 119 MPa, which takes place at 20 seconds into the

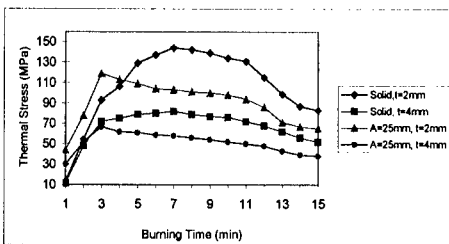


Figure 7. Maximum thermal stress vs. time during burnout process.

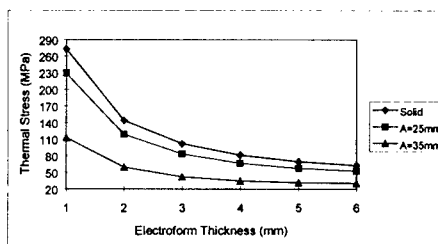


Figure 8. Maximum thermal stress vs. electroform thickness for burnout process.

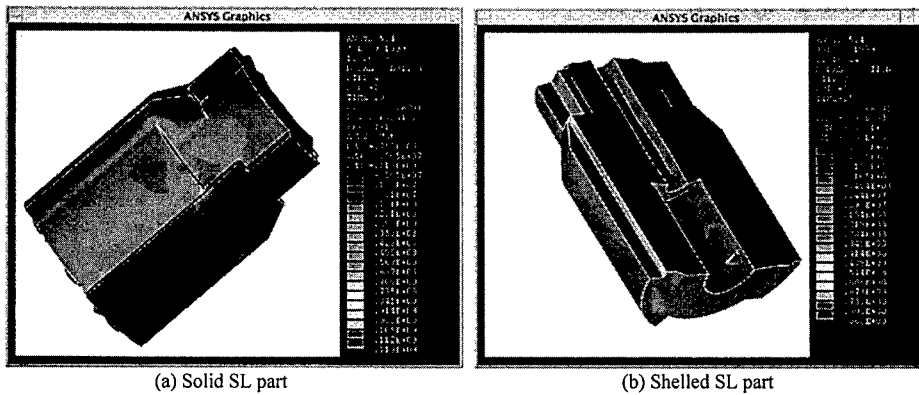


Figure 9. Thermal stress simulation for solid and shelled SL parts with 2 mm thick of nickel electroforms.

burning process, for the solid SL part (see Fig.9a), to 86.7 MPa, which takes place at 15 seconds into the burning process, for the shelled SL part (see Fig.9b). These numbers demonstrate that some empty space inside the SL part can substantially reduce the maximum thermal stress when the electroformed part is burned. Also the thermal loading condition significantly affects the thermal stresses. Our analysis shows a ramp thermal load generates much larger thermal stresses than a step thermal load. The shelled SL part always generates smaller thermal stresses compared with the solid SL part. This demonstrates that thermal stresses induced during the burnout process can be reduced by appropriately designing the RP part to include some empty space. The shelled RP part needs to be strong enough to resist deformation due to the electroforming stress induced during the deposition of nickel. In this particular example, if the electroforming stress exerted on the SL part is 5 MPa, the maximum deformations caused by this stress will be 0.0008 mm and 0.0021 mm for solid and shelled SL parts, respectively. Like the cylindrical part, the empty space in the part not only reduces thermal stresses but also saves material cost and build time.

## CONCLUSION

The method of solid freeform fabrication combined with electroforming for fabricating metal molds and EDM electrodes is presented. The case studies indicate that the described method is viable for rapid tooling of molds and EDM electrodes. The electroforming thickness affects the mechanical property and dimensional accuracy of the molds and EDM electrodes. Thermal deformations caused by burning out the SL part and backfilling the electroformed shell with molten metal are identified as the major sources of inaccuracy. The thermomechanical modeling followed with FEM based numerical simulation of the stresses induced during the burnout process is performed. The results demonstrate that the geometry of the rapid prototyping part and the electroform thickness can be properly designed to reduce the manufacturing time and cost while satisfying the tooling accuracy requirement.



## ACKNOWLEDGMENT

This work was partially supported by the New Jersey Commission on Science and Technology via the Multi-lifecycle Engineering Research Center at the New Jersey Institute of Technology. Dr. Ming C. Leu was on leave at the National Science Foundation as a Program Director for Manufacturing Processes and Equipment when the research work was performed.

## REFERENCES

1. Spiro, P., 1968, Electroforming, Robert Draper Ltd.
2. Yang, B., Leu, M. C., 1999, Integration of Rapid Prototyping and Electroforming for Tooling Application. *Annals of the CIRP*, 48/1.
3. Yang, B., Leu, M. C., 2000, EDM Tooling by Electrodeposition of Rapid Prototyping Parts. *International Journal of Agile Manufacturing*, Vol. 5.
4. Safranek, W. H., 1986, *The Properties of Electrodeposited Metals and Alloys*. Second edition, American Electroplaters and Surface Finishers Society, Orlando, Florida.
5. Degarmo, E.P., Black, J.T., Kohser, R.A., 1984, *Materials and Processes in Manufacturing*, Sixth edition, Macmillan Publishing Company, New York.
6. Kruth, J. -P., Leu, M. C., Nakagawa, N., 1998, Progress in Additive Manufacturing and Rapid Prototyping, *Annals of the CIRP*, 47/2.
7. Leu, M.C., Zhang, W., 1998, Research and Development of Rapid Prototyping and Tooling in the United States, Proc. of First International Conference on Rapid Prototyping and Manufacturing, Beijing, China.
8. Jacobs, P.F., 1997, Recent Advances in Rapid Tooling from Stereolithography, Proc. of the Seventh International Conference on Rapid Prototyping, San Francisco.
9. Sachs, E., Cima, M., Cornie, J., 1990, Three-Dimensional Printing: Rapid Tooling and Prototyping Directly from a CAD Model, *Annals of the CIRP*, 39/1.
10. Bourell, D.L., Crawford, R.H., Marcus, H.L., Beaman, J.J., Barlow, J.W., 1994, Selective Laser Sintering of Metals, *J. of Manufacturing Science and Engineering*, 68/2.
11. Yang, B., 2000, Rapid Tooling by Integration of Solid Freeform Fabrication and Electrodeposition, Ph.D. Dissertation, New Jersey Institute of Technology.
12. Leu, M.C., Yang B., Yao, W.L., 1998, A Feasibility Study of EDM Tooling Using Metalized Stereolithography Models. *Technical Papers of NAMRC*, XXVI, Atlanta.
13. Stein, B., 1996, A Practical Guide to Understanding, Measuring and Controlling Stress in Electroformed Metals, Proc. of AESF Electroforming Symposium, Las Vegas.
14. Duffy, J. I., 1980, *Electroless and Other Non-Electrolytic Plating Techniques*, Noyes Data Corporation, New Jersey.
15. Yang, B., Leu, M.C., 1999, Rapid Production of Engineering Tools and Hollow Bodies by Integration of Electroforming and Solid Freeform Fabrication, US patent application filed.
16. Boley, B. A., Weiner, J. H., 1960, *Theory of Thermal Stresses*, John Wiley & Sons, New York.

---

## SELECTIVE LASER SINTERING OF ZIRCONIA

NICOLE R. HARLAN, DAVID BOURELL, SEOK-MIN PARK, JOSEPH J. BEAMAN, JR.  
Texas Materials Institute, Department of Mechanical Engineering, The University of Texas at  
Austin

### ABSTRACT

A combination of Selective Laser Sintering and colloidal infiltration has been used to create partially stabilized zirconia molds for titanium casting. The mold material system was chosen for its low reactivity with molten titanium and thermal shock resistance. The base material, stabilized zirconia mixed with a copolymer binder, was pre-processed before laser sintering into the desired green shape. The average density of the fired parts could be increased to twice that of the green density. Hole sizes as small as 180  $\mu$ m are possible in thin ceramic components.

### INTRODUCTION

Aspects of rapid prototyping and titanium casting have been combined in a system to produce titanium replicas of human bones. Data acquired using MRI, CT Scanning, X-ray or laser scanning can be converted to a solid geometric model using standard software. Subsequently, data stored in a drawing format can be converted to an STL format for use in rapid prototyping machines. Complicated and exact reproductions and negatives of human structures can be constructed without specific tooling or a physical pattern. Additionally, design changes and additions may be added to the computer model prior to physical construction. Selective Laser Sintering was used to create a casting mold for a human femur, based on laser scanned data from a real bone. The mold was then cast with molten titanium using standard casting technology.

Because of molten titanium's strong chemical activity, only a limited number of materials are resistant to chemical attack [1,2]. Hence, the development of a suitable mold material system was a key aspect of the project. Several studies show that zirconia is one of the least reactive materials with molten titanium [1,3,4]. However, zirconia undergoes a destructive phase transformation at 1100°C that can crack a mold during casting. It converts from a monoclinic to a tetragonal atomic structure, resulting in 3 to 7 percent volume shrinkage [3,5]. The addition of a small amount of yttria stabilizes the zirconia in a cubic structure that does not change phase at 1100°C [6]. If a mold based in stabilized zirconia is infiltrated with zirconia in the unstabilized form, a partially stabilized mold is created. This partially stabilized structure has better thermal shock resistance than either the unstabilized or fully stabilized forms of zirconia [3].

Mold green shapes were Selective Laser Sintered at low temperature from a powder bed of stabilized zirconia and sacrificial polymer binder. The green shapes were infiltrated with an unstabilized zirconia precursor solution and pyrolyzed to remove the sacrificial binder. The fired molds were cast with Ti-6Al-4V alloy. Both the mold material and the castings were characterized.

## EXPERIMENT

### Material Preparation

Granulated yttria-stabilized zirconia powder from Tosoh Ceramic Corporation was selected as the base material for the casting mold. The Tosoh powder consists of zirconia crystallites, 24 nm average size, granulated into 50  $\mu$ m size spheres with a water-soluble binder. To minimize post-process shrinkage and prevent granulate dissolution during infiltration, the granulated particles were pre-sintered for one hour at 500°C and two hours at 1250°C to pyrolyze the binder and densify each particle. The sintering schedule was determined from a sintering map, shown as Figure 1 [7].

The sacrificial SLS binder, an 80:20 molar blend of methylmethacrylate and butylmethacrylate, respectively, was produced by methods discussed elsewhere [8]. This particular copolymer binder was chosen because it completely unzips during firing, leaving no contaminating residue. The copolymer binder was spray dried into fine particles using an Anhydro Laboratory 1 Model Spray Drier. The density of the binder was measured using a Quantachrome Ultracycrometer 1000.

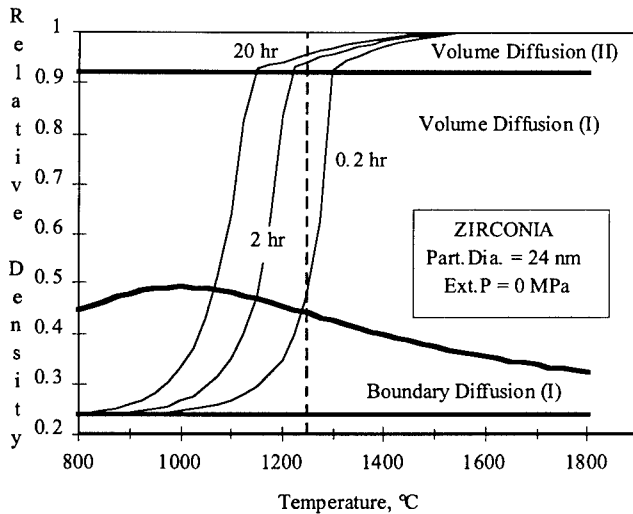


**Figure 1: Zirconia Sintering Map**

### Material Processing and Characterization

The pre-sintered zirconia powder and 30vol% copolymer were mixed in a rolling mill for 24 hours. An SLS Model 125 Workstation was used to build a series of bend test specimens. A layer thickness of 0.005 inches, scan spacing of 0.003 inches and CO<sub>2</sub> laser power of 5 watts

---

were used. Laser scan speed was 16 in/s, and laser spot size was approximately 0.02 inches (500  $\mu$ m). To prevent part curling, the powder bed was pre-heated to 80 $\beta$ C [9].

Five green bend specimens were produced and tested per ASTM C1161-94 using a four point bend apparatus. Density was measured using the Archimedes principle with ethanol. Roughness ( $R_a$ ) was measured using a Surfalyzer 5000. The remaining green bend specimens were measured and weighed. The specimens were infiltrated with a colloidal solution of hydrous zirconia (Nyacol Zr100/20). Wetting of the green parts was improved by adding a surfactant to the colloid. After a number of infiltration and curing cycles, the green shapes were pyrolyzed at 500 $\beta$ C to burn off the copolymer binder, ramped to 1500 $\beta$ C and soaked for 10 hours to promote zirconia crystallization and grain growth. After the firing cycle, each specimen was re-weighed and re-measured. Samples were set aside for density measurements, flexural testing, microscopy and roughness measurements. The infiltration and firing sequence was continued for two more cycles. Material characterization was done after each firing step. X-ray diffraction was used to determine the resulting zirconia phases in the final mold material.

To measure the minimum feature size possible in SLS produced zirconia, a plate containing a series of small holes was fabricated following the sintering and post-processing procedures described above. The plate was 0.015 inches (380  $\mu$ m) thick, and the holes decreased in diameter to about 0.004 inches (100  $\mu$ m). After post-processing, the plate was photographed and the minimum hole size was measured using an optical microscope and Clemex vision software.

#### Mold Preparation and Casting

A human femur bone was scanned using a Digabotics 3-D laser scanner to produce an 80,000-facet three-dimensional model in a Drawing eXchange Format (DXF). The model was converted to an STL format using STL\_UTIL. Because of the immensity of the file size, the model was decimated from 80,000 to 30,000 facets using Visualization Toolkit software. The femur model was divided into pieces, separating the femur shaft from the femur head. The surface normals of the femur ball were inverted and used for the inside of the casting mold. A sphere was constructed for the outer surface of the casting mold, and three cylinders were introduced to create a relief vent and a gate. Boolean operations combined the objects in 3D Studio Max to create the complete mold design. Custom software converted the 3D Studio Max model to an STL format. The completed STL file was transferred via FTP to an SLS Model 125 workstation. The model was sliced using custom software and two molds were constructed using the SLS processing parameters given in the previous section. The femur molds were scaled to half-size to conserve material.

After post-processing, the casting molds were transported to Howmet Research Corporation in Michigan. The molds were attached to a standard casting runner using a proprietary mud and left to dry overnight. The most widely used titanium alloy, Ti-6Al-4V, was cast into the zirconia molds. The titanium castings were returned to The University of Texas at Austin for metallographic examination. A section of the cast cylinder was mounted, polished and etched with a 10% hydrofluoric acid solution for microstructural analysis and alpha-case thickness determination. Roughness measurements were taken on the as-cast surface.

## RESULTS AND DISCUSSION

Figure 2 shows SEM micrographs of the pre-sintered Tosoh zirconia powder. The 50 nm spherical shape was maintained, yet no smaller crystals could be observed at high magnification. The pre-sintered particles did not dissolve when placed in an ultra-sonic water bath.

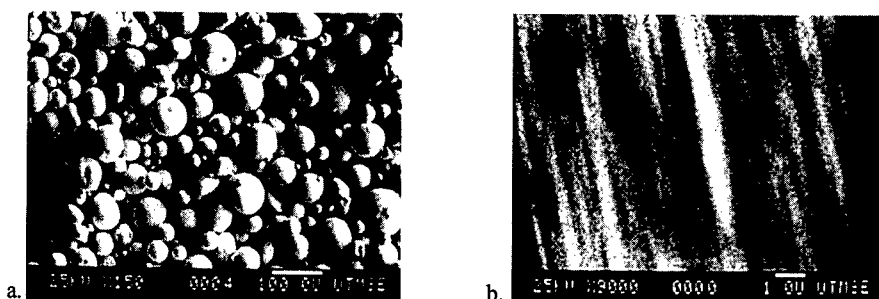


**Figure 2: (a) Pre-sintered Tosoh zirconia powder at low magnification; (b) Polished cross-section of Tosoh particle showing extensive sintering at high magnification**

The 80:20 methylmethacrylate butylmethacrylate copolymer had comparable material properties to the same copolymer produced by Vail [8]. The spray dried powder had a mean diameter of approximately 5  $\mu\text{m}$  and a density of 1.24  $\text{g}/\text{cm}^3$ . Based on the reported density of the stabilized zirconia powder (5.9  $\text{g}/\text{cm}^3$  from Tosoh specification) and the experimental copolymer density, the theoretical density of the zirconia-30vol% copolymer blend was calculated as 4.5  $\text{g}/\text{cm}^3$ .

Initially the copolymer necks provided strength to the green parts. After copolymer burn out, the infiltrated zirconia provided strength. Figure 3 shows the flexural strength of zirconia specimens as a function of infiltrant weight gain. Weight gain was calculated with respect to the original Tosoh zirconia weight (without the copolymer). After the copolymer burn-out, the strength dropped. However, infiltrant weight gain reinforced the zirconia mold material and strength reached over 5 MPa. This strength level is three times the reported value for a similar zirconia mold material system used for titanium casting [2].

Plots of shrinkage and density are shown in Figure 4. Theoretical densities of 4.5  $\text{g}/\text{cm}^3$  and 5.9  $\text{g}/\text{cm}^3$  were assumed for the green and fired mold material, respectively. The x direction is the scan direction. The y direction is orthogonal to the x direction and in the build plane. The z direction is the build direction.

A linear shrinkage of 13% was observed in each direction, on average, after the first firing cycle. In subsequent firing cycles, little additional shrinkage occurred. This is in accordance with reported shrinkage behavior of porous compacts infiltrated with liquid precursors [10]. The density of the mold material increased significantly with infiltrated zirconia weight gain, to a final value near 60% of theoretical. The largest increase in density occurred after the first firing step due to particle rearrangement in initial stage sintering.

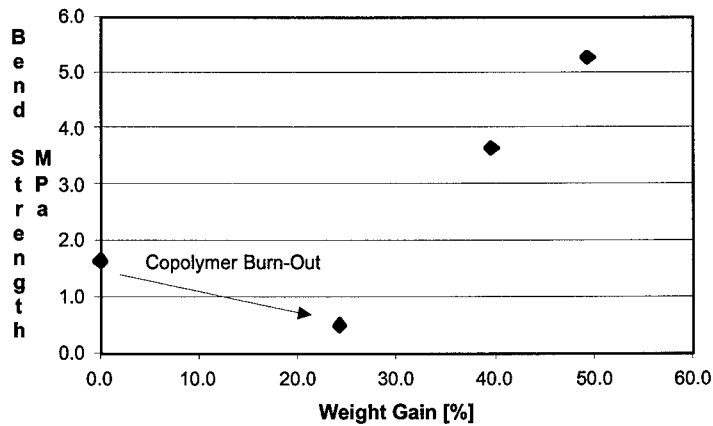


Figure 3: Flexural strength vs. infiltrant weight gain

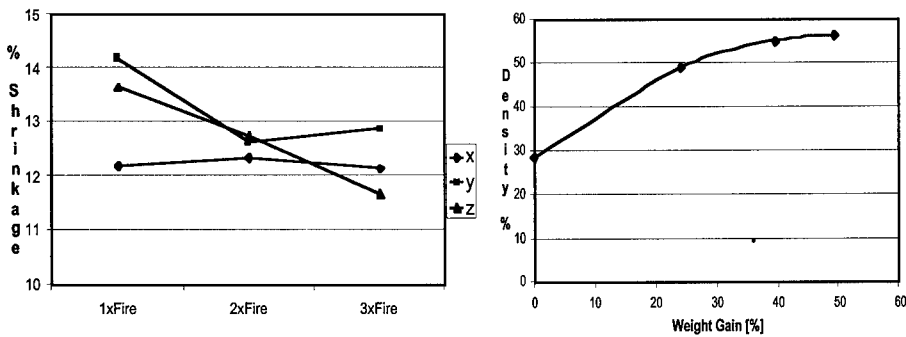
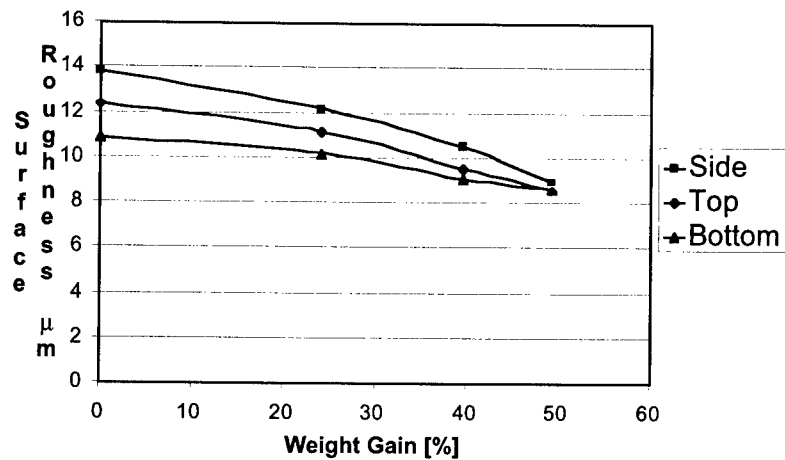


Figure 4: Shrinkage and density of zirconia mold material

The increase in density was not uniform throughout the material. SEM micrographs revealed that the majority of the colloidal particles collected at the surface of the porous body, resulting in a density gradient. The pore walls act as a filter for the infiltrating colloidal particles, and the outer surface captures the most colloidal particles. Additionally, research on colloidal sols shows that colloidal particles migrate to the surface of the porous body with the evaporating liquid during drying, thereby creating a concentration gradient [10]. In thin walled samples, such as the plate with a series of holes in it, a very dense material was achieved.

Multiple infiltration cycles smoothed the surface of the SLS produced parts. The roughest surface on an SLS green part is on its side, where the stair-stepping effect is prominent. The average roughness,  $R_a$ , of the side of the zirconia green part was 14  $\mu\text{m}$ . After multiple infiltrations, the average roughness decreased to 9  $\mu\text{m}$  on all surfaces. Roughness value as a function of infiltrant weight gain is shown in Figure 5.



**Figure 5: Roughness vs. infiltrated zirconia weight gain**

X-ray diffraction revealed that the final mold material consisted of mainly yttria stabilized zirconia and some monoclinic zirconia. The monoclinic zirconia formed when the hydrous zirconia precursor crystallized during firing. Hence, a partially stabilized structure was created, similar to that previously reported in the literature [3].

The smallest hole diameter achieved in the thin zirconia plate was 180 μm. An optical micrograph of a representative hole is shown in Figure 6. This hole size is impressive considering the laser spot size on the SLS Model 125 Workstation is on the order of 500 μm. It is reasonable to suppose that a finer hole size can be created using a finer laser spot size. Because the surrounding plate material is so thin, it reached a very high density after multiple infiltration cycles.

Photos of the cast femur balls and a nylon model are shown in Figure 7.

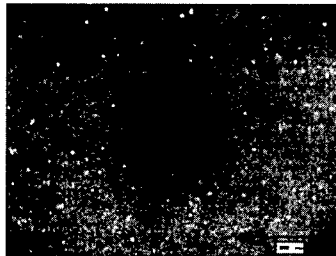


**Figure 6: Hole in thin zirconia plate. The hole is approximately 250 μm in diameter.**

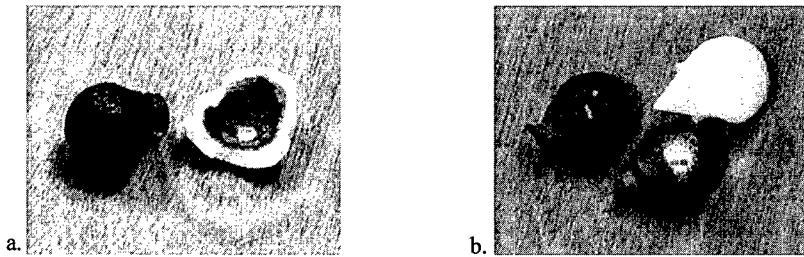


**Figure 7: (a) As-cast femur ball next to casting mold remnant; (b) As-cast and sand-blasted femur ball castings next to nylon model**

Optical micrographs of an etched section of the casting neck revealed a surface alpha case. The alpha case consisted of plate-like  $\alpha$  and intergranular  $\beta$ . The case thickness was approximately 300  $\mu\text{m}$ . The interior portion of the casting exhibited transformed  $\beta$  containing acicular  $\alpha$ . This interior microstructure is typical for as-cast Ti-6Al-4V [11]. The average surface roughness of the as-cast specimen was 8  $\mu\text{m}$ . This roughness value lies between those reported for sand casting (6.25 to 25  $\mu\text{m}$ ) and investment casting (1.25 to 2.5  $\mu\text{m}$ ) [12]. Considering the molds were created using a pattern-less free-form fabrication process and that the base zirconia size in the mold is 50  $\mu\text{m}$ , the as-cast roughness value is quite good.

## CONCLUSIONS

Pre-sintered cubic zirconia powder and a low melting temperature copolymer were Selective Laser Sintered to create titanium casting molds. The green shapes were infiltrated with colloidal zirconia and subsequently fired to pyrolyze the copolymer and crystallize the colloidal particles. The resulting mold material consisted of cubic and monoclinic zirconia phases.

Increasing infiltrant weight gain improved flexural strength, increased density and decreased surface roughness of the mold material. Final flexural strength reached above 5 MPa, exceeding values reported for titanium investment casting molds. Average density reached almost 60% of theoretical, but porosity was graded from the surface to the interior of the part. The majority of shrinkage occurred during the first firing cycle, resulting in approximately 13% shrinkage in each dimension. Roughness decreased from a maximum of 14  $\mu\text{m}$  in the green state to 9  $\mu\text{m}$  in the infiltrated and fired state. Hole sizes as small as 180  $\mu\text{m}$  (diameter) were achieved in a thin zirconia plate.

Casting molds for the head of a human femur, half scale, were created from laser scanned data. Metallographic examination of the cast titanium revealed a thin alpha case and an interior composed of acicular alpha. The as-cast surface roughness of the titanium casting was 8  $\mu\text{m}$ .

## ACKNOWLEDGMENTS

We would like to acknowledge Dr. John Kappelman in the Department of Anthropology and Reuben Reyes in the ASE/EM Learning Resource Center for their assistance in creating the femur mold file. We would also like to acknowledge Dr. Neal Vail for his guidance and assistance



in preparing the copolymer. Finally, we would like to thank Stewart Veeck and Howmet Research Corporation for casting the titanium.

## REFERENCES

1. R.L. Saha and K.T. Jacob, Casting of Titanium and Its Alloys , *Defense Science Journal*, **36** [2] (April, 1986), p. 125-141.
2. A. Karwinski, J. Stachanczyk and K. Zapalska-Nowak, Titanium Casting , *Foundry Trade Journal*, **169** [3513] (Dec. 1995), pp. 566-570.
3. E.D. Calvert, An Investment Mold for Titanium Casting , *U.S. Bureau of Mines Report of Investigations*, [8541], (1981).
4. R.A. Brown and C.A. Brown, *Method of Making Investment Shell Molds for the High Integrity Precision Casting of Reactive and Refractory Metals*, U.S. Patent 3,422,880, (1969).
5. R. Stevens, *Zirconia and Zirconia Ceramics*, 2nd Ed., Magnesium Elektron Ltd., (1986).
6. D.W. Richerson, *Modern Ceramic Engineering*, Marcel Dekker, Inc., (1992), p. 21.
7. D.L. Bourell, Parimal, and W. Kaysser, Sol-Gel Synthesis of Nanophase Yttria-Stabilized Tetragonal, Zirconia and Densification Behavior Below 1600K , *J. Am. Ceram. Soc.*, **76** [3] (March, 1993), p.709.
8. N.K. Vail, *Preparation and Characterization of Microencapsulated, Finely Divided Ceramic Materials for Selective Laser Sintering*, Ph.D. Dissertation, The University of Texas at Austin, (1994).
9. B. Badrinarayan and J.W. Barlow, Effect of Processing Parameters in SLS of Metal-Polymer Powders , *SFF Symposium Proc.*, **6** (1995), pp. 55-63.
10. W. Tu and F.F. Lange, Liquid Precursor Infiltration Processing of Powder Compacts: I, Kinetic Studies and Microstructure Development , *J. Am. Ceram. Soc.*, **78** [12] (1995), pp. 3277-3282.
11. R. Boyer, Titanium and Titanium Alloys , *Metals Handbook*, 9th ed., ASM, **9** (1985) pp. 458-475.
12. K.G. Budinski, *Engineering Materials — Properties and Selection*, 5th ed., Prentice Hall, (1996), p. 45.

---

## Processing-Structure-Property Relations of Polymer-Polymer Composites formed by Cryogenic Mechanical Alloying for Selective Laser Sintering Applications

J. P. Schultz, J. P. Martin, R. G. Kander, and C. T. A. Suchicital  
MSE Department, Virginia Tech, 213 Holden Hall, Blacksburg, VA 24061-0237,  
rkander@vt.edu

### ABSTRACT

Cryogenic mechanical alloying (CMA) has been shown to be an effective means for producing composite powders for selective laser sintering (SLS). Unlike composite particles made by a coating process, both phases are continuous throughout the particles formed by CMA. Consolidation of these composite particles via SLS offers the possibility of forming parts with a co-continuous microstructure. In this research, the microstructure of mechanically alloyed polymer-polymer composites for use in the SLS process is investigated using transmission electron microscopy. By varying the charge ratio and milling time of the CMA process, the phase domain size of the resulting composite powder can be manipulated. This ongoing work explores the microstructural evolution as the composite powders are consolidated via SLS into macroscopic parts, as well as the relationships between microstructure and bulk properties.

### INTRODUCTION

The mechanical alloying (MA) process was originally developed in the late 1960s for solid state processing of dispersion-strengthened metal powders with fine microstructures. Pan and Shaw<sup>1</sup>, pioneers in the field of mechanically alloyed polymers, assert that the “mechanical alloying technique promises to provide the ability to make almost infinite permutations of polymeric alloys. This means that once the process is better understood the properties of the alloy may be specifically designed resulting in a truly *Engineered Material*.”

The mechanically alloyed materials are produced using a ball mill. The initial materials (in powder or pellet form) are placed in the ball mill's vial with two or more metallic or ceramic balls (Figure 1). In a vibratory ball mill, high-energy impacts between the balls and the material occur when the mill's motor vigorously shakes the vial, trapping material between the balls (and between the balls and the vial walls) with each agitation (Figure 2).

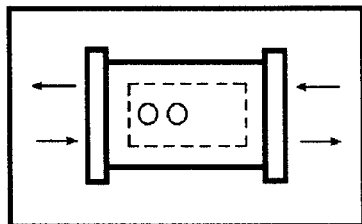


Figure 1. Schematic of vibratory ball mill vial and balls<sup>2</sup>.

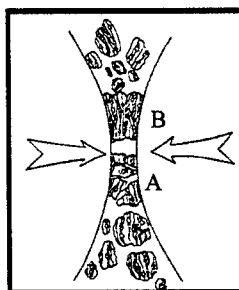
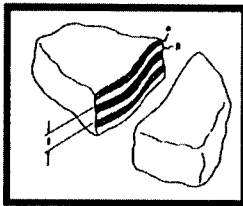


Figure 2. High-energy ball-powder-ball collision, resulting in welding (B), extensional flow, and fracture (A)<sup>2</sup>.

As MA occurs, the particles are repeatedly fractured, deformed, and fused together. This process of repeated, fracturing and cold-welding causes a refinement in microstructure with milling time. The result is a two-phase lamellar or plate-like microstructure with an interlamellar distance dependent on processing time<sup>3</sup> (Figure 3). Other processing parameters which affect the composite microstructure include the energy input, which can be controlled by manipulating the ratio of the total ball mass to the powder mass (charge ratio), milling temperature, ball mill design, and number and size of balls used. The milling temperature can be critical because of its affect on material ductility, recrystallization kinetics, and thermally-aided diffusion across interfaces.

Extrusion and injection molding require the polymers to flow on a macroscopic level, which would destroy the MA microstructure. Selective laser sintering (SLS), a process commercialized by DTM Corp., Austin, Texas, offers a means of consolidating polymer powders into part geometries with minimal flow of the polymers. Thus, SLS presents a means of producing functional part geometries while retaining the refined microstructure created during MA. Upon SLS of the MA powders it is postulated that co-sintering the two polymer phases present in each particle can occur (Figure 4).



**Figure 3.** Two-phase lamellar microstructure of powder particles produced by mechanical alloying<sup>4</sup>.

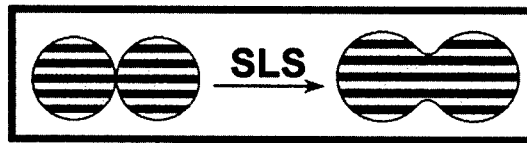


**Figure 4:** SLS of a two-phase lamellar powder.

This work investigates processing-microstructure relationships of two MA micro-composites: 1) poly(ether ether ketone) (PEEK) and a thermoplastic polyimide (LaRC-TPI) and 2) nylon-12 and PEEK. The aim of this study is to systematically control mechanically alloyed polymer-polymer composite microstructures by varying processing conditions, both in the mechanical alloying stage and the post-alloying selective laser sintering. A vibratory ball mill was used to produce blends, and electron microscopy techniques were used to investigate the effects of mechanical alloying time and temperature on the microstructure of these materials. Nylon-12/PEEK powders were consolidated into tensile specimens using a lab-scale SLS unit. Mechanical testing and electron microscopy techniques were used to investigate the mechanical and morphological characteristics of the laser sintered nylon-12/PEEK.

## EXPERIMENTAL

### *Mechanical Alloying Process*

A novel vibratory ball mill that is capable of operating at either ambient or cryogenic temperatures was designed and built by the authors. When operated at cryogenic temperatures, the vial is continuously exposed to a liquid nitrogen bath throughout the milling process. The ball mill can also be operated at ambient temperature by omitting the liquid nitrogen. The milling vial and balls (shown schematically in Figure 1) are stainless steel; the vial has an inside diameter of 77mm, a length of 70mm, and the diameter of each ball is 20 mm. A schematic of the ball mill is shown in Figure 5.

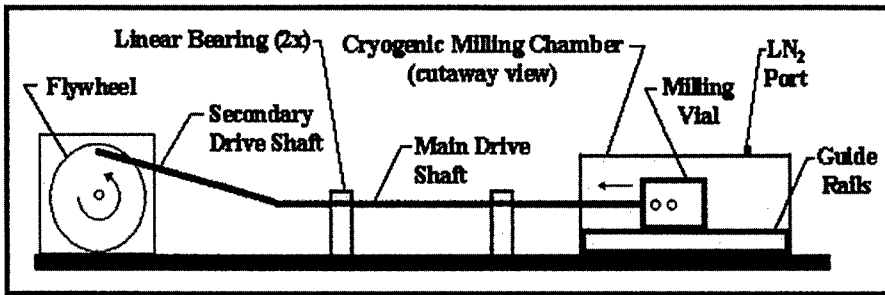


Figure 5. Vibratory ball mill with both ambient and cryogenic capabilities.

Mechanically alloyed micro-composites consisting of Victrex® PEEK 150PF / Mitsui Toatsu LaRC-TPI were produced from the individual components, in powder form, in a 50/50 weight percent ratio. The powders were mechanically alloyed for periods of time ranging from 5 to 90 minutes at both cryogenic and ambient temperatures. Nylon-12/PEEK powders were MA cryogenically in 75-25 and 50-50 vol%, for times of 30 and 60 minutes. The nylon-12 used was DTM DuraForm™ Polyamide, which is specifically engineered for SLS applications.

*Laboratory Scale Selective Laser Sintering Unit*

The selective laser sintering unit, shown in Figure 6, was designed and built by the authors to be used to test the applicability of a material to SLS processing on the laboratory-scale. Design and development of the lab-scale SLS unit was necessitated by the fact that approximately 40 ml of composite powder are produced for every run of the cryogenic vibratory ball mill. In the lab-scale SLS unit's present configuration, part geometries are limited to plaques and other flat test specimens.

The laser, mounted vertically in the SLS unit, is a CO<sub>2</sub> laser with a nominal power of 10W. The translation of the system, mounted in the bottom of the enclosure, has a travel of 152mm x 152mm. The part build area, shown in Figure 7, is a typical configuration in that the powder bed is indexed down after each layer is scanned then additional powder is delivered by the motion of a counter-rotating roll traveling over the powder bed. Tensile specimens were fabricated from DTM DuraForm™ Polyamide in the lab-scale SLS unit to provide a benchmark for the capabilities of the unit and guide the design improvements. The average ultimate tensile strength of DuraForm™ Polyamide sintered in the lab-scale SLS unit was 38.5±3 MPa and the average strain at max stress was 9%; DTM reports a UTS of 44 MPa<sup>5</sup> and a strain to failure of 9%<sup>5</sup> for parts built using a Sinterstation® 2500plus.

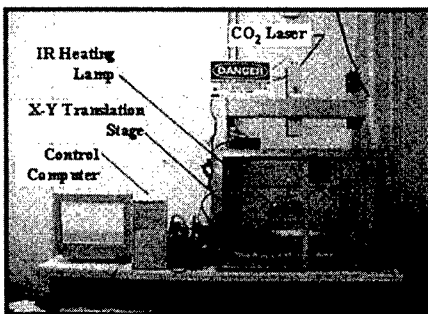


Figure 6. Laboratory scale selective laser sintering unit.



Figure 7. Laboratory scale selective laser sintering unit part build area.

### *Electron Microscopy (SEM & TEM)*

SEM was used to characterize both PEEK/LaRC-TPI and nylon-12/PEEK powders before and after cryogenic mechanical alloying (CMA). The powders were sputtered with gold prior to imaging to avoid sample charging. The MA powders and the nylon-12/PEEK tensile specimens made via SLS were embedded in an epoxy mount and microtomed at room temperature. PEEK/LaRC-TPI sections were collected on copper grids and preferentially stained with RuO<sub>4</sub> to reveal the lamellar morphology. A Philips 420T Transmission Electron Microscope was used to image the microstructures at 100kV.

### *Image Analysis*

An image analysis technique has been developed which will allow comparison of phase domain sizes between samples mechanically alloyed with different conditions. This technique utilizes Sigma ScanPro5 software to enhance phase domain edges and measure individual phase domain widths.

### *Mechanical Testing*

Stress-strain curves, the ultimate tensile stress (UTS) and the strain at the UTS, were recorded for nylon-12/PEEK. Both the mean and standard deviation of the mechanical properties were calculated.

## **RESULTS**

### *PEEK/LaRC-TPI*

A scanning electron micrograph of a single PEEK/LaRC-TPI powder particle MA cryogenically for 1 hour is shown in Figure 8. While the flake-like structure of the alloyed particle is apparent from the micrograph, the individual PEEK and LaRC-TPI phase domains are not discernable via scanning electron microscopy.

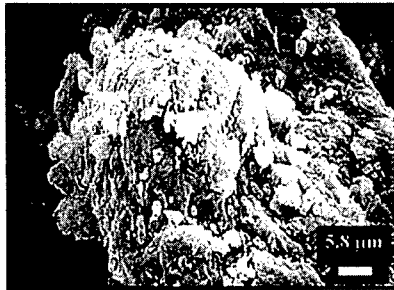


**Figure 8.** SEM micrograph of MA PEEK/LaRC-TPI cryogenically for 60 min. A 5.8 μm bar is shown.

In order to distinguish the phase domains present in the alloyed microstructure, transmission electron microscopy, in conjunction with microtoming and a preferential staining technique, were employed. The resultant TEM micrographs of the PEEK/LaRC-TPI blend (Figures 9 and 10) show the PEEK phase as the darker phase and the LaRC-TPI phase as the lighter phase. Figures 9 and 10 show the microstructure of an MA powder particle milled cryogenically for 15 and 60 minutes, respectively. The TEM micrographs reveal an extremely fine, regular microstructure similar to the one depicted schematically in Figure 3. The effect of alloying time is apparent by

comparing the two micrographs of these blends produced at cryogenic temperature. A 100 nm bar is shown for each micrograph.

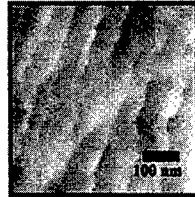
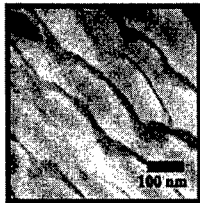


**Figure 9.** Microstructure of PEEK/LaRC-TPI micro-composite, MA 15 min. cryogenically.

**Figure 10.** Microstructure of PEEK/LaRC-TPI micro-composite, MA 60 min. cryogenically.

The Sigma ScanPro5 software package was used to quantify the size of the phase domains imaged via TEM. Analysis of one micrograph (from Figure 9) has been completed as a proof-of-concept. Ten parallel lines were overlaid on the distance-calibrated micrograph. Each line was then retraced in smaller segments corresponding to each phase, while the width of each phase was measured by the software. The boundary between phases was determined by eye after applying an edge enhancing filter to the micrograph. Figure 11 shows the parallel lines overlaid on the micrograph along with a higher magnification illustration of how individual phase domains were measured.

The resulting measurements represent individual phase widths. When plotted in histogram form (Figure 12), two distinct average widths are seen, corresponding to the PEEK and LaRC-TPI phases. Two Gaussian peaks were fitted to the histogram data in order to calculate mean width values for the phase domains. The center of the fitted Gaussian curves corresponds to the average phase domain width for each population. The mean width value measured for the PEEK phase is 27.9 ( $\pm$  0.3) nm, while the mean width for the TPI phase is 86.5 ( $\pm$  0.4) nm.

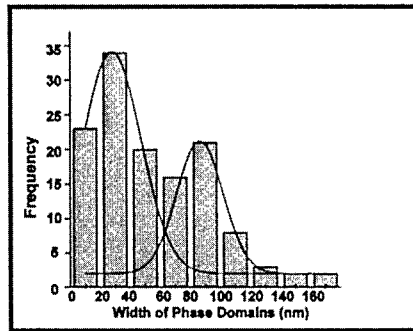
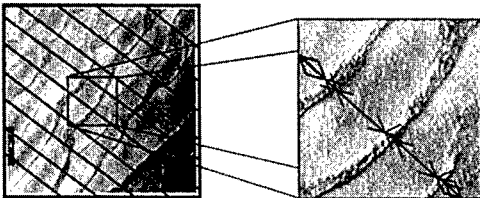


**Figure 11.** MA microstructure (with edge enhancing filter applied) overlaid with lines for measurement.

**Figure 12.** Histogram of measured phase domain widths fitted with Gaussian curves.

#### *Nylon-12/PEEK*

Difficulties in achieving a dense powder bed led to lower than desired mechanical properties in nylon-12/PEEK 75-25vol% (CMA 30min.) tensile specimens consolidated via SLS. The tensile specimens displayed visible cracks in each layer of the build due to the bed porosity. Selected mechanical property data and the SLS processing parameters are listed in Table 1.

**Table 1.** Mechanical properties and SLS processing parameters for nylon-12/PEEK 75-25vol% CMA 30 min.

Nylon-12 / PEEK (75/25 v/v)	UTS (MPa)	% Elong. at Break
	19.5 +/-2.8	9.8 +/-1.8
Laser Power = 0.7W		Scan Speed = 17 mm/s
Layer Thickness = 0.1 mm		Scan Spacing = 0.9 mm

SEM of the fracture surface of a nylon-12/PEEK 75-25vol% tensile specimen is shown in Figure 13. The fracture surface shows particles imbedded in a matrix. Figure 14 shows a TEM micrograph of a laser sintered nylon-12/PEEK 50-50vol% CMA 60 min. Again, particle dispersed in a matrix are observed. The particulate phase is PEEK and the matrix is nylon-12. The microstructure observed in Figures 13 and 14 is not the desired co-continuous phases structure. This helps explain the low UTS of the laser-sintered composite powders.

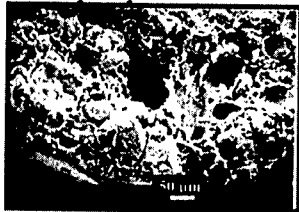


**Figure 13.** Fracture surface of nylon-12/PEEK 75-25vol% tensile specimens.



**Figure 14.** Microtomed surface of laser sintered nylon-12/PEEK 50-50vol%.

## CONCLUSIONS

This on-going research into the processing-structure-property relationship of polymer composites for SLS made by CMA has demonstrated the ability to image and quantify phase domain size in CMA polymers, consolidate CMA polymers via SLS, and image the as-laser-sintered microstructure. Powder bed density problems, which led to low mechanical strength in the nylon-12/PEEK 75-25vol%, need to be addressed in order obtain adequate strength. Future work will include modification of MA and SLS processing parameters to determine if a co-continuous microstructure is attainable. The microscopic image analysis techniques presented will be used in further research.

## ACKNOWLEDGEMENTS

The authors wish to thank DTM Corp. (Austin, Texas) for supporting the nylon-12/PEEK study and Steve McCartney for assistance with the TEM and sample preparation.

## REFERENCES

1. Shaw, W. J. D., Pan, J. and Gowler, M.A., *Proceedings of the Second International Conference on Structural Applications of Mechanical Alloying*, 1993, 431-437.
2. Gilman, P. S. and Benjamin, J. S., *Annual Review in Materials Science*, 13,1983, 279-300.
3. Farrell, M.P., Kander, R.G., and Aning, A.O., *Journal of Materials Synthesis and Processing*, 4,1996,151-161.
4. Maurice, D.R. and Courtney, T.H., *Metallurgical Transactions A*, 21A, 1990, 289-303.
5. <http://www.dtm-corp.com/products/matprop/duraform.pdf>

## **FREEFORM FABRICATION OF FUNCTIONAL SILICON NITRIDE COMPONENTS BY DIRECT PHOTO SHAPING**

S. VENTURA\*, S. NARANG\*, P. GUERIT\*, S. LIU\*, D. TWAIT\*\*, P. KHANDELWAL\*\*\*,  
E. COHEN\*\*\*\* and R. FISH\*\*\*\*

\*SRI International, 333 Ravenswood Avenue, Menlo Park California 94025

\*\*Honeywell Ceramic Components, 2525 West 190<sup>th</sup> Street, Torrance, California 90504

\*\*\*Rolls-Royce Allison, P.O. Box 420, Speed Code W-05, Indianapolis, Indiana 46206-0420

\*\*\*\*University of Utah, Department of Computer Science, 3190 Merrill Engineering Bldg., Salt Lake City, Utah 84112

### **ABSTRACT**

This paper describes a new multilayer solid freeform fabrication process, "Direct Photo Shaping" (DPS), where visible digital light projection is used as a maskless tool to build images on photocurable ceramic dispersions (ceramic powders in photopolymerizable liquid monomers) by flood exposure. For each layer, the projected image is changed according to the CAD data describing the object being built and solidification takes place by photocuring the exposed areas. Multiple layers are dispensed and photocured to fabricate the object of interest. A final rinse with a suitable solvent allows the removal of any uncured ceramic dispersion. The porous free formed "green" ceramic object can then be fired and sintered into a highly dense ceramic part. Digital Light Processing™ technology (developed by Texas Instruments) enables SRI International to project digital, high resolution, high brightness, high contrast visible light to photocure and form components with a good degree of accuracy. This paper describes the Direct Photo Shaping process and its advantages, and how DPS is being applied to the fabrication of ceramic (Honeywell AS800) gas turbine components for military and commercial applications. AS800 test specimens with flexural strength in excess of 800MPa were fabricated by DPS. A first-stage AS800 turbine vane for the Rolls-Royce Allison Model 501-K industrial gas turbine was fabricated by DPS and tested in a gas-burner test rig at 1204°C. Initial tests show that ceramic samples with optimized surface finish (comparable to that achieved by ceramic bisque machining) can be fabricated by applying a pixel anti-aliasing filter along the boundaries of the sample projected slice images.

### **INTRODUCTION**

The Solid Freeform Fabrication (SFF) approach holds great promise for rapid prototyping of ceramic components through simplification of the processing cycle, including the elimination of the time consuming steps of pattern making and mold fabrication. SFF of ceramics will allow fast turnaround design validation of new advanced ceramic components for gas turbine engines. In comparison with conventional spark ignition engines, gas turbine engines offer greater fuel efficiency, lower particulate levels, and multiple fuel capability. Turbine engine technology is critical not only to maintaining US military superiority but also to continuing commercial prominence in the aviation, marine and industrial sectors.

Selective laser sintering [1], 3-D ink jet printing [2], laser stereolithography [3], fused deposition [4] and layer object manufacturing [5] are examples of rapid prototyping process applied so far to the fabrication of ceramic components.



## **DIRECT PHOTO SHAPING PROCESS AND EQUIPMENT DESCRIPTION**

SRI International has developed a new multilayer fabrication process called Direct Photo Shaping [6]. The process is based on the layer-by-layer photocuring of polymerizable compositions curable by visible light. Each layer is selectively photoimaged by digital light projection via a Digital Micromirror Device (DMD) array that performs the function of an electronic maskless tool. While Direct Photo Shaping promises to be generally applied to the fabrication of polymer, ceramic, or metal components, the focus of this paper is to describe its application to ceramics.

The Direct Photo Shaping ceramic forming process may be referred to as photogelcasting, since the "green body" is formed by photocuring of a slurry of the ceramic powder in a solution of photopolymerizable monomers. Photogelcasting closely relates to the gelcasting process [7] which is used for forming ceramics from molds and has been shown to produce complex-shaped, near-net-shape parts with high reliability. While in gelcasting a thermal initiator is used to promote polymerization upon heating, in photogelcasting the polymerizable ceramic slurries are cured by exposure to radiation in the presence of a photoinitiator. As in the gelcasting process, the formed green bodies are generally strong and machinable, and after sintering, highly dense ceramic parts are obtained. The potential advantages and enhancements offered by Direct Photo Shaping, relative to other rapid prototyping processes, are described in the next section.

### **Process Description**

The Direct Photo Shaping process is described in Figure 1. CAD slice images are projected on the photocurable composition which is dispensed and leveled on a build platform. Each layer is photoimaged by digital light projection through a digital micromirror array which modulates the image with a switching time of less than 1 msec. After each exposure, a new layer of photopolymerizable dispersion is applied on the build platform. When the fabrication is complete, the formed ceramic green part is removed from the platform and rinsed with a suitable solvent to dislodge any uncured material. The final ceramic part is obtained after binder removal and sintering. The machine operates in a three-step cycle described as follows.

**Step 1: Apply Slurry.** The ceramic slurry is dispensed on the build table by means of a peristaltic pump and uniformly applied as a thin layer by a doctor blade. Typically, a layer thickness of 2 mil with a control of +/- 0.5 mil is used. Thicker layers may be fabricated and the layer thickness can be adaptively controlled.

**Step 2: Photoexpose.** The layer is shaped into the desired cross section profile by digital light projection of visible light (the light source is a 270 watt metal halide lamp). The exposure time, which is material dependent, is typically 15 seconds or less.

**Step 3: Lower Platform.** The photoexposed portion of the layer is cured into a solid film. The platform is then moved to a lower position and a new layer fabrication cycle starts. The size of the working area is determined by the light projection settings, thus the light can be projected on smaller or larger areas as desired. To optimize resolution, light projection on a small area is desirable. The current system typically operates on a projected area of 6 x 8 inches down to 2 x 3 inches.

The process makes use of compositions photocurable by visible light. This allows us to achieve good depth of cure especially for highly filled compositions such as ceramic slurries [8]. Other advantages of Direct Photo Shaping include:

1. Fast build time because each layer is shaped by flood exposure, thus curing the entire profile at once (unlike the case with a scanning laser); typically for making silicon nitride

components, each layer is dispensed and imaged in less than 45 seconds. On the other hand the dispensing and imaging of other ceramics, such as alumina, may take as low as ten seconds.

2. Minimum number of steps (no postprocessing after the fabrication of each layer is needed).
3. Low cost.
4. High resolution (each pixel is a 16-micron-square mirror and DMD arrays with resolution of 1280x1024 and fill factor of about 90% are available [9]).

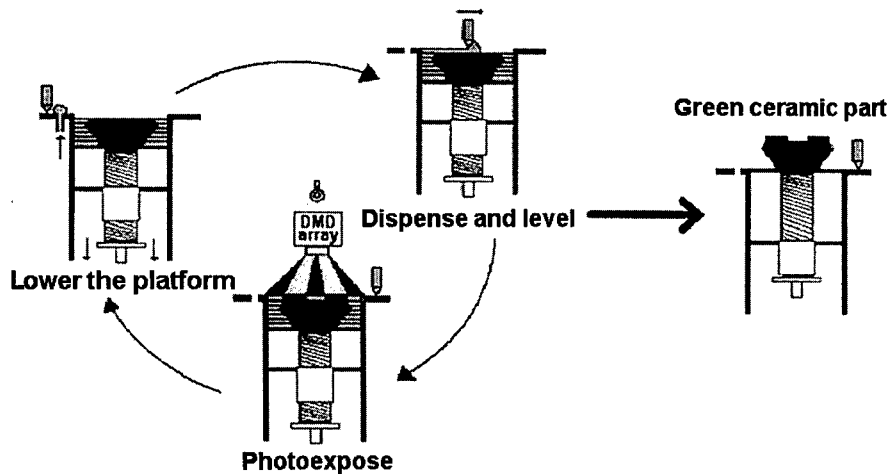


Figure 1. Schematic representation of the Direct Photo Shaping process.

**DMD Array - A Maskless Imaging Tool:** Digital Light Processing by means of digital micromirror devices is a new light projection technology developed by Texas Instruments [9]. Digital micromirror arrays are constituted by digital light switches, aluminum mirrors,  $16 \mu\text{m} \times 16 \mu\text{m}$  square, that precisely control and modulate light. The DMD array is interfaced with a suitable light source and optics, and each pixel mirror is electronically controlled to reflect the incident light in or out of the projection area. Because DMD is a reflective digital light switch, its optical efficiency, 62%, is more than ten times higher than that of a liquid crystal display light transmitting pixel (about 5%). This makes the DMD array a superior tool for maskless imaging of photocurable compositions. Previous attempts of using a LCD programmable mask in combination with UV light to photocure polymers were not successful because of the poor stability of liquid crystal polymers to UV radiation [10].

**Photocurable Composition:** SRI has developed ceramic photocurable compositions that are photoactive in the visible region. This allows us to readily interface the chemistry with the DMD technology and to obtain better depth of curing for the ceramic filled compositions. SRI's photocurable compositions contain photoactive monomers, a suitable photoinitiator, a dispersant and the ceramic powder. The ceramic content typically varies from 45 % to 55% on a volume basis. Ceramic slurries are prepared by ball-milling the silicon nitride powder in the photocurable monomers, after addition of a suitable dispersant, a solvent/plasticizer and the photoinitiator. Ceramic slurries with viscosity of 10,000 cps or less are generally used. The ceramic slurry composition is optimized to improve interlayer adhesion and eliminate any

possible delamination during debinderization. This is achieved by reducing the layer stiffness and by using additives to produce a tacky top layer.

## **DIRECT PHOTO SHAPING OF AS800 SILICON NITRIDE CERAMICS**

Silicon nitride ceramics are of great commercial and military interest because of their excellent mechanical properties, good oxidation resistance and thermal shock behavior both at room and high temperatures.

### **DPS AS800 Silicon Nitride Material Characterization**

Tile specimens (3" x 3"x 0.25") of AS800 silicon nitride were prepared by Direct Photo Shaping at SRI International and shipped to Honeywell Ceramic Components for thermal processing and mechanical property measurements, to be compared with data published by Honeywell Ceramic Components for standard, slip cast AS800. After debinderization, the tiles were gas-pressure sintered to >99% dense and machined into flexure bars. No evidence of the original layers was observed by SEM examination of cross-sectional surfaces of the DPS flexure bars. Figure 2 shows a representative polished surface of an AS800 flexure bar prepared by the DPS method, displaying a pronounced acicular microstructure as is typical of *in situ* reinforced  $\text{Si}_3\text{N}_4$ .

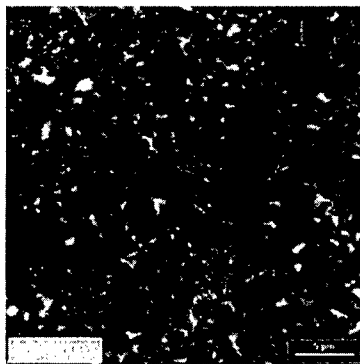


**Figure 2.** Representative microstructures of silicon nitride samples prepared by DPS

Sintered densities of DPS parts, typically >99% theoretical, were measured in deionized water using the Archimedes method. Flexure bars for mechanical testing were machined from eleven DPS plates. The room temperature flexure strength was determined on 3 x 4 x 50 mm bars per ASTM C1161 using a semi-articulating four-point bend fixture having 20 x 40 mm spans [12]. The elevated temperature flexure strength was determined on 3 x 4 x 50 mm bars per ASTM C1121 using a semi-articulating four-point bend fixture made of SiC and having 20 x 40 mm spans [13]. The elevated temperature flexural stress rupture testing was also performed per ASTM C1121 except the load was held constant for the allotted time. The AS800 material formed by Direct Photo Shaping showed similar properties to AS800 formed by the standard slip cast process (Table I). Moreover, the flexure strengths for the layered tiles were not dependent on the orientation relative to the casting direction.

Table I  
**MECHANICAL PROPERTY TESTING OF DPS AS800  
 COMPARED TO STANDARD SLIPCAST AS800**

Test / Conditions	DPS AS800 Results	Standard Slip Cast AS800 Results
Flexural Strength / Machined Surface / 20° C	786 MPa	734 MPa
Flexural Strength / As-sintered Surface / 20° C	797 MPa	588 MPa
Flexural Strength / Machined Surface / 1370° C	558 MPa	580 MPa
Fracture Toughness / 20° C	9 MPa(m) <sup>1/2</sup>	8.1 MPa(m) <sup>1/2</sup>
Flexural Stress-Rupture / 1316° C / 310 MPa applied for 10 hours	No failures	No failures

Additional strength tests of DPS AS800 flexure bars were performed at Rolls-Royce and the results, summarized in Figure 3, support the mechanical properties test results shown in Table I.

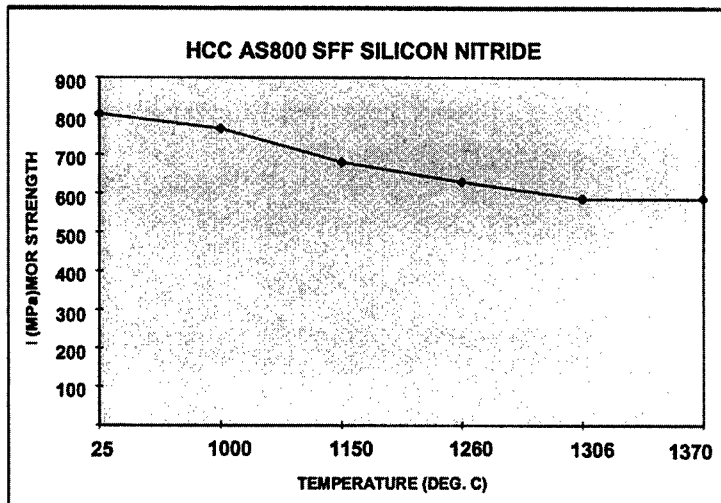
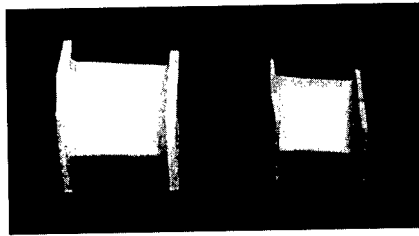


Figure 3. Strength of DPS formed AS800 silicon nitride.

### **Fabrication of DPS AS800 Silicon Nitride Vanes**

First-stage AS800 silicon nitride turbine vanes for the Rolls-Royce Allison Model 501-K industrial gas turbine were fabricated by DPS and processed to >99% density. The component, which is approximately 40 mm high with a chord length of 34 mm, was chosen to demonstrate the feasibility of the Direct Photo Shaping process to build complex geometry components. Three vanes are built at the same time on the DPS build platform. The vanes are fabricated from 523 layers, each 50  $\mu\text{m}$  thick. This layer thickness was found to be optimal, to ensure good interlayer adhesion and to generate smooth curved layers. The total time required for the fabrication of three green vanes was about seven hours, thus just over two hours per vane.

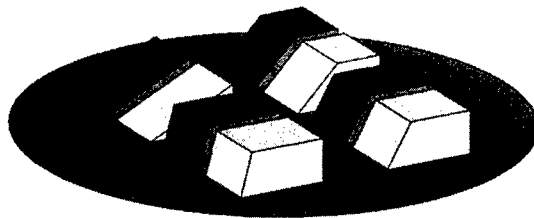
After binder removal, the silicon nitride vanes were densified by gas pressure sintering using Honeywell Ceramic Components standard thermal cycles. The vanes were presintered in order to smooth the surface by a minimal amount of hand-finishing. Figure 4 illustrates a green silicon nitride turbine vane sample next to a hand-finished, sintered one. One silicon nitride vane was evaluated in a gas-fired burner test rig and subjected to a total of 20 thermal cycles at an average gas temperature of 1204°C. Nondestructive inspection of the component after testing was performed by fluorescent penetrant inspection and real-time microfocus X-radiography. No cracks or defects were found on the part after test.



**Figure 4.** “Green” (left) and sintered (right) silicon nitride turbine vanes.

### **EFFECT OF PIXEL ANTI-ALIASING ON SURFACE FINISH**

The use of digital light projection to photocure the ceramic layer offers capabilities not available with the traditional laser scanning systems. The DMD-array can be used to project gray images, and the intensity of the gray can be modulated to control light transmission. We have performed experiments that show that for a given light projector resolution (1024x768 pixel array and a projected area of 5.4”x4.1”) and layer thickness (50  $\mu\text{m}$ ), the surface finish of parts fabricated by DPS can be improved by applying an anti-aliasing filter along the boundary of the projected slice images. Thus we have fabricated silicon nitride wedge-shaped parts with four different angles, 25°, 45°, 60° and 75°, with and without 4-pixel wide anti-aliasing filter applied on their boundary (Figure 5). The anti-aliasing filter turns the pixel-to-pixel black-and-white stair-steps into smooth grey-scale boundaries, as schematically illustrated in Figure 6. This translates into a gradient of power density along the periphery of each slice that smooths the surface of the photocured sample over multiple layers. Table II summarizes the results on the root mean square (RMS) roughness on the inclined surface of the sintered samples with and without anti-aliasing effect as a function of the surface angle.



**Greysteps:** with antialiasing effect.  
**White steps:** without antialiasing effect

**Figure 5.** Silicon nitride wedge-shaped parts built by DPS to study the effect of pixel anti-aliasing filter on surface finish.

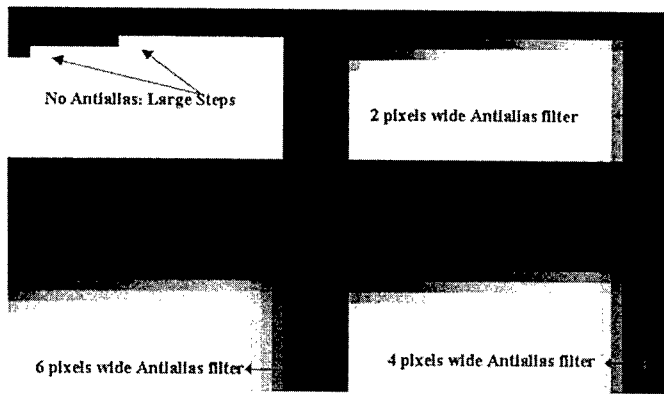


**Figure 6.** Illustration of the pixel anti-aliasing filter on the projected slice image boundaries.

Table II  
 EFFECT OF THE ANTI-ALIASING FILTER ON THE SURFACE ROUGHNESS OF INCLINED SURFACES

Inclined Surface Angle (Degree)	4-Pixel Anti-Aliasing Filter	Estimated RMS Roughness <sup>(*)</sup> (μm)
25	no	7
25	yes	1.8
45	no	3.5
45	yes	1.8
60	no	7
60	yes	3.5
75	no	14
75	yes	3.5

(\*) The surface roughness was estimated by visual comparison with calibrated standards.

---

The Table II results indicate that the use of the 4-pixel anti-aliasing filter reduces the RMS roughness to values comparable to that achieved by ceramic bisque machining ( $\sim 1.8\mu\text{m}$ ). Better surface finish (RMS roughness of  $1\mu\text{m}$  or less) may be achievable by using DMD arrays with higher number of pixels, by projecting the light over a smaller area or by making thinner layers. The effect of pixel anti-aliasing on the tolerance control of the part being built is currently being investigated.

## CONCLUSIONS

SRI International has developed a new multilayer solid freeform fabrication process, Direct Photo Shaping, where visible digital light projection is used as a maskless tool to photocure cross sections from CAD data. This process has been applied to the fabrication of AS800 silicon nitride ceramic components. Tile specimens ( $3''\times 3''\times 0.25''$ ) were found to be more than 99% dense and to have flexure strengths slightly in excess of 800 MPa and comparable mechanical properties to those of tiles formed by conventional slip cast processing techniques. Silicon nitride turbine vanes were fabricated and validated for their mechanical properties by subjecting them to repeated thermal cycling at  $1204^\circ\text{C}$ . Initial tests show that ceramic samples with optimized surface finish can be fabricated by applying a pixel anti-aliasing filter along the projected slice image boundaries.

## ACKNOWLEDGEMENTS

This work was supported by the Defense Advanced Research Projects Agency (DARPA) and the Office of Naval Research (ONR). We thank Dr. William Coblenz and Dr. Steven Fishman for their continuous support and valuable suggestions.

## REFERENCES

1. J.V. Tompkins, B.R. Birmingham, and H.L. Marcus, Proceedings of the First International Symposium on Advanced Synthesis and Processing, Cocoa Beach, FL, January 1995.
2. J. Grau, J. Moon, S. Uhlund, M. Cima, and E. Sachs, Proceedings of the Solid Freeform Fabrication Symposium (Austin, TX, August, 1997), pp.371-8.
3. M.L. Griffith and J.W. Halloran, *J. Am. Ceram. Soc.*, 79(10), 2601-8 (1996); T. Himmer, T. Nakagawa and H. Naguchi, "Stereolithography of Ceramics", pp. 363-370.
4. R. Clancy, V. Jamalabad, P. Whalen, P. Bhargava, C. Dai, R. Rangarajan, W. Wu, S. Danforth, N. Langrana and A. Safari, Proceedings of the Solid Freeform Fabrication Symposium (Austin, TX, August, 1997), pp. 185-194.
5. D. Klosterman, R. Chartoff, N. Osborne, G. Groves, A. Lightman and G. Han, Proceeding of the Seventh International Conference on Rapid Prototyping, San Francisco, CA, April 1997, pp.43-50.
6. S. Ventura, S. Narang, S. Sharma, J. Stotts, D. Annavajula, L.Ho, S. Lombardo, A. Hardy, M. Mangaudis, and L. Groseclose, Proceeding of the Seventh International Conference on Rapid Prototyping, San Francisco, CA, April 1997, pp.271-8.

- 
7. O.O. Omatete, M.A. Janney, and R.A. Strehlow, *Ceram. Bull.* 70(10), 1991.
  8. C.G. Roffey, *Photopolymerization of Surface Coatings*, edited by John Wiley & Sons Ltd. 1982.
  9. L.J. Hornbeck, "Digital Light Processing for High Brightness, High-Resolution Applications", Presented at "Electronic Imaging, EI '97", 10-12 February 1997, San Jose, California; L.J. Hornbeck, "Digital Light Processing and MEMS: Timely Convergence for a Bright Future"; Presented at Micromachining and Microfabrication '95, 23-24 October 1995, Austin, Texas.
  10. M. Burns, *Automated Fabrication: Improving Productivity in Manufacturing*; edited by Prentice Hall, Englewood Cliffs, NJ, 1993.
  11. K. N. Seibein and W. M. Lovington, in *Microstructural Science*, vol.16, pp. 319-329. Edited by H.J. Cialoni, M.E. Blum, G.W.E. Johnson, and G.F. VanderVoort, ASM International, Metals Park, OH, 1985
  12. "Standard Test Method for Flexural Strength of Advanced Ceramics at Ambient Temperature", ASTM C1161, *Annual Book of ASTM Standards*, Vol. 15.01, American Society for Testing and Materials, West Conshohocken, PA, 1999.
  13. "Standard Test Method for Flexural Strength of Advanced Ceramics at Elevated Temperature", ASTM C1211, *Annual Book of ASTM Standards*, Vol. 15.01, American Society for Testing and Materials, West Conshohocken, PA, 1999.



## REFRIGERATIVE STEREOGRAPHY USING SOL-GEL TRANSFORMABLE PHOTOPOLYMER RESIN AND DIRECT MASKING\*

T. MURAKAMI, A. KAMIMURA, N. NAKAJIMA

Department of Engineering Synthesis, The University of Tokyo

Hongo 7-3-1, Bunkyo-ku, Tokyo 113-8656, Japan, murakami@mech.t.u-tokyo.ac.jp

### ABSTRACT

The authors have been studying a new fabrication method termed "refrigerative stereolithography" which uses a gel resin layer instead of a liquid layer as in conventional stereolithography. This paper proposes the "direct masking method" in which a masking pattern is drawn to block direct light exposure to the surface of the gel resin layer. With such masks, we can avoid surplus growth only in the regions where it is unnecessary to improve height direction accuracy and resolution. Also, we can solidify the required section shape selectively using the masks and a lamp instead of laser scan patterns. The effectiveness of refrigerative stereolithography with the direct masking method is discussed and confirmed by some experimental results.

### INTRODUCTION

The authors have been studying a new fabrication method termed "refrigerative stereolithography" [1] [2]. In this process (Figure 1), a liquid photopolymer resin as a new layer is supplied, cooled to the gel state, and then photopolymerized. After repeating this process for all layers, a photopolymerized object is fabricated in a gel resin block. The object can be obtained by heating the block, and then melting and removing only the non-photopolymerized resin. The use of a gel layer, instead of a liquid layer as in conventional stereolithography, leads to some advantages.

First, the so-called "support" structures for isolated or overhanging shapes are unnecessary, and distortion by photopolymerization should be reduced because the object being fabricated is buried in and held by gel resin. This can extend the range of shapes that can be fabricated and improve fabrication accuracy.

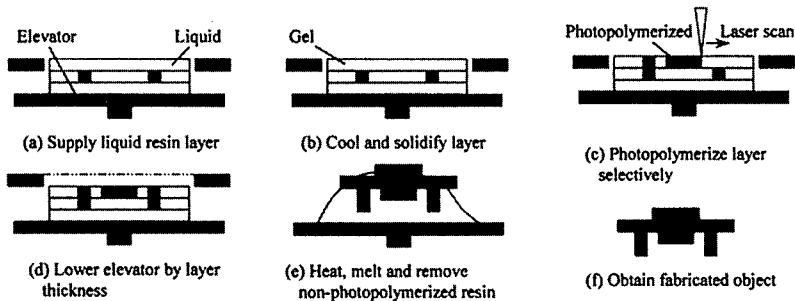


Figure 1. Refrigerative Stereolithography Process

\* This work was done as a doctoral research of the second author.

Second, additional treatments for layers can easily be introduced. For example, we can draw some mask patterns directly on the surface of the gel layer. In this paper, we discuss and confirm the effectiveness and possibility of using such masks to avoid surplus growth only in the regions where it is unnecessary to improve height direction accuracy and resolution and to solidify the required section shape selectively using a lamp instead of laser scan patterns.

### SOL-GEL TRANSFORMABLE PHOTOPOLYMER RESIN

In our previous study [1], we used a commercially available urethane-acrylate resin for the conventional stereolithography (SCR-500, JSR: Japan Synthetic Rubber Co., Ltd.) and a urethane-acrylate resin (KC1026-8, JSR) which was specially prepared for obtaining improved temperature-viscosity characteristics. However, we needed to cool the resins SCR-500 and KC1026-8 to  $-50^{\circ}\text{C}$  and  $-10^{\circ}\text{C}$ , respectively, to make them sufficiently solid. The problem with these low temperatures is that they result in inactive photopolymerization reaction, frost on the resin surface, and a large and complex cooling mechanism (e.g., that involving liquid nitrogen).

As a resin more suitable for refrigerative stereolithography, a new sol-gel transformable photopolymer resin was composed of urethane-acrylate photopolymer resin and sol-gel transformable resin by Kuraray Co., Ltd. The sol-gel resin consists of iso-PMMA (polymethyl methacrylate) and syn-PMMA molecules. At a low temperature, iso- and syn-PMMA molecules become entangled and the resin is in the gel state. At a high temperature, the entangled molecules separate and the resin becomes a sol. This sol-gel transformation occurs sharply in a rather narrow temperature range and is thermally reversible. By adding this sol-gel transformable resin of 15 weight % to a urethane-acrylate liquid photopolymer resin UV1214, a sol-gel transformable photopolymer resin (UV1214-15) was prepared by Kuraray Co., Ltd. This composed resin can be photopolymerized both in the sol and gel states. Note that solidification by photopolymerization occurs only by the photopolymer component, and sol-gel resin molecules remain as they are in the photopolymerized resin.

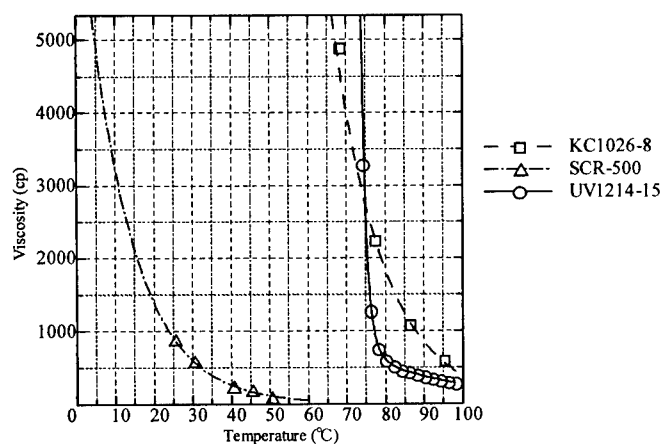


Figure 2. Relationship between Temperature and Viscosity of Photopolymer Resins

Figure 2 shows the relationship between temperature and viscosity of photopolymer resins SCR-500, KC1026-8 and UV1214-15. UV1214-15 changes between the sol and gel states sharply at about 80°C, and its gel strength is 600 kPa which has been experimentally proven to be sufficiently solid to support fabricated objects during the refrigerative stereolithography process. Table I shows the properties of the sol-gel transformable photopolymer resin. Addition of sol-gel resin reduces the tenacity and hardness of the photopolymer resin when photopolymerized. Table II lists the properties of three photopolymer resins. Although the temperature-viscosity characteristics are good, the mechanical properties after photopolymerization of the sol-gel transformable photopolymer resin need to be improved in the future.

### DIRECT MASKING TO RESTRAIN SURPLUS GROWTH

In a stereolithography fabrication process, excessive laser exposure to solidify the resin beyond one layer thickness is required because a solidified layer must be bonded firmly to the previous layer. Therefore, surplus growth caused by overcuring occurs at the bottom surface of the solidified layers and leads to a dimensional error in the height direction [3]. To improve height direction accuracy and resolution by avoiding surplus growth only where it is unnecessary, we propose the "direct masking method" to draw mask patterns to block direct light exposure to the surface of the gel resin layer in refrigerative stereolithography. As depicted in Figures 3(a) and (b), liquid resin for the new layer is supplied and becomes a gel after mask patterns are drawn with material to intercept light on the surface of the previous gel (or photopolymerized) layer (Figure 3(a)). When photopolymerizing the new layer, surplus growth can be avoided only in the regions where the mask patterns are drawn (Figure 3(c)). Note that the surface of a liquid resin layer in conventional stereolithography cannot realize such a direct mask rigidly.

**Table I.** Properties of Sol-Gel Photopolymer Resin

	UV1214	UV1214-15
Breaking elongation (%)	22.1	11.7
Breaking strength (kgf/mm <sup>2</sup> )	1.79	2.15
Bending elongation (%)	23.8	8.3
Bending strength (kgf/mm <sup>2</sup> )	2.43	6.42
Vickers hardness (Hv)	4.85	3.97

**Table II.** Properties of Photopolymer Resins

	SCR-500	KC1026-8	UV1214-15
Breaking elongation (%)	17	11.2	11.7
Breaking strength (kgf/mm <sup>2</sup> )	7.43	8.8	2.15
Refrigeration temperature (°C)	-50	-10	28

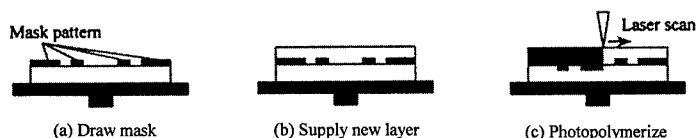


**Figure 3.** Direct Masking to Restrain Surplus Growth

## FABRICATION SYSTEM IMPLEMENTATION

We implemented a fabrication system based on refrigerative stereolithography with the direct masking method. The photopolymer resin is stored in a tank and led to a coater through a pipe. The tank, pipe and coater are heated to 100°C to keep the resin liquid. The amount of resin supply is controlled by an electric valve. The laser beam derived from the laser source is reflected by four sets of optical mirrors and then focused on the resin surface by an optical convexo-plane lens, which is placed on a carrier equipped with the XY-plotter. The XY-plotter mechanism works to scan the laser beam across the resin surface. The masks for intercepting the surplus light from upper layers are drawn by an inkjet head, which is located below the XY-plotter carrier and moves with it. The inkjet head has a nozzle 40 μm in diameter. The diameter of the ink dot when it drops onto the resin surface was experimentally measured to be approximately 200 μm, which is the current resolution limit for masking patterns. As for the masking material, we used pigment ink for inkjet printers which was experimentally confirmed to intercept ultraviolet sufficiently for our fabrication system.

## FABRICATION EXPERIMENT FOR SURPLUS GROWTH RESTRAINT

To confirm the effectiveness of refrigerative stereolithography with direct masking to restrain surplus growth, we fabricated a joint model that is an assembly of two blocks and one arm meshed with cylindrical axes and holes (Figure 4(a)). The laser power, scanning speed and layer thickness for this fabrication were 9.6 mW, 400 mm/sec and 100 μm, respectively. As a result, a gel block (Figure 4(b)) and then the final object (Figure 4(c)) were obtained. Figure 4(d) shows the dimensions of the fabricated object measured using a micrometer and a measuring microscope and the original numerical value in the CAD data. The clearance between the planar faces of the block and the arm was 100 μm (at each side) in CAD data, and this clearance was accurately realized in the height direction and was not decreased by surplus growth. From this result, the effectiveness of direct masking to restrain surplus growth and to improve height direction accuracy was experimentally confirmed.

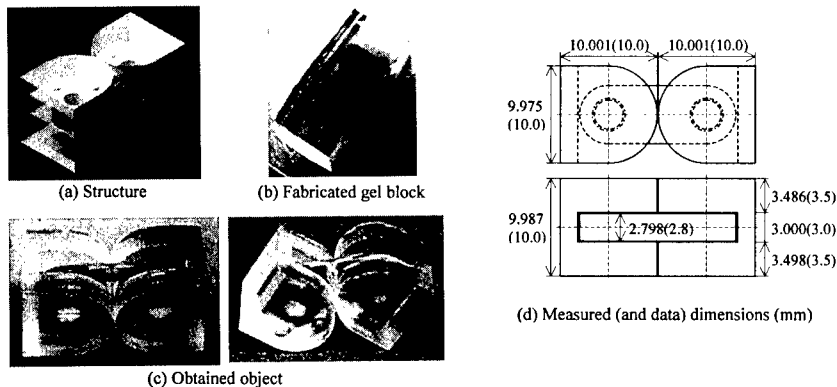


Figure 4. Joint Model

The fabricated object is colored with residual ink from the masking layers. Since conventional pigment ink is currently used, there exist the problems of reflection and penetration of UV light, and also loss of transparency for visible light. Each mask is drawn three times on one resin surface to achieve sufficient interception of UV light. However, this causes an increase of the mask thickness. These problems should be solved if we use ink with particulate oxidized titanium, which intercepts UV light sufficiently but is visibly transparent.

### DIRECT MASKING FOR SELECTIVE LAMP EXPOSURE

As shown in Figure 5, another possible advantage of the direct masking method is to selectively photopolymerize section shapes on a resin layer with lamp exposure instead of laser scanning. Lamp exposure should photopolymerize every portion of the section shape more uniformly than laser beam scanning. Although the time required for mask drawing must be considered, the total fabrication time should be reduced because the areas are fabricated simultaneously whereas the laser scans and fills the areas line by line. Also, a lamp should cost less than a laser. If there is some distance between the mask and fabrication surface as in the solid ground curing method [4], divergence of the light definitely reduces fabrication accuracy.

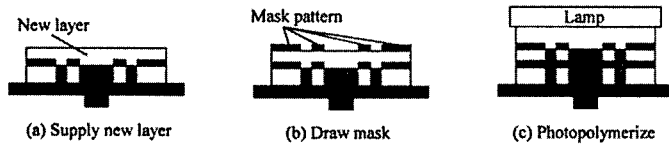


Figure 5. Direct Masking for Selective Light Exposure

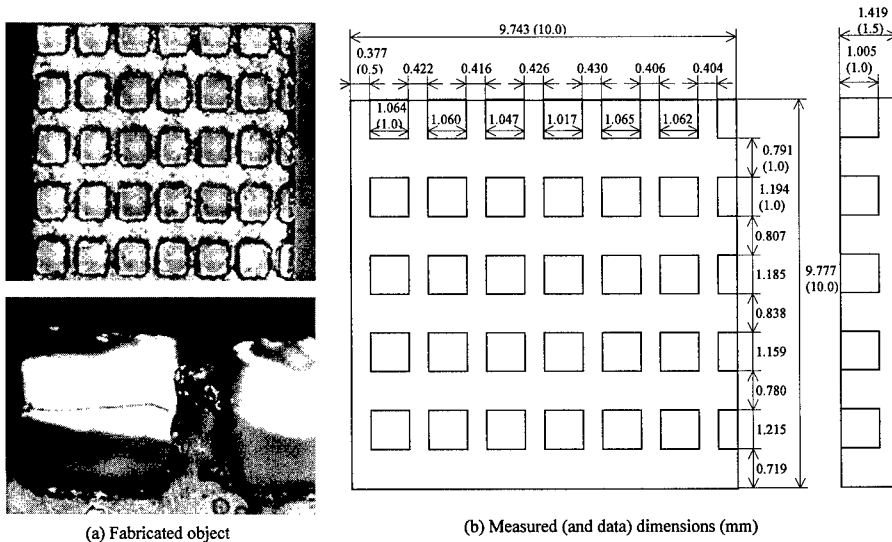


Figure 6. Grid Model

Since the mask is drawn directly on the fabrication surface (distance is 0) in our approach, divergence of the light is less critical.

To confirm the possibility of selective photopolymerization by direct masking, we fabricated a grid model (a plate with cubical concaves) as in Figure 6 by using a UV lamp in our system instead of laser scanning. Lamp power, exposure time for one layer and layer thickness for the fabrication are  $408 \text{ mW/cm}^2$ , 0.4 sec and  $100 \mu\text{m}$ , respectively. Figure 6(a) shows the fabricated object and Figure 6(b) shows the measured dimensions and original values in CAD data. Since the basic shape is fabricated, the possibility of selective photopolymerization by direct masking is confirmed. However, the corners are rounded and dimensions are not accurate mainly because of the limitations of the size and accuracy of ink dots.

## CONCLUSIONS

This paper is summarized as follows:

- (1) Refrigerative stereolithography with the direct masking method is proposed.
- (2) As a resin suitable for refrigerative stereolithography, a sol-gel transformable photopolymer resin is composed of urethane-acrylate photopolymer resin and sol-gel transformable resin.
- (3) A fabrication system is implemented based on the proposed concept.
- (4) The effectiveness of direct masking to restrain surplus growth and improve resolution in the height direction is confirmed.
- (5) The possibility of direct masking for selective photopolymerization with lamp exposure is confirmed.

Direct masks for surplus growth restraint are inserted at the bottom of the shape to be fabricated, i.e., the boundary of photopolymerized and non-photopolymerized portions. Also, direct masks for selective light exposure are placed over non-photopolymerized portions. Therefore, direct masks do not in principle ruin the bonding between two photopolymerized layers. Although the accuracy and resolution of masking requires further improvement, we believe that refrigerative stereolithography with direct masking can become a promising rapid prototyping technology.

## REFERENCES

1. T. Murakami, A. Kamimura and N. Nakajima, Refrigerative Stereolithography for Rapid Product Prototyping, Proc. of the 8th Int. Conf. on Production Eng., (1997) pp.73-82.
2. A. Kamimura, T. Murakami and N. Nakajima, Refrigerative Stereolithography for Support-Free and Accurate Fabrication, 10th Annual Solid Freeform Fabrication Symposium, (1999) pp.583-590.
3. T. Watanabe, A. Matsumura and T. Ukachi, Study on Spectral Sensitivity of Resins for Stereolithography, Proc. of RadTech Asia '95, (1995) pp.301-306.
4. P. F. Jacobs, Rapid Prototyping & Manufacturing: Fundamentals of Stereolithography, (Society of Manufacturing Engineers, 1992) pp.416-419.

---

## **Direct Patterning**

---

**Matrix Assisted Pulsed Laser Evaporation Direct Write (MAPLE DW): A New Method to Rapidly Prototype Active and Passive Electronic Circuit Elements**

J.M. Fitz-Gerald, D.B. Chrisey, A. Piqu, R.C.Y. Auyeung, R. Mohdi, H.D. Young,  
H.D. Wu, S. Lakeou, and, R. Chung

Naval Research Laboratory, Washington, D.C.

**Abstract**

We demonstrate a novel laser-based approach to perform rapid prototyping of active and passive circuit elements called MAPLE DW. This technique is similar in its implementation to laser induced forward transfer (LIFT), but different in terms of the fundamental transfer mechanism and materials used. In MAPLE DW, a focused pulsed laser beam interacts with a composite material on a laser transparent support transferring the composite material to the acceptor substrate. This process enables the formation of adherent and uniform coatings at room temperature and atmospheric pressure with minimal post-deposition modification required, i.e.,  $\leq 400^\circ\text{C}$  thermal processing. The firing of the laser and the work piece (substrate) motion is computer automated and synchronized using software designs from an electromagnetic modeling program validating that this technique is fully CAD/CAM compatible. The final properties of the deposited materials depend on the deposition conditions and the materials used, but when optimized, the properties are competitive with other thick film techniques such as screen-printing. Specific electrical results for conductors are  $< 5X$  the resistivity of bulk Ag, for BaTiO<sub>3</sub>/TiO<sub>2</sub> composite capacitors the k can be tuned between 4 and 100 and losses are  $< 1-4\%$ , and for polymer thick film resistors the compositions cover 4 orders of magnitude in sheet resistivity. The surface profiles and fracture cross-section micrographs of the materials and devices deposited show that they are very uniform, densely packed and have minimum resolutions of  $\sim 10\ \mu\text{m}$ . A discussion of how these results were obtained, the materials used, and methods to improve them will be given.



## Introduction

There is a strong need in industry for new design and Just In Time Manufacturing (JITM) methods, materials, and tools to direct write for rapid prototyping passive circuit elements on various substrates, especially in the mesoscopic regime, i.e., electronic devices that straddle the size range between conventional microelectronics (sub-micron-range) and traditional surface mount components (10 mm-range). The need is based on the desire: to rapidly fabricate prototype circuits without iterations in photolithographic mask design, in part, in an effort to iterate the performance on circuits too difficult to accurately model, to reduce the size of PCB s and other structures (~30-50% or more) by conformally incorporating passive circuit elements into the structure, and to fabricate parts of electronic circuits by methods which occupy a smaller footprint, which are CAD/CAM compatible, and which can be operated by unskilled personnel or totally controlled from the designers computer to the working prototype. Mesoscopic direct write approaches are not intended to compete with current photolithographic circuit design and fabrication. Instead, these technologies will enable new capabilities satisfying next generation applications in the mesoscopic regime.

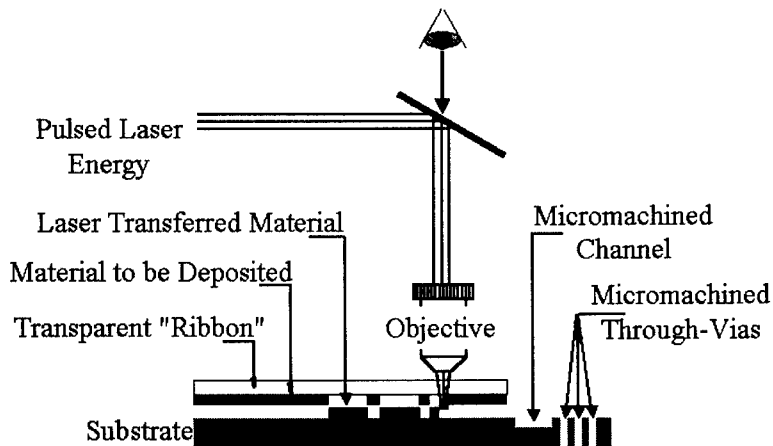


Figure 1. Schematic diagram of the MAPLE DW process. The process lends itself to both additive and subtractive processing.

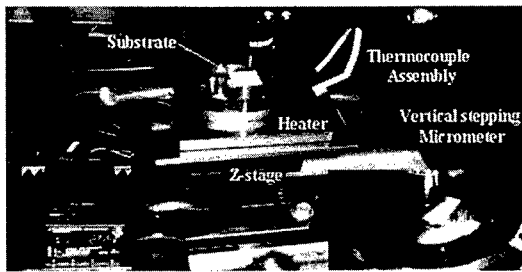


Figure 2. MAPLE DW system incorporating computer controlled X\_Y\_Z stages for ribbon and substrate manipulation with in-situ heating.

Many different CAD/CAM approaches exist to direct write or transfer material patterns and each technique has its own merits and shortcomings. The different approaches include plasma spray, laser particle guidance, MAPLE DW, laser CVD, micropen, ink jet, e-beam, focused ion beam, and several novel liquid or droplet microdispensing approaches. One common theme to all techniques is their dependence on high quality starting materials, typically with specially tailored chemistries and/or rheological properties (viscosities, densities and surface tension). Typical starting materials, sometimes termed pastes or inks, can include combinations of powders, nanopowders, flakes, surface coatings and properties, organic precursors, binders, vehicles, solvents, dispersants, surfactants, etc. This wide variety of materials with applications as conductors, resistors, and dielectrics are being developed especially for low temperature deposition ( $< 400^{\circ}\text{C}$ ).<sup>10</sup> This will allow fabrication of passive electronic components and RF devices with the performance of conventional thick film materials, but on low temperature flexible substrates, e.g., plastics, paper, fabrics, etc.<sup>11</sup> Examples include silver, gold, palladium, and copper conductors, polymer thick film and ruthenium oxide-based resistors and metal titanate-based dielectrics. Fabricating high quality crystalline materials at these temperatures is nearly impossible. One strategy is to form a high density packed powder combined with chemical precursors that form low melting point nanoparticles *in situ* to chemically weld the powder together. The chemistries used are wide ranging, but include various thermal, photochemical and vapor, liquid, and/or

gas co-reactants. The chemistries are careful to avoid carbon and hydroxide incorporation that will cause high losses at microwave frequencies or chemistries that are incompatible with other fabrication line processing steps. To further improve the electronic properties for low temperature processing, especially of the oxide ceramics, laser surface sintering is often used to enhance particle-particle bonding. In most cases, individual direct write techniques make trade-offs between particle bonding chemistries that are amenable with the transfer process and direct write properties such as resolution or speed. The resolution of direct write lines can be on the micron scale, speeds can be greater than 100 mm/sec, and the electronic material properties are comparable to conventional screen-printed materials. Optimized materials for direct write technologies result in: deposition of finer features, minimal process variation, lower prototyping and production cost, higher manufacturing yields, decreased prototyping and production time, greater manufacturing flexibility, and reduced capital investments.

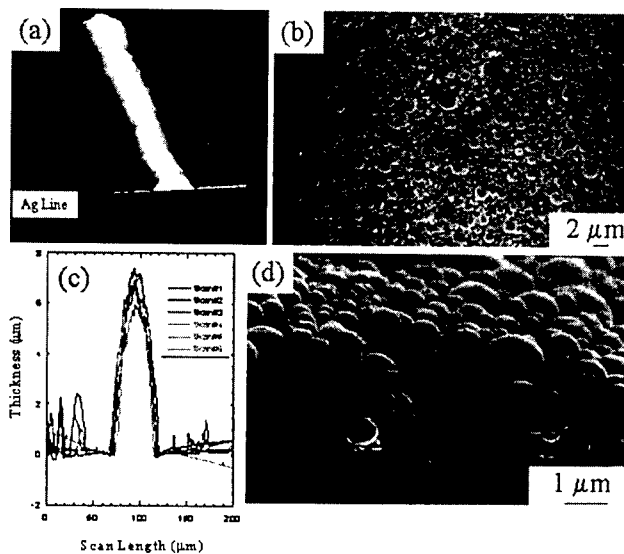


Figure 3 Ag line written on kapton by MAPLE DW, (a) shows a Tencor 3-D partial image of the 1 cm long line, (b) SEM micrograph showing the high packing density that the transferred materials exhibits, (c) Tencor 2-D line profile scans showing a 40 μm line width, (d) SEM micrograph of the Ag line further illustrating the packing density of the transferred material.

### Background

Shortly after the discovery of lasers researchers representing all disciplines of science began aiming them at materials in different forms. The interaction of lasers with

materials can result in a wide range of effects that depend on the properties of the laser, the material, and the ambient environment. As a function of beam energy, these effects can start from simple photothermal heating to photolytic chemical reactions and to ablation and plasma formation. We have successfully extended conventional PLD to include organic materials through a process we have termed Matrix Assisted Pulsed Laser Evaporation or MAPLE [1-4]. In this process, the excimer laser is set to a lower fluence ( $\sim 0.2 \text{ J/cm}^2$ ) from conventional PLD and impacts a dilute matrix target that is typically frozen to low temperatures ( $\sim 77 \text{ K}$ ). The dilute matrix is made up of the organic molecules to be deposited in thin film form and a frozen solvent. Ideally, the laser is then preferentially tuned to interact with the solvent matrix, but independent of that, the laser warms a local region of the target. The laser-produced temperature rise is large compared to the melting point of the solvent, but small compared to the decomposition temperature of the organic solute. When the MAPLE process is optimized, the collective collisions of the evaporating solvent with the organic molecule act to gently desorb the organic molecule intact, i.e., with only minimal decomposition as determined by FTIR and mass spectrometry. The evaporating solvent has a near zero sticking coefficient with the substrate and is rapidly pumped away or it can be trapped for re-use.

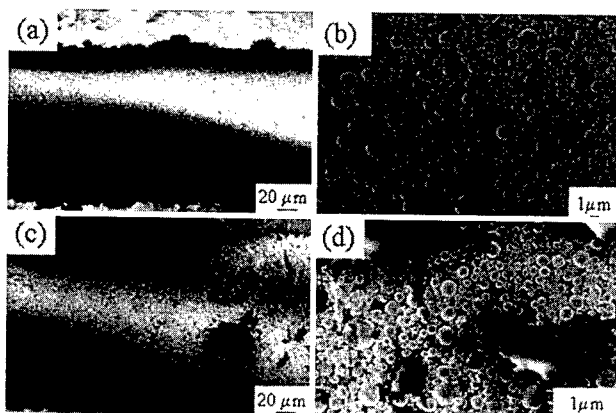


Figure 4. SEM micrographs of 1 cm Ag lines before and after scotch tape adhesion testing, written by MAPLE DW. Images a) and b) represent the Ag line prior to testing and c) and d) illustrate the lines after scotch tape removal, noting the excellent adhesion and residual polymer adhering to the surface of the Ag line.

LIFT is a simple direct write technique that employs laser radiation to vaporize and transfer a thin film (target) from an optically transparent support onto a substrate placed next to it [5-11]. Patterning is achieved by moving the laser beam (or substrate) or by pattern projection. The former is a method of direct writing patterns. There are several experimental requirements for LIFT to produce useful patterns including: the laser fluence should just exceed the threshold fluence for removing the thin film from the transparent support, the target thin film should not be too thick, i.e., less than a few 1000 Å, the target film should be in close contact to the substrate, and the absorption of the target film should be high. Operating outside these regime results in problems with morphology, spatial resolution, and adherence of the transferred patterns. Repetitive transfer of material can control the film thickness deposited on the substrate. LIFT is a simple technique that is used on mostly metallic targets, because the laser energy absorbed in the coated substrate atomizes the layer making LIFT inherently a pyrolytic technique. It cannot be used to deposit complex crystalline, multicomponent materials whose crystallization temperature is well above room temperature.

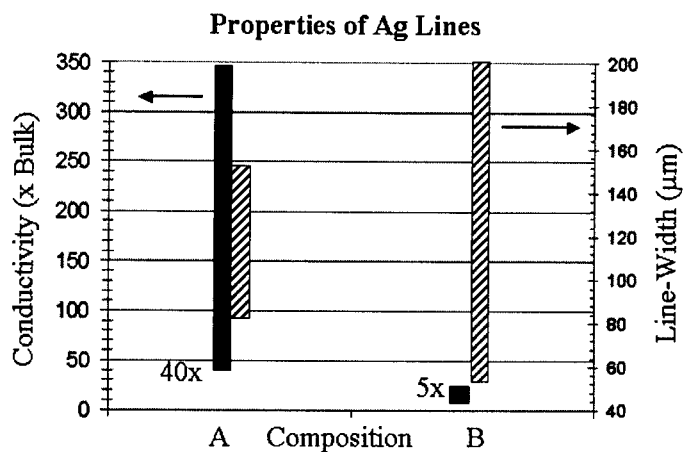


Figure 5. Schematic diagram showing the current progress writing metal lines with MAPLE DW at NRL.

The MAPLE DW technique utilizes the technical approach of LIFT and the basic mechanism of MAPLE to produce a laser driven direct write process capable of transferring materials, such as metals, ceramics, and polymers onto polymeric, metallic and ceramic substrates at room temperature and at atmospheric pressure and with a resolution on the order of 10 µm [12-14]. MAPLE DW uses a highly focused laser beam

that can be easily utilized for micromachining, surface annealing, drilling and trimming applications, by simply removing the ribbon from the laser path. The flexible nature of MAPLE DW allows the fabrication of multi-layered structures in combination with patterning. Thus, MAPLE DW is both an *additive* as well as *subtractive* process. MAPLE DW can also be adapted to operate with two lasers of different wavelengths, whereby the wavelength from one laser has been optimized for the transfer and micromachining operations, i.e., the UV laser, while the second laser is used for modifying the surface as well as annealing of either the substrate or any of the already deposited layers (i.e., IR or visible).

In MAPLE DW, a laser transparent substrate such as a quartz disc is coated on one side with a film a few microns thick. The film consists predominantly of a mixture or matrix of a powder of the material to be transferred and a photosensitive polymer or organic binder. The polymer assists in keeping the powders uniformly distributed and well adhered to the quartz disc. The coated disc is called the ribbon and is placed in close proximity (5 to 100  $\mu\text{m}$ ) and parallel to the acceptor substrate. As with LIFT, the laser is focused through the transparent substrate onto the matrix coating, see Figure 1. When a laser pulse strikes the coating, it transfers the powders, nanoparticles, and precursors, to the acceptor substrate. Using MAPLE DW, the material to be transferred is not vaporized allowing complex compounds to be transferred without modifying their composition, phase, and functionality. Furthermore, there is no heating of the substrate on which the material is transferred. Both the acceptor substrate and the ribbon are mounted onto stages that can be moved by computer-controlled stepper motors. By appropriate control of the positions of both the ribbon and the substrate, complex patterns can be fabricated. By changing the type of ribbon, multicomponent structures can easily be produced.

## Experimental

Fused silica quartz disks, 5.0 cm diameter x 1.5 mm thick were used as ribbon supports. Precursor Ag metal and  $\text{BaTiO}_3$  (barium titanium oxide (BTO)) materials were applied to the quartz disk using conventional deposition techniques with a resultant thickness ranging from 1.5-10  $\mu\text{m}$ . Ribbons are difficult to fabricate and the precursors must transfer without significant decomposition. On the other hand, by using ribbons we can effectively quantize the material transferred making MAPLE DW coatings highly reproducible. Each laser pulse deposits an identical mesoscopic brick of electronic material. In addition, the laser fires 100 thousand times a second synchronously with the computer-controlled stages thereby depositing the bricks very fast.

The size distribution of the Ag spherical particles ranged from 400 nm to 2  $\mu\text{m}$ . The BTO particles ranged from 125 to 175 nm with a  $\text{TiO}_2$  precursor. For all the transfers described in this paper, a computer-controlled stage (Z-stage) was used to control the relative travel and positioning of the substrate relative to the ribbon, as shown in Figure 2. The substrate to ribbon gap was set at 50 and 75  $\mu\text{m}$  for the Ag and BTO transfers respectively. Both the substrate and ribbon were held in place using a vacuum chuck over the X-Y substrate translation stage. The third harmonic of a pulsed Nd:YAG laser (355nm, 15 ns pulse width) was used for all transfer experiments. By changing the aperture size, beam spots ranging from 20 to 80  $\mu\text{m}$  were generated. The laser fluence

was estimated by averaging the total energy of the incident beam over the irradiated area to be 1.6 — 2.2 J/cm<sup>2</sup>. Various substrates were used for the transfer experiments including silicon, glass, alumina, and polyimide. Transfer tests were performed using Ag and BTO ribbons over each of these substrates. The adhesion of the transferred was excellent on all substrate materials after proper deposition parameter optimization as determined by standard tape tests.

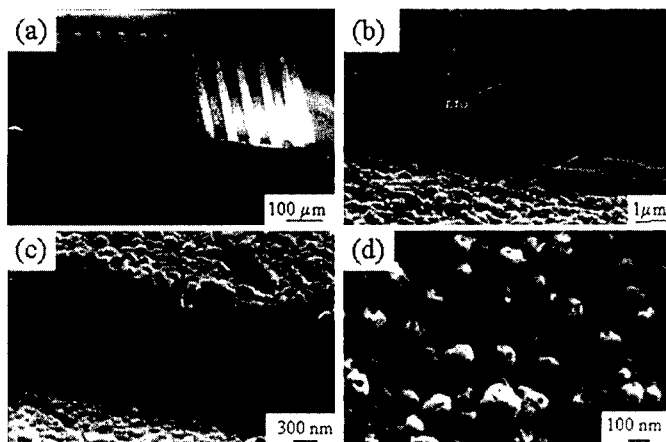


Figure 6. SEM micrographs of MAPLE DW of BTO on an interdigitated capacitor structure. Cross-section micrographs (b), (c), and (d) reveal that the material is uniform, dense and exhibits low matrix porosity.

## Results and Discussion

Silver lines were fabricated as shown in Figure 1 using Ag ribbons 3 μm thick, with a size distribution ranging from 400 nm to 2 μm in diameter. Figure 3 illustrates a 40 μm wide line that is ~6 μm thick written with two passes with MAPLE DW on a kapton substrate. Figure 3(a) shows that the line morphology is uniform and the aspect ratio is within 20% as shown in (c). Figure 3(b) and (d) show that the MAPLE DW process can clearly produce lines with high density and uniform thickness. In addition to density and conductivity, the adhesion of the written devices is important as well. Figure 4 shows the results of a scotch tape testing experiment performed on Ag lines written on a glass substrate. Figure 4 (a) and (b) show SEM micrographs prior to tape application, whereas (c) and (d) show SEM micrographs after the tape has been removed. The Ag lines survived the tape test. On closer inspection, it can be observed partial polymer glue

from the tape is still left on the line from the pull off, showing that the metal line has a degree of self adhesion in addition to the general concern at the glass/metal line interface.

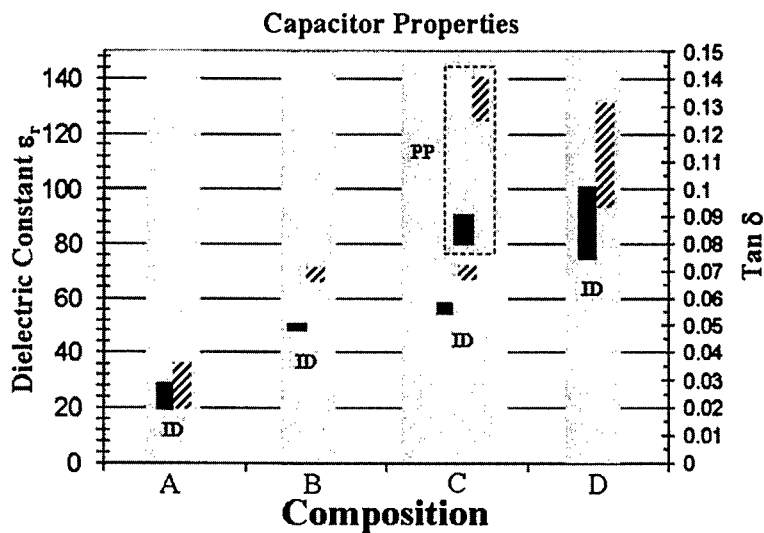


Figure 7. Properties of capacitors fabricated by MAPLE DW in both interdigitated (ID) and parallel plate (PP) geometries. A range of compositions are shown: A) commercial BTO powder 2-3  $\mu\text{m}$  diameter (irregular shaped), no precursor, B) 150 nm BTO (spherical), 100 nm titania (spherical), no precursor, C) 150 nm BTO (spherical), no precursor, D) 150 nm BTO (spherical), titania precursor

Figure 5 shows the current progress at NRL in terms of conducting metal lines, without laser annealing. The two parameters listed, conductivity and line width are shown for qualification. Figure 5 compares two of the current Ag materials, compositions A, B. The differences in the materials range in amount of precursor, shape, and thickness. Currently, using MAPLE DW we have written adherent lines with 4X bulk conductivities that are uniform and reproducible on glass, alumina, kapton, and silicon substrates.

Dielectric materials were written in both line and device arrangements, such as the interdigitated capacitor structure shown in Figure 6. Interdigitated capacitor structures (1 mm x 1 mm) were fabricated by writing BTO precursor materials onto a typical interdigitated capacitor finger structure. The material composition was 70% 150 nm BTO powder (spherical), 30% titania precursor. The metal fingers were fabricated by



conventional lithography techniques. Figure 6 (a) shows a low magnification SEM image of the interdigitated capacitor device structure deposited on an alumina substrate with Pd metal fingers. The density of the transferred material (post-transfer furnace anneal at 280°C) is clear from SEM micrographs in Figure 6 (b) and (c), including the Pd metal fingers. Figure 6 (d) shows a high magnification SEM micrograph of the fracture cross-sectioned region. The packing density is uniform with clear evidence of the TiO<sub>2</sub> precursor filling the voids between the particles. Device measurements made on these materials have shown that depending on the precursor choice, particle size, composition, and processing parameters, devices with a wide range of dielectric properties can be fabricated by MAPLE DW as shown in Figure 7.

It is clear that the material and precursor choice and amount significantly affect the final properties of the capacitor structures illustrated above. The importance of the as-deposited density is more generally critical to all electronic materials for device performance. The effect of density or microstructure on different passive components and the parallel effect on device performance are given in Table I. In all cases, the density degrades the electrical performance. For conductors and resistors this is directly proportional to the cross-sectional area, but for dielectrics the dependence is exponential and based on the relative packing of different k materials, i.e., air and BTO in our case. For ferrites this will also result in a higher coercive field, H<sub>c</sub>.

Table I. Microstructural and devices issues for passive components.

<i>Passive Component</i>	<i>Microstructure Issues</i>	<i>Device Issues</i>
<b><i>Metallic Conductors</i></b>	Intermediate melting point, Necking, Porosity	Microwave Surface Resistance, Power Loss
<b><i>Dielectrics (Ceramic Oxides)</i></b>	High melting point, Difficult to Neck Particles, Oxygen Loss	Porous Material has Drastic Effect on k, Lossy
<b><i>Resistors (Ceramic/Insulator)</i></b>	High melting point, Most Difficult to Neck Around Insulator	Conductor/Insulator Composite
<b><i>Resistors (Polymer/Insulator)</i></b>	Low Processing Temperature, Necking Around Insulator	Aging, Electromigration
<b><i>Ferrites</i></b>	High melting point, Difficult to Neck Particles, Oxygen Loss	Porous Material has Drastic Effect on M <sub>s</sub> , Lossy, High H <sub>c</sub>

The temperatures that these samples and in particular the precursors are reacted is < 400°C. One way to effectively increase the processing temperature, but still maintain low temperature processing for plastic substrates, is to use *ex situ* laser surface sintering. Bulk diffusion is not going to occur for the short times that the laser sinters the sample. The low reacting temperature precursors provide chemical welding between particles (particle-to-particle adhesion). By using *in-situ* laser sintering, some of the following benefits may be realized: smaller/thinner region to sinter, less organic to remove, lower sensitivity to laser fluence, faster and better alignment, less thermal stress to the substrate, and lastly, less processing steps will result in a higher yield. We are modifying our

---

current experimental set-up to include laser sintering. This will be done in situ with an acoustic modulated CW Nd:YAG laser.

### Conclusion

We have demonstrated that MAPLE DW is a rapid and versatile prototyping tool for fabricating mesoscale devices (conductors, resistors, capacitors, inductors, phosphors, sensors) in a 3-D structure on any surface. The material transfer works as predicted. It is clear that the process is probably more gentle and general than previously thought, but the MAPLE DW mechanism requires further research. There are many advantages to MAPLE-DW compared to other existing direct write technologies for 3D-structure fabrication. These advantages include the ability to do adherent depositions at room temperature and in air and the ability to rapidly change between different materials. The latter is accomplished because MAPLE-DW is a dry technique meaning there is no interval of time required for transferring one layer on top of another. We have shown that ceramic powder, nanoparticles, and precursor composites need to be densified through laser sintering. Therefore, we need low reacting temperature precursors to work with the proper laser annealing parameter both in the spatial and temporal regimes.

### Acknowledgements

We gratefully acknowledge the support provided for this work from the Office of Naval Research and the DARPA MICE Program.

### References

1. D.B. Chrisey and G.K. Hubler eds., Pulsed Laser Deposition of Thin Films, (New York, NY: Wiley, Inc. 1994).
2. Method of producing a coating by matrix assisted pulsed laser evaporation, U.S. Pat. No. 6,025,036.
3. R.A. McGill, R. Chung, D.B. Chrisey, P.C. Dorsey, P. Matthews, A. Piqu, T.E. Mlsna, and J.L. Stepnowski, *IEEE Trans. on Ultrasonics, Ferroelectrics, and Frequency Control*, vol. 45, p. 1370 (1998).
4. A. Piqu, D.B. Chrisey, B.J. Spargo, M.A. Bucaro, R.W. Vachet, J.H. Callahan, R.A. McGill, and T.E. Mlsna, in Advances in Laser Ablation of Materials, MRS Proceedings, vol. 526, p. 421, (1998).
5. J. Bohandy, B.F. Kim, and F.J. Adrian, *J. Appl. Phys.* 60 (1986) pp. 1538-1539.
6. J. Bohandy, B.F. Kim, F.J. Adrian, and A.N. Jette, *J. Appl. Phys.* 63 (1988) pp. 1158-1162.
7. I. Zergioti, S. Mailis, N.A. Vainos, C. Fotakis, S. Chen, C.P. Grigoropoulos, *Appl. Surf. Sci.* 127-129 (1998) pp. 601-605.
8. F.J. Adrian, J. Bohandy, B.F. Kim, A.N. Jette, and P. Thompson, *J. Vac. Sci. Tech. B5* (1987) pp. 1490-1494.
9. I. Zergioti, S. Mailis, N.A. Vainos, P. Papakonstantinou, C. Kalpouzos, C.P. Grigoropoulos, and C. Fotakis, *Appl. Phys. A* 66 (1998) pp. 579-582.

- 
10. H. Esrom, J-Y. Zhang, U. Kogelschatz, and A. Pedraza, *Appl. Surf. Sci.* 86, pp. 202-207 (1995).
  11. S. M. Pimenov, G.A. Shafeev, A.A. Smolin, V.I. Konov, and B.K. Bodolaga, *Appl. Surf. Sci.* 86, pp. 208-212 (1995).
  12. A. Piqu , D.B. Chrisey, R.C.Y. Auyeung, J.M. Fitz-Gerald, H.D. Wu, R.A. McGill, S. Lakeou, P.K. Wu, V. Nguyen and M. Duignan, *Appl. Phys. A* 69, pp. S279-S-284 (1999).
  13. D.B. Chrisey, A. Piqu , J.M. Fitz-Gerald, R.C.Y. Auyeung, R.A. McGill, H.D. Wu, and M. Duignan, *Appl. Surf. Sci.* 154, pp. 593-600 (2000).
  14. J.M. Fitz-Gerald, A. Piqu , D.B. Chrisey, P.D. Rack, M. Zeleznik, R.C.Y. Auyeung, and S. Lakeou, *Appl. Phys. Lett.* 76, pp. 1386-1388 (2000).

## Pattern Writing by Implantation in a Large-scale PSII System with Planar Inductively Coupled Plasma Source

Lingling Wu\*, Hongjun Gao\*\*, Dennis M. Manos\*

\*Applied Science Department, College of William and Mary, Williamsburg, VA 23187,  
[dmanos@as.wm.edu](mailto:dmanos@as.wm.edu)

\*\*Solid State Division, Oak Ridge National Laboratory, Oak Ridge, TN 37831. Present Address:  
Beijing Laboratory of Vacuum Physics, P. O. Box 27024, Beijing, P. R. China

### Abstract

A large-scale plasma source immersion ion implantation (PSII) system with planar coil RFI plasma source has been used to study an inkless, deposition-free, mask-based surface conversion patterning as an alternative to direct writing techniques on large-area substrates by implantation. The apparatus has a 0.61 m ID and 0.51 m tall chamber, with a base pressure in the  $10^{-8}$  Torr range, making it one of the largest PSII presently available. The system uses a 0.43 m ID planar rf antenna to produce dense plasma capable of large-area, uniform materials treatment. Metallic and semiconductor samples have been implanted through masks to produce small geometric patterns of interest for device manufacturing. Si gratings were also implanted to study application to smaller features. Samples are characterized by AES, TEM and variable-angle spectroscopic ellipsometry. Composition depth profiles obtained by AES and VASE are compared. Measured lateral and depth profiles are compared to the mask features to assess lateral diffusion, pattern transfer fidelity, and wall-effects. The paper also presents the results of MAGIC calculations of the flux and angle of ion trajectories through the boundary layer predicting the magnitude of flux as a function of 3-D location on objects in the expanding sheath.

### Introduction

High-energy ion implantation is an important surface modification technique, which causes minimal dimensional change, and avoids thermal distortion of the surface profile of the treated object [1, 2, 3]. Plasma source immersion ion implantation (PSII) is advantageous compared to traditional beam line implantation technique for large areas, complicated work piece shapes, and high dose applications [1, 2]. The uniformity of implantation is determined by the spatial plasma density distribution and the plasma sheath distribution. It does not require beam rastering to achieve dose uniformity over large implantation areas. There is also no need for tilting or rotating of the work piece to treat all the surfaces. This greatly simplifies the mechanical construction of the implantation chamber and reduces the cost of building the system.

Different plasma sources for PSII have been used, such as hot filament [2, 3, 4], cylindrical coil RF inductively coupled plasma [5], rf capacitively coupled plasma [2, 6], microwave plasma [7], and glow discharge [2]. To realize PSII technique's potential of treating large work pieces, several large-scale PSII systems have also been built, including PSII systems at Los Alamos National laboratory [6], Hughes Research Laboratories [3], and the University of Wisconsin [2]. None of these large-scale PSII systems takes advantages of the planar coil rf inductively (RFI) coupled plasma source, which is widely used to generate low-pressure, high-density discharge and demonstrates the potential for large area processing and improved spatial uniformity [1, 8]. Since rf power is coupled to the plasma inside the vacuum chamber usually through a quartz window, there are no electrical connections or supporting apparatus inside the chamber to take up extra chamber space to complicate chamber geometry.

Prior operations of the PSII system at the College of William and Mary with hot filament and DC glow discharge plasmas resulted in ion densities estimated to be in the low  $10^9 / \text{cm}^3$  range [4], in agreement with values previously reported for other large implantation systems [3, 6]. Such low values of  $n_e$  made it difficult to produce the desired pulse shape and to control the pulse temporal profile. Although higher densities in the filament driven source were achieved by increasing the filament temperature and bias [4], this led to shortened filament life and the possibility of contamination of work pieces. Similarly, sputtered contaminants made it difficult to increase electron density in a dc glow by raising voltage. The requirement of long mean-free-path for the implanted ions eliminated pressure control of  $n_e$  as an option. In addition, both filament and dc glow discharge plasmas demonstrated large non-uniformity over the large radial and vertical dimensions of this chamber (0.61 m ID and 0.51 m tall), which is unacceptable for large area uniform materials processing.

To overcome these difficulties, a large rf inductively coupled (RFI) plasma source has been designed and built for the PSII system. With a 0.43 m in diameter rf antenna sitting on a 0.57 m in diameter quartz window, stable and uniform plasma can be generated in the chamber. More details of the system characterization and operation will be given in a later paper.

In this work, pattern writing has been performed by exposing metal and semiconductor samples through masks, to high ion doses. AFM calibration gratings, made from Si, were also implanted. Implantation depth profiles were characterized by variable-angle spectroscopic ellipsometry (VASE) and AES and compared to TEM results. Measured lateral and depth profiles are compared to the feature morphology to assess lateral diffusion, pattern transfer fidelity, and wall-effects on the depth profile. The paper also presents the results of MAGIC modeling of flux and angle of ion trajectories through the boundary layer predicting the magnitude of flux as a function of 3-D location on objects in the expanding sheath, and to evaluate the fidelity of pattern transfer as a function of feature size.

## Experiment

Two kinds of substrates were used for studying pattern transfer: flat substrates and silicon gratings. Flat substrates, including silicon wafers (100 mm in diameter, 0.5 mm thick), polished stainless steel plate (9.12 cm in diameter, 1.2 cm thick), and pure Ti and Ta sheets (25 mm  $\times$  25 mm, 0.5 mm thick for Ta, 1 mm thick for Ti), were implanted through a 150  $\mu\text{m}$  thick metal mask with 100  $\mu\text{m}$  wide lines and 100  $\mu\text{m}$  ID holes. The mask was weighted to secure it to the stage using a shaped metal ring and a metal cube. The ring is 2.5 cm tall, with a 2.5 cm OD and 2.3 cm ID. The cube is 3.8 cm  $\times$  3.8 cm  $\times$  3.8 cm. The ring and the cube were carefully positioned on the 100-mm Si wafer to study wall effect on dose and sheath distributions. Pure silicon gratings with trapezoidal groove cross-sections and of 10  $\mu\text{m}$  groove separation were also implanted.

Research grade nitrogen (99.999%) was used as the gas source. A base pressure of  $\sim 10^{-8}$  Torr and operating pressures of  $5 \times 10^{-4}$  Torr to  $2.5 \times 10^{-3}$  Torr were used. Silicon wafer implants were performed at pulse voltages of 50 kV and repetition rate of 20 Hz for 10 hrs. Stainless steel was implanted at 50 kV at 25 Hz for 9 hrs. The Ti and Ta sheets were implanted through the mask at 40 kV at 25 Hz for 7.5 hrs. Si gratings were implanted at 25 kV at 40 Hz for 5 hrs. Estimated temperature rise for these implantation runs was less than 50° C.

AES and XPS spectra were taken using a VG Scientific MARKII ESCALAB equipped with EX05 ion gun for depth profiling. Nitrogen concentration depth profiles for high dose nitrogen implanted Si and Ti were obtained by AES. The sputtered depths were calibrated by surface

profilometry. The overlapping of nitrogen and titanium peaks and compensation for the presence of oxygen were considered when calculating the nitrogen concentration [9].

A variable-angle spectroscopic ellipsometer (VASE) [10] was used to study the optical properties of the nitrogen-implanted silicon and stainless steel samples. Three incident angles (70, 75, and 80 degrees) were used for each area. The incident optical beam was about 3 mm in diameter. Because the as-received Ti and Ta samples did not have smooth optical surfaces, ellipsometry could not be used to examine them.

The cross-section of nitrogen implanted Si gratings was examined by TEM at Solid State Division of Oak Ridge National Laboratory.

## Results and Discussion

The implanted Ti surface showed the gold color characteristic of stoichiometric TiN, with slight pink hue because of the slightly oxidized surface layer. The AES depth profile for high dose nitrogen implantation is shown in Figure 1 for a Ti substrate. The nitrogen concentration fluctuates around the level for stoichiometric TiN (50%) throughout most of the implanted depth, decreasing sharply at  $\sim 5000 \text{ \AA}$ . The native oxide layer of the original substrate was not stripped prior to implantation, accounting for the relatively low nitrogen concentration in this range. Similar nitrogen depth profiles were obtained for the implanted Si wafer, again showing a thick native oxide layer that reduced the nitrogen reaction with silicon, producing low nitrogen concentration. The experimental implantation depth profiles are in good agreement with the high-dose model calculation of Profile Code, which predicts constant concentration for most of the implanted depth and the steep decrease at the end of range [11].

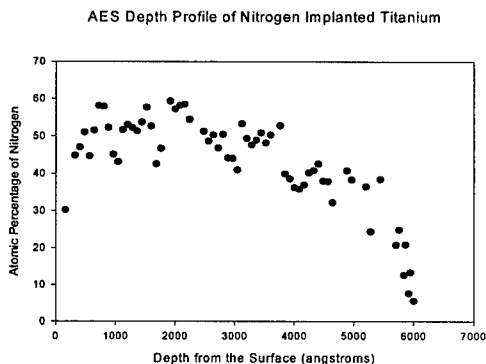


Figure 1. Implanted nitrogen concentration depth profile for Ti substrate obtained by AES depth profiling.

The ellipsometry results for nitrogen implanted Si and stainless steel samples confirmed the film-like depth profiles observed by AES and predicted by Profile Code. Table I shows VASE results for 7 different spots on implanted Si wafer. Adding a graded optical layer to model the gradual concentration changes typical of low-dose implantation depth profile, did not improve

Table I. Implanted layer thickness obtained by variable angle spectroscopic ellipsometry (VASE) study of different surface areas on nitrogen implanted Si wafer

Test Position	A	B	C	D	E	F	G
Thickness of Layer (Å)	1770±20	914±3	1055±3	1580±20	851±2	1620±20	1820±20
Color of Spot	Golden	Blue	Light Blue	Golden (lighter)	Blue	Golden (lighter)	Golden

the fits to the data. The optical properties of the implanted layer closely resemble that of a thin film. These optical methods thus provide a distribution for high dose implantation, since the dose is in proportion to converted layer thickness and thickness can be correlated to area color. They are non-destructive and quick compared to other depth profiling techniques, such as AES and SIMS. The color of 100  $\mu\text{m}$  lines and 100  $\mu\text{m}$  I.D. dots produced by implanting through the metal mask were studied using an optical microscope fitted with a CCD color camera and TV monitor. The edges between the implanted and un-implanted area were narrower than the resolution of our camera, indicating pattern transfer contrast considerably sharper than 2  $\mu\text{m}$ . A 5.7  $\mu\text{m}$  wide, blue-colored annular zone appears along the circumference of the exposed area. Ellipsometry indicated that this annulus received only  $\approx 40\%$  of the maximum dose received at the center of a 100  $\mu\text{m}$  hole. The sample stage temperature did not rise significantly during implantation. Analysis of the annular zone just outside the implanted circle confirmed our assumption that lateral thermal diffusion may be ignored.

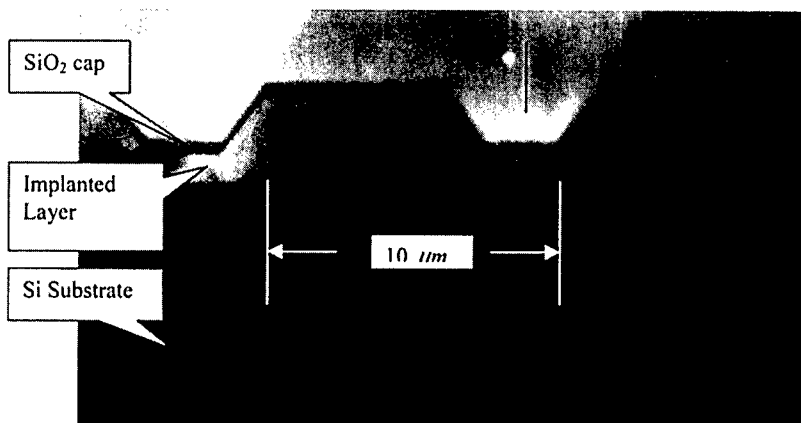


Figure 2. TEM picture of cross-section of nitrogen implanted Si gratings, showing the nitrogen-implanted layer, the Si substrate, and the SiO<sub>2</sub> cap layer.

The AFM calibration gratings were exposed to study the dose distribution in and around narrow features. The trapezoidal groove cross-sections provide virtual mask stripes over the flat Si surface. Our apparatus may be operated in a manner which allows us to co-deposit  $\text{SiO}_2$ . This mode will be discussed in a future paper. Figure 2 shows TEM picture of Si gratings implanted in this mode. As seen in that figure, the implanted layer is capped with co-deposited  $\text{SiO}_2$ . The flat tops and bottoms of the grooves show a similar implanted layer thickness. The sloped sidewalls were not uniformly implanted. The converted layer near the corner where the bottom and the sidewalls meet is apparently thinner, while the layer near the corner where the top and the sidewall meet is much thicker.

We modeled the dose and angle distribution for mask-based pattern writing using MAGIC, an electromagnetic particle-in-cell, finite-difference, time-domain code for simulating plasma physics process [12], which we adapted for this purpose. The chamber and sample stage geometry included in the models is assumed to be azimuthally symmetric. Thus only a 2D half-plane cut is necessary for full simulation. We have used this simulation to examine matrix sheath

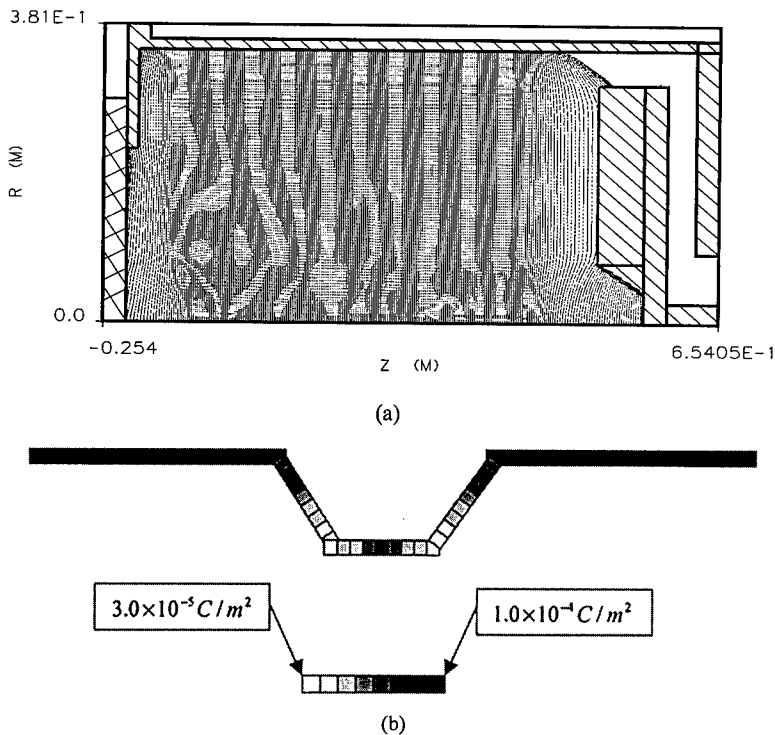


Figure 3. MAGIC modeling of PSII process in a trench. (a) Positive nitrogen ion distribution at time  $1.2 \times 10^{-7} \text{ s}$ . (b) Ion flux distribution along the trench surface for a  $2.5 \times 10^{-7} \text{ s}$  simulation. (The gray scale is shown below the profile)



formation, sheath propagation, evolving to the steady Child-Law sheath; ion trajectories, ion depletion, and the distribution of ion flux for different mask shapes and aspect ratios. In the simulations shown here, the time step was  $5 \times 10^{-10}$  s over a simulated implantation time of  $2.5 \times 10^{-7}$  s, representing the initiation phase of a quasi-steady state lasting throughout the  $10^{-5}$  s pulses. The modeled ion plasma density was  $10^{10} / \text{cm}^3$  and applied voltage  $\sim 10$  kV. The positive ion distribution at  $t = 1.2 \times 10^{-7}$  s modeled for a groove with a sidewall to bottom angle of 54.4 degrees is shown in Figure 3. The shallower angle of incidence at the slopes sidewall predicts a non-uniform distribution consistent with TEM observations. The ion flux distribution (Figure 3b) predicts that the bottom of the slope will receive a factor of 2 to 3 less flux, also in agreement with TEM results.

## Conclusion

High dose nitrogen implantation into various substrates was performed, yielding film-like depth profiles. A stoichiometric  $TiN$  layer was produced on the Ti surface. Depth profiles obtained experimentally by AES, VASE and those modeled with Profile Code are in good agreement. Patterns  $100 \mu\text{m}$  in line-width were transferred by implantation, with lateral contrast better than  $2 \mu\text{m}$ . The TEM study of nitrogen implanted Si gratings showed implantation can produce sharp patterns as small as  $3 \mu\text{m}$  with good uniformity, in agreement with MAGIC code simulation. With carefully designed masks and good control of implantation parameters, PSII can be used for pattern writing of smaller features.

## Reference

- [1] M. A. Lieberman, A. J. Lichtenberg, Principles of Plasma Discharges and Materials Processing, John Wiley & Sons, INC., 1994, pp. 387-411.
- [2] S. M. Malik, K. Sridharan, R. P. Fetherston, A. Chen, and J. R. Conrad, JVST B, 12 (2), p. 843 (1994).
- [3] J. N. Matossian, JVST B, 12 (2), p. 850 (1994).
- [4] T. J. Venhaus, Plasma Source Ion Implantation of High Voltage Electrodes, Ph.D dissertation, College of William and Mary, 1999, pp. 25-80.
- [5] M. Tuszewski, J. T. Scheuer, I. H. Campbell, and B. K. Laurich, JVST B, 12 (2), p. 973 (1994).
- [6] B. P. Wood, I. Henins, R. J. Gribble, W.A. Reass, R. J. Faehl, M. A. Nastasi, and D. J. Rej, JVST B, 12 (2), p. 870 (1994).
- [7] S. Qin, C. Chan, JVST B, 12 (2), p. 962 (1994).
- [8] J. Hopwood, Plasma Sources Sci. and Technol., 1, p. 109 (1992).
- [9] A. Chen, J. Firmis, and J. R. Conrad, JVST B, 12 (2), p. 918 (1994).
- [10] Guide to using WVASE32™, J. A. Woollam Co. Inc., Lincoln, NE 68508, USA.
- [11] Profile Code Software Instruction Manual, Version 3.20, Implant Sciences Corporation, Wakefield, Massachusetts.
- [12] Bruce Goplen, Larry Ludeking, David Smithe, Magic User's Manual, 1997, Mission Research Corporation, Newington, Virginia.

## INK JET DEPOSITION OF CERAMIC SUSPENSIONS: MODELLING AND EXPERIMENTS OF DROPLET FORMATION

N. REIS AND B. DERBY

Manchester Materials Science Centre, UMIST, Grosvenor St., Manchester, M1 7HS, U.K.

### ABSTRACT

We have successfully printed green ceramic objects from slurries of  $\text{Al}_2\text{O}_3$  dispersed in paraffin wax using a commercial ink-jet printer developed for pattern making (Sanders Prototype MM6PRO). Concentrated suspensions are generally more viscous than the fluids normally passed through ink jet heads. This may alter the response of the printing system to its process parameters, e.g. driving voltage and frequency. We have explored the influence of fluid properties on the ink jet behaviour using Computational Fluid Dynamics (CFD) modelling and a parallel experimental study to determine the optimum printing conditions for particulate suspensions.

### INTRODUCTION

Ink jet printing is an attractive option for direct write technologies and for the micro-manufacture of parts. Drop-on-demand printers provide a relatively inexpensive means of accurately delivering small volumes of material to precise locations enabling the reproduction of predetermined patterns stored in computer files. By overprinting, three dimensional objects can be constructed. Multi-material or composite structures can be readily fabricated if more than one ink jet droplet formation device is used. If the building droplets are sufficiently small, graded or functionally gradient structures can also be deposited.

We have recently demonstrated that ink jet printing, using a piezoelectric drop-on-demand printer, can be used to successfully deposit ceramic suspensions with a very high volume loading of ceramic particles [1, 2]. This paper reports on our current progress on printing concentrated ceramic suspensions. In it we present the results of a simple computational fluid mechanics model of the ink jet printer, assuming Newtonian flow. This can be used to successfully predict the jetting parameters of a number of fluids and thus allow the identification of the optimum printing parameters.

### EXPERIMENTAL

#### Suspension preparation

Alumina suspensions were prepared by dispersing a fine, sub-micron powder ( $\alpha\text{-Al}_2\text{O}_3$  RA45E, Alcan Chemicals Ltd., U.K.) in paraffin wax (Mobilwax135<sup>®</sup>, Mobil Special Products, U.K.) containing variable additions of sterylamine (1-Octadecylamine, Lancaster Synthesis, U.K.) and a proprietary dispersant (Hypermer LP1, ICI Surfactants, U.K.). All formulations were mixed by conventional ball milling at 100...C for periods of 10 hours. By controlling the ratio between surfactants molecular weight, and terminal group functionality (i.e., acidic or basic), suspension shear viscosities as low as 40 mPa.s were obtained for apparent particulate volume fractions of 0.4 (steady shear viscosity was measured in a concentric cylinder Brookfield Viscometer at 100s<sup>-1</sup> and 100...C). Detailed preparation procedures and findings have been reported previously [1].

### **In situ monitoring of drop formation**

In this study, phase change drop on demand print heads were used (Sanders Design Inc., Wilton, NH). These are tubular piezoelectric transducers surrounded with a temperature controlled heating tape to ensure temperature stability. Monitoring and recording of drop formation at the jet nozzle outlet were performed using a conventional CCD camera and a PC frame grabber card. Since CCD frame rates are not compatible with typical jet repeat rates, a sub-microsecond light emitting diode strobe was used to back-lit the forming droplets, at controllable delays from the transducer excitation pulse. The set-up allows freezing the droplet motion at constant delays, and also following their perceived motion using linear voltage vs. time ramps. Details on this set-up can be found elsewhere [3].

### **CFD modelling**

To model the jet dynamics, a commercial CFD package (FLOW-3D<sup>®</sup>) was used. It is based on a refined Volume of Fluid (VOF) method coupled with Fractional Area-Volume Obstacle Representation (FAVOR<sup>™</sup>) algorithms to define obstacle s geometry within an Eulerian grid. This was primarily chosen because of its simplicity and robustness to model the free surface flow characteristic of drop formation in ink jet heads.

For this study, all models of drop ejection use a pressure pulse condition at the bottom boundary of the computational domain, as introduced by Fromm [4]. For the evolving free surface, an outflow continuative boundary condition was used. This consists of zero normal derivatives at the boundary for all quantities to ensure smooth continuation of the flow through the boundary. Although convenient for sub-sonic incompressible flows, this condition must be regarded with caution since it has no physical foundation.

The flow was assumed to be laminar and axisymmetric, which are valid assumptions for ink jet printing given the steadiness and repeatability of the process. Other assumptions included isothermal conditions, no wall slip and Newtonian viscosity. Although the first two are fair assumptions, the latter only applies to simple fluids and dilute suspensions, and hence is not applicable to concentrated suspensions. An effort is currently being made to include shear and temperature dependence of the viscosity and also introduce mass particles in the flow. Due to the flow symmetry, only a two dimensional representation of half of the jet was used in the computations. Grids were refined until no significant changes were observed for the description of flow. All computations used cylindrical coordinates, with the mesh becoming finer towards the nozzle axis.

## **RESULTS AND DISCUSSION**

### **Experimental observations**

Our experiments revealed three key aspects regarding drop ejection and stability in piezoelectric ink jets, operating in air at atmospheric pressure:

1. The acoustic pressure at the nozzle inlet, which depends on the fluid acoustic properties, chamber (including the piezoelectric) properties, geometry and dimensions of the fluid filled cavity, and the voltage pulse train used to excite the transducer. This pressure is responsible for the momentum imparted to the fluid at the nozzle and also the deceleration forces causing constriction of the jet [5].

2. The viscous loss at the nozzle due to the constriction of flow, dependent on the nozzle configuration and dimensions, and fluid viscosity. For a given acoustic pressure wave at the nozzle, the lower the viscosity the greater are both velocity and the amount of fluid propelled forwards, which usually lead to the formation of long tails behind the head of the drop.
3. The surface tension forces acting at the free surface. These depend not only on the fluid surface tension but also on the wetting characteristics between the fluid and nozzle material. The former is responsible for the spheroidisation (tail recoil or satellite disruption) of the liquid thread emerging from the nozzle. The latter is important in controlling the wetting of the nozzle outlet face, which inevitably results in spray formation. Its effect on drop volume and velocity due to meniscus reverberations has been recently discussed [6].

All the above considerations are still valid at high frequencies. Operating in the high frequency regime has a number of advantages. First it is easier to tune variables such as drop velocity and mass deposition rate, which are crucial for the splat formation mechanisms, [3] and reduce building times. Secondly, it is possible to manipulate the acoustic pressure wave by tuning the pulse train applied to the piezoelectric transducer for jetting higher viscosity fluids. Figure 1 shows that above a certain frequency, sub-harmonic effects can be used to increase the acoustic pressure amplitude and hence drop velocity

Jetting at high frequencies however, brings additional considerations into play, since the rate of droplet generation is usually faster than the time required to form a single drop. This results in the formation of two or more connected droplets near the nozzle, which detach during flight. As a consequence the tail behind a forming droplet is now merged with the droplet immediately behind and thus regular droplets can be obtained at distances acceptable for printing — figure 2a.

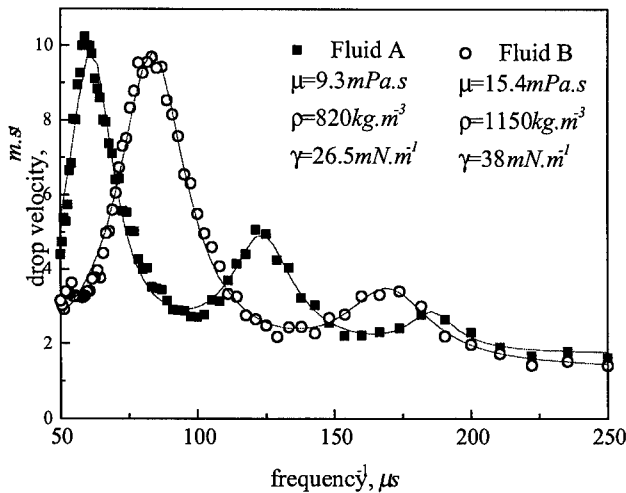


**Figure 1-** Effects of driving pulse frequency and fluid properties on drop velocity for the same jet head construction . The peaks and valleys correspond to sub-harmonic resonance and anti-resonance for each fluid.



**Figure 2** — Drop formation at high frequencies for different fluids. (a) is Protosupport™; (b) is an eutectic mixture of camphor and naphthalene; (c) and (d) are 30 and 40 vol.% Al<sub>2</sub>O<sub>3</sub> suspended in paraffin, respectively.

	$\rho$ [kg.m <sup>-3</sup> ]	$\mu$ [mPa.s]	$\gamma$ [mN.m <sup>-1</sup> ]	$f / \Delta V / T$ [kHz / V / ...C]
(a)	820	9.3	26.5	10 / 70 / 110
(b)	970	1.3	46	10 / 70 / 110
(b)	1800	14.5	25	10 / 70 / 100
(d)	2100	38	25	13 / 80 / 110

Although higher acoustic pressure amplitudes characteristic of high operating frequencies can be used to compensate for viscous losses, care must be taken while jetting low viscosity fluids. The inevitable long threads of fluid expelled from the nozzle may cause the formation of satellites for slightly higher values in surface tension— figure 2b. Figures 2c and 2d show the jetting behaviour of 30 and 40 vol.% Al<sub>2</sub>O<sub>3</sub> suspended in paraffin, respectively.

For the 40 vol.% suspension, a small pressure had to be applied to force the flow of the fluid through the lines and replenish of the fluid in the jet head chamber. Since the tested suspensions are shear thinning, this is assumed to be due to the highly viscous flow of concentrated suspensions under low shear.

### **CFD calculations**

In order to assess the assumptions and numerical schemes used to track the free surface, candelilla wax was used as model fluid. This wax chosen since it has viscosity similar to other fluids of interest (steady shear viscosity of 17 mPa.s at 100...C) and exhibits Newtonian behaviour.

Figure 3 shows a comparison between numerical calculations and in situ monitoring of the forming droplets, for which a good agreement was found. It can also be observed that for the same velocity, the model has predicted shorter detaching times and hence smaller tails following the head of the drop. This was found to depend not only on the fluid properties but also, and in accordance with earlier studies using different numerical schemes [4,7], on the shape and amplitude of the pressure pulse applied as bottom boundary condition. Another factor that has not been considered is the extensional character of the flow and hence the introduction of elongational viscosity as opposed to shear viscosity.

We are currently developing the capability to model the acoustics of the ink jet chamber in order to, optimally synchronise driving parameters and obtain higher pressures needed for jetting higher viscosity fluids. These results will also be used to improve our free surface modelling assumptions, primarily regarding boundary conditions.

Numerical simulations can also be explored to provide useful information regarding the mechanisms of drop formation, and determine the window of fluid properties needed for jetting. Figure 4 shows how surface tension and viscosity can affect drop volume and velocity. These numerical predictions confirm our experimental findings regarding drop formation. It can be seen that viscosity has a great effect in the velocity and amount of fluid ejected from the nozzle, whereas surface tension is responsible for the minimising the surface area by spheroidising the fluid columns. High values of both properties can restrain jetting by retracting the fluid column

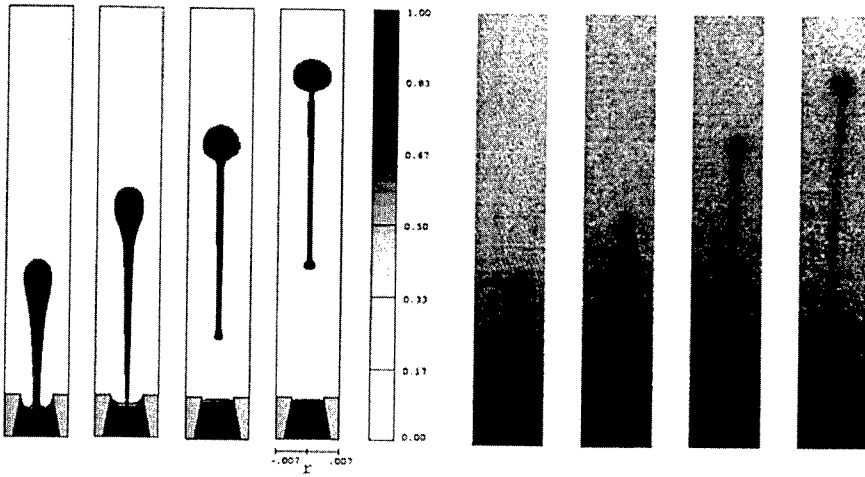


**Figure 3** CFD calculations (left) and experimental observations (right) of candelilla wax being jetted at 100...C. Frames are separated by 50  $\mu$ s intervals, and are 1 mm in height. Length units (r and z) are displayed in cm.

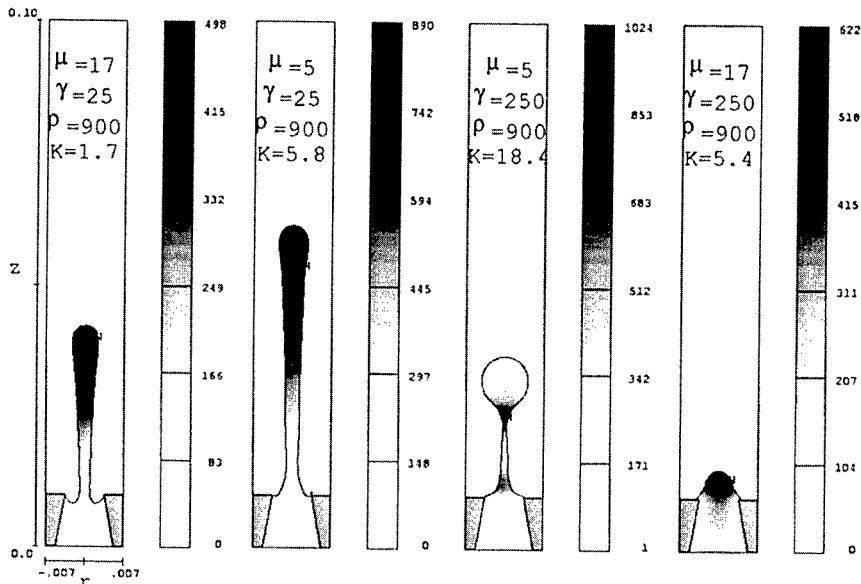


**Figure 4** — Velocity magnitude contours after 80  $\mu$ s, for the fluid properties indicated in the frames and using the same numerical schemes and boundary conditions as in figure 3 (velocity in  $\text{cm}\cdot\text{s}^{-1}$ ). The parameter K indicates the ratio between Reynolds and Weber numbers ( $K=(\rho L\gamma)/\mu$ ).

---

back into the nozzle before conditions for droplet detachment are achieved. It was also numerically predicted the formation of satellite droplets as illustrated in figure 2b.

## CONCLUSIONS

The feasibility of direct ink jet deposition of concentrated suspensions up to 40% solids by volume has been proved, by using drop on demand piezoelectric print heads. Viscous losses due to the particulate filling can be compensated controlling the process acoustics through excitation pulse adjustments.

Simple CFD calculations were developed to simulate the jetting process with considerable success when compared to experimental observations. These can be used to narrow the number of experiments needed to determine optimum jetting conditions for each fluid. These codes are being improved to include more realistic assumptions concerning boundary conditions, introduce elongational viscosity and also to consider the non-Newtonian behaviour of concentrated suspensions.

## ACKNOWLEDGEMENTS

We would like to acknowledge the support of the EPSRC and the Ministry of Defence through grant GR/L42537. We would also like to thank Julian Evans, John Halloran and Kitty Seerden for helpful comments and discussion.

## REFERENCES

1. N. Reis, K.A.M. Seerden, P.S. Grant, B. Derby, and J.R.G. Evans, presented at the IoM Annual Ceramics Convention, 10-11 April 2000, Cirencester, U.K.
2. B. Derby, N. Reis, K.A.M. Seerden, P.S. Grant, and J.R.G. Evans, in this issue, MRS Spring Meeting 2000, San Francisco, U.S.A.
3. N. Reis, K.A.M. Seerden, B. Derby, J. W. Halloran and J.R.G. Evans, Mater. Res. Soc. Symp. Proc., **542**, p. 147-152 (1999).
4. J. E. Fromm, IBM J. Res. Develop., **28**, p. 322-333 (1984).
5. R. Badie and D. F. de Lange, Proc. R. Soc. Lond. A, **453**, p. 2573-2581 (1997).
6. J. F. Dijkman, Flow Turbul. Combust. **61**, p. 211-237 (1998).
7. R. L. Adams and J. Roy, ASME J. Appl. Mech. **53** [1], p. 193-197 (1986).

## Lateral Dye Distribution with Ink-Jet Dye Doping of Polymer Organic Light Emitting Diodes

Conor F. Madigan, Thomas R. Hebner, and J. C. Sturm

Department of Electrical Engineering, Princeton University, Princeton, NJ 08544

Richard A. Register, Sandra Troian

Department of Chemical Engineering, Princeton University, Princeton, NJ 08544

### ABSTRACT

In this work we investigate the lateral dye distribution resulting from the dye doping of a thin polymer film by ink-jet printing (IJP) for the integration of color organic light emitting diodes (OLED's). The dye is found to segregate into distinct outer rings following rapid droplet evaporation, while slower evaporation rates are found to significantly reduce (or eliminate) this effect. The dye segregation phenomena are found to depend critically on the mechanisms of droplet evaporation. Good dye uniformity was obtained using a low vapor pressure solvent, and integrated, 250 micron red, green, and blue polymer organic light emitting diodes (OLED's) were fabricated with this technique. These devices had good color uniformity over most of the device area and similar electrical properties to comparable spin-coated devices without IJP.

### I. INTRODUCTION

Polymer OLEDs are a promising technology for flat panel displays [1]. These devices typically consist of a multi-layer sandwich of a transparent substrate, a transparent anode (in our work, Indium Tin Oxide), a thin film of an organic polymer blend (in our work, the hole-transporting polymer Poly(N-vinyl carbazole) (PVK) doped with an emissive dye), and a reflecting cathode. (The device structure and principle of operation are illustrated in Fig. 1.) When current is driven through the device, holes and electrons from the anode and cathode combine in the organic film to form excitons, which emit light as they decay. It has been shown that by doping the organic active layer with a small amount of dye one can tune the emission wavelength [2]. Currently, spin coating is the standard method for depositing a polymer blend film, which produces a uniform layer of polymer. However, this does not allow one to integrate multiple colors onto a single substrate, because the film is the same everywhere.

It has been proposed previously [3,4] to locally dope an initially undoped PVK film by depositing droplets of a dye solution onto the film surface and allowing the droplet to evaporate. This task is ideally suited to IJP. This basic procedure is outlined schematically in Fig. 2. To integrate red, green, and blue devices onto a single substrate, solutions of red, green, and blue dyes are locally printed onto the same substrate. Our

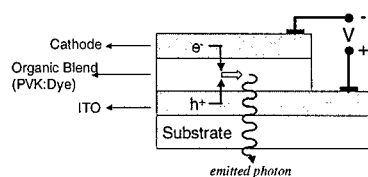


Fig. 1. Basic OLED structure and operation.



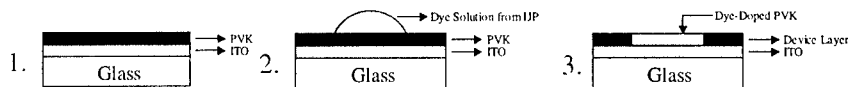


Fig. 2. Procedure for dye-doping by ink jet printing.

objectives in developing this technique are to (a) produce a uniform dye distribution over the device area and film depth and (b) maintain the initial film morphology (so that the electrical device characteristics are not degraded). In employing IJP, this technique should be relatively inexpensive to perform and applicable to large area substrates.

## II. IJP DROPLET FORMATION

Our experimental apparatus consists of a piezo-electric type ink jet printer (supplied by MicroDrop GmbH) with a glass print head (which is therefore resistant to solvent damage) and x-y-z print head stage motion. In addition, our system has integrated digital imaging equipment, allowing us to view droplet ejection from the print head nozzle directly and to view drying droplets (from above) under high magnification. The print nozzle consists of a 25  $\mu\text{L}$  capillary cavity surrounded by a piezo-electric sleeve which can contract and expand the fluid cavity (see Fig. 3). To drive a droplet out of the nozzle, a first positive then negative pressure pulse is applied to the fluid through the voltages applied to the piezo-electric sleeve.

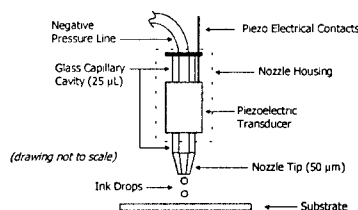


Fig. 3. Schematic of Ink Jet Nozzle. (The negative pressure line is used to balance gravitational forces.)

The positive pulse drives the fluid down into the nozzle tip (which is 50  $\mu\text{m}$  in diameter), and if sufficient energy is supplied by this pulse, a droplet (with diameter slightly larger than the nozzle diameter) will be ejected. The essential free parameters for controlling droplet ejection are the piezo voltage and the pulse duration.

Several parameters are relevant to understanding droplet formation from an ink jet printer: system geometry (i.e. of capillary cavity and nozzle), properties of the fluid being printed (i.e. viscosity, surface tension, and density), and the relationship between the applied voltage and the resulting pressure pulses. Even each of these parameters is known in detail, a closed-form analysis of the governing Navier-Stokes equations is not possible. However, there is a rapidly growing literature on approximate solutions and numerical simulations of ink-jet flow (e.g. [5-7]), and some important trends are observed.

Droplet formation can be divided up into four regimes, based on the applied voltage. At very low voltages, no droplet is ejected, because the applied pressure pulse has insufficient energy. At higher voltages, single, stable droplet ejection is observed. At still higher voltages, satellite droplets are observed along with the main droplet, and this regime is generally less stable than the single droplet regime. Finally, at yet higher voltages, the ejected fluid will not form into a main droplet and satellites, but break up into an uncontrolled spray, or "jet." These four regimes were clearly demonstrated experimentally on our system with Dimethyl Sulfoxide (DMSO) (see Fig. 4).

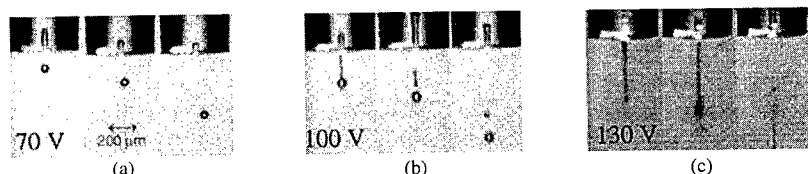


Fig. 4. Observation of droplet formation regimes with DMSO. No drops were observed for voltages below 60V. (a) Single droplet regime. (b) Satellite droplet regime. (c) "Jet" regime.

We investigated droplet formation with numerous solvents, and found that we could not form droplets (stable or otherwise) at any voltage or pulse duration for solvents with low viscosity and low surface tension on our system. This phenomenon is not reported in the literature. Nevertheless, this introduced a new constraint on solvent selection for our work. The results of our solvent IJP characterization experiments are summarized in Figure 5.

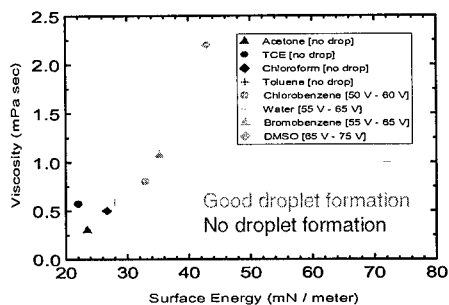


Fig. 5. IJP Solvent Space. For printable solvents, the voltage range for the single droplet regime is given in the legend in brackets.

### III. LATERAL DYE DISTRIBUTION

Once a droplet of dye solution is deposited on the polymer film, the actual dye doping occurs over the course of the evaporation of the solvent. Understanding how the dye is laterally distributed in the film, therefore, requires an understanding how the droplet dries. There are essentially two basic types of droplet drying: unpinned and pinned (see Fig. 6).

It is well known that a droplet of fluid on surface has a characteristic contact angle,  $\theta_c$ , which is dependent primarily on the fluid-surface interface (and only weakly on the surface-air and fluid-air interfaces). In unpinned evaporation,  $\theta_c$  remains constant as fluid from the droplet surface evaporates, and the droplet radius shrinks correspondingly. In pinned evaporation, the droplet radius remains constant, and instead  $\theta_c$  shrinks. Though the phenomenon of pinning is not fundamentally understood, it has been proposed that it is the result of surface roughness (including possible "self-roughening" by solute deposition) [8-10]. In addition, it is believed that for the droplet

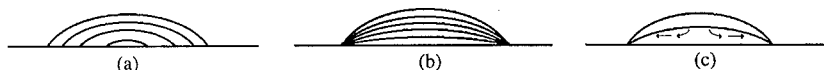


Fig. 6. Evaporation phenomena. (a) Unpinned. (b) Pinned. (c) Flow during pinned evaporation.

radius to remain constant during evaporation, fluid must flow out from the center to the edge of the drop, leading to a possible mass flow of solute towards the edges [8], as illustrated schematically in Fig. 6c.

Our first dye doping experiments were performed on ~100 nm PVK films, using a solution of the green emitting dye Coumarin 6 (C6) in acetone. Since we could not print acetone with our ink-jet printer, in these experiments we used a syringe to deposit individual droplets of ~1  $\mu$ L, which had a deposited radius of ~7mm. We found that for room temperature evaporation, the acetone droplet remained pinned at its initial radius for ~35 s, and then its radius fell rapidly during the remaining 15 s of evaporation (see Fig. 7a). The resulting dye distribution was observed under ultraviolet (UV) photoluminescence (PL) (see Fig. 7b), and revealed distinct rings of high dye concentration corresponding to droplet pinning, while between the rings, the dye concentration was very low. This observation of dye pile-up into rings was further confirmed by X-ray microprobe. These results clearly demonstrated that mass transport of solute from the center of the droplet to the edges (through some mechanism) occurred. Reducing the evaporation rate by cooling the substrate to 4°C greatly improved the dye distribution uniformity over the droplet area; however, substantial segregation of dye towards the edges was still clearly observed.

Many solvents were considered when determining the best choice for our initial IJP experiments. Essentially, we required a *printable* solvent that dissolved the dye and not the PVK films we would be printing on. In addition, because our work with acetone suggested that slower evaporation times would improve the dye distribution, we desired a solvent with a low vapor pressure. Among the common solvents we tried, DMSO was the only one to meet all these requirements (see Table I).

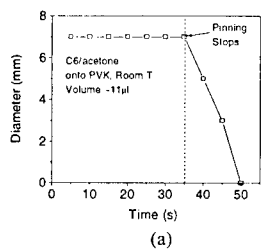


Fig. 7. Acetone:C6 Deposition. (a) Droplet radius with time during evaporation. (b) Photoluminescence of dye doping, where brightness corresponds to C6 concentration.

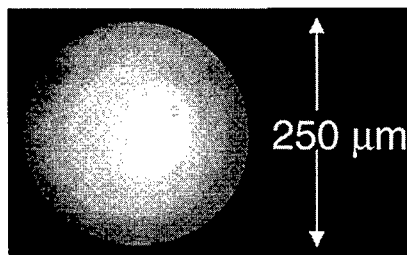
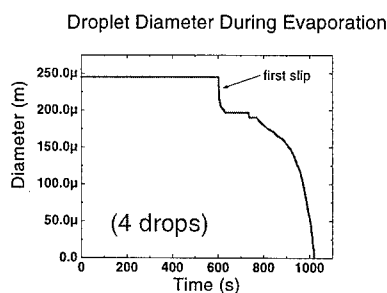
Table I. Solvents Investigated for IJP Dye Doping Candidacy. (All values for 25°C.)

Name	Formula	Viscosity* ( $\eta$ ) (mPa·s)	Surface Energy* ( $\gamma$ ) (mN/m)	Vapor Pressure* ( $p_v$ ) (kPa)	Dissolves Dyes	Dissolves PVK	Prints
Chlorobenzene	$C_6H_5Cl$	0.753	32.99	1.6	Yes	Yes	Yes
Cyclohexanone	$C_6H_{10}O$	2.02	34.57	0.53	Yes	Yes	Yes
Tetrachloroethane	$C_2H_2Cl_4$	1.84	35.58	1.6	Yes	Yes	Yes
<b>Dimethyl sulfoxide</b>	<b><math>C_2H_6SO</math></b>	<b>2.20</b>	<b>42.92</b>	<b>0.08</b>	<b>Yes</b>	<b>No</b>	<b>Yes</b>
Water	$H_2O$	1.00	71.99	1.00	No	No	Yes
Chloroform	$CHCl_3$	0.58	26.67	26	Yes	Yes	No
Acetone	$C_3H_6O$	0.30	23.46	31	Yes	No	No

We printed droplets of C6 in DMSO onto PVK films, and observed the drying phenomena. We found that the droplet was pinned for the first 600 s, and for the remaining 400 s evaporation proceeded through a complex sequence of pinning and

slipping (see Fig. 8a). The resulting dye distribution was observed using a PL image of the droplet, which revealed a fairly uniform dye distribution, but with a noticeable segregation of dye towards the center (see Fig. 8b). There were no high concentration outer rings observed as in the acetone results. Closer inspection of the PL image shows that instead, a small number of thick, circular bands of uniform dye distribution are present around an essentially uniform central region, with increasing dye concentration towards the center. The edges of these regions correspond well to the pinned radii observed during evaporation, suggesting that in a region of PVK suddenly exposed by a droplet slip, the absorbed solvent evaporates without any dye redistribution. This is consistent with the assumption that the evaporation of the solvent absorbed into the  $\sim 100$  nm film should occur extremely rapidly and evenly over the exposed film area. (This result also suggests that in the PVK *under* the solvent droplet, the dye concentration is uniform at the time of the slip.)

We fabricated integrated red, green, and blue electrical devices on a single substrate, using the dyes Nile Red, C6, and Coumarin 47 to produce each respective color. The resulting  $250 \mu\text{m}$  devices demonstrated similar electrical characteristics to spin-coated devices without IJP, suggesting that the IJP dye doping process did not adversely affect the electrical behavior of the PVK film. The observed electroluminescence (EL) was investigated for uniformity, and an image of a characteristic device is given in Fig. 9. The color uniformity is good over most of the device area, however, there is a distinct dark spot observed in the center of the device, with a slight darkening of the luminance just around this spot. The increased dye concentration in the center of the device (observed in the PL results) could explain a darkening of the luminance (due to dye concentration quenching [11]) in the center, but this effect cannot explain the sharp,



(b)

Fig. 8. DMSO:C6 IJP Deposition.  
(a) Droplet radius with time during evaporation.  
(b) Photoluminescence of dye doping.

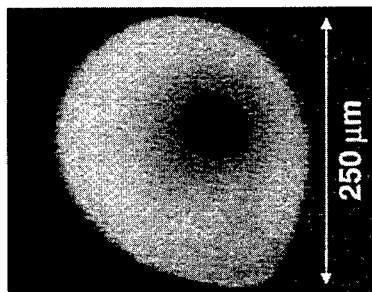


Fig. 9. Electroluminescence of IJP dye doped OLED.

---

completely dark spot observed. This dark spots appears to be correlated with the surface deposition of some material during the extremely fast drying which occurs in the last stages of the evaporation process over a total region with a radius of about 20 microns, but the details are still unknown.

#### IV. SUMMARY

We have developed a system to investigate the dye doping by IJP of polymer OLED's, including a highly controllable, all-glass ink jet printer and digital imaging equipment for studying IJP droplet formation and droplet drying phenomena. Using a very low vapor pressure solvent, very uniform dye distribution over the droplet area was achieved. It is show that the dye distribution is critically effected by the dynamics of the drying process, which at present are only qualitatively understood. Integrated, 250 micron RGB devices were demonstrated with good color uniformity and with electrical properties comparable to spin-coated devices without IJP.

#### V. ACKNOWLEDGEMENTS

This work was supported by DARPA/AFOSR, NSF, and NJCST. The authors would also like to thank Joe Goodhouse for his expert assistance in obtaining PL images.

#### VI. REFERENCES

- [1] J.H. Burroughs *et al.*, Nature, **347**, 539 (1990)
- [2] J. Kido *et al.*, Appl. Phys. Lett., **61**, 761 (1992).
- [3] T.A. Hebner *et al.*, APL, **73**, 1775 (1998).
- [4] Chang *et al.*, APL, **73**, 2561 (1998).
- [5] E.D. Wilkes *et al.*, Phys. of Fluids, **11**, 3577 (1999).
- [6] X.G. Zhang, J. Coll. Int. Sci., **212**, 107 (1999).
- [7] T.W. Shield *et al.*, IBM J. Res. Dev., **31**, 96 (1987).
- [8] R.D. Deegan, Phys. Rev. E, **61**, 475 (2000)
- [9] E. Adachi *et al.*, Langmuir, **11**, 1057 (1995)
- [10] P.G. de Gennes, Revs. Mod. Phys., **57**, 827 (1985)
- [11] C.-C. Wu *et al.*, IEEE Trans. on Elec. Dev., **44**, 1269 (1997).

---

## CALCULATION OF HAMAKER CONSTANTS IN NONAQUEOUS FLUID MEDIA

Nelson Bell and Duane Dimos

Ceramic Materials Department, Sandia National Laboratories, 1515 Eubank Blvd. SE, MS 1411, Albuquerque, NM 87123

### ABSTRACT

Calculations of the Hamaker constants representing the van der Waals interactions between conductor, resistor and dielectric materials are performed using Lifshitz theory. The calculation of the parameters for the Ninham-Parsegian relationship for several non-aqueous liquids has been derived based on literature dielectric data. Discussion of the role of van der Waals forces in the dispersion of particles is given for understanding paste formulation. Experimental measurements of viscosity are presented to show the role of dispersant truncation of attractive van der Waals forces.

### INTRODUCTION

Thick film pastes are complicated examples of colloidal processing and engineering. The desired rheological characteristics for thick film printing include a shear thinning viscosity to allow flow during printing and a yield stress to maintain printed feature definition. These properties are achieved through control of the range and magnitude of interparticle forces. All similar materials experience attractive forces due to permanent or induced dipolar interactions, and the effect of these interactions between materials is expressed macroscopically in terms of the Hamaker constant,  $A_{132}$ . This attractive force generates an agglomerated particle network that resists flow. In order to make a suspension fluid, a stabilizing mechanism must be employed that controls the magnitude of the attractive forces between the particles to give the desired rheological behavior. By keeping particles at a fixed separation distance, the strength of their attraction can be controlled. The Hamaker constant provides a baseline for understanding how much separation is required. Understanding the strength of the Hamaker constant helps determine the type and properties of the stabilizing mechanism needed to form an effective thick film paste composition.

The Hamaker constant was first calculated by summing the interactions between the dipole-pairs in a material [1]. This laborious procedure was greatly simplified when Lifshitz described how the dielectric response function of a material could be used to perform the same function more accurately as it incorporates many-body effects directly into the calculation [2]. Assuming materials to be continuous media, the Ninham-Parsegian (N-P) imaginary function can be used to represent the dielectric response as a function of frequency [3-5]. This N-P representation has no direct physical basis but can be constructed based on knowledge of the static dielectric constant, index of refraction, and infrared, ultraviolet and microwave absorption spectra. One of the properties of the N-P relationship is that it is evaluated at discrete imaginary frequencies which are distributed so that the ultraviolet and (to a lesser degree) infrared spectra dominate the determination of the Hamaker constant. Accuracy of the calculation therefore depends greatly on the accuracy of the IR and UV spectra used to construct the N-P function for the material.

Most calculations of Hamaker constants have focused on aqueous media. Much of the reason for attention being paid to water is its environmentally benign nature. Yet, the majority of thick film pastes used in the electronics industry are in nonaqueous solvents, and the availability of information for these systems are not common in the literature. It is the drive of this work to fill the gap in the literature of the functions required to calculate Hamaker constants in nonaqueous media. In doing so, the role of dispersants in these media to control rheological response will be improved, and the possibility of tailoring solid and liquid to provide desired rheological properties can be explored.

## EXPERIMENTAL

Rheological measurements were performed with a Bohlin CS-10 rheometer<sup>1</sup>. Silver slurries<sup>2</sup> were prepared at 40 volume % in methanol and isopropanol. Pluronic F68<sup>3</sup> dispersant was added at 0.4 weight % to powder to evaluate the control of interparticle force on rheological response. This dispersant is a triblock copolymer of polyethylene oxide stabilizing blocks bonded to an adsorbing block of polypropylene oxide. Experiments were performed using a 60 second preshear at 400 rpm followed by a hold time of 30 seconds. Tests were run from low shear rate to high and back to zero.

The parameters for the Ninham-Parsegian expression for liquids can be found in a variety of literature sources. Water has been most extensively characterized, and the spectral parameters for water are given in [5]. Six infra-red and five ultraviolet damped oscillators with a single Debye microwave relaxation represent the dielectric behavior very well. However, this level of detail is hard to compile for most nonaqueous solvents. The static dielectric constant and index of refraction at the sodium D line are commonly tabulated [6], and the infra-red adsorption spectra for many liquids are relatively easy to find [7]. The microwave parameters for several liquids are referenced in the compilation of Buckley and Maryott [8]. Determination of the ultraviolet characteristics for several solvents has proven to be more difficult. This is a serious complication as the ultraviolet terms are the most critical for calculating the Hamaker constant. In the absence of a full spectra, UV relaxation is commonly represented by a single oscillator of magnitude equal to  $n^2 - 1$ . The UV adsorption edge was chosen as the critical frequency of this oscillator and damping terms were omitted [6]. Further searches are being performed to determine the UV spectra for these nonaqueous fluids and refine the parameters for Hamaker constant calculation.

From the collected data, the oscillator strengths were determined by the changes in the value of the real dielectric constant between spectral regions. The microwave strength can be determined directly from [8]. Groups of peaks located very closely together in the infra-red spectrum are represented by a single oscillator and damping terms were omitted. The index of refraction was used to determine the magnitude of the transition between the microwave and visible region due to adsorption in the IR, and individual oscillator strengths were assigned based on the area of each IR adsorption. The ultraviolet adsorption was represented by a single oscillator at the UV adsorption edge. This collected data is presented in Table 1.

The optical parameters for solids have been tabulated in several sources that can be used to fit the oscillator models for dielectric behavior [5,9,10]. Most metal oxides can be fit in a

<sup>1</sup> Bohlin Instruments Inc., Suite 1, 11 Harts Lane, East Brunswick, NJ 08816.

<sup>2</sup> Superior Micropowders, 3740 Hawkins NE, Albuquerque, NM 87109.

<sup>3</sup> BASF Corporation, 3000 Continental Drive North, Mount Olive, NJ 07828-1234.

**Table 1. Spectral Parameters for the Ninham-Parsegian expression of  $\epsilon''(\omega)$  for Nonaqueous Solvents.**

Name	Type	Dielectric Constant	$C_{MW}$	$\omega_{MW}$ (rad/sec)	$C_{IR}$ (#)	$\omega_{IR}$ (#) (rad/sec)	$n$	$C_{UV}$	$\omega_{UV}$ (rad/sec)
Methanol	Amphiprotic	33.64	27.64	$2 \times 10^{12}$	0.254 0.123 1.042 2.801	$3.0579 \times 10^{13}$ $4.149 \times 10^{13}$ $8.682 \times 10^{13}$ $1.007 \times 10^{14}$	1.3288	0.76571	$9.1885 \times 10^{15}$
1-Propanol	Amphiprotic	20.8	17.4	$3 \times 10^9$	0.2134 0.1778 0.3808 0.70977	$3.148 \times 10^{13}$ $4.317 \times 10^{13}$ $8.8019 \times 10^{13}$ $9.977 \times 10^{13}$	1.3850	0.91823	$8.9698 \times 10^{15}$
2-Propanol	Amphiprotic	20.18	17.12	$1 \times 10^{10}$	0.0198 0.05927 0.1441 0.1801 0.2208 0.53462	$2.4343 \times 10^{13}$ $2.842 \times 10^{13}$ $3.4656 \times 10^{13}$ $4.125 \times 10^{13}$ $8.8739 \times 10^{13}$ $9.9172 \times 10^{13}$	1.3776	0.89778	$9.1885 \times 10^{15}$
1-Butanol	Amphiprotic	17.84	14.84	$2 \times 10^9$	0.13545 0.13233 0.26674 0.50743	$3.1778 \times 10^{13}$ $4.2871 \times 10^{13}$ $8.7840 \times 10^{13}$ $9.9172 \times 10^{13}$	1.3993	0.95804	$8.7612 \times 10^{15}$
2-Butanol	Amphiprotic	17.26	13.32	$2 \times 10^9$	0.2582 0.2185 0.4767 0.9931	$2.9979 \times 10^{13}$ $4.1132 \times 10^{13}$ $8.9039 \times 10^{13}$ $1.0037 \times 10^{14}$	1.3978	0.95385	$7.2448 \times 10^{15}$
Benzene	Inert	2.28	N/A	N/A	0.00969 0.00561 0.0114	$2.0146 \times 10^{13}$ $4.437 \times 10^{13}$ $9.144 \times 10^{13}$	1.5011	1.25330	$6.7757 \times 10^{15}$
Toluene	Inert	2.38	N/A	N/A	0.0642 0.02295 0.0545	$2.1825 \times 10^{13}$ $4.4849 \times 10^{13}$ $9.0778 \times 10^{13}$	1.4961	1.23832	$6.6326 \times 10^{15}$



similar manner to the liquids. Values for alumina and barium titanate were taken from the compilation of Bergstrom [5]. Parameters for silver were taken from Parsegian and Weiss [11]. The parameters have been converted from eV to rad/sec. The first term has no critical frequency, and it represents the hyperbolic dependence of the conduction electrons.

**Table 2. Spectral Parameters for the Ninham-Parsegian expression of  $\epsilon(i\xi)$  for Solid Materials.**

Name	Dielectric Constant	Index of Refraction	$C_j$	$\omega_j$ (rad/sec)	$g_j$ (rad/sec)	Source
Silver	$\infty$	--	$2.1209 \times 10^{32}$	--	--	16
			1.51997	$7.8997 \times 10^{15}$	$2.8864 \times 10^{15}$	
			0.54527	$2.3547 \times 10^{15}$	$8.20349 \times 10^{15}$	
			0.17327	$3.4333 \times 10^{16}$	$5.46899 \times 10^{15}$	
			2.24565	$5.2563 \times 10^{16}$	$1.43105 \times 10^{17}$	
Alumina	10.1	1.753	2.072	$2.0 \times 10^{16}$	--	5
			7.03	$1 \times 10^{14}$	--	
Barium Titanate	o 3600	2.284	4.218	$0.841 \times 10^{16}$	--	5
			3595	$0.7-1.0 \times 10^{14}$	--	

## RESULTS

Using the parameters from Tables 1 and 2, the Hamaker constant between identical particles in various liquid media was determined by the N-P method [3-5]. These values are given in Table 3.

**Table 3. Hamaker Constants between Identical Particles in Various Solvents**

Solvent	Silver (zJ)	Alumina (zJ)	Barium Titanate (zJ)
Water	149.1	36.9	106.8
Methanol	175.2	84.4	142.8
1-Propanol	168	76.0	134.4
2-Propanol	224.5	149	203.9
1-Butanol	167.3	75.0	133.2
2-Butanol	175.4	84.7	142.5
Benzene	166.4	77.0	131.5
Toluene	168	78.6	133.3

From the values in Table 3, there is a general trend regardless of solvent that ranks the Hamaker constants in the order silver > barium titanate > alumina. This trend relates to the material dielectric constant which results from Keesom and Debye electrostatic interactions. The London (dispersive) interactions that affect the IR and UV adsorption cannot compensate for the difference in static properties. The high magnitudes of the dielectric constant for barium titanate (3600) and of silver (infinity) makes it unlikely that any solvent exists which will match the dielectric properties of these materials and cause a minimum in the Hamaker constant. Alumina however has a low dielectric constant, so the possibility to choose a solvent that minimizes van der Waals interactions is available.

In comparison of the solvents, the values for each solid material with water as the solvent can be expected to be more accurate than the nonaqueous solvents due to the higher degree of characterization of the dielectric spectra available for water. No solvent that was evaluated has a Hamaker constant lower than water, and in general they are significantly higher. Most of the

nonaqueous values are of comparable magnitude with the exception of 2-propanol. The high value of  $A_{132}$  for 2-propanol predicts that with a similar dispersing mechanism, values of shear stress and viscosity will be higher in 2-propanol versus another solvent.

To test this hypothesis and the accuracy of the parameters used in calculation, silver dispersions were made in methanol and 2-propanol using a nonionic dispersant recommended for use in water and alcohols. The viscosity data was normalized for the intrinsic solvent viscosity, and the samples are compared in Figure 1. Contrary to the Hamaker constant prediction, the attractive forces in methanol seem higher than in 2-propanol. Reasons for the discrepancy include: the Hamaker values for 2-propanol are too high, there may be electrostatic forces present in the 2-propanol, or the dispersant may have different solvation characteristics in each solvent. The viscosity curves have the same qualitative behavior and exhibit little hysteresis between the rising and falling shear rate test. This suggests that the dispersant is behaving similarly between the two solvents, but it does not rule out the possibility that there may be differing adsorbed amount of polymer or a difference in the extension of the polymer from the surface. However, the estimations used in the ultraviolet spectra of 2-propanol may need to be corrected to give the most correct values. Further examination of the surface chemistry of the silver powder in each solvent and the behavior of the dispersant need to be performed before definite answers can be concluded.

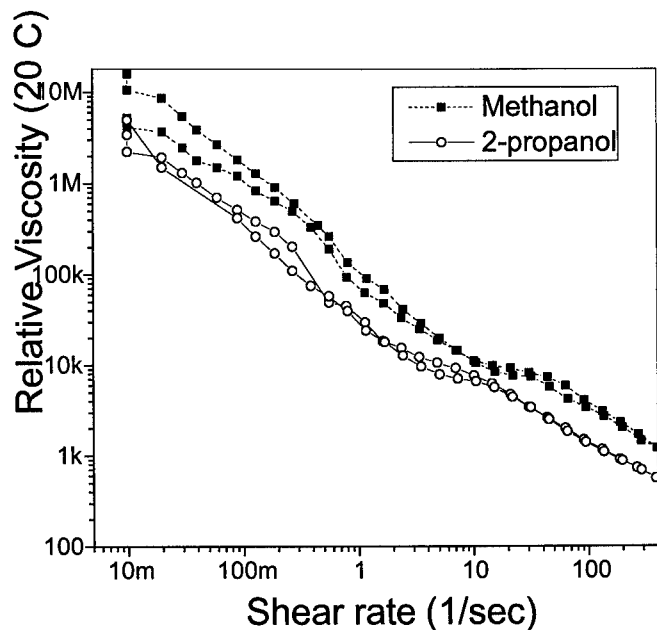


**Figure 1.** Relative viscosity comparison of silver powder dispersed with Pluronic F68 in methanol and isopropanol.

## CONCLUSIONS

Terms needed for calculating the Hamaker constant of several nonaqueous liquids have been collected from the literature, and the Hamaker constant for three materials systems have been calculated for identical particles in these solvents and in water. Within each solid system, the Hamaker constant scales with dielectric constant. The nonaqueous solvents were calculated to have larger Hamaker constants than water, but their accuracy could be improved by using more accurate representations of the ultraviolet adsorption spectra. The examination of two nonaqueous solvents for differences in van der Waals attractive forces did not agree with values of the Hamaker constant. Reasons for the discrepancy require more investigation of each system.

## ACKNOWLEDGEMENTS

Sandia is a multiprogram laboratory operated by Sandia Corporation, a Lockheed Martin Company, for the United States Department of Energy under contract DE-AC04-94AL85000. This work was performed under the DARPA MICE program under the leadership of CMS Technitronics. Special thanks go to Superior Micropowders for supplying the silver powder.

## REFERENCES

1. H.C. Hamaker, *Physica*, **4** 1058 (1937).
2. E.M. Lifshitz, *Soviet Physics*, **2** 73-83 (1956).
3. D.B. Hough and L.R. White, *Adv. Colloid Interface Sci.*, **14** 3-41 (1980).
4. J. Israelachvili, *Intermolecular and Surface Forces*, 2nd Ed., (Academic Press, London, 1995) p. 176-209.
5. L. Bergstrom, *Adv. Colloid Interface Sci.*, **70** 125-169 (1997).
6. D.R. Lide, Ed., *CRC Handbook of Chemistry and Physics*, 78<sup>th</sup> Ed., (CRC Press, New York, 1997) p. 6-139-172, 8-113.
7. C.J. Pouchert, *The Aldrich Library of Infrared Spectra*, 3<sup>rd</sup> Ed., Aldrich Chemical Co., 1981.
8. F. Buckley and A.A. Maryott, *Tables of Dielectric Dispersion Data for Pure Liquids and Dilute Solutions*, NBS Circular 589, 1958.
9. E.D. Palik, *Handbook of the Optical Constants of Solids*, (Academic Press, Orlando, Fl, 1985).
10. E.D. Palik, *Handbook of the Optical Constants of Solids II*, (Academic Press, New York, 1991).
11. V.A. Parsegian and G.H. Weiss, *J. Colloid Interface Sci.*, **81** 285-289 (1981).

---

## **All-Printed Inorganic Logic Elements Fabricated by Liquid Embossing**

Colin Bulthaupt, Eric Wilhelm, Brian Hubert, Brent Ridley, and Joe Jacobson

Media Lab, Massachusetts Institute of Technology, Cambridge, MA 02139

### **ABSTRACT**

The liquid embossing process, devices made by this process, and their characteristics are presented. Structures fabricated and discussed here include: conductive lines with cross line resistance greater than 100 G $\Omega$  and resistivities 4 times that of the bulk material, multilayer structures with etched sacrificial materials, vias that conduct through an embossed insulating layer, photodetectors made with nanocrystal solutions of CdSe, and all printed inorganic field effect transistors.

### **EXPERIMENT**

#### **Process**

Liquid embossing<sup>[1,2]</sup> is a physical process used to create features in functional materials. Though this process can pattern a wide range of materials this paper is restricted to a discussion of patterning solutions of nanocrystals, spin on glasses (SOG) (Ohka T7), and insulating polymers (Japanese Synthetic Rubber AL 3046). Our paper gives a brief overview of the process, then descriptions of the types of devices produced with liquid embossing and their characteristics. The devices discussed include conducting metal lines, released mechanical structures, and transistors.

A stamp is created by casting an elastomer (PDMS) from a master. The master is typically made of photoresist on a silicon wafer, but can be any surface with raised physical features. As shown in Fig. 1, the stamp is brought into contact with a thin film of functional material in liquid phase. The raised features on the stamp emboss through the thin film to the underlying substrate and remove material. The stamp is then removed while the functional material is still in liquid phase; the material can reflow if embossed again but otherwise will remain patterned. Finally the material is cured, which removes the solvents and sinters or cures the material.

Thin films are created by either a drawdown bar or conventional spin coating. In the draw down process a drop of liquid material is placed on a substrate, and a ground metal cylinder is pulled over the substrate. The only pressure on the substrate is the weight of the cylinder. The thin films obtained are very consistent for a range of liquid material properties including viscosity, vapor pressure, and surface wetting.

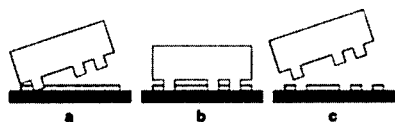


**Figure 1: Schematic of the liquid embossing process: (a) the elastomeric stamp is brought into contact with a thin film of liquid, (b) the stamp contacts the underlying substrate and selectively patterns the liquid film, (c) the stamp is removed and the liquid film remains patterned.**

### Single-Layer Structures

We have patterned structures with a wide variety of resolutions and geometries. 200 nm line width gratings were fabricated over areas greater than 4 cm with high reliability, (Fig. 2a). Other structures with non-repeating features have been fabricated over the entire surface of a 4" wafer, (Fig. 2b). Typical solid film thickness range from 50 nm – 400 nm.

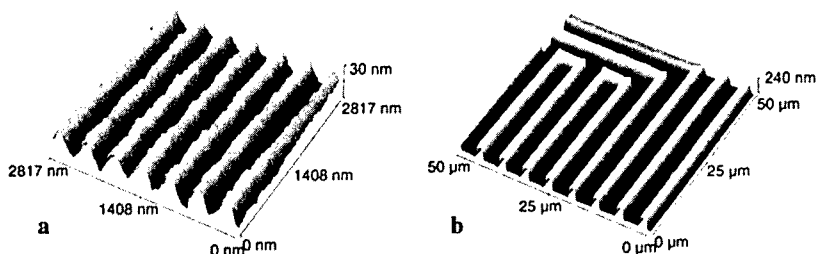


**Figure 2: Atomic Force Microscope images of single layers of patterned Au: (a) 400nm grating structure, (b) 3um wide lines in a circuit pattern.**

### Resistors

Colloidal suspensions of Au nanoparticles in  $\alpha$ -terpineol were used as a conducting material. These suspensions were patterned via liquid embossing and then cured at 300° C for 30 minutes to produce a solid metallic film. It was important that the stamp was removed prior to curing in order to guarantee that all of the organic solvent could boil off. Serpentine resistor structures (Fig. 3) were patterned in order to measure the resistivity of the material. These resistors had widths of 1, 3, and 5 $\mu$ m, and lengths of 6, 12, and 30mm. For the narrowest / longest resistor these dimensions corresponded to an aspect ratio of roughly 30,000 to 1. The calculated resistivity for these resistors was  $8.32 \times 10^{-6} \Omega\text{-cm}$ , with a standard deviation of  $5 \times 10^{-7} \Omega\text{-cm}$ . The cross-channel resistance between pairs of unconnected gold lines was greater than 100 G $\Omega$ .



Figure 3: Optical image of a serpentine resistor structure for measuring the resistivity of Au material.

### Multi-Layer

Self-planarization and conformal patterning over rough features are very important aspects of liquid embossing. Multilayer structures can be built up by simply embossing on top of a previously patterned and cured layer. Registration between layers is achieved to approximately  $5\mu\text{m}$  of error with a stationary stamp, and a substrate mounted on an x-y positioning stage. Due to the conformability of the PDMS stamp the embossing process can actually clear out material from a previous patterning, as shown in Fig. 4.

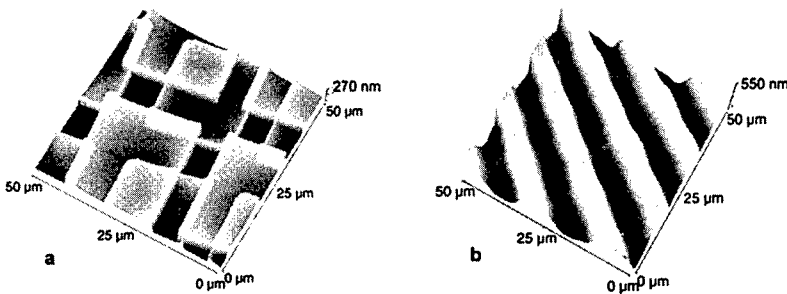
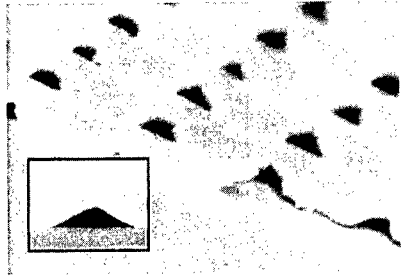


Figure 4: Atomic Force Microscope images of multilayer structures fabricated in Au: (a) two arrays of squares patterned on top of each other, demonstrating conformal patterning, (b) two diffraction gratings patterned on top of each other, demonstrating self-planarization of patterned liquid films.

### MEMS

Nanocrystals have already been proven to be able to form heatuators and other MEMS devices by inkjet deposition<sup>[3]</sup>. Fig. 5 shows a structure we call an aqueduct: triangular profile lines of Au are patterned on top of triangular lines of SOG (spin-on glass). The glass is then etched away leaving only the Au. This method is a route to creating embossed MEMS devices with many layers.



**Figure 5: Scanning Electron Microscope image of patterned Au lines with etched away sacrificial lines running perpendicular to the Au lines, (inset) side-view of Au lines.**

**Transistors & Photodetectors**

Recently, it was demonstrated that nanocrystalline films of CdSe could be used as a high mobility semiconductor for thin film transistors (TFTs)<sup>[4]</sup>. Partially printed TFT structures were created by growing a 300 nm thick thermal oxide on a n+ wafer and then patterning Au source/drain electrodes on top of the oxide by liquid embossing. CdSe was then deposited by pipet in the channel between the electrodes, sintered at 300° C, and encapsulated with a photo-curable adhesive (Norland 73). The device was probed in ambient conditions and showed a mobility of 0.1 cm<sup>2</sup>V<sup>-1</sup>s<sup>-1</sup> and an on/off ratio of 10<sup>3</sup> (Fig. 6a) which is within an order of magnitude of previously reported results using evaporated Au electrodes. Additionally, photodetectors were created by fabricating similar structures without the Norland encapsulant. These devices showed a strong correlation between relative light intensity and source-drain current (Fig. 6b).

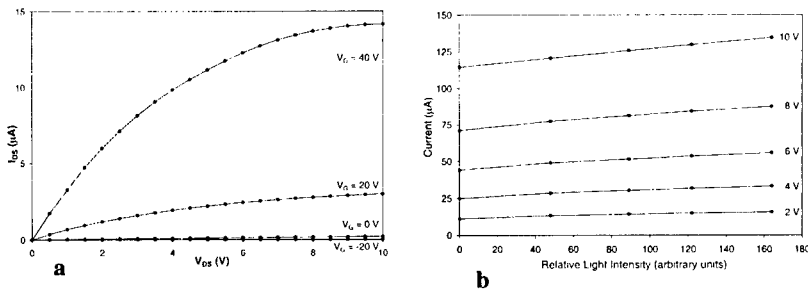


**Figure 6: Half-printed devices measured in ambient conditions: (a) Transistor: source/drain current vs. voltage for various gate voltages, (b) Photodetector: source/drain current at a fixed voltage for various different light intensities**

### Capacitors & Vias

Low-K dielectric capacitors have been made by liquid embossing. A thin film of Au was patterned on top of previously deposited and cured layers of Au and insulator. The insulator was typically SOG or a polyimide. The capacitors, which were fabricated outside of a clean room, were able to insulate between conductive metal layers over areas in excess of  $10 \text{ cm}^2$ . Combining these low-K dielectric materials with our ability to pattern multiple functional layers allowed us to fabricate vias between electrically isolated metal layers, (Fig. 7).

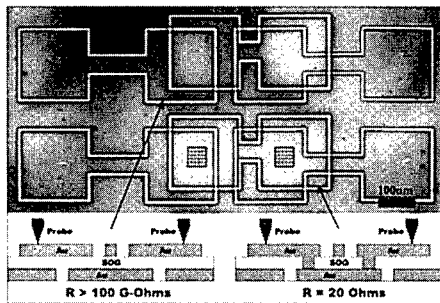


**Figure 7: Three layer via structure fabricated entirely by liquid embossing. In the first device there were no vias present and thus no conduction between the two probes. In the second device vias were patterned in the SOG, creating a direct conduction path between the two probes.**

### All-Printed Transistors

All of the previously mentioned results are necessary constituent elements for fabricating logic. By combining these techniques, we were able to fabricate the first all-printed, all-inorganic transistor. An initial layer of Au was deposited, followed by a 200 nm - 300 nm thick layer of SOG. Source/drain electrodes were then patterned in Au by liquid embossing, and a drop of CdSe was deposited in the channel region and encapsulated with Norland 73. The total fabrication time required was 5 hours, with the vast majority of that time spent curing the SOG. The devices were probed in ambient conditions and showed an on/off ratio of  $10^3$  (Fig. 8).



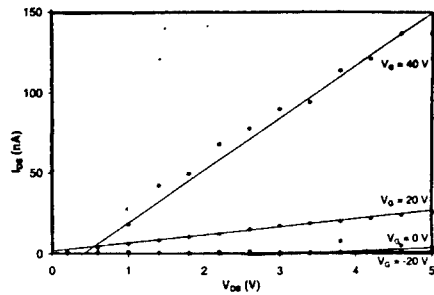


**Figure 8: All-printed all-inorganic transistor fabricated by liquid embossing. Source/drain current vs. voltage at various gate voltages, measured in ambient conditions.**

## CONCLUSION

This paper has discussed some of the structures fabricated by liquid embossing of functional materials. The results are quite exciting since it has been shown that many of the things typically made in clean rooms and billion-dollar silicon fabs can actually be made outside of a clean room for very little cost. Since the process uses inorganic materials, the possibility exists for making devices that have functional characteristics identical to those produced by conventional means. Liquid embossing also presents a possible route to the fabrication of three dimensional logic and memory, and a viable method for creating MEMS with very large numbers of layers.

## REFERENCE

1. Ridley, B. A., Nivi, B., Hubert, B. N., Bulthaupt, C., Wilhelm, E. J. & Jacobson, J. M. Solution-Processed Inorganic Transistors and Sub-Micron Non-Lithographic Patterning Using Nanoparticle Inks. 1999 MRS Fall Meeting Proc., Nanophase and Nanocomposite Materials III (1999).
2. Jacobson, J. M., Ridley, B. A., Hubert, B. N., Bulthaupt, C., Griffith, S. & Fuller, S. B. Printed Micro-Electro-Mechanical Systems and Logic. Invited talk, 1999 MRS Fall Meeting, Boston, Massachusetts (1999).
3. Fuller, S., & Jacobson, J. Ink Jet Fabricated Nanoparticle MEMS, Proceedings of IEEE MEMS 2000 Conference, Miyazaki, Japan (2000)
4. Ridley, B. A., Nivi, B. & Jacobson, J. M. All-Inorganic Field Effect Transistors Fabricated by Printing. *Science* **286**, 746-749 (1999).

---

## RAPID PROTOTYPING OF PATTERNED MULTIFUNCTIONAL NANOSTRUCTURES

Hongyou Fan, Gabriel P. López, and C. Jeffrey Brinker

The University of New Mexico/NSF Center for Micro-Engineered Materials, The Advanced Materials Laboratory, Sandia National Laboratories, Albuquerque, NM

### ABSTRACT

The ability to engineer ordered arrays of objects on multiple length scales has potential for applications such as microelectronics, sensors, wave guides, and photonic lattices with tunable band gaps. Since the invention of surfactant templated mesoporous sieves in 1992, great progress has been made in controlling different mesophases in the form of powders, particles, fibers, and films. To date, although there have been several reports of patterned mesostructures, materials prepared have been limited to metal oxides with *no specific functionality*. For many of the envisioned applications of hierarchical materials in micro-systems, sensors, waveguides, photonics, and electronics, it is necessary to define both form and function on several length scales. In addition, the patterning strategies utilized so far require hours or even days for completion. Such *slow* processes are inherently difficult to implement in commercial environments. We present a series of new methods of producing patterns within seconds. Combining sol-gel chemistry, Evaporation-Induced Self-Assembly (*EISA*), and rapid prototyping techniques like pen lithography, ink-jet printing, and dip-coating on micro-contact printed substrates, we form hierarchically organized silica structures that exhibit order and function on multiple scales: on the molecular scale, functional organic moieties are positioned on pore surfaces, on the mesoscale, mono-sized pores are organized into 1-, 2-, or 3-dimensional networks, providing size-selective accessibility from the gas or liquid phase, and on the macroscale, 2-dimensional arrays and fluidic or photonic systems may be defined. These rapid patterning techniques establish for the first time a link between computer-aided design and rapid processing of self-assembled nanostructures.

### INTRODUCTION

Living systems exhibit form and function on multiple length scales, and the prospect of imparting life-like qualities to man-made materials has inspired many recent efforts to devise hierarchical materials assembly strategies. For example, Yang et al.<sup>[1]</sup> grew surfactant-templated mesoporous silica<sup>[2]</sup> on hydrophobic patterns prepared by micro-contact printing  $\mu CP$ <sup>[3]</sup>. Trau et al.<sup>[4]</sup> formed oriented mesoporous silica patterns, using a micro-molding in capillaries *MIMIC* technique<sup>[3]</sup>, and Yang et al.<sup>[5]</sup> combined *MIMIC*, polystyrene sphere templating<sup>[6]</sup>, and surfactant-templating to create oxides with three levels of structural order. Overall, great progress has been made to date in controlling structure on scales ranging from several nanometers to several micrometers. However, materials prepared have been limited to oxides with no specific functionality, whereas for many of the envisioned applications of hierarchical materials in micro-systems, sensors, waveguides, photonics, and electronics, it is necessary to define both form and function on several length scales. In addition, the patterning strategies employed thus far require hours or even days for completion<sup>[1, 4, 5]</sup>. Such slow processes are inherently difficult to implement in commercial environments.

We have combined evaporation-induced (silica/surfactant) self-assembly *EISA*<sup>[7]</sup> with rapid prototyping techniques like pen lithography<sup>[8, 9]</sup>, ink-jet printing<sup>[10, 11]</sup>, and dip-coating on micro-contact printed substrates to form hierarchically organized structures in seconds. In addition, by co-condensation of tetrafunctional silanes ( $Si(OR)_4$ ) with tri-functional organosilanes  $((RO)_3SiR')$ <sup>[12-14]</sup> or bridged silsesquioxanes  $(RO)_3Si-R'-Si(OR)_3$  or by inclusion

of organic additives, we have selectively derivatized the silica framework with functional R' ligands or molecules. The resulting materials exhibit form and function on multiple length scales: on the molecular scale, functional organic moieties are positioned on pore surfaces, on the mesoscale, mono-sized pores are organized into 1-, 2-, or 3-dimensional networks, providing size-selective accessibility from the gas or liquid phase, and on the macroscale, 2-dimensional arrays and fluidic or photonic systems may be defined.

## EXPERIMENTAL

Precursor solutions used as inks were prepared by addition of surfactants (cationic, CTAB;  $\text{CH}_3(\text{CH}_2)_{15}\text{N}^+(\text{CH}_3)_3\text{Br}$  or non-ionic, Brij-56;  $\text{CH}_3(\text{CH}_2)_{15}(\text{OCH}_2\text{CH}_2)_{10}\text{-OH}$  and Pluronic P123,  $\text{HO}(\text{CH}_2\text{CH}_2\text{O})_{20}(\text{CH}(\text{CH}_3)\text{CH}_2\text{O})_{70}(\text{CH}_2\text{CH}_2\text{O})_{20}\text{-H}$ ), organosilanes ( $\text{R}'\text{-Si}(\text{OR})_3$ , see Table 1), or organic molecules (see Table 1) to an acidic silica sol prepared from TEOS [ $\text{Si}(\text{OCH}_2\text{CH}_3)_4$ ] (A2\*\*). The acid concentration employed in the A2\*\* synthesis procedure was chosen to minimize the siloxane condensation rate, thereby promoting facile self-assembly during printing[20]. In a typical preparation, TEOS, ethanol, water and dilute HCl (mole ratios: 1:3.8:1:5 $\times 10^{-5}$ ) were refluxed at 60 °C for 90 min. The sol was diluted with 2 volumes of ethanol followed by further addition of water and HCl. Organosilanes ( $\text{R}'\text{-Si}(\text{OR})_3$ , where R' is a non-hydrolyzable organic functional ligand) were added followed by surfactants and (optionally) organic additives (see Table 1). Surfactants were added in requisite amounts to achieve initial surfactant concentrations  $c_0$  ranging from 0.004 to 0.23 M ( $c_0 \ll \text{cmc}$ ). The final reactant molar ratios were: 1 TEOS : 22  $\text{C}_2\text{H}_5\text{OH}$  : 5  $\text{H}_2\text{O}$  : 0.093 – 0.31 surfactant : 0.039 – 0.8 organosilanes : 2.6 $\times 10^{-5}$  organic additives. For the ethylene-bridged silsesquioxane,  $(\text{RO})_3\text{Si-R}'\text{-Si}(\text{OR})_3$  ( $\text{R}' = \text{CH}_2\text{CH}_2$ ,  $\text{R} = \text{OC}_2\text{H}_5$ ), the neat precursor was diluted in ethanol and mixed with 1-8 wt% CTAB or Brij-56 surfactant followed by addition of an aqueous solution of HCl. The final reactant molar ratios were: Si:EtOH:H<sub>2</sub>O:HCl:surfactant = 1:22:5:0.004:0.054-0.18. Co-hydrolysis of organosilanes with TEOS in the initial A2\*\* sol preparation generally resulted in disordered worm-like mesostructures[21]. After pattern deposition and drying, the surfactant templates were selectively removed by calcination in a nitrogen atmosphere at a temperature sufficient to decompose the surfactant molecules (~350 °C) without degrading the covalently bound organic ligands R' (confirmed by <sup>29</sup>Si MAS NMR spectroscopy) or by solvent extraction.

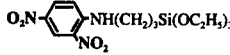
## Patterning Procedures

Micropen lithography was performed using a Model 400a micropen instrument purchased from Ohmcraft Inc., Pittsford, NY. The pen orifice was 50 μm and the writing speed was 2.54 cm/s. The pattern was designed using AutoCAD 14 software.

Dip-coating of patterned (hydrophilic/hydrophobic) substrates was performed at a withdrawal speed of 7.6 – 51 cm/min under ambient laboratory conditions. Hydrophilic/hydrophobic patterns were created by microcontact printing of hydrophobic, n-octadecyltrichlorosilane ( $\text{CH}_3(\text{CH}_2)_{17}\text{SiCl}_3$ ) self-assembled monolayers  $\text{SAMs}^{[15]}$  on hydrophilic silicon substrates (hydroxylated native oxide) or by a technique involving electrochemical desorption of a hydroxyl-terminated SAM prepared from 11-mercaptoundecanol ( $\text{HO}(\text{CH}_2)_{11}\text{SH}$ ) from patterned, electrically isolated gold electrodes followed by immersion in a 1 mM ethanolic solution of 1-dodecanethiol,  $\text{CH}_3(\text{CH}_2)_{11}\text{SH}^{[16]}$ .

Ink jet printing was performed using a Model HP DeskJet 1200C printer purchased from Hewlett-Packard Co., San Diego, CA. The pattern was designed using Microsoft PowerPoint 98 software.

**Table 1.** Functional organosilanes and properties of resultant thin film mesophases

	Functional Silanes <sup>†</sup> /additives <sup>‡</sup> R <sup>†</sup> -Si(OR) <sub>3</sub>	Mesophase	Pore Size <sup>*</sup> (Å)	Surface Area <sup>*</sup> (m <sup>2</sup> /g)	Properties and Applications
<b>1</b>	F <sub>3</sub> C(CF <sub>2</sub> ) <sub>2</sub> CH <sub>2</sub> CH <sub>2</sub> Si(OC <sub>2</sub> H <sub>5</sub> ) <sub>3</sub> Tridecafluoro-1,1,2,2-tetrahydrooctyltriethoxysilane (TFTS)	3-dH	25	850	Hydrophobic; low k dielectrics
<b>2</b>	HS-(CH <sub>2</sub> ) <sub>3</sub> Si(OCH <sub>3</sub> ) <sub>3</sub> Mercaptopropyltrimethoxysilane (MPS)	3-dH	25	1060	Coupling of noble metals
<b>3</b>	NH <sub>2</sub> -(CH <sub>2</sub> ) <sub>3</sub> Si(OCH <sub>3</sub> ) <sub>3</sub> Aminopropyltrimethoxysilane (APS)	cubic	22	750	Coupling of noble metals, dye, and bioactive molecules
<b>4</b>	Dye <sup>§</sup> -NH-(CH <sub>2</sub> ) <sub>3</sub> Si(OCH <sub>3</sub> ) <sub>3</sub>	cubic	21	545	pH sensitive
<b>5</b>	 NH(CH <sub>2</sub> ) <sub>3</sub> Si(OC <sub>2</sub> H <sub>5</sub> ) <sub>3</sub>	3-dH	22	560	Chromophore; nonlinear optical material (χ <sup>2</sup> )
<b>6</b>	(H <sub>3</sub> C <sub>2</sub> O) <sub>3</sub> SiCH <sub>2</sub> CH <sub>2</sub> Si(OC <sub>2</sub> H <sub>5</sub> ) <sub>3</sub>	cubic	40	430	low k dielectrics

<sup>\*</sup>Pore size and surface area were determined from N<sub>2</sub> sorption isotherms obtained at -196°C, using a surface acoustic wave (SAW) technique. Mass change due to nitrogen sorption was monitored (~80 pg.cm<sup>-2</sup> sensitivity) as a function of nitrogen relative pressure. Pore size and surface area were determined from the isotherms using the BET equation and the BJH algorithm, respectively.

<sup>§</sup> Functional groups are retained through selective surfactant removal during heat treatment in nitrogen. TGA and DTA were used to establish the appropriate temperature window enabling complete surfactant removal without silane decomposition

<sup>†</sup> Additives investigated include rhodamine-B, cytochrome c (from Fluka), oil blue N, disperse yellow 3 (from Aldrich), silver ions and silver nanoparticles.

<sup>#</sup> **4** was prepared by a conjugation reaction between a thin film mesophase containing **3** and the dye molecule (5,6-carboxyfluorecein, succinimidyl ester (5,6-FAM, SE) from Molecular Probes).

## RESULTS AND DISCUSSION

### Scheme 1

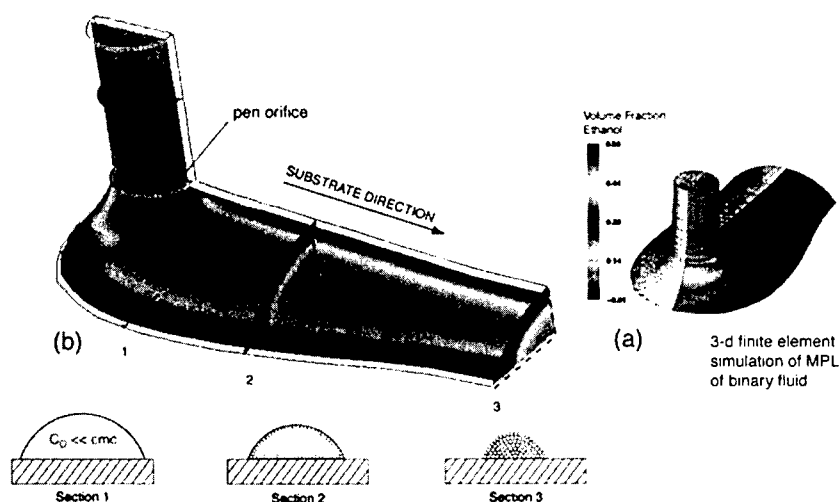


Figure 1. Scheme 1: micro-pen lithography *MPL* of a surfactant-templated mesophase.

Scheme 1 (Figure 1) schematically illustrates direct writing of a mesoscopically ordered nanostructure, using micro-pen lithography *MPL*.<sup>[9]</sup> (a) shows the simulation of 3-D, binary fluid pattern dispensed on a flat substrate with substrate speed = 2.54 cm/s and fluid injection rate (inlet velocity) = 3.985 cm/s. Color contours represent evaporation-induced, 3-D gradients in alcohol-composition. Fluid was modeled as 54 volume % ethanol and 46 volume % non-volatile phase with Reynolds number = 1.25 and  $Ca = 0.000833$ . An ad hoc value of  $45^\circ$  was chosen for the static contact angle. Note that this angle persists at all points on the dynamic contact line because of the dominance of surface tension at this low value of  $Ca$ . (b) shows the schematic process: the initially homogeneous sol metered on to the moving substrate experiences preferential evaporation of alcohol creating a complex 3-D (longitudinal and radial) gradient in the concentrations of water and non-volatile surfactant and silicate species. Progressive enrichment of silica and surfactant induces micelle formation and subsequent growth of silica/surfactant mesophases inward from solid-liquid and liquid-vapor interfaces as recently demonstrated for thin films<sup>[17]</sup> and aerosols<sup>[18]</sup>. The numerical method utilized for (a) and (b) consisted of a 3D finite element discretization of the Navier Stokes equations augmented with a three dimensional boundary-fitted mesh motion algorithm to track the free surface<sup>[19, 20]</sup>. Special relations at the 3D dynamic wetting line were also applied. For *ink* we use homogeneous solutions of TEOS, ethanol, water, surfactant, acid, and (optionally) organosilanes and other organic ingredients (see Table 1). These solutions are prepared with an initial surfactant concentration  $c_0$  less than the critical surfactant concentration  $c_{mc}$  and an acid concentration designed to minimize the siloxane condensation rate, thereby enabling facile silica/surfactant self-assembly within the brief time span of the writing operation. As the ink is metered onto the

surface, preferential ethanol evaporation causes enrichment of water, surfactant, and silica, establishing a 3-D (longitudinal and radial) gradient in their respective concentrations (Figure 1). Where *cmc* is exceeded, cooperative silica/surfactant self-assembly creates micelles. Further evaporation, of predominantly water, promotes the continuous self-organization of micelles into silica/surfactant liquid crystalline mesophases. As demonstrated previously for *EISA* of films<sup>[17]</sup> and aerosols<sup>[18]</sup>, liquid crystalline domains are nucleated by incipient surfactant monolayers formed at solid-liquid<sup>[21, 22]</sup> and liquid-vapor interfaces<sup>[23]</sup> (at  $c < cmc$ ) and grow inward as evaporation proceeds.

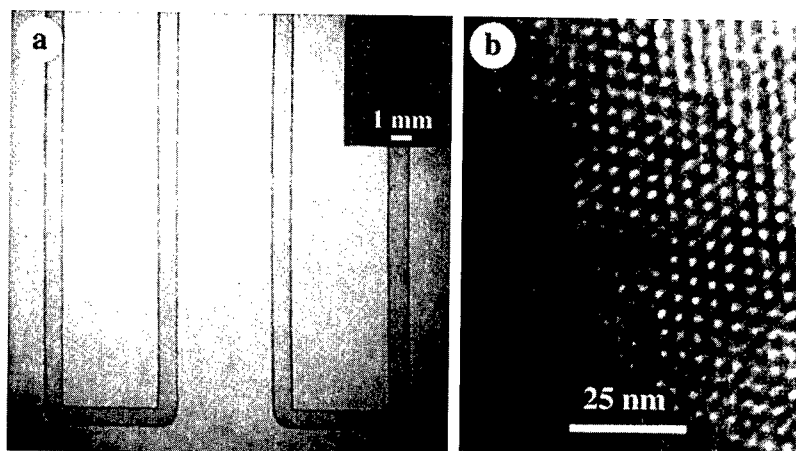


Figure 2. Meandering patterned mesophase created by *MPL*. a) Optical micrograph of patterned rhodamine-B containing silica mesophase deposited on an oxidized [100]-oriented silicon substrate at a speed of 2.54 cm/s. Inset is a fluorescence image of rhodamine-B emission acquired through a 610-nm band pass filter, demonstrating retention of rhodamine-B functionality. b) Representative TEM micrograph of a fragment of the patterned rhodamine-B containing film corresponding to a [110]-oriented cubic mesophase with lattice constant  $a = 10.3$ -nm. The sol was prepared by adding 0.01wt% rhodamine-B to a silica/4wt% Brij-56 sol. The TEOS:EtOH:water:HCl:Brij-56:rhodamine-B molar ratio = 1:22:5.0:0.004:0.075:2.6 $\times 10^{-5}$ .

Figure 2a shows a meandering macroscopic pattern formed in several seconds by *MPL* of a rhodamine B-containing solution on a hydrophilic surface (hydroxylated native oxide of <100> silicon). The inset in Figure 2a shows the corresponding fluorescence image of several adjacent stripes, and the TEM micrograph (Figure 2c) reveals the ordered pore structure characteristic of a cubic thin film mesophase. The *MPL* line width can vary from micrometers to millimeters. It depends on such factors as pen dimension<sup>[8]</sup>, wetting characteristics, evaporation rate, capillary number ( $Ca = \text{ink viscosity} \times \text{substrate speed} / \text{surface tension}$ ) and ratio of the rates of ink supply and withdrawal (inlet velocity/substrate velocity). The effect of wetting has been demonstrated by performing *MPL* on substrates pre-patterned with hydrophobic, hydrophilic or mixed SAMs. Generally, line widths are reduced by increasing the contact angle and by reducing the inlet/substrate velocity ratio. The conditions providing the minimum stable line width are bounded by a regime of capillary instability – we anticipate that this instability could be exploited to create periodic arrays of dots.

## Scheme 2

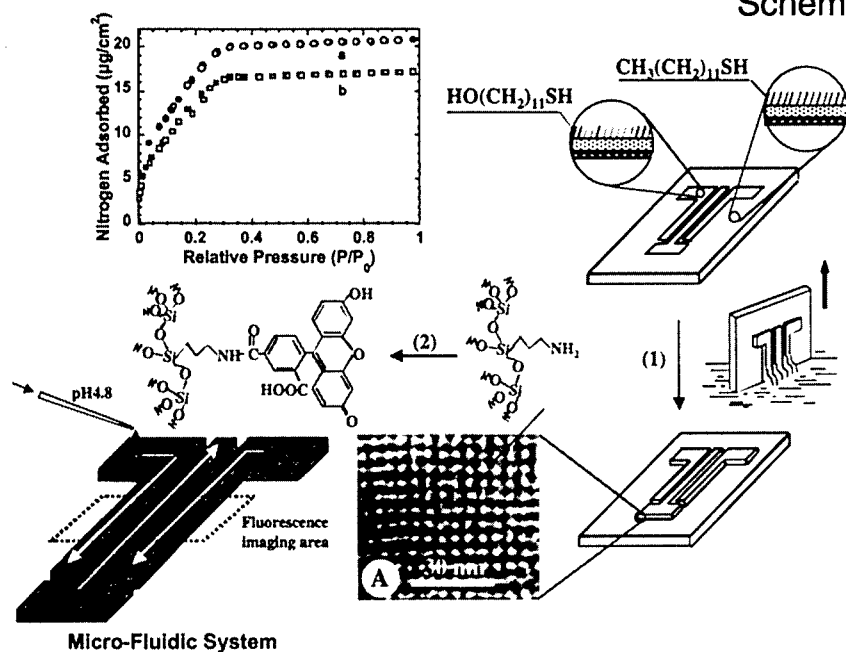


Figure 3. Scheme 2: Patterned functional mesostructure formed by selective de-wetting. The sol was prepared by adding aminopropyltrimethoxysilane ( $\text{NH}_2(\text{CH}_2)_3\text{Si}(\text{OCH}_3)_3$ , APS) to a silica/4wt% Brij-56 sol, resulting in a final molar ratio TEOS:APS:EtOH:water:HCl:Brij-56 = 1:0.8:22:5.0:0.011:0.075.

The advantages of *MPL* are that we can use computer-aided design to define any arbitrary 2-D pattern and that we can use any desired combination of surfactant and functional silane as ink to selectively define different functionalities at different locations. However *MPL* is a serial technique. In situations where it is desirable to create an entire pattern with the same functionality, it would be preferable to employ a parallel technique in which the deposition process occurred simultaneously in multiple locations. Scheme 2 (Figure 3) illustrates a rapid, parallel patterning procedure, dip-coating on patterned SAMs. This procedure uses micro-contact printing<sup>[24]</sup> or electrochemical patterning<sup>[16]</sup> of hydroxyl- and methyl-terminated SAMs to define hydrophilic and hydrophobic patterns on the substrate surface. Then using homogenous solutions identical to those employed for *MPL*, preferential ethanol evaporation during dip-coating enriches the depositing film in water, causing *selective de-wetting* of the hydrophobic regions. In this fashion, lines, arrays of dots, or other arbitrary shapes can be deposited on hydrophilic patterns in seconds. As described for *MPL*, further evaporation accompanying the dip-coating operation induces self-assembly of silica/surfactant mesophases. Using micro-contact printing or electrochemical desorption techniques, substrates are prepared with patterns of hydrophilic, hydroxyl-terminated SAMs and hydrophobic methyl-terminated SAMs. Preferential ethanol evaporation during dip-coating (1), causes water enrichment and selective de-wetting of the hydrophobic SAMs. Correspondingly film deposition occurs exclusively on the patterned hydrophilic SAMs. Selective de-wetting followed by calcination results in a patterned, amine-functionalized, cubic mesoporous film as is evident from the plan-view TEM

micrograph (Inset A), showing a [100]-oriented cubic mesophase with  $a = 10.3$ -nm and nitrogen adsorption-desorption isotherm (Inset B, curve a) acquired for the thin film specimen using a surface acoustic wave<sup>[25]</sup> (SAW) technique. The dye conjugation reaction (2) was conducted by immersion in a 0.00002mM solution of 5,6-FAM, SE (Table 1) prepared in dimethylsulfoxide (DMSO) followed by exhaustive, successive washing in DMSO, ethanol, and water. The SAW-based nitrogen adsorption-desorption isotherm of the dye-conjugated mesoporous film is shown in Inset B, curve b, confirming its pore accessibility. BET analyses of the sorption isotherms indicate that the dye conjugation reaction reduces the surface area from 750 to 545 m<sup>2</sup>/g and the hydraulic radius from 2.2 to 2.1-nm, but pore accessibility is completely retained as evident from combined TEM, SAW, and fluorescent-imaging results (Figure 4a).

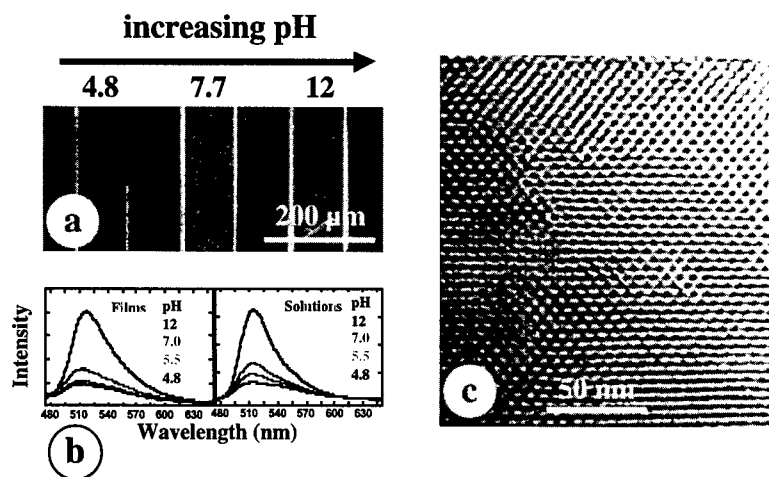
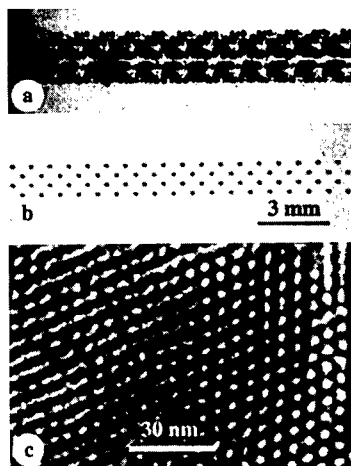


Figure 4. Patterned pH-sensitive fluidic system. a) Fluorescence image of three adjacent 5,6-FAM, SE-conjugated pore channel networks after introduction of aqueous solutions prepared at pH 4.8, 7.7, or 12.0. Patterned dye-conjugated thin film mesophases were prepared according to Scheme 2 (Figure 3). Aqueous solutions of varying pH were introduced on the terminal pads (Figure 3) and transported into the imaging cell by capillary flow. Image was acquired using a Nikon Diaphot 300 inverted microscope and 520-nm band pass filter. b) Fluorescence spectra of 5,6-FAM, SE-conjugated mesoporous films upon exposure to aqueous solutions of pH 4.8, 7.7, and 12.0. Shown for comparison are fluorescence spectra of 0.1 micromolar solutions of 5,6-FAM, SE prepared in aqueous solutions of pH 4.8, 7.7, and 12.0. The similarity of the two sets of spectra confirms the maintenance of dye functionality upon conjugation within the mesoporous channel system. c) Cross-sectional TEM micrograph of the patterned, dye-conjugated thin film mesophase, providing evidence of the 3-D pore channel network.

The patterned dip-coating procedure may be conducted with organic dyes or functional silanes (see Table 1). Scheme 2 illustrates patterned deposition of a propyl-amine derivatized cubic mesophase followed by a conjugation reaction with a pH-sensitive dye, 5,6-carboxyfluorescein, succinimidyl ester (5,6-FAM, SE). The uniform continuous porosity of the amine-derivatized and dye-conjugated films is confirmed by TEM and surface acoustic wave (SAW)-based nitrogen sorption isotherms<sup>[25]</sup> of the corresponding films deposited on SAW



Figure 5. Patterned dot arrays created by ink-jet printing. a) Optical micrograph of dot array created by ink jet printing of standard ink (from Hewlett-Packard Co., San Diego, CA) on a non-adsorbent surface. b) Optical micrograph of an array of hydrophobic, mesoporous silica dots created by evaporation-induced silica/surfactant self-assembly during *IJP* on an oxidized [100]-oriented silicon substrate followed by calcination. c) Representative TEM micrograph of a dot fragment prepared as in (b). The sol was prepared with molar ratio TEOS:TFTS(1):EtOH:water:HCl:Brij-56 = 1:0.05:22.0:5.0:0.004:0.075. The dot pattern used in a) and b) was designed using Microsoft PowerPoint 98 software. The printing rate was approximately 80 dots/s and printer resolution 300 dots/inch. The resolution achieved compared to standard ink and our ability to selectively functionalize the ink suggest applications in display technologies.



substrates (Figure 4). The reduction in film porosity after dye conjugation reflects the volume occupied by the attached dye moieties. The patterned, functional array can be used to monitor the pH of fluids introduced at arbitrary locations and transported by capillary flow into the imaging cell. Figure 4a shows the fluorescence image of an array contacted with three different aqueous solutions prepared at pH 4.8, 7.7, and 12.0. Figure 4b shows the corresponding emission spectra and provides a comparison with solution data. In combination, the fluorescence image (Fig. 4a) and plan-view and cross-sectional TEM micrographs (Figures 3 and 4c) of the dye-conjugated film demonstrate the uniformity of macro- and mesoscale features achievable by this evaporation-induced, de-wetting and self-assembly route. In comparison, films formed by nucleation and growth of thin film mesophases on patterned SAMs<sup>[1]</sup> are observed to have non-homogeneous, globular morphologies.

Finally we can create patterned nanostructures by combining *EISA* with a variety of aerosol processing schemes. For example, Figure 5 compares an optical micrograph of a macroscopic array of spots formed by ink jet printing *IJP*<sup>[10, 11]</sup> on a silicon wafer with *IJP* of standard ink on a non-adsorbent surface. The *IJP* process dispenses the *ink* (prepared as for *MPL*) as monosized, spherical aerosol droplets. Upon impactation the droplets adopt a new shape that balances surface and interfacial energies. Accompanying evaporation creates within each droplet a gradient in surfactant concentration that drives radially-directed silica/surfactant self-assembly inward from the liquid-vapor interface<sup>[18]</sup>. The inset in Figure 5 shows a representative TEM micrograph of a hydrophobic, fluoroalkylated silica mesophase formed by *IJP*. The resolution achieved compared to standard ink and our ability to selectively functionalize the ink suggest applications in display technologies. Continuous, nanostructured lines are created by coalescence of overlapping droplets. Patterns may also be created by aerosol deposition through a mask or by aerosol deposition on patterned hydrophilic/hydrophobic surfaces (H. Fan, Y. Lu, and A. Stump, unpublished).

## CONCLUSIONS

We have combined evaporation-induced (silica/surfactant) self-assembly *EISA* with rapid prototyping techniques like pen lithography, ink-jet printing, and dip-coating on micro-contact

printed substrates to form hierarchically organized structures in seconds. In addition, by co-condensation of tetrafunctional silanes ( $\text{Si}(\text{OR})_4$ ) with tri-functional organosilanes ( $(\text{RO})_3\text{SiR}'$ ) or by inclusion of organic additives, we have selectively derivatized the silica framework with functional R' ligands or molecules. The resulting materials exhibit form and function on multiple length scales and multiple locations.

#### ACKNOWLEDGEMENTS:

This work was supported by the US Department of Energy Basic Energy Sciences Program, the Sandia National Laboratories Laboratory-Directed Research and Development Program, and the Defense Advanced Research Projects Agency Bio-Weapons Defense Program. The authors also thank Mr. Pin Yang, Mr. Scott Reed for technical assistance with micro-pen lithography, and Dr. Tom Baer and Dr. Randy Schunk for 3D simulation of micropen. TEM investigations were performed in the Department of Earth and Planetary Sciences at the University of New Mexico. Sandia is a multiprogram laboratory operated by Sandia Corporation, a Lockheed-Martin Company, for the U.S. DOE under Contract DE-AC04-94AL85000.

#### References

- [1] H. Yang, N. Coombs, G. A. Ozin, *Adv. Mater.* **1997**, *9*, 811.
- [2] C. Kresge, M. Leonowicz, W. Roth, C. Vartuli, J. Beck, *Nature* **1992**, *359*, 710.
- [3] Y. Xia, G. M. Whitesides, *Angew. Chem. Int. Ed.* **1998**, *37*, 550.
- [4] M. Trau, N. Uao, E. Lim, Y. Xia, G. M. Whitesides, I. A. Aksay, *Nature* **1997**, *390*, 674.
- [5] P. Yang, T. Deng, D. Zhao, P. Feng, D. Pine, B. F. Chmelka, G. M. Whitesides, G. D. Stucky, *Science* **1998**, *282*, 2244.
- [6] M. Antonietti, B. Berton, C. Goltner, H. P. Hentze, *Adv. Mater.* **1998**, *10*, 154.
- [7] c. J. Brinker, Y. Lu, A. Sellinger, H. Fan, *Adv. Mater.* **1999**, *11*, 579.
- [8] R. D. Piner, J. Zhu, F. Xu, S. Hong, C. A. Mirkin, *Science* **1999**, *283*, 661.
- [9] P. Yang, D. Dimos, M. A. Rodriguez, R. F. Huang, S. Dai, D. Wilcox, *Mat. Res. Soc. Symp. Proc.* **1999**, *542*, 159.
- [10] S.-C. Chang, J. Liu, J. Bharathan, Y. Yang, J. Onohara, J. Kido, *Adv. Mater.* **1999**, *11*, 734.
- [11] D. Pede, G. Serra, D. De Rossi, *Mat. Sci. and Eng.* **1998**, *C5*, 289.
- [12] S. L. Burkett, S. D. Sims, S. Mann, *Chem. Commun.* **1996**, 1367.
- [13] C. E. Fowler, S. L. Burkett, S. Mann, *Chem. Commun.* **1997**, 1769.
- [14] M. H. Lim, C. F. Blanford, A. Stein, *J. Am. Chem. Soc.* **1997**, *119*, 4090.
- [15] C. D. Bain, E. B. Troughton, Y.-T. Tao, J. Ewall, G. M. Whitesides, R. G. Nuzzo, *J. Am. Chem. Soc.* **1989**, *111*, 321.
- [16] L. M. Tender, W. R.L., H. Fan, G. P. Lopez, *Langmuir* **1996**, *12*, 5515.
- [17] Y. Lu, R. Ganguli, C. A. Drewien, M. T. Anderson, C. J. Brinker, W. L. Gong, Y. X. Guo, H. Soyez, B. Dunn, M. H. Huang, J. I. Zink, *Nature* **1997**, *389*, 364.
- [18] Y. Lu, H. Fan, A. Stump, T. L. Ward, T. Reiker, C. J. Brinker, *Nature* **1999**, *398*, 223.
- [19] R. A. Cairncross, P. R. Schunk, T. A. Baer, R. R. Rao, P. A. Sackinger, *Int. J. Numer. Meth. Fluids to appear 2000*.
- [20] T. A. Baer, R. A. Cairncross, P. r. Schunk, R. R. Rao, P. A. Sackinger, *Int. J. Numer. Meth. Fluids to appear 2000*.
- [21] I. A. Aksay, *Science* **1996**, *273*, 892.
- [22] H. Yang, A. Kuperman, N. Coombs, S. Mamiche-Afara, G. A. Ozin, *Nature* **1996**, *379*, 703.
- [23] H. Yang, N. Coombs, I. Sokolov, G. A. Ozin, *Nature* **1996**, *381*, 589.
- [24] J. L. Wilbur, A. Kumar, H. A. Biebuyck, E. Kim, G. M. Whitesides, *Nanotechnology* **1996**, *7*, 452.

- 
- [25] G. C. Frye, A. J. Ricco, S. J. Martin, C. J. Brinker, in *Better Ceramics Through Chemistry III, Vol. 121* (Eds.: C. J. Brinker, D. E. Clark, D. R. Ulrich), Mat. Res. Soc., Reno, Nevada, **1988**, pp. 349.

## ELECTROSTATIC PRINTING, A VERSATILE MANUFACTURING PROCESS FOR THE ELECTRONICS INDUSTRIES

Robert H. Detig, Ph.D.  
Electrox Corporation, Denville, NJ 07834

### ABSTRACT

Functional materials configured as liquid toners are printed on a variety of substrates for various manufacturing processes. The materials include metal toners, resistor toners, high k dielectric toners, phosphors and glass. The substrates printed upon include glass, bare and coated metal, polymeric films and even paper. A fixed configuration electrostatic printing plate is used in most manufacturing applications though traditional photo receptor plates can be used if electronic addressability is desired.

Applications of electrostatic printing for electronic packaging products (printed wiring boards and flex circuits) and of passive electronic components themselves will be shown. Results with a pure silver toner printed on both glass and paper will be reported. Examples of passive electronic components like resistors, capacitors, and even inductors that have been electrostatically printed with liquid toners will be shown. Possible applications of toners to the manufacture of flat panel displays will be discussed.

### EXPERIMENT

There are three key elements to the electrostatic printing process:

1. The Electrox electrostatic plate<sup>1,2</sup>
2. Functional materials configured as liquid toners
3. Non-contact or gap transfer in which toner particles are transferred by an electric field across a gap of the order of 50 to 150 $\mu$  to the receiving surface<sup>3</sup>

The steps of the process are best illustrated in the following figures. Figure 1 shows the plate-making step. A photopolymer layer is coated on an electrically grounded substrate. The substrate can be metal, metallized polyester or polyimide film, or even glass made conductive with an indium tin oxide coating (ITO). The photopolymers typically vary in thickness from 10 $\mu$  to 50 $\mu$ . The photopolymer is exposed to UV radiation in the 300 to 400nm region which causes exposed areas to undergo a chemical change. This raises the electrical resistivity of these regions significantly so that they can store electrostatic charge for a useful period of time. The plate-making step is now complete; there is no chemical or aqueous processing of the plate.

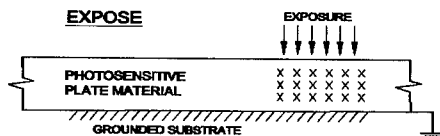


Figure 1. Plate Making

The plate is sensitized by corona charging it. The resulting surface potential for a typical 37 $\mu$  thick plate is from 500 to 1000 volts. After a short period of time the unexposed regions of the plate self discharge due to their relatively low electrical resistivity. We now have a

traditional latent electrostatic image. The latent image is processed by development with an electrophoretic liquid toner

Figure 2 shows the transfer step wherein the toner is transferred across a finite mechanical gap to a receiving glass plate by an electrical field created by the electric field plate

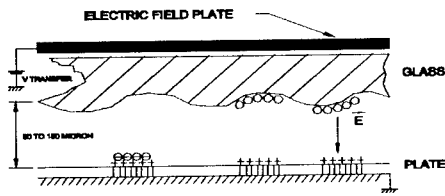


Figure 2: Toner Transfer Across a Gap

on the other side of the glass driven to a suitable potential. An alternate scheme not shown in Figure 3 is to corona charge the other side of the glass with a charge of polarity opposite that of the toner. Figure 3 shows a highly irregular surface, not an exaggeration. This is a particular advantage of electrostatic printing over other printing or deposition techniques. The toner travels across the gap following the parallel electric field lines and it does not disperse as a function of distance between glass and plate. Therefore high resolution images, true to their design, can be deposited on the glass substrate, even if it has imperfections or a relief structure already on it. We have also printed on metal plates, polymeric films and paper. An example of printing on steeply relieved metal surfaces is the printing of images on U.S. coins.

**The Plate**

While a photo addressable drum or plate could be used. Electroch chose an electrostatic plate for the following reasons:

1. The electrostatic plate offers a superior latent image over that of the photo receptor plate.
2. Small features like 10 microns or even smaller are possible.
3. The electrostatic plate offers reasonable process speeds of 250 mm/sec for high through put.

**The Toner**

In this area, our toner technology, is far removed from traditional liquid electrographic toners. The following table shows these differences

	Materials	Particle
Metals	Aluminum	30 micron
	Silver	0.2 micron
Glasses, Ceramics	Glass frits	0.5 to 7 micron
	Phosphors	0.6 to 80 microns
Catalysts	Palladium	0.33 micron
	Tin	0.8 microns
Composites	Conductor-Silver filled resin	
	Resistors-Carbon filled resin	
	Capacitor Barium Titanate filled resin	

---

### Capabilities of Functional liquid Toners:

High densities, up to  $10 \text{ gm/cm}^3$

Board range of Electrical resistivity

Silver  $1.63 \times 10^{-6} \text{ ohm cm}$

Glass  $10^{+15}$

Board range of particle sizes 0.05 micron to 100 micron

Broad range of mechanical properties, soft resins to very hard materials

Resinless or very little unwanted materials

Virtually any material not swelled nor dissolved by the Isopar diluent liquid can be made into a liquid toner. There are few "process burden" materials required to make the liquid toner. Our solid silver particle toner is 96% silver with no resin to interfere with electrical conductivity.

### Non-contact or Gap Transfer

One of the principle advantages of liquid toner systems is their ability to be transferred across a significant mechanical gap between image plate and receiving plate (3). This is very important in some manufacturing applications where the receiving surface is either metal or irregular (like glass); or where high overlay accuracy is needed thereby eliminating elastometric roller transfer. We will show samples of US coins printed with toners where the edge of the coins were spaced  $125^\circ \text{ C}$  above the printing plate. The image show fine features with good edge acuity.

### Fusing or Sintering

Necessarily the toner image is particulate and must be fused to result in a useful structure. In some cases, like metal, heating to near their melting point is not allowable. A significant enhancement of toner technology is the silver Parmod Toner of Parelec LLC of Rocky Hill, NJ. Here we have a solid silver particle coated with a MOD coating (metallic organo decomposition product). Which when heated to a modest temperature ( $230^\circ \text{C}$ -2min) reduces itself to pure silver thereby chemically sintering the Ag particles together.

Printed on paper and processed at  $230^\circ \text{C}$  for 2 min yields a bulk resistivity of about 5 micron ohm. cm, 10 to 20 times better than the best silver filled resins. Printed on glass with processing at 400 to  $430^\circ \text{C}$  range gives bulk resistivity values close to that of pure silver.

### RESULTS

Recently we have found that certain thin coatings of resins on PET will chemically enhance the MOD decomposition process allowing it to function in the  $125^\circ \text{C}$  to  $150^\circ \text{C}$  range, compatible with PET and PEN films and useful for many commercially attractive applications.

At these processing conditions we get bulk resistivities of 15 micro ohm cm, 3 to 6 times better than the best composite inks and useful, as is, for many applications where low cost of production is essential.

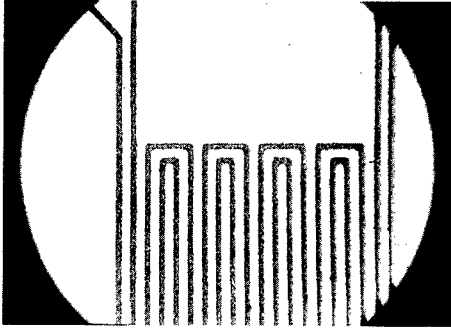


Figure 3. Silver Toner Printed on Soda Lime Glass

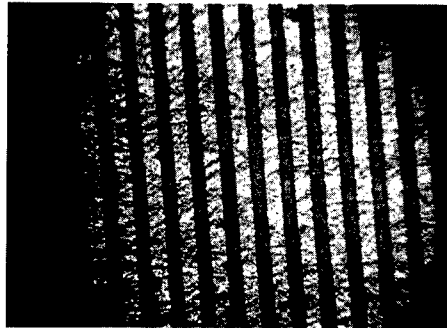


Figure 4. Silver Toner Printed on Paper and Sintered at 230°C

Figure 3 show the silver toner printed on glass. The conductor patterns are 40 microns wide with 60 micron spaces; the metal is 1 to 2 microns thick. Figure 4 shows that same silver toner printed on paper with thermal processing at 230°C-2mins. Even though it is a smooth coated sheet of food packaging paper, the discrete fibers shown in the photomicrograph are of the order of 12 microns. Again the silver patterns are about 1 micron thick

Figure 5 shows the silver toner printed on coated 75 micron thick PET, heat processed at 125°C for 30 min. Bulk resistivity of the silver material with this low temperature processing is 15 micro ohm cm. Adhesion of the silver metal traces to the coated PET is excellent.

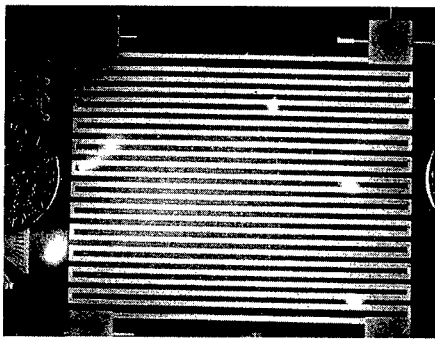


Figure 5. Silver Toner Printed on Special Resin Coated PET, Sintered at 125°C

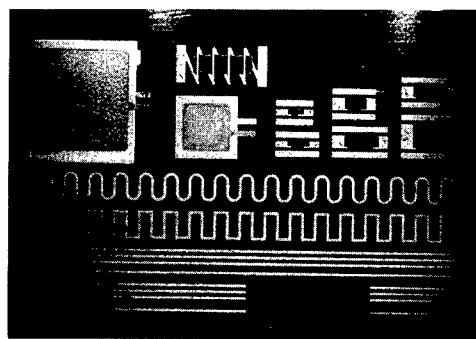


Figure 6. A Nest of Electronic Components Printed on Glass

Figure 6 shows a nest of electronic components printed on glass. On the bottom are 200 micron wide silver conductor patterns. Upper left shows a 9mm x 9mm and a 5mm x 5mm capacitor. Upper center shows a 5 turn inductor and the upper right shows six resistors.

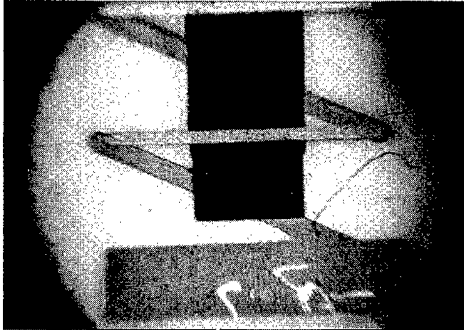


Figure 7. A Detail of the Inductor, Four layer part

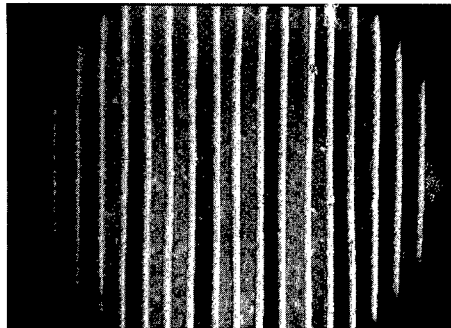


Figure 8. Phosphor Toner Printed at the Bottom of Plasma Panel Trenches

Figure 7 shows a detail of the inductor. This is a four layer part. The bottom terminal and the silver lines at 30 degrees comprise the first layer; then two layers of ferrite toner and finally the fourth layer which is the silver metal printed horizontally. This five turn coil has a dc resistance of 4 ohms.

In another venue figure 8 shows a phosphor toner printed in the trenches of an ac plasma display back plate. The dark vertical line are the barrier ribs, approx 120 microns high and 40 micron across. The width of the trench is 120 microns. Every third trench is one of the primary colors; red, green, and blue.

## CONCLUSIONS

We have assembled the elements of a generic manufacturing technology. A wide variety of materials can be formulated into liquid toners. They can be imaged by a suitable plate or drum then transferred in a non-contact mode to a wide range of substrates. In this program we have primarily printed on glass plates, usually soda lime class 2.25 mm thick. But printing on copper, brass, aluminum, stainless steel, and US coins is easily done.

Electrostatic printing of functional materials configured as liquid toners is a versatile manufacturing process. A solid, resinless Ag toner allows one to print pure metal in an additive process. Furthermore it can be printed on low temperature substrates like PET films and paper as well as glass. With resistive barium and ferrite toners one can print resistors, capacitors and inductors. Finally phosphors were printed in 120 micron deep trenches for ac plasma display manufacture.

## REFERENCES

1. J Reisenfeld, US Patent No 4,732,831 (22 March 1988)
2. R Detig and D Bujese, US Patent No 4,859,557 (22 August 1989) and 5,011,758 (30 April 1991)
3. D Bujese, US Patent No 4,786,576 (22 November 1988) and 4,879,184 (7 November 1989)



---

## **Composites and Ceramics**

---

## MODELING AND OPTIMIZATION OF NOVEL ACTUATORS PRODUCED BY SOLID FREEFORM FABRICATION

B.A. CHEESEMAN\*, X.P. RUAN\*\*, A. SAFARI\*\*\*, S.C. DANFORTH\*\*\* and T.W. CHOU\*

\*University of Delaware, Department of Mechanical Engineering, Newark, DE 19716

\*\*University of Delaware, Department of Mechanical Engineering, Newark, DE 19716

(currently with EASi Engineering, 1551 E. Lincoln Avenue, Madison Heights, MI, 48071

\*\*\*Rutgers University, Department of Ceramic Science and Engineering and Center for Ceramic Research, Piscataway NJ 08855

### ABSTRACT

The ability of Solid Freeform Fabrication (SFF) to produce complex piezoceramic architectures has enabled the development of novel designs for PZT actuators. Recently, it has been shown that through the intelligent application of actuator geometry, poling direction, piezoelectric material, and electric field direction, the force and displacement output of a piezoelectric actuator could be optimized. The current investigation examines several piezoceramic actuator geometries, including dome, spiral and a telescoping shaped actuators. Using finite element analysis (FEA), parametric studies are performed to identify some key issues in the optimization of actuator performance. Results of the dome study indicate that an actuator having a tangentially alternating poling direction and applied electric field exhibits a much larger displacement when compared to dome actuators having either a through-the-thickness or tangential poling direction. Analysis of spiral actuators indicates that the spiral geometry results in pronounced displacement amplification when compared to the displacement of an equivalent length piezoelectric strip. In summary, some remarks will be made on the optimal use of piezoelectric material properties and actuator geometry in actuator design.

### INTRODUCTION

Piezoelectric materials have the ability to develop an electric charge when stressed or deform when exposed to an electric potential. Discovered in single crystals by Pierre and Jacques Curie in 1880 [1], it was the development of the piezoelectric effect in polycrystalline ceramics during World War II that has seen piezoelectric materials progress from a laboratory phenomenon to a multi-billion dollar a year industry. Piezoelectric ceramics are used in devices such as microphones, loud speakers, ink jet printers, medical imaging equipment and recently, in 'smart' skis and bats [2]. Haertling [3] notes that while the strain of the piezoelectric ceramic itself is appealing for small ( $<10\mu\text{m}$ ), precise mechanical movements, large displacement actuators ( $>1000\mu\text{m}$ ) are needed for applications such as linear motors and switches. Recent efforts have focused on novel actuator designs for improved displacement performance [3-7]. Actuator performance is dependent on three complex factors, the properties of the ceramic, the design of the actuator and its drive technique [8]. The present investigation will focus on actuator design. With the development of Solid Freeform Fabrication techniques, such as the Fused Deposition of Ceramics (FDC) process [9], that enable the ready fabrication of complex shapes, the current investigation will study the effect of actuator geometry, poling direction and applied potential direction on the displacement performance of several novel piezoelectric actuators having either a dome, spiral or telescoping shape.

### BACKGROUND

The analytical theory of piezoelectricity has been developed since the early 1900s [1]. In linear piezoelectricity, the linear elastic equations are coupled with the charge equation of

electrostatics. For an orthotropic piezoelectric material, the constitutive relations, expressed in terms of stress, are given as [10]

$$S_{ij} = s_{ijkl} \sigma_{kl} + d_{kij} E_k \quad (1)$$

$$D_i = d_{ikl} \sigma_{kl} + \epsilon_{ik} E_k \quad (2)$$

where  $\sigma_{kl}$  and  $S_{ij}$  are the components of the stress and strain tensor, respectively,  $E_k$  the components of the electric field vector,  $D_i$  the components of the electric displacement vector,  $s_{ijkl}$  the components of the elastic compliance matrix,  $d_{kij}$  the components of the piezoelectric matrix, and  $\epsilon_{ik}$  the components of the dielectric permittivity matrix. For piezoelectric and permittivity coefficients,  $d_{ikl}$  and  $\epsilon_{ik}$ , respectively, the first subscript 'i' denotes the direction of the electric field vector. Properties for the piezoelectric material used in this study, PZT-5H, are given in Table 1. It should be noted that the properties are given with  $x_3$  direction as its poling direction.

**Table 1: Elastic, piezoelectric and dielectric constants of PZT-5H [11].**

Elastic Compliance ( $10^{-12} \text{ m}^2/\text{N}$ )	$s_{11}$ 16.5	$s_{33}$ 20.7	$s_{12}$ -4.78	$s_{13}$ -8.45	$s_{44}$ 43.5	$s_{66}$ 42.6
Piezoelectric Constant ( $10^{-12} \text{ C/N}$ )	$d_{15}$ 741	$d_{24}$ 741	$d_{31}$ -274	$d_{32}$ -274	$d_{33}$ 593	
Dielectric Permittivity ( $10^{-9} \text{ F/m}$ )	$\epsilon_{11}$ 15.05	$\epsilon_{22}$ 15.05	$\epsilon_{33}$ 13.01			

Due to the complexity of the constitutive relations and material properties, analysis of piezoelectric materials is difficult. Analytical solutions are limited to a few cases having simple geometries and boundary conditions. As a result, computational methods such as finite element analysis (FEA) have proven a valuable tool in the study of piezoelectric devices. By discretizing the domain into a number of elements and solving the governing equations over each subdomain, FEA is able to readily analyze complex geometries and boundary conditions. For the current investigation, the commercial FEA software ABAQUS was utilized, while the software PATRAN was used as a pre-processor to develop the geometries and finite element meshes.

## ACTUATOR INVESTIGATIONS

There exist several different types of actuators whose design serves to amplify the displacement of piezoelectric elements. Recently reviewed by Haertling [12], these include composite flextensional and bender actuators. Composite flextensional actuators consist of a piezoceramic element bonded to a metallic or polymer shell structure that is used to amplify the displacement of the piezoceramic. Bender actuators usually consist of two layers, one being a piezoceramic, the second being either a nonpiezoelectric substrate (unimorph bender) or a second piezoelectric (bimorph bender). Bender operators act on the differences in longitudinal expansion between the two layers, which results in bending. Both the composite flextensional

and bender actuators utilize piezoceramic elements that have a basic shape such as a plate or disk. Recent investigations [4, 13] have focused on amplifying actuator displacement by designing the geometry of the actuator to better utilize the anisotropy of the piezoelectric material. As in Table 1, Jiao and Zhang [13] note that the shear coefficient,  $d_{15}$ , is larger in magnitude than the in-plane terms,  $d_{31}$ ,  $d_{32}$  and  $d_{33}$  and designed a piezoelectric helical spring to be driven by the  $d_{15}$  term, which resulted in large displacements. Ruan et al. [4] have studied dome shaped actuators having an different poling configurations and have found that alternating the poling directions resulted in a substantial increase in the displacement performance of the actuator. Details of this investigation will be discussed in the following section along with recent results from studies investigating both spiral shaped and telescoping actuators.

### Dome Actuators

Dome shaped actuators have been successfully fabricated using the FDC process and investigated using FEA by Ruan et al. [4]. Figure 1(a-c) shows an axisymmetric representation of the dome and the three poling schemes investigated. Case A depicts the dome poled in the thickness direction, Case B illustrates the dome poled in the tangential direction and Case C shows a tangentially alternating poling scheme. Corresponding electrode configurations are also given and in all cases of the study an electric potential of  $E=1000V$  was applied. Figure 1(a) shows the geometric parameters of the dome actuator,  $t$ ,  $h$  and  $b$ , the thickness, depth and radius, respectively. For all cases of the current investigation, the radius was kept a constant  $b=17.5mm$ , while the depth was varied from 2.5mm to 12.5mm and the thickness from 1mm to 3mm. When varying the thickness, a constant height or 7.5mm was used and when changing the height, the thickness was held at 2mm. To study the displacement of the apex, point  $p$  in Figure 1(b), axisymmetric finite element models were developed having the boundary conditions shown in Figure 1(b): symmetry along  $r=0$  surface, while a sliding boundary condition was used along  $z=0$  surface. Results from the analysis are plotted in Figures 2(a-b), which show the calculated apex displacement as a function of height and thickness, respectively. As can be seen in Figure 2, tangentially alternating poling results in higher apex displacements than the other two cases. From the configuration of the tangentially alternating poling and the applied electric field, the  $d_{33}$  term causes an expansion of the actuator in the tangential direction, which drives the apex upward. The  $d_{31}$  terms in this case causes a contraction in the thickness direction, which brings the apex downward. This explains the trends shown in Figure 2. As the depth of the dome increases, the length of the tangential direction increases, which results in a larger influence of the  $d_{33}$  term. Therefore, the apex displaces more when the dome depth increases. As the thickness of the dome actuator increases, so does the influence of the  $d_{31}$  term, which results in a decrease of the apex displacement.

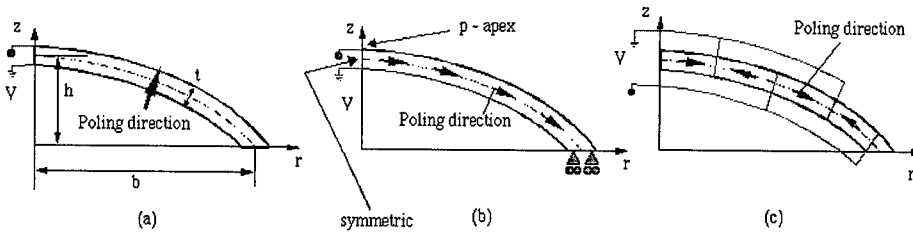


Figure 1: (a) Thickness poling direction, (b) tangential poling direction, (c) tangentially alternating poling direction.

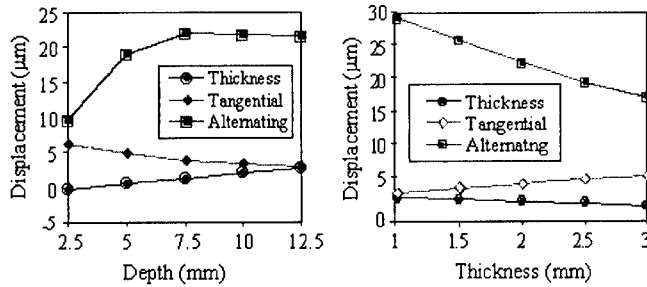


Figure 2: Displacement at the dome apex as a function of actuator (a) depth and (b) thickness.

### Spiral Actuators

Recent experimental investigations by Mohammadi et al. [14] have reported that the tangential displacement of spiral-shaped PZT actuators is several times higher than that of a straight PZT actuator with the same length and cross-section. Finite element analysis supports the experimental observations. Using a mesh consisting of ten biquadratic, linear piezoelectric elements through the thickness, actuators in the shape of Archimedes' spirals, consistent with those studied in [14], were analyzed. Shown in Figure 3(a), the spiral actuators had a wall thickness of 1.35mm, a wall spacing of 1.7mm, poled in the thickness direction and subjected to an electric field of 500 V. Figure 3(b) gives the tangential displacement of the spiral actuator as a function of the length of the spiral actuator. (Here, length refers to the equivalent straight line length of the actuator if it were unrolled).

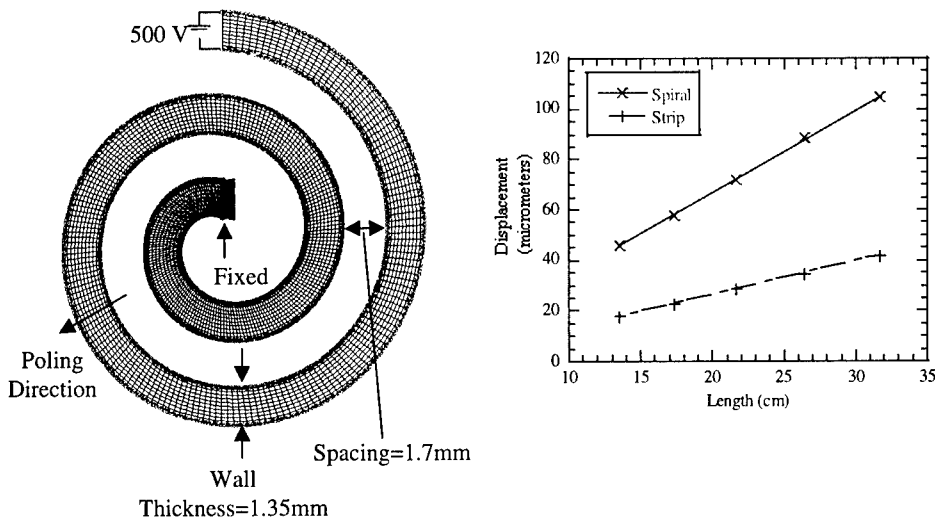


Figure 3: (a) Representative FE mesh on the spiral actuator, (b) Displacement as a function of length for the spiral actuator and a straight strip.

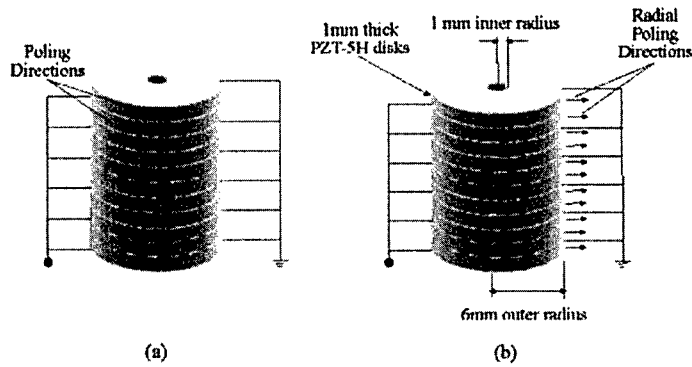


Figure 4: (a) Multi-layer actuator utilizing the  $d_{33}$  piezoelectric coefficient, (b) Multi-layer actuator utilizing the shear piezoelectric coefficient.

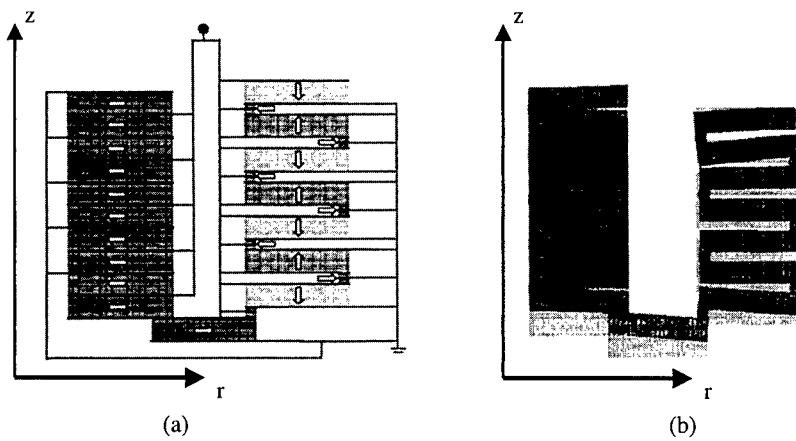


Figure 5: (a) Undeformed axisymmetric telescoping actuator (arrows indicate poling directions), (b) resulting deformed telescoping actuator (undeformed actuator is also shown as the light grey image).

Also, the displacement of a straight piezoelectric strip, poled in the thickness direction, under the same loading is given in Figure 3(b). From this figure, it can be seen that the spiral geometry results in an amplification of approximately 2.5 times the displacement of straight strip of equal length. Further investigations are ongoing to understand the mechanisms of displacement amplification for this geometry.

### Telescoping Actuators

As a final study, a telescoping actuator is investigated. Although the results are preliminary, they are reported to illustrate the concept of improving performance by the consideration of the material properties and actuator geometry. From Table 1, it can be seen that the shear terms,  $d_{15}$  and  $d_{24}$ , have the largest magnitude of the piezoelectric coefficients. In order

to utilize these terms, consider the case of a tube actuator. Figure 4(a-b) shows a multi-layer tube actuator. Figure 4(a) shows the poling and potential direction configured to utilize the  $d_{33}$  piezoelectric coefficient. Poled in the radial direction with the electric field applied in the axial direction, the multi-layer actuator in Figure 4(b) is constructed to allow the resulting shear deformation. By designing the actuator to utilize the shear deformation, the displacement is improved by 144% ( $4.5\mu\text{m}$  vs.  $11.0\mu\text{m}$ ). To illustrate the concept of a telescoping actuator, consider the axisymmetric finite element model shown in Figure 5(a). Again, utilizing the shear mode, an axisymmetric piezoelectric FEA was performed using an applied electric potential of 750V. The resulting deformed geometry is shown in Figure 5(b) had a maximum upward displacement of  $18.4\mu\text{m}$ .

## CONCLUSIONS

While most piezoelectric actuators utilize piezoelectric elements that have a typical shape, such as a disk or a plate, the results of the current investigation show that actuators exhibiting higher performance can be developed if the geometry, material property orientation and the poling and applied field direction are considered. With the advance of manufacturing techniques such as the FDC process that allow the ready fabrication of complex piezoceramic shapes, further studies of different atypical actuator geometries are warranted.

## ACKNOWLEDGEMENTS

This work was supported by the Office of Naval Research MURI program, grant number N00014-96-1-1175 at Rutgers, the State University of New Jersey. The authors also acknowledge the support of Ralph Wachter, program manager.

## REFERENCES

1. C. Y. K. Chee, L. Tong, and G. P. Steven. *J. Intell. Mater. Systems and Struct.* **9**, 3 (1998).
2. Active Control Experts, Inc. [www.acx.com/cool\\_products.html](http://www.acx.com/cool_products.html). (2000).
3. G. H. Haertling. *Am. Ceram. Soc. Bull.* **73**, 93 (1994).
4. X. P. Ruan, B. A. Cheeseman, A. Safari, S. C. Danforth and T. W. Chou. *IEEE Trans. on UFFC.* **46**, 1486 (1999).
5. K. Onitsuka, A. Dogan, J. F. Tressler, Q. Xu, S. Yoshikawa and R. E. Newnham. *J. Intell. Mater. and Struct.* **6**, 447. (1995).
6. A. Dogan, K. Uchino and R. E. Newnham. *IEEE Trans. on UFFC.* **44**, 597 (1997).
7. K. M. Mossi, G. V. Selby and R. G. Bryant. *Mater. Letters.* **35**, 39 (1998).
8. K. Uchino. *Acta Mater.* **46**, 3745 (1998).
9. M. K. Agarwala, A. Bandyopadhyay, R. van Weeren, A. Safari and S. C. Danforth. *Am. Ceram. Soc. Bull.* **75**, 61 (1996).
10. H. F. Tiersten. *Piezoelectric Plate Vibrations*. (Plenum Press, New York, 1969).
11. *Piezoceramics Data Sheet*. (Vernitron, Bedford, Ohio, 1990).
12. G. H. Haertling. *J. Am Ceram. Soc.* **82**, 797 (1999).
13. B. L. Jiao and J. D. Zhang. *IEEE Trans. on UFFC.* **46**, 147 (1999).
14. F. Mohammadi, A. L. Kholkin, B. Jadidian, and A. Safari. *Applied Physics Letters* **75**, 2488 (1999).

## PROCESSING OF ORGANIC/INORGANIC COMPOSITES BY STEREO LITHOGRAPHY

J. H. LEE, R. K. PRUD'HOMME, and I. A. AKSAY

Department of Chemical Engineering and Princeton Materials Institute  
Princeton University, Princeton, NJ 08544

### ABSTRACT

*Ceramic StereoLithography (CSL) is used to fabricate complex shaped ceramic powder compacts by laser photocuring a concentrated ceramic dispersion in photocuring solutions layer-by-layer. The main processing parameters in CSL such as layer thickness, resolution, hatch spacing, and overcure depend on knowledge of the light propagation in a concentrated dispersion. In studies dealing with the processing of ceramic-filled organics, we investigated the depth of curing for model resin systems as a function of photoinitiator concentration. An optimal photoinitiator concentration that maximized the gel cure depth was observed. The study showed that photoinitiator plays a significant role in controlling the quality and performance of the formed gel network, with special regard to thickness of cured layers. This has potential application to fields as diverse as industrially cured coatings and dental fillings, and more generally, 3-dimensional fabrication techniques.*

### INTRODUCTION

Stereolithography is a sequential layering process that converts a "virtual" object into a real structure [1,2]. A 3-dimensional, computer-aided design (CAD) model is computationally sliced into a series of 2-dimensional, thin patterns. Each 2-D pattern is then transmitted to another computer which controls a scanning laser [1,2]. The laser is rastered across the surface of a photocurable monomer resin to solidify the layer in the shape of the 2-D pattern. A new layer of resin is swept across the surface, and the process repeated. By sequentially depositing layers in this layer-additive fashion, the entire structure is replicated in solid form [1,2].

By their very nature, composite materials encompass a wide range of applications. Since stereolithography lends itself especially well to the fabrication of complex shaped objects, we narrow our focus to the processing of organic/inorganic hybrids for use as biomaterials. A specific goal is to produce bone graft or implant materials with complex internal geometry tailor-designed by computer. We desire to produce composites that are biocompatible from an immunological point of view, as well as mechanically functional in supporting loads. Current bone graft techniques suffer from a series of drawbacks [3]. Autogenous strategies are limited by finite supply and issues of morbidity. Allografts often involve issues of immunogenicity (potential for viral transmission) as well as efficacy, depending on sterilization method [3]. Commercial products such as ultra high molecular weight polyethylene lack bone inductivity and/or strength [4].

In processing of organic/inorganic composites by stereolithography, we have taken a two-pronged approach. We have previously developed techniques to produce fully ceramic compacts [5], and since the stereolithography apparatus (SLA) is designed for



pure polymeric constructs, we now marry both approaches to achieve the fabrication of ceramic/polymer hybrids. In developing these composites, we have found it necessary to develop monomer resins not available commercially. Furthermore, in optimizing these systems, we are currently studying the effect of photoinitiator concentration on curing depth.

## MATERIALS AND METHODS

Organic/inorganic composites comprised of submicron size alumina ( $\text{Al}_2\text{O}_3$ ) powder<sup>a</sup> as the inorganic phase (15% by volume) and a multi-functional monomer, *2,2-bis(4-(2-hydroxy-3-methacryloxypropoxy)phenyl) propane* (Bis-GMA)<sup>b</sup> as the organic matrix. We have fabricated the parts with an SLA<sup>c</sup>. Bis-GMA is a commonly employed monomer in the dental industry, and alumina is used by virtue of its extensive history as a biocompatible material [3]. The photoinitiator used was *2-benzyl-2-N,N-dimethylamino-1-(4-morpholinophenyl)-1-butanone* (DBMP)<sup>d</sup> (Fig. 1).

Because Bis-GMA has a viscosity of approximately 1200 Pa-s, trichloroethylene (TCE) was used as a diluent solvent for the monomer in a 40/60 weight ratio. Resin was pipetted into cylindrical wells and filled to the brim. A glass coverslide placed in contact with the top of the solution acted as a substrate for attachment during the polymerization. Samples were cured by writing a cross-hatched pattern with dimensions shown in Fig. 2(a). Solid composites were formed at energy dosages of 1.702 J/cm<sup>2</sup> and 22.255 J/cm<sup>2</sup>.

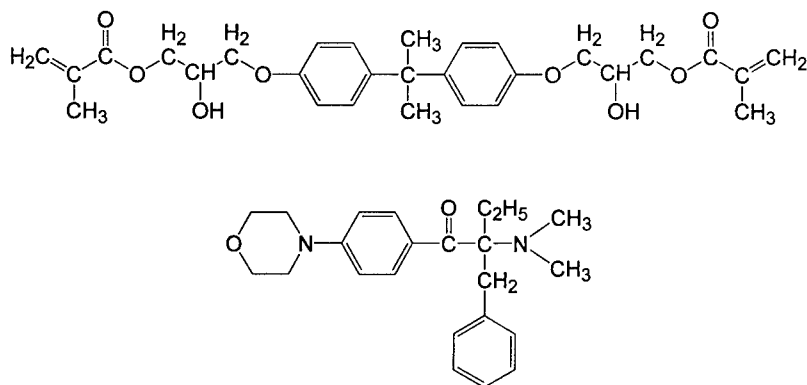


**Figure 1:** Chemical structures for *2,2-bis(4-(2-hydroxy-3-methacryloxypropoxy)phenyl) propane* (Bis-GMA) and *2-benzyl-2-N,N-dimethylamino-1-(4-morpholinophenyl)-1-butanone* (DBMP).

<sup>a</sup> AKP-50, Sumitomo Chemical, 335 Madison Avenue, Suite 830, New York, NY 10017

<sup>b</sup> Polysciences, 400 Valley Road, Warrington, PA 18976

<sup>c</sup> Model 250, 3D Systems, 26081 Avenue Hall, Valencia, CA 91355

<sup>d</sup> Irgacure 369, Ciba Specialty Chemicals, 540 White Plains Road, P.O. Box 2005, Tarrytown, NY 10591

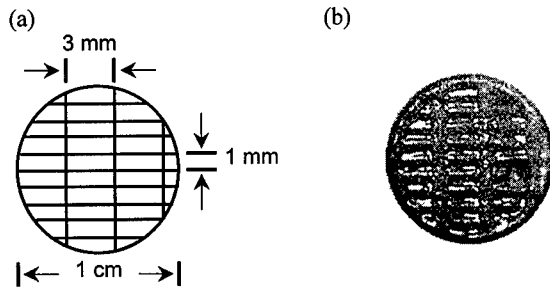


**Figure 2:** (a) CAD schematic of UV-cured disc. Black lines represent cross-hatched laser rastering pattern (laser beam diameter of 250  $\mu\text{m}$  and wavelength of 325 nm); (b) Bis-GMA/alumina (10/90 by volume) thin film composite formed in the SLA. Note that the designed architecture of the CAD file has been reproduced successfully.

In the fabricated composites, the CAD cross-hatched pattern was replicated successfully (Fig. 2(b)). Use of the glass coverslide facilitated removal of the gel for thickness measurements. Because of operating constraints with the SLA, individual layer thicknesses should have an order of magnitude of 100  $\mu\text{m}$  to achieve successful layer lamination and adhesion. As clarified in earlier work, the introduction of ceramic filler particles into the photocurable resin results in scattering effects, which effectively decrease the mean transport length of photons through the resin [6,7]. Thus, it is desirable to maximize the curing depth in the homopolymer resin before the addition of ceramic to ensure suitable cure depths are obtained in the composite material.

The “standard design equation” for stereolithography presented by Jacobs provides a relationship between cure depth and energy dosage as follows [1,2]:

$$C_d = D_p \ln \left( \frac{E_{max}}{E_c} \right), \quad (1)$$

where  $C_d$  is the cure depth,  $D_p$  is the depth of penetration of the laser beam into the solution,  $E_{max}$  is the energy dosage per area, and  $E_c$  represents the critical energy dosage. This empirical equation is used to fit experimental data on cure depth versus energy dose ( $E_{max}$ ) to determine values for  $D_p$  and the empirical constant  $E_c$ . These values are then used to determine layer thicknesses of each layer for stereolithographic fabrication. Thus, one way to increase cure depth is to increase energy dosage. Noting, however, that the energy dosages employed in fabrication of the Bis-GMA/alumina composites described above are higher than those typically required for the commercially available resins the SLA was designed for, another method of increasing cure depth is desired. Therefore, the effect of photoinitiator concentration on cure depth was probed to this end.

Solutions of Bis-GMA and TCE were again prepared in the manner described above. Photoinitiator (PI) concentration was varied from  $0.3 \times 10^{-3}$  to  $5.1 \times 10^{-3}$  moles/liter, corresponding to 0.010 to 0.150 weight percent of total solution and 0.0167 to 0.2500 weight

percent based on Bis-GMA monomer weight. These values are comparable to typical industrial formulations. Samples were cured at 3 dosage levels: 0.931, 1.702, and 22.255 J/cm<sup>2</sup>. Dosages were varied by varying the laser beam writing speed on the SLA. Cure depth was then measured using a micrometer.

### RESULTS AND DISCUSSION

The experimental results are shown in Fig. 3 for the patterned photopolymerized films. The ordinate is the gel thickness in millimeters and the abscissa the photoinitiator concentration from 0.3 to 5.1 mM, which corresponds to 0.017 to 0.250 weight percent based on Bis-GMA monomer weight. The corresponding weight percent photoinitiator (0.01 to 0.15) based on total weight of solution is shown above. The three data curves correspond to three different laser energy dosages.

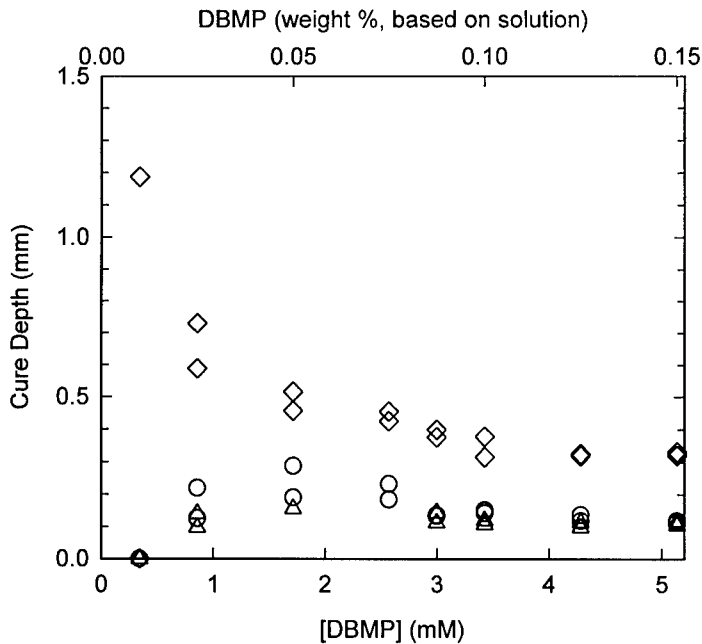


**Figure 3:** Gel thickness versus photoinitiator concentration. The three data curves correspond to the three different laser energy dosages (◇ 22.255 J/cm<sup>2</sup>, ○ 1.702 J/cm<sup>2</sup>, and △ 0.931 J/cm<sup>2</sup>). Photoinitiator concentration is given in millimoles/liter on the bottom abscissa, and as weight percent based on total solution on the top abscissa. Note the existence of an optimal photoinitiator concentration that maximizes cure depth.

It might be expected that cure depth should increase with increasing photoinitiator concentration [8-10]; however, this is not the case. The experimental data show that an optimal photoinitiator exists for which cure depth is maximized. Furthermore, this dependence is not adequately explained by the standard design equation for stereolitho-

graphy, which only directly considers the effect of energy dosage on cure depth. Extended data points (not shown) were taken for higher photoinitiator concentrations to confirm that the curve continues to decrease monotonically.

Returning to the filled resin, the degree of attenuation of the laser beam into the colloidal suspension medium is exacerbated by a multiple scattering effect. As filler is introduced into the system, the mean transport path of photons into the solution decreases, thereby altering the curing properties of the resin [6,7]. With the assumption that interference effects in the medium (modeled here as semi-infinite) can be neglected, a complete description of photon transport can be made in terms of the number of photons per unit volume per unit direction. In this diffusion model for scattering, two length scales characteristic of the medium, are important in describing the photon density in the medium [6]. The absorption length,  $l_a$ , represents the average distance traveled by the photon before being absorbed. For purely absorbing resin this represents the penetration depth. The transport mean free path-length,  $l_{tr}$ , is the average distance the photon travels before its propagation direction is completely randomized. Using a Percus-Yevick structure factor,  $S(\theta)$ , for hard sphere scatterers,  $l_{tr}$  may be calculated as [6]:

$$l_{tr} = (n\sigma_{tr})^{-1}, \quad (2)$$

where  $n$  is the number density of scatterers and  $\sigma_{tr}$  is the transport scattering cross-section of a single scatterer, found as:

$$\sigma_{tr} = \int \frac{d\sigma}{d\Omega} (1 - \cos(\theta)) S(\theta) d\Omega, \quad (3)$$

where  $d\sigma/d\Omega$  is the differential scattering cross-section scaled by  $(1-\cos(\theta))$  to account for anisotropic scattering. This in turn allows the calculation of the actinic intensity profile as a function of  $l_a$ . Solution of the diffusion equation gives expressions that allow for the rescaling of the absorption length in medium without particles,  $l_m$ , based on volume fraction filler,  $\phi$ , as:

$$\frac{1}{l_a} = \left(\frac{\phi}{\phi_m}\right)^{1/3} \left( \frac{\phi_m^{1/3} - \phi^{1/3}}{\phi^{1/3} l_m} + \frac{1}{l_p} \right), \quad (4)$$

where  $\phi_m$  is the maximum packing fraction for the colloidal dispersion and  $l_p$  is defined as the length scale where the light intensity decays by a factor  $e^{-1}$  traveling through the particle. Support for this determination of the absorption length for photon propagation through dense colloidal dispersion was provided by pulse-chase dye experiments to simulate the actinic absorption of the photocuring resin [6,7]. Figure 4 summarizes the results of the experiment [6]. As the data show, the transport length decreases dramatically with increasing filler volume fraction. Note that without correction for multiple scattering, the deviation between actual transport length and calculated value grows as

volume fraction rises. Thus, rescaling of the transport length by Eq. (4) is necessary in order to accurately predict the curing profile for ceramic resin.

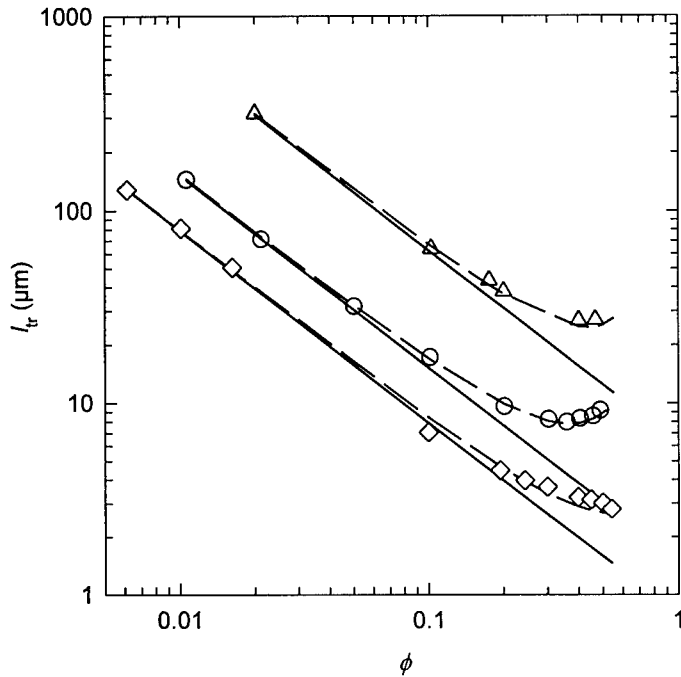


**Figure 4:** Transport mean free path versus volume fraction,  $\phi$ , of scattering particles on log-log scale. Solid curves are computed values without correlation and  $\sigma_{r,r}$ ; dashed curves are computed values obtained by using equations (2)-(4) and  $S(\theta)$  from Percus-Yevick theory. Symbols represent transport lengths obtained from experiment:  $\diamond$  0.51  $\mu\text{m}$  alumina,  $\triangle$  0.46  $\mu\text{m}$  silica, and  $\circ$  0.32  $\mu\text{m}$  alumina, and. The curve for 0.51  $\mu\text{m}$  alumina has been shifted up by  $\log(3)$  for clarity. (reprinted by permission [6])

While the model described above elucidates the dependence of the curing profile on filler fraction, it does not suggest the shape of the cure depth versus photoinitiator concentration curve seen in Fig. 3. To address this second issue, we have explored this dependence through experimental work with the homopolymerization reaction of Bis-GMA. We have also developed a model from first principles to incorporate the photoinitiator dependence [11].

---

## CONCLUSIONS

In this paper, we report the successful processing of Bis-GMA/alumina organic/inorganic biocomposites via stereolithography. Additionally, controlled patterning of the composite has been demonstrated through replication of designed architecture via CAD. In obtaining feasible cure depths to enable fabrication of multi-layered objects, we note the desire to increase cure depth by an alternative route than simply increasing energy dosage. A model for the role of volume fraction ceramic filler on the curing profile was developed and corroborated with experiment. We now demonstrate the dependence of the curing depth on photoinitiator concentration, and show the existence of an optimal photoinitiator concentration for which cure depth is maximized. Elsewhere [11], we quantitatively probe this dependence using a model derived from first principles to explain the experimental results. Once clarified, dependence of the cure depth on photoinitiator concentration should provide implications to fields as diverse as industrially cured coatings and dental fillings, in addition to our own particular interest in 3-dimensional fabrication techniques.

## ACKNOWLEDGEMENTS

This work was funded by the Army Research Office under a MURI Grant No. DAAH04-95-1-0102. Partial support for the work was obtained from Johnson & Johnson (CBC), the New Jersey Center for Biomaterials, and 3D Systems.

## REFERENCES

1. P.F. Jacobs, *Rapid Prototyping & Manufacturing*, (Soc. of Manufacturing Engineers, Dearborn, MI 1992).
2. P.F. Jacobs, *Stereolithography and other RP&M Technologies* (Soc. of Manufacturing Engineers, Dearborn, MI 1996).
3. L.L. Hench, "Bioceramics," *J. Am. Ceram. Soc.* **81** [7] 1705-28 (1998).
4. W. Bonfield, M.D. Grynopas, A.E. Tully *et al.*, "Hydroxyapatite Reinforced Polyethylene - a Mechanically Compatible Implant Material For Bone-Replacement," *Biomaterials* **2** [3] 185-86 (1981).
5. R. Garg, "*Stereolithography of Ceramics*," Ph.D. dissertation (Princeton University, Princeton, NJ, 1999).
6. R. Garg, R.K. Prud'homme, I.A. Aksay, F. Liu, and R. Alfano, "Optical Transmission in Highly-Concentrated Dispersions," *J. Opt. Soc. Am.* **15** [4] 932-35 (1998).
7. R. Garg, R.K. Prud'homme, I.A. Aksay, F. Liu, and R. Alfano, "Absorption Length for Photon Propagation in Highly Dense Colloidal Dispersions," *J. Mater. Res.* **13** [12] 3463-67 (1998).
8. G.A. Brady and J.W. Halloran, "Differential Photo-calorimetry of Photopolymerizable Ceramic Suspensions," *J. Mater. Sci.* **33** [18] 4551-60 (1998).

- 
9. F.A. Rueggeberg, P.E. Lockwood, and J.W. Ergle, "Effect of Post-cure Heating and Photoinitiator Level on a Model Resin System," *J. Dental Res.* **76** 472-72 (1997).
  10. F.A. Rueggeberg, J.W. Ergle, and P.E. Lockwood, "Effect of Photoinitiator Level on Properties of a Light-cured and Post-cure Heated Model Resin System," *Dental Materials* **13** [5-6] 360-64 (1997).
  11. J.H. Lee, R.K. Prud'homme, and I.A. Aksay, "Cure Depths in Photopolymerization: Theory and Experiments," *J. Mater. Res.* submitted (2000).

## **AUTOMATED FABRICATION OF CERAMIC ELECTRONIC PACKAGES BY STEREO-PHOTOLITHOGRAPHY**

W.R. ZIMBECK\*, J. H. JANG\*\*, W. SCHULZE\*\*, R. W. RICE\*\*\*

\*Technology Assessment and Transfer, Inc. Annapolis, MD 21401, zimbo@techassess.com

\*\*NYSCC, Alfred University, Alfred, NY 14802

\*\*\*Consultant, Springfield, VA 22310

### **ABSTRACT**

Significant cost and timesavings can be realized by applying automated freeform fabrication techniques to the fabrication of ceramic electronic packaging. The widely used thick film/screen printing approach for ceramic packaging involves multiple separate processing stations to build up a multilayer package with embedded electrical connectivity. The current process steps include tape casting, conductor pattern screen-printing, punching/filling of vias, dicing, alignment and lamination. The development of low and high temperature co-fire ceramic systems (LTCC and HTCC) has streamlined the firing process, but significant inefficiencies remain in constructing the green state package, such that prototyping of ceramic packages is often very expensive with substantial lead times. This paper describes an integrated approach that combines the automated three-dimensional capabilities of stereolithography of ceramics and metals with the high resolution and precision of advanced photolithography systems. The process utilizes photocurable resins filled with sinterable ceramic and metal particles, which are applied layer-by-layer and photopatterned to build up a multilayer package. Materials development has focused on a glass-ceramic dielectric, a silver conductor and a barium titanate dielectric. Resin rheology and photocuring characteristics, thermal processing and sintered properties of the materials are described. A breadboard processing system was constructed and the results of fabricating test circuits are presented.

### **INTRODUCTION**

Electronic packaging provides protection for and connectivity between the passive elements (resistors, capacitors, inductors) and active devices (transistors, integrated circuits-ICs, sensors/actuators, power sources, etc.) that make up an electronic system. Ceramic electronic packages are generally favored over polymer-based packages (e.g., printed circuit boards) where durability in extreme environments (e.g., high temperature) and/or high performance (e.g., low loss at high frequency) is required. Ceramic packages are also favored where miniaturization is a high priority. High conductor density, embedded passive elements and multi-layer circuitry enable ceramic multi-chip modules with greater functionality per unit volume compared to printed circuit boards. Despite the performance advantages, the cumbersome multi-layer fabrication process results in relatively high costs and long lead times. This is especially true in prototyping and small lot production where six to eight week lead times are common for new package designs. Given the rapid pace of new electronic product introductions, it is apparent that the industry would make great use of rapid, functional prototyping method offering turnaround times of 1 - 3 days.

In this paper, a novel method of fabricating multilayer ceramic packages that are normally made by the green tape process is introduced. The stereo-photolithography process takes advantage of materials developments made in stereolithography-based fabrication of ceramic [1], [2] and metal [3] parts and combines that capability with high-resolution photopatterning of



advanced photolithography systems. The general process utilizes photocurable resins filled with sinterable ceramic (insulators, capacitors, resistors) or metal (conductors) powders. The automated build process will provide deposition of thin layers of the materials, a means for photopatterning each layer and a means for removing unexposed material from the layer. Ultimately, the process will be capable of depositing an insulator, a conductor, capacitor and resistor materials. For the initial purpose of demonstrating feasibility, a two material system has been studied consisting of a low temperature co-fire ceramic insulator and a silver conductor.

### EXPERIMENT

Several approaches to photopatterning conductor traces on the surface or embedded in a ceramic substrate can be used. The approach presented here is shown in Figure 1. Step a) shows the deposition head applying a layer of insulator resin on the build surface. The desired areas are selectively exposed through a photomask by a UV flood lamp and cured. The build platform is lowered by one layer thickness relative to the tip of the deposition head. Multiple insulator layers are deposited as desired. Step b) shows deposition of a conductor filled photoresin on top of the insulator layers. The conductor resin is selectively exposed. Step c) shows removal of the uncured conductor resin using a "developer head", leaving only the exposed regions (conductor lines and vias) attached to the previous insulator layer. Without lowering the build platform, a layer of insulator resin is applied such that it surrounds the conductor patterns and is exposed (Step d). Repetition of these basic steps allows the layer-by-layer fabrication of green state electronic packages with embedded conductors. Use of additional deposition heads will enable fabrication of packages with embedded passive elements (capacitors and resistors).

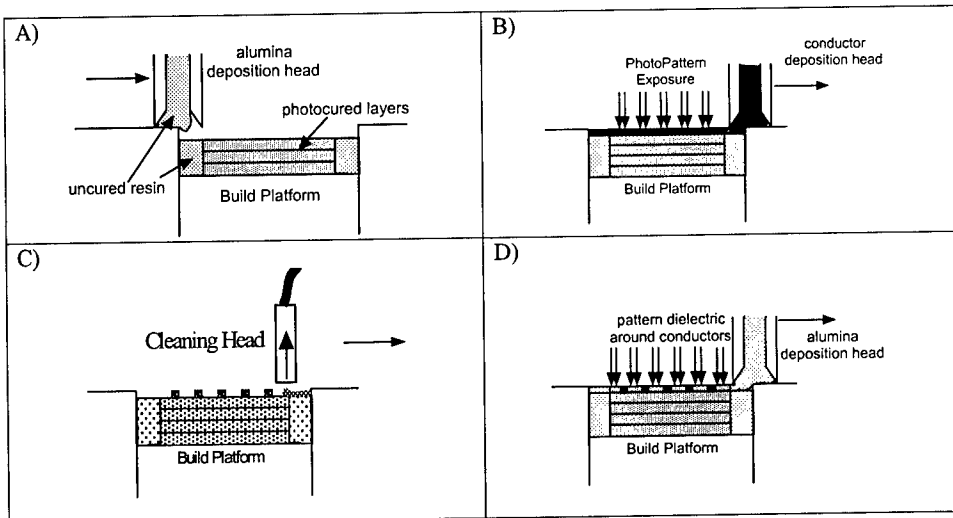


Figure 1. Process flow of a photopatterning approach for multilayer ceramic packages.

For these feasibility studies, a manual system was set-up using an Oriel photolithography machine, which provided an 8-inch diameter of collimated, uniform intensity UV/Vis light (1,000 Hg/Xe bulb). The mask holder of this system was modified by adding a blade supported on bearing rails to allow application of thin layers onto the build platform. Removal of uncured

---

material was performed using a suction head and a solvent spray bottle. Emulsion-on-film photomasks were adhered to plate glass, which fit into the mask holder. The light intensity at the resin surface varied in the range 22 - 23 mW/cm<sup>2</sup> over the six-inch square build platform.

A calcium borosilicate glass powder (L1, Ferro Corp, Electronic Materials Division, Santa Barbara, CA) was selected as the insulator material (dielectric constant = 6 at 10 MHz). L1 is similar in composition to Ferro's A6 green tape, a low temperature co-fire ceramic widely used in making multilayer ceramic electronic packages. The L1 particles have angular and roughly equiaxed morphology with average size in the 1 - 2 micron range. Silver was chosen as the conductor material since it is co-fireable in air with the L1 powder. Silpowder 172 was purchased from Technic, Inc., Woonsocket, RI. The silver particles have a rounded irregular morphology with average size in the 1 - 2 micron range.

The L1 powder was dispersed into an acrylate photoresin blend developed previously by TA&T for an alumina-filled stereolithography resin. The photoresin blend consisted of mono-, di- and tri-acrylate monomers and viscosity reducing agents. The liquid ingredients were mixed by ball milling using ceramic milling balls. The viscosity of this mixture prior to adding the ceramic powder was about 20 cPs (at 10 s<sup>-1</sup>). The L1 powder was added to this jar at a concentration of 50-vol%. The material was allowed to mill overnight to achieve a uniform dispersion of powder. A free-radical initiator (Irgacure 1700, Ciba Specialty Chemicals) was added at a concentration of 2% based on the weight of the photocurable monomers and the mixture was milled for one hour prior to use. Viscosity was measured at room temperature using a Brookfield DVE digital viscometer with a small sample adapter.

Silver-filled resin was formulated in a similar manner. Mono-, di- and triacrylate monomers were selected based on viscosity compatibility with the Silpowder 172. Resins were formulated at 35 and 45vol% silver. Additional solvent (isopropyl alcohol) was added to the 45vol% formulation to reduce the viscosity and aid dispersion of the silver powder during ball milling. After milling overnight, a visible light initiator package (based on H-Nu 470, Spectra Group Limited) was added to the mixture and milled for one hour. The solvent was removed by evaporation prior to use.

The dependence of depth of cure on exposure dose was measured by exposing a volume of resin (in a petri dish) through a rectangular mask for times ranging from 1 - 10 seconds. After exposure the cure thickness was measured with calipers. The exposure dose (in mJ/cm<sup>2</sup>) was calculated by measuring the light intensity (in mW/cm<sup>2</sup>) at the build platform with a radiometer and multiplying this intensity by the exposure time in seconds. Using this information, multilayer samples were built on the modified photolithography apparatus. Exposure dose was varied to determine the effect of overcure on interlayer bonding.

Dilatometry was used to measure the match in shrinkage rate with temperature and ultimate shrinkage amount of photocured silver and L1 multilayer samples. The dilatometry test used nominally 0.5-inch samples and a heating rate of 3°C/min to 800°C. SEM microscopy was utilized for microstructural analysis of sintered samples. The dielectric constant (K) and loss (D) were measured for L1 samples fired at 850°C. About 30 nm thick Pt-Pd thin layer was sputtered as an electrode. A silver/epoxy paste was painted onto the Pt-Pd coating improve mechanical durability of the electrode. K and D were measured during cooling from 200°C to -60°C (2°C/min) while the frequency was varied from 0.1 kHz-100 kHz.

## RESULTS

The L1 photoresins prepared with 55vol% powder showed viscosity of 500 cPs at a shear rate of 10 s<sup>-1</sup>. The viscosities of the silver resins were too high to measure using the small

sample configuration of the viscometer. The 45vol% silver resin was not flowable under gravitational influence, but could easily be spread into a thin layer (12.5  $\mu\text{m}$  thick) by blade casting. The 35vol% resin exhibited lower viscosity and could also be applied in thin layers by blade casting. Both silver resins exhibited shear-thinning behavior.

A working curve plot (exposure dose vs. cure thickness) was made for the L1 resin. Based on the Beer-Lambert relationship between exposure dose and cure thickness, a semi-log plot is linear. The slope of the line is referred to as the penetration depth,  $D_p$  and the X-intercept is the critical exposure dose needed to cause gelation,  $E_c$ . Typical values of  $E_c$  and  $D_p$  for commercial stereolithography resins are in the range 5 – 15  $\text{mJ}/\text{cm}^2$  and 100 – 200  $\mu\text{m}$ , respectively. The  $E_c$  and  $D_p$  for the L1 resin were 11.65  $\text{mJ}/\text{cm}^2$  and 197  $\mu\text{m}$ , respectively.

Cure parameters were tested to determine how much overcure would be required to achieve strong interlayer bonding. The modified photolithography apparatus was used to build samples consisting of 10 – 15 layers using a layer thickness of 125  $\mu\text{m}$ . Samples were built with 75 $\mu\text{m}$  and 125 $\mu\text{m}$  overcure (total cure depths of 200 and 250 $\mu\text{m}$ , respectively). The L1 working curve was used to determine the corresponding exposure time for a light intensity of 23  $\text{mW}/\text{cm}^2$ . After building, the samples were removed from the build platform and their interlayer bonding was qualitatively evaluated by breaking in flexure. No delaminations or artifacts of the laminar build process could be seen on the fracture surfaces of the samples by naked eye or optical microscopy. Both exposure doses resulted in good interlayer bonding.

Figure 2 shows the results of dilatometry testing of a multi-layer L1 sample. Approximately 2.5% linear shrinkage occurs during binder burnout. Sintering shrinkage begins sharply at 700°C. The instrument did not record the total shrinkage during this test due to improper settings. The linear shrinkage of samples sintered at 850°C for 30 minutes was ~17%.

The cure depth of the two silver resins was too small to develop a working curve plot for these materials. Multilayer samples were fabricated with the 45-vol% silver resin using layer thickness of 25 microns and an exposure time of 15 seconds (dose of 345  $\text{mJ}/\text{cm}^2$ ). Figure 3 shows dilatometry results for a multi-layer silver sample. Shrinkage in the silver sample started at 200°C, increased rapidly at 350°C, and ended at about 580°C. Shrinkage at the lower temperatures may be due to binder decomposition. The rate increase at 350°C is probably the onset of sintering, as observed in other heating tests performed with loosely packed silver powder. The total shrinkage was 20%, slightly higher than that observed in the L1 samples.

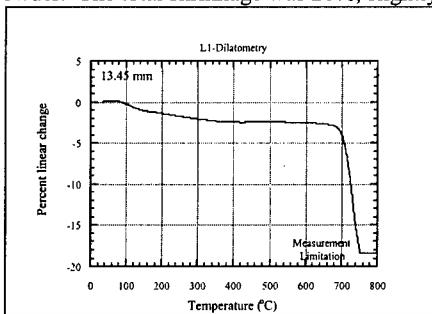


Figure 2. Dilatometry plot of L1 sample.

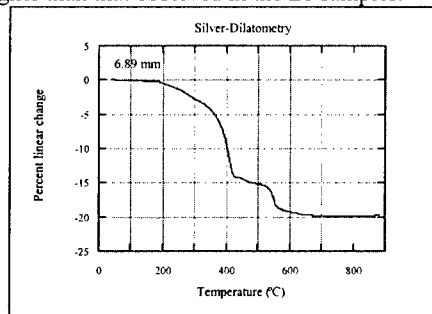


Figure 3. Dilatometry plot of silver sample.

L1 multi-layer samples were fired for 30 minutes at 850°C. L1 sintered specimens were compared to a single layer specimen of Ferro's A6 green tape fired under the same conditions as the L1 samples (850 °C for 30 minutes). SEM micrographs of the top and fracture surfaces

indicate the L1 multi-layer photocured sample and the A6 green tape sample have similar microstructures. SEM micrographs of the fracture surface of the L1 sample did not show artifacts (layer interfaces) of the layered build process.

The dielectric loss,  $D$ , and dielectric constant,  $K$ , of an L1 sample fired at  $850^{\circ}\text{C}$  were measured versus temperature at 0.1, 1, 10 and 100 KHz. The dielectric constant was about 6, and did not vary significantly with temperature or frequency. Dielectric loss remained below 0.05 for all temperatures and the three higher frequencies. Loss at 0.1 kHz was higher reaching a maximum of 0.1. Ferro specifies sintered L1 having a dielectric constant of 6 at 10 MHz and a dielectric loss  $< 0.1$  at 1 MHz.

Figure 4 shows SEM microscopy of a silver sample after binder burnout ( $450^{\circ}\text{C} - 30$  minutes). The silver particles are already in an advanced stage of sintering, showing a relatively dense microstructure and the presence of pores with stable morphology. This is in agreement with the dilatometry results showing the onset of sintering at about  $350^{\circ}\text{C}$ . After sintering at  $850^{\circ}\text{C}$  for 30 minutes, significant grain (particle boundary) growth has occurred with most particles  $5 - 15 \mu\text{m}$  in size.

The electrical resistance of fired silver patterns was measured using a four-point probe. Single layer ( $25\mu\text{m}$ ) silver lines were photopatterned onto a 10-layer ( $125\mu\text{m}$ ) photocured L1 substrate using the 35vol% silver resin and the 45 vol% silver resin. An emulsion-on-Mylar photomask was placed in close proximity to the silver layer, which was exposed for 10 seconds. The uncured resin was removed manually by solvent spray and vacuum extraction. The samples were removed from the build platform and co-fired at  $850^{\circ}\text{C}$  for 30 minutes (see Figure 5). The typical electrical resistivity of pure silver is  $1.63\mu\Omega\cdot\text{cm}$  at room temperature. The 35vol% sample showed a resistivity of  $133\mu\Omega\cdot\text{cm}$  and the 45vol% sample showed a resistivity of  $2.32\mu\Omega\cdot\text{cm}$ .

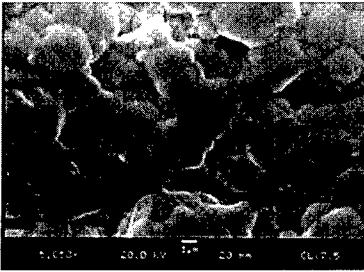


Figure 4. SEM of silver sample fired at  $450^{\circ}\text{C}$  showing advanced stage of sintering.

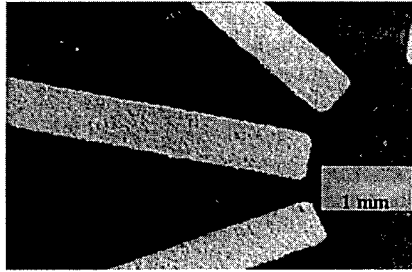
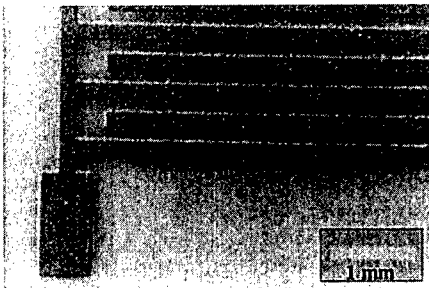


Figure 5. Silver lines on L1, fired at  $850^{\circ}\text{C}$  (45vol% sample).

Photopatterning resolution was tested using an emulsion-on-Mylar photomask with a test pattern having linewidths and spacings varying from  $400\mu\text{m}$  down to  $56\mu\text{m}$ . Ten layers ( $125\mu\text{m}$  thick) of L1 substrate were built in a 2" square shape by exposure through a photomask. A  $25\mu\text{m}$  thick layer of the 35vol% silver resin was applied to the L1 substrate and photocured using the test pattern mask. Exposure dose was varied from  $115 \text{ mJ}/\text{cm}^2$  (5 seconds) to  $345 \text{ mJ}/\text{cm}^2$  (15 seconds). After exposure, uncured resin was removed by solvent spray and vacuum extraction. The optimal exposure dose was  $184 - 230 \text{ mJ}/\text{cm}^2$  (8 - 10 seconds). Longer exposure times resulted in undercutting of the masks, broadening of the cured linewidths and loss of resolution. Partial curing of resin in the spaces between closely spaced lines prevented the silver in these regions from being removed by the solvent wash, which would have resulted in short circuiting. Lower exposure times resulted in inadequate cure depth and insufficient bonding to the L1 layer.

Without sufficient exposure dose, the solvent readily washed under cured lines away. Resolution was also substantially improved by minimizing the standoff distance between the mask and the silver layer. Mask standoff distance was estimated to be about 250 $\mu\text{m}$ .

Figure 6 shows an interdigitated pattern having 187.5 $\mu\text{m}$  (7.5 mils) lines and 175 $\mu\text{m}$  (7.0 mil) spaces. The edge definition is sharp and the space between lines is free of silver residue. Figure 7 shows a serpentine line pattern with 56 $\mu\text{m}$  lines and 84 $\mu\text{m}$  spaces. The silver pattern is 12.5 $\mu\text{m}$  thick and was exposed for 8 seconds. The uncured silver resin between the lines was successfully removed, although some fine residual silver particles remain.



**Figure 6.** Interdigitated pattern (187.5 $\mu\text{m}$  linewidth, 175 $\mu\text{m}$  spaces).

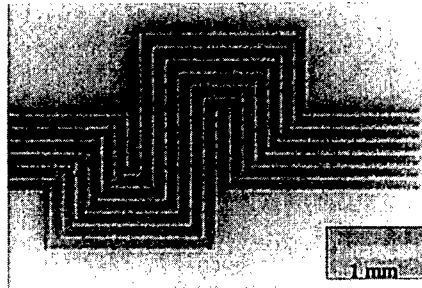


**Figure 7.** Serpentine silver line pattern on L1 substrate (56 $\mu\text{m}$  linewidth, 84 $\mu\text{m}$  spacing).

## CONCLUSIONS

The feasibility of a photopatterning approach to automated fabrication of ceramic multilayer electronic packages was demonstrated. LTCC insulator and conductor materials were developed and samples were fabricated that exhibited electrical properties comparable to conventionally processed material. Further development will focus on improving the match in shrinkage onset and rate during firing between the conductor and insulator materials, as well as implementing an automated system based on these materials.

## ACKNOWLEDGEMENTS

The authors would like to thank the Office of Naval Research for sponsoring this work.

## REFERENCES

1. W.R. Zimbeck, R.W. Rice, "Rapid Prototyping and Manufacturing of Ceramic using Photocurable Binders," presented at the 24<sup>th</sup> Annual Cocoa Beach Conference and Exposition, The American Ceramic Society, January 23 – 28, 2000.
2. M.L. Griffith, and J. W. Halloran, *J. Am. Cer. Soc.* **79** [10] 2601 - 608 (1996).
3. W.R. Zimbeck, R.W. Rice, "Freeform Fabrication of Components with Designed Cellular Structure," 1998 Fall Meeting of the Materials Research Society, Dec. 1-3, 1998.
4. Paul F. Jacobs, *Rapid Prototyping and Manufacturing, Fundamentals of Stereolithography*, Soc. of Manufacturing Engineers, 1992, pp. 29 – 30.

---

## USING LAYERED MANUFACTURING TO CREATE TEXTURED MICROSTRUCTURES IN $\text{Si}_3\text{N}_4$ CERAMICS

S. RANGARAJAN, B. HARPER, R. McCUISTON, A. SAFARI, Z. KALMAN, W. MAYO, and S. C. DANFORTH \*; C. GASDASKA \*\*

\* Department of Ceramic and Materials Engineering, Rutgers University, Piscataway, NJ 08854

\*\* Honeywell Technology Center, Morristown, NJ 07962

### ABSTRACT

In recent years, seeding has been shown to be an effective method to create textured microstructures in  $\text{Si}_3\text{N}_4$ ,  $\text{Al}_2\text{O}_3$  and PZT ceramics. The objective of this research is to create anisotropic and textured  $\text{Si}_3\text{N}_4$  parts using the Fused Deposition of Ceramics (FDC) process. This technique is currently being developed to fabricate high performance structural  $\text{Si}_3\text{N}_4$  based components. In order to create the textured microstructures, rod-like  $\beta\text{-Si}_3\text{N}_4$  seed particles are introduced into the FDC feedstock filaments. In this study, anisometric  $\beta\text{-Si}_3\text{N}_4$  seeds were introduced into the starting  $\alpha\text{-Si}_3\text{N}_4$  powder (Honeywell's AS800 grade) at a 10 vol.% loading. The effects of the seeds (aspect ratio  $\sim 4$ ) on the viscosity and resultant microstructure were evaluated using capillary rheology, scanning electron microscopy, coefficient of thermal expansion (CTE) measurements, and x-ray diffraction. It is observed that the seeds do align during filament extrusion and a significant texture has been detected by x-ray diffraction and CTE measurements in FDC feedstock filaments and sintered FDC parts.

### 1.0 INTRODUCTION

Solid Freeform Fabrication (SFF) technologies are being actively developed to fabricate net shaped ceramic components. Apart from being able to manufacture complex shapes and designs, these techniques has the added advantage of being an inexpensive tool for prototyping. Additionally, SFF techniques do not require any component specific tooling and can be used with a wide variety of materials, therefore finding a variety of applications.

The fused deposition process, Fused Deposition Modelling (FDM™ Stratasys™ Inc., Eden Prairie, MN)[1,2] is one of the commercially available SFF techniques. In the FDM process, a thermoplastic polymer filament is unwound from a continuous spool and driven through a liquefier, which is heated to a temperature slightly above the melting point of the polymer. The liquefier extrudes a continuous bead, or "road", of material through a nozzle (typically 250 to 750  $\mu\text{m}$  in diameter) and deposits it onto a z-stage platform. The liquefier movement is controlled along the X and Y directions by a computer, based on a tool path that has been generated to manufacture the object. When deposition of the first layer is completed, the platform indexes down, and a second layer is built on top of the first layer. This process continues until the whole part is completed. This fused deposition modeling process, has been adapted to make ceramic parts directly through a process known as Fused Deposition of Ceramics (FDC). In the FDC process, ceramic powders are mixed with a multicomponent thermoplastic binder to 50 to 60 volume % and extruded into a filament, which acts as the feed material for the green part fabrication process. Post processing involves binder removal and sintering to obtain final parts.

Work in the tape casting of  $\text{Si}_3\text{N}_4$  ceramics has shown that textured microstructures are developed in the sintered part due to the alignment of intentionally added beta silicon nitride "seed" particles during processing [3,4]. This texturing leads to anisotropy in the microstructure and enhanced material properties in certain directions. Due to the extrusion based nature of the

FDC process, the ceramic loaded thermoplastic binder encounters a variety of shear stresses and shear stress gradients during part building. For this reason it was thought that texture could be intentionally induced in FDC parts through a similar seeding process. If this is the case, it would be possible to make custom designed microstructures on a scale never before achieved (on the order of the size of the nozzle used, 250 to 750  $\mu\text{m}$ ). The aim of this study is to investigate the possibility of introducing microstructural texture into FDC parts, thereby enhancing properties in specific directions.

## 2.0 EXPERIMENTAL PROCEDURE

The process of  $\text{Si}_3\text{N}_4$  part fabrication for FDC has many sequential operations. The feedstock material, i.e. filaments, are fabricated first. Filaments are then used to fabricate green parts by FDC. These constitute two extrusion steps that the powder/binder mixture undergo on route to a finished part, which should aid in the alignment of the beta silicon nitride seed particles. The green parts are subjected to thermal binder removal and gas pressure sintering operations. Filaments were fabricated using Honeywell's AS800 powder, beta silicon nitride seed powder made at Rutgers University, and RU9 binder (Honeywell). Many process improvements have considerably increased the homogeneity and powder dispersion in the filament. The details of filament fabrication can be found elsewhere [5].

### 2.1 FDC PART MANUFACTURING, BINDER BURNOUT AND SINTERING

Green FDC part manufacturing was performed using a modified Stratasys FDM@1650. The standard build conditions were: a 406  $\mu\text{m}$  diameter nozzle, road width of 508  $\mu\text{m}$ , slice thickness of 254  $\mu\text{m}$ , liquefier temperature of 170  $^\circ\text{C}$ , and a build envelope temperature of 42  $^\circ\text{C}$ . A negative offset between adjacent roads was used for part building, but the flow rate was knowingly decreased to a value of 90% which lead to final parts that were not fully dense. This was done to minimize road distortion caused by the smearing of neighboring roads which commonly happens during dense part building. For the purposes of this study, it was not necessary to produce fully dense parts, although future work will include such parts.

Optimization of FDC parameters to obtain fully dense green parts has been established earlier. Details of process optimization can be found elsewhere [6]. Post processing techniques of parts after FDC, i.e., binder removal and sintering were developed at Rutgers University and Honeywell Technology Center respectively. Further details of the binder removal cycle development can be obtained from reference [7]. It should be noted that binder removal cycles are similar to those of injection molded parts, and sintering cycles are essentially identical to those of FDC parts made by conventional ceramic processes.

### 2.2 MATERIALS CHARACTERIZATION

As mentioned above, 10 vol.% of the total ceramic powder used to make the FDC filament feedstock was  $\beta\text{-Si}_3\text{N}_4$  seed particles. The addition of these particles to the filament feedstock may also have other than the desired effects, such as changing the materials rheological properties at FDC temperatures. The  $\beta\text{-Si}_3\text{N}_4$  seed powder used in these experiments, seen below in Figure 1, has an acicular morphology with an aspect ratio of approximately four. Because of the nature of the way the FDM@1650's material feed system works, the rheological behavior of the filament feedstock at FDC temperatures is a critical issue. If the viscosity of the material is too high, the force necessary to drive the extrusion through the nozzle may lead to

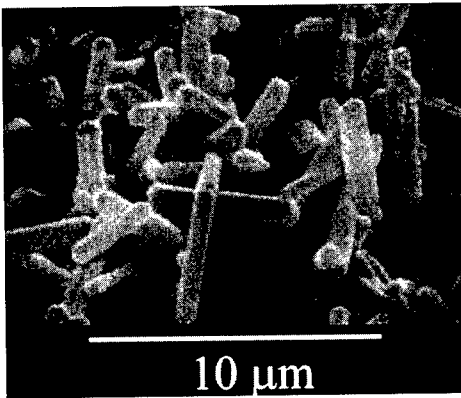


Figure 1. SEM micrograph of the  $\beta$ - $\text{Si}_3\text{N}_4$  seed particles that were introduced into the FDC filament feedstock in order to induce texture. The aspect ratio of these particles is  $\sim 4$ .

filament buckling and thus interruption of the process. To assess the effect of the  $\beta$ - $\text{Si}_3\text{N}_4$  powder addition to the feedstock material capillary rheology was used.

In order to conduct this texture study, rectangular bars were fabricated for characterization. To make the analysis simpler, in the build strategy used to make these bars, all of the roads in each layer were parallel (ignoring turn around points). Thus, any texture arising from this process should be uniform and in the same direction throughout the bar. A schematic representation of this can be seen in Figure 2, which shows the tool path.

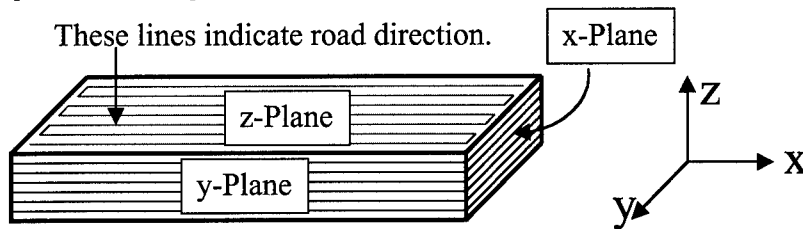


Figure 2. Schematic representation of how the roads are oriented in the bars used for this study. All of the roads in all of the layers are parallel and aligned in the x-direction. It is expected that the acicular  $\beta$ -seed particles will align parallel with the roads.

Scanning electron microscopy (SEM) was used to visually inspect the microstructure of the sintered, polished, and etched test bars. As this method of texture assessment is rather qualitative, x-ray diffraction was utilized to better describe the microstructure.

Two different, yet complementing, methods of x-ray diffraction (XRD) analysis were used. The first involved doing a standard  $\theta/2\theta$  coupled scan, like that commonly done for phase identification, to obtain the intensities of the (320) and (002) peaks. In a randomly oriented AS800  $\text{Si}_3\text{N}_4$  sample, the ratio of these two peak intensities,  $I(320)/I(002)$ , is 1.0. As texture develops in a sample, this ratio deviates away from 1.0, with the magnitude of the deviation proportional to the amount of texture in the sample.

The second type of x-ray diffraction analysis used was rocking curve analysis. In this analysis, a scan, similar to the ones described above, was done to locate the  $2\theta$  position of the various peaks in the diffraction pattern. A peak was then chosen and the detector fixed at the position of that peak, while the sample was "rocked" through the Bragg diffraction condition. In a sample that has a completely randomly oriented microstructure, the intensity of x-rays coming from the sample should be constant (ignoring some geometry effects) regardless of sample rocking angle. In a sample that is textured a peak in intensity will occur as the sample is rocked through the Bragg diffraction angle. The sharpness of the peak will indicate the degree of texture (sharper peaks = more texture).



### 3.0 RESULTS AND DISCUSSION

The effects of the addition of the  $\beta$ - $\text{Si}_3\text{N}_4$  seed particles, at 2.5 and 10 vol.% loading levels, on the rheology of the RU9- $\text{Si}_3\text{N}_4$  system were studied using a capillary rheometer. The viscosity was measured at 140 °C over a shear rate range from 8.4 to 841 (1/sec) using a capillary nozzle of length 28.85 mm and diameter of 1.422 mm. This shear rate range covers the shear rates typical of FDC. Results show that the viscosity of the system is not significantly altered at the volume % loadings studied here. The viscosity of the  $\beta$ -seed loaded material systems is very similar to that of the base material. All three work quite well in the FDC process without buckling.

SEM analysis was conducted on two sintered, polished, and etched faces (x-plane and z-plane) of the seeded FDC bars. Figure 3 shows the typical microstructure of these samples. According to what is expected, the  $\beta$ - $\text{Si}_3\text{N}_4$  seed particles should align along the direction of the road. During sintering, the precipitating beta phase should nucleate and grow on these previously oriented seeds. If this is the case, when looking at the x-plane one should see the ends of the rod-like  $\beta$ - $\text{Si}_3\text{N}_4$  grains (basal planes; Figure 3a). When looking at the z-plane one should see the long side (prism planes) of these grains (see Figure 3b). Comparing Figure 3(a) and (b) one can see a larger number of what appear to be small equiaxed grains in 3(a) than in 3(b). These small equiaxed grains are actually cross-sections of the long rod-like grains, indicating that they are oriented with their long axis running perpendicular to the plane of the paper, confirming the expectations. Accordingly, there are more of what appear to be long thin grains in figure 3(b) than in 3(a). These micrographs also show a bimodal distribution of grain sizes. This is a result of the seeding process. The  $\beta$ -seed particles present in the starting powder act as nucleation sites and grow during sintering, thus a bi-modal grain size distribution is expected [8].

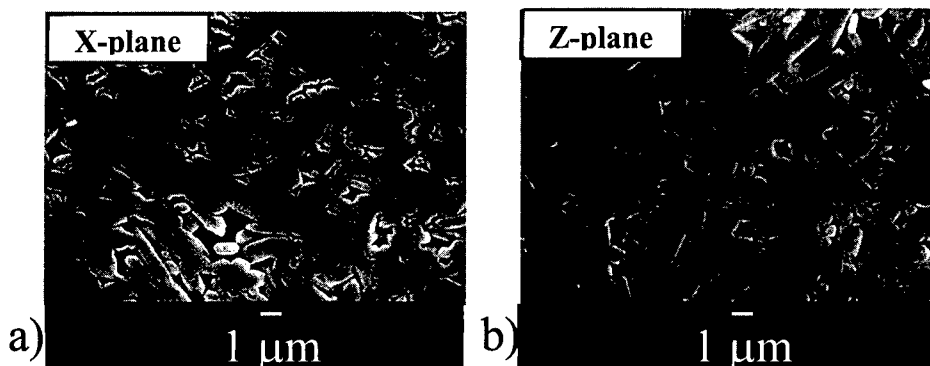


Figure 3. SEM micrographs showing the microstructures of (a) the x-plane, and (b) the z-plane of the beta seeded sintered FDC bar. The microstructure as seen in the x-plane appears to have more small equiaxed grains (cross-sections of rod-like grains) while the z-plane appears to have more long thin grains, confirming the expectation that the acicular beta particles align along the road direction.

As discussed earlier, XRD studies were conducted on an unseeded sintered GS44 FDC bar, (which should have very little texture) and three perpendicular sections through a 10 wt.%  $\beta$ -seeded AS800 sintered FDC bar (sample 205). Beta (320) and (002) peak ratios were obtained for each of these samples, Table I. While the ratio for the unseeded GS44,  $I(320)/I(002) = 1.34$ ,

sample does show some deviation from the value of 1.0 for randomly oriented samples, the deviation is slight and this sample is largely untextured. However, the peak intensity ratios obtained for sample 205 deviate significantly from 1.0 with the largest deviations coming from the x (0.09) and z-planes (7.14) of the sample. This indicates that the highest amounts of texture are in these planes.

Table I. Peak Intensity Ratios For Random and FDC Samples With and Without  $\beta$ -Seeds.

Sample	I(320)/I(002)
Randomly Oriented Sample (Theoretical)	1.0
FDC Unseeded GS44 Sample	1.34
FDC Seeded 205 x-plane	0.09
FDC Seeded 205 y-plane	1.80
FDC Seeded 205 z-plane	7.14

To supplement these findings, x-ray rocking curve analysis was done on each of the samples included in Table I. For each sample, three rocking curves were done; one with the detector fixed on the (320) peak position, one with the detector fixed on the (002) peak position, and one with the detector fixed in a position where no peak existed to obtain a background. All of the curves obtained can be seen in Figure 4. In all of the

scans, the sample position was rocked from 10 to 60 ° theta.

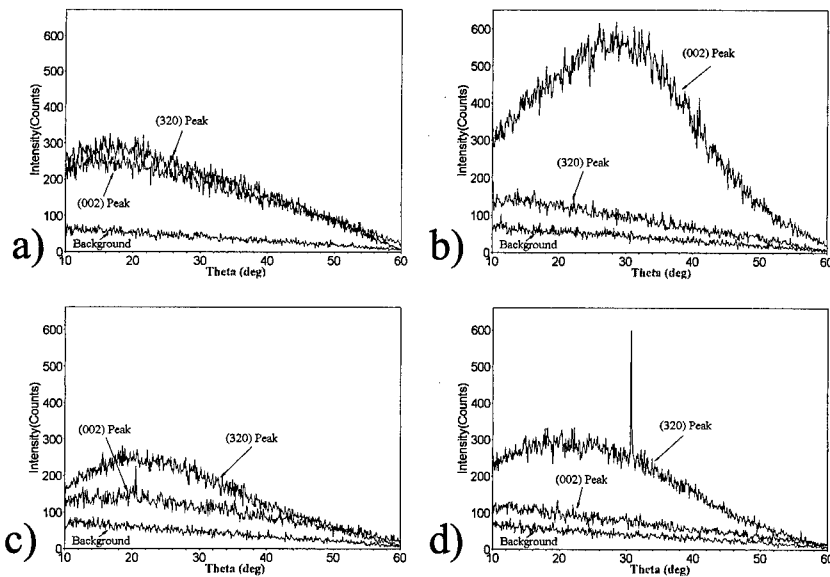


Figure 4. Shows the rocking curve analysis results for (a) the unseeded sintered GS44 bar, (b) sample 205 x-plane, (c) sample 205 y-plane, and (d) sample 205 z-plane. Each plot contains a curve for the (320) peak, the (002) peak, and a background scan. For each of the scans the sample was rocked from 10 to 60 ° theta. Texture in sample 205 can best be seen when investigating the (002) peak in the x-plane of the sample.

As one can see, when the rocking curve analysis is done on the unseeded GS44 sample the intensity scans obtained for the (320) and (002) peaks are very similar, falling right on top of

each other, with a gradual intensity decrease as the sample position moves out toward 60 ° theta. This intensity decrease is due to geometry effects inherent in the way the equipment is oriented and not an artifact of the sample itself. The results from sample 205 x-plane, seen in Figure 5b, exhibit the largest peak of all the samples when the analysis is done on the (002) peak (basal plane). When the analysis is done on the (320) peak (prism plane) of this sample no intensity increase can be seen at all. This suggests that the rod-like  $\beta$ -Si<sub>3</sub>N<sub>4</sub> grains have aligned, to some degree, in the direction of the rod and in the build plane, as it was initially theorized. The rocking curve results from samples 205 y-plane and 205 z-plane complement these findings. These curves are very similar showing a peak, with a maximum in the range of 250 to 300 counts in the data when the (320) plane is investigated, and no peak when the (002) peak is investigated. All of peaks seen in these rocking curves are roughly 30 ° theta wide. This shows that there is a distribution of grain orientations in the microstructure that are aligned in a given direction  $\pm 15$  °. One sharp peak is seen in the rocking curve done on sample 205 z-plane. It is believed that this is a result of an abnormally large grain coming into a diffracting condition resulting in this peak and is not a good indicator of the overall orientation in the microstructure.

Coefficient of thermal expansion (CTE) measurements were also performed on the various faces of  $\beta$ -seeded sintered FDC sample 205. The results can be seen below in Table II. They revealed that sample 205 exhibits a higher CTE in the x-direction ( $3.32 \times 10^{-6}/^{\circ}\text{C}$ ) than in the z-direction ( $2.96 \times 10^{-6}/^{\circ}\text{C}$ ). This anisotropy correlates well with the above XRD results in the following way. Single crystal  $\beta$ -Si<sub>3</sub>N<sub>4</sub> has a much higher CTE along its' c-axis ( $2.84 \times 10^{-6}/^{\circ}\text{C}$ ) than along its' a-axis ( $2.01 \times 10^{-6}/^{\circ}\text{C}$ ) [9]. Since the XRD results revealed texture of the microstructure of sample 205 with the preferred orientation having the c-axis of the  $\beta$ -Si<sub>3</sub>N<sub>4</sub> phase in the x-direction, these CTE results follow the expected trend. It is not surprising that the CTE measurements of sample 205 are higher than those found in a single crystal as part of the

Table II. Thermal expansion coefficients of single crystal  $\beta$ -Si<sub>3</sub>N<sub>4</sub> and  $\beta$ -seeded sintered FDC bar sample 205.

Sample	Coefficient of Thermal Expansion ( $\times 10^{-6}/^{\circ}\text{C}$ )
Single Crystal $\beta$ -Si <sub>3</sub> N <sub>4</sub> c-axis[10]	2.84
Single Crystal $\beta$ -Si <sub>3</sub> N <sub>4</sub> a-axis[10]	2.01
$\beta$ -Seeded Sintered FDC Bar x-direction	3.32
$\beta$ -Seeded Sintered FDC Bar z-direction	2.96

sintered polycrystalline sample is made up of a glassy phase matrix.

The ability to make use of and control texture in ceramic parts made by FDC may allow an additional degree of freedom, to design the microstructure and texture into the net shape part. In some instances, the common mode of failure of a ceramic part is known. Knowing this failure mode and having the ability to control texture, the anisotropic properties resulting from texture can be designed into the parts such that the highest possible

strength and toughness values are oriented normal to the expected crack growth direction leading to better part performance. Another way of utilizing texture could be to orient the microstructure such that the materials thermal conductivity is higher in a particular direction, thus aiding in heat transfer. Previous work relating to the use of anisotropic properties in Si<sub>3</sub>N<sub>4</sub> has been done by Hirao, et. al.[3].

## 4.0 CONCLUSIONS

When an aligned road vector build strategy is used to make rectangular FDC bars using Honeywell's AS800 grade  $\text{Si}_3\text{N}_4$  seeded with 10 vol.%  $\beta\text{-Si}_3\text{N}_4$  seed particles, texture can be induced in the resulting sintered microstructure. Capillary rheology measurements have shown that the rheology of the filament feedstock at FDC temperatures is only minimally affected by the addition of  $\beta$ -seed particles to the powder mixture and does not cause buckling problems of the filament during part building. Scanning electron microscopy was not helpful in assessing the texture in the microstructure of the  $\beta$ -seeded sintered FDC bars. Two methods of x-ray diffraction, however, peak intensity ratio measurements and rocking curve analysis, and coefficient of thermal expansion measurements have proven useful in describing the texture in these parts. Results have shown that there is a significant amount of texture created in FDC parts made using feedstock with 10 wt.%  $\beta$ -seeds ( $L/D \sim 4$ ). There is a distribution of grain orientations in the microstructure of the sintered  $\beta$ -seeded bars aligned along the direction of the roads and in the build plane  $\pm 15^\circ$ .

## ACKNOWLEDGEMENTS

DARPA: W. S. Coblenz, Contract #: N00014-94-0115; ONR: S. Fishman, R. Wachter, Grant #: N00014-96-1-1175; New Jersey Commission on Science and Technology; Jesse Greco, Andy Schwager, and Umair Suri

## REFERENCES

1. J. W. Comb and W. R. Priedeman in *Solid Freeform Fabrication Proceedings, 4*, edited by H. L. Marcus, J. J. Beaman, J. W. Barlow, D. L. Bourell and R. H. Crawford, Austin, TX, pp. 86-91 (1992).
2. U. S. Patent No. 5,121,329 (June 1992).
3. K. Hirao, T. Nagsoka, M. E. Brito, and S. Kanzaki, *J. Am. Ceram. Soc.*, 77[7]1857-62(1994).
4. K. Hirao, M. Ohashi, M. E. Brito, and S. Kanzaki, *J. Am. Ceram. Soc.*, 78[6]1687-90(1995).
5. S. Rangarajan, G. Qi, A. Bandyopadhyay, C. Dai, J. W. Han, P. Bhargava, S. Wu, A. Safari, and S. C. Danforth in *The Role of Materials Processing Variables, in the FDC Process*, edited by D. L. Bourell, J. J. Beaman, R. H. Crawford, H. L. Marcus, and J. W. Barlow (Solid Freeform Fabrication Symposium, Austin, TX, 1997) pp. 431-440.
6. C. Dai, G. Qi, S. Rangarajan, S. Wu, N. A. Langrana, A. Safari, and S. C. Danforth in *High Quality, Fully Dense Ceramic Components Manufactured Using Fused Deposition of Ceramics (FDC)*, edited by D. L. Bourell, J. J. Beaman, R. H. Crawford, H. L. Marcus, and J. W. Barlow (Solid Freeform Fabrication Symposium, Austin, TX, 1997) pp. 411-420.
7. P. Bhargava, A. Bandyopadhyay, S. Rangarajan, G. Qi, C. Dai, S. Wu, S. C. Danforth, and A. Safari in *Shrinkage, Weight Loss, and Crack Prevention During Binder Burn Out of Components Produced by Fused Deposition of Ceramics (FDC)*, edited by D. L. Bourell, J. J. Beaman, R. H. Crawford, H. L. Marcus, and J. W. Barlow (Solid Freeform Fabrication Symposium, Austin, TX, 1997) pp. 395-402.
8. P. F. Becher, E. Y. Sun, K. P. Plucknett, K. B. Alexander, C. H. Hsueh, H. T. Lin, S. B. Walters, and C. G. Westmoreland, *J. Am. Ceram. Soc.*, 81[11]2821-30(1998).
9. E. Sun, P. F. Becher, K. P. Plucknett, C. H. Hsueh, K. B. Alexander, and S. B. Walters, *J. Am. Ceram. Soc.*, 81[11]2831-40(1998).

## **μ-MOLD SHAPE DEPOSITION MANUFACTURING OF CERAMIC PARTS**

S.W. NAM, J. STAMPFL, H.C. LIU, S. KANG, F. B. PRINZ  
Rapid Prototyping Laboratory, Building 530, Room 226, Stanford University,  
Stanford CA 94305, USA

### **ABSTRACT**

Rapid Prototyping is a versatile method to build complex-shaped ceramic or metallic parts on a mesoscopic scale. In this work the fabrication of ceramic gas turbine engine parts with Mold Shape Deposition Manufacturing (Mold SDM) is described. Mold SDM exists of two steps: The pattern generation in wax using deposition and machining of wax layers and the pattern transfer process with gel-casting. For parts with feature sizes that are too small for machining, microfabrication methods are used to fabricate the mold. By combining micro- and macro-fabrication, complex parts in a wide variety of sizes can be manufactured. The surface quality of the mold significantly influences the mechanical properties of the final ceramic part. The contribution of the mold quality to the final mechanical properties is studied in this work.

### **INTRODUCTION**

Non-oxide ceramic materials such as silicon nitride and silicon carbide have been thought to be good candidates for high-temperature engine applications. In particular, silicon nitride has been recognized for high temperature applications because of its excellent high temperature strength, high temperature stability, high toughness, good creep resistance, excellent thermal shock resistance, low density and good chemical resistance. However, the application of  $\text{Si}_3\text{N}_4$  material is inhibited by the difficulty and high cost of fabrication of ceramic parts that have complex shapes as shown in Fig. 1. Rapid prototyping is one of the candidates to build a complex-shaped part easily and cost-effectively.

For mesoscopic parts such as a turbine and inlet nozzle, Mold SDM is applied which is a variation of Shape Deposition Manufacturing (SDM), an additive-subtractive layered manufacturing process that has been used to build metal or polymer parts.<sup>1</sup> In Mold SDM, the mold is built with the SDM technique that can make such a sophisticated, complex shaped mold by machining of a mold material and a temporary part material. After building a mold with SDM, the temporary part material such as solder mask can be removed by etching with water, thereby allowing us to mold the green parts with gel-casting. As a result of this combination of SDM and the gel-casting technique, the final surface quality is only limited by the ability of CNC machining. Fig. 1 shows the turbine engine parts fabricated with Mold SDM and Fig. 2 shows the simplified process of Mold SDM.

For microscopic mechanical parts such as a thrust bearing, we used conventional thin film fabrication process such as photolithography, plasma etching and electroplating with various materials such as silicon nitride, silicon and nickel.<sup>2</sup>

In this study, the possibility of rapid prototyping on the fabrication of engine parts is reviewed and the mechanical properties of Mold SDM parts are analysed.

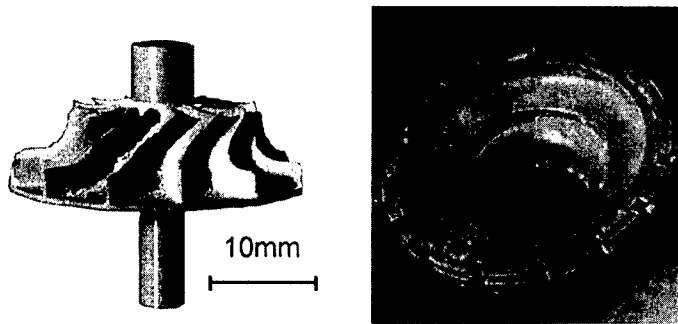


Fig. 1 Silicon nitride turbine engine parts fabricated with Mold SDM: turbine-rotor (Left), inlet nozzle (Right).

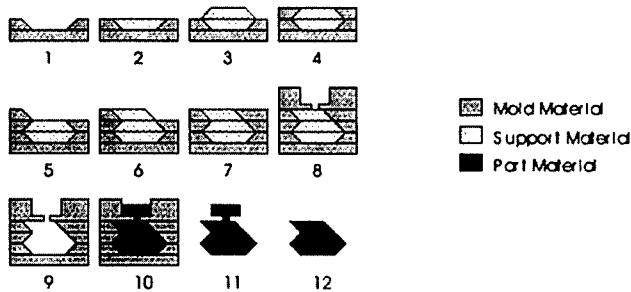


Fig. 2 Schematic representation of the Mold SDM process: the mold is constructed layer by layer. After that, the support material is dissolved and the ceramic part is gel-cast.

## EXPERIMENTAL PROCEDURE

For building molds of mesoscopic parts such as a turbine rotor and inlet nozzle, the Haas VF-0E 3-axis CNC milling machine is used that can deposit and cure the wax materials and the solder mask. This CNC machine can be controlled by a computer system which can read and manipulate machining code generated by the CAD program, UniGraphics. For mechanical testing, the wax molds for standard testing specimen (3×4×45mm) are prepared with this Haas CNC machine. The bottom of the testing specimen mold is machined in short raster patterns with two types of end mills: 1/8 inch flat-end mill and 1/8 inch ball-end mill.

For building microscopic parts such as the herring-bone type thrust bearing, negative photoresist SU-8 50 (MicroChem Corp.) is deposited on the silicon wafer with a thickness of 250 micron and developed with the desired pattern.

After that, these molds are filled with a gel-casting slurry containing ceramic powder (Advanced Ceramic Research, AZ, USA). The composition of the ceramic powders is 87wt% Si<sub>3</sub>N<sub>4</sub>, 7.4wt% Y<sub>2</sub>O<sub>3</sub> and 5.6wt% Al<sub>2</sub>O<sub>3</sub> are added as sintering aids. Before casting, additives of the slurry are added for curing with the amounts shown in Table 1. Lauroyl peroxide ((CH<sub>3</sub>(CH<sub>2</sub>)<sub>10</sub>CO)<sub>2</sub>O<sub>2</sub>, Aldrich, USA) is added as the initiator of the polymerization of the silicon nitride slurry and dibutyl phthalate (C<sub>6</sub>H<sub>4</sub>-1,2-[CO<sub>2</sub>(CH<sub>2</sub>)<sub>3</sub>CH<sub>3</sub>]<sub>2</sub>) is added as a solvent

for the lauroyl peroxide. Small amounts of N,N-dimethyl-m-toluidine (Aldrich,USA) are added to accelerate the polymerization process.

Then, the slurry is gelled at 55°C for 12 hours in a nitrogen atmosphere. After the slurry has solidified completely, the surrounding mold is melted off. After drying and de-binding, the part is sintered at 1750°C in a nitrogen atmosphere.

Room and high temperature four point flexural strengths were measured with a mechanical testing system with a lower span of 40mm, upper span of 20mm and a cross-head speed of 0.5mm/min (Shimitzu, Japan)

Table 1. The recipe of the additives for curing of ACR slurry.

Additive	Quantity
Lauroyl peroxide	0.16g
Dibutyl phthalate	0.48g
N,N-dimethyl-m-toluidine	27μl
ACR Slurry	70g

## RESULTS

The flaking on the surface of the silicon nitride green parts, which occurs when the parts are gelled in air, can be avoided by performing the gelling process in nitrogen. The so obtained surface quality can be seen in Fig. 3.

However, large surface cracks can be found with SEM (Scanning Electron Microscope, S-4200, Hitachi, Japan). Cracks like that, which can cause an abrupt strength drop, might have been generated during the drying and de-binding procedure which removes the solvent and polymers from the green part<sup>4</sup>. In order to reduce these processing defects, a more careful drying and de-binding schedule is needed as the dimension of the specimens become larger and thicker. Except for these rare surface cracks, no other process defects were observed.

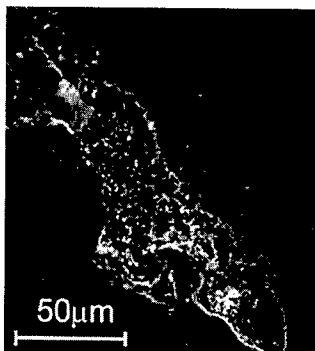


Fig. 3 Surface crack on the surface of the Mold SDM Si<sub>3</sub>N<sub>4</sub> specimen.

For as sintered specimens the mechanical testing of 4-point-bend-beams gave an average strength of 430MPa. Fig. 4 shows the strength distribution of the as-sintered specimens as a function of the failure probability. With this Weibull diagram, we can predict the failure probability of the  $\text{Si}_3\text{N}_4$  specimens under certain stress conditions. In order to measure the bulk properties of gel-cast silicon nitride, polished specimens were prepared and tested under 4-point bend conditions. The mean strength of the polished specimens was 950MPa. However, the strength of some of the as-sintered specimens nearly approached this value and it can be expected that improved processing conditions could yield higher strength values of as sintered beams.

Fig. 5 shows the strength variation as a function of the height of the machined scallop patterns. The strength decreases abruptly when the scallop height of the wax mold increases. We can assume that processing defects are the dominant factor for mechanical failure if the scallop height is between 0.001 and 0.01mm. Above 0.01mm the machining defects seem to be dominant because the strength as well as the standard deviation of the strengths is significantly lower when the scallop height is larger than 0.01mm. By examining the beams after failure it could be found that nearly all cracks initiate on the surface of the specimen.

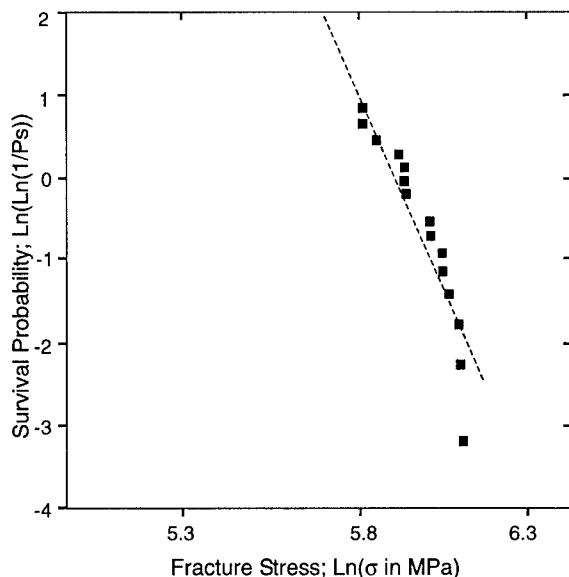


Fig. 4 Strength distribution of as-sintered  $\text{Si}_3\text{N}_4$  specimens relative to the survival probability at a certain strength.



Fig. 6 (Left) shows a herring-bone air bearing pattern fabricated with SU-8 50 photoresist (PR). The replication of the pattern is very good up to a depth of 1mm. This is due to the low

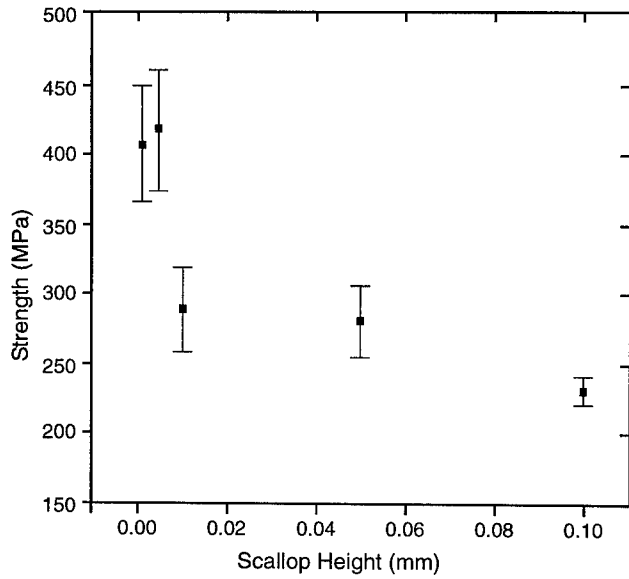


Fig. 5 The strength degradation of Mold SDM parts in dependence of the scallop height. The scallops were machined into the wax mold using a ball mill.

absorption coefficient of SU-8. Fig. 6 (Right) shows the green micro ceramic parts fabricated by gel-casting in a SU-8 50 mold. It shows sharp edges and good replication of the pattern of the SU-8 PR mold can be achieved by gel-casting. The low viscosity and small particle size of the silicon nitride slurry allows the fabrication of such small features.

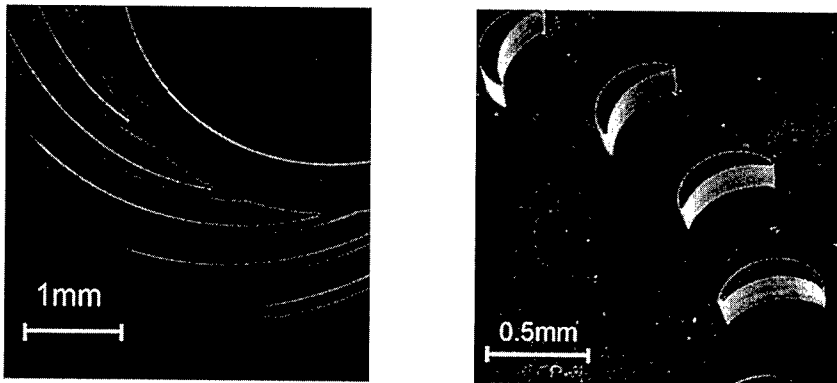


Fig. 6 SEM picture of an herring-bone bearing pattern generated by photolithography with SU-8 50 (Left) ; gel-cast ceramic green body fabricated with SU-8 PR mold (Right).

## CONCLUSIONS

Mold SDM which is the combination of SDM and gel-casting can build high quality mechanical parts which can be used without any post processing such as machining. The surface quality improved dramatically after introducing nitrogen during the curing process. To improve the reliability of final product, a more careful drying and de-binding procedure is required.

The result of mechanical testing shows that the mean strength of as-sintered specimens is 430 MPa, and the polished specimens show somewhat higher mean strength, 950 MPa. It shows the surface condition of the specimen is important on the mechanical properties and we can improve the strength of the ceramic parts with improving the surface condition.

The Weibull modulus of as-sintered specimen was 10.5, which is a relatively high value for specimens without any surface modification. The relation between the machining condition of molds and strength is studied. The scallop pattern can act as the initial crack on the surface which can degrade the mechanical properties of Mold SDM parts. The critical value of the scallop height is thought to be 0.005 mm and if we set this machining variable below this value, the ceramic parts with higher quality can be manufactured more effectively.

The microscopic mold can be fabricated with photolithography of SU-8 50 photoresist. The ceramic body can be built with gel-casting and this method shows a high potential for making parts with small features easily and cost-effectively.

## REFERENCE

1. A.G.Cooper, S. Kang, J.Stampfl, F.B. Prinz, Ceramic Transactions, 2000, in print.
2. J. Stampfl, H.-C. Liu, S. W. Nam, S. Kang and F. B. Prinz, in *Proceedings Micromaterials 2000*, edited by B.Michel, in print, Berlin, April 2000.

For further information contact:

Hao Chih Liu  
Rapid Prototyping Lab  
Stanford University  
Building 530 Room 226  
Stanford CA 94305-3030  
<http://www-rpl.stanford.edu>

---

## **Ceramics and Solution Processes**

## **FREEFORM FABRICATION OF CERAMICS BY HOT-MELT INK-JET PRINTING**

B. Derby<sup>1</sup>, N. Reis<sup>1,2</sup>, K.A.M. Seerden<sup>2</sup>, P.S. Grant<sup>2</sup>, J.R.G. Evans<sup>3</sup>

<sup>1</sup>Manchester Materials Science Centre, UMIST, Grosvenor St., Manchester, UK.

<sup>2</sup>Department of Materials, University of Oxford, Parks Rd., Oxford, UK.

<sup>3</sup>Department of Materials Engineering, Queen Mary and Westfield College, Mile End Rd., London, UK.

### **ABSTRACT**

Ink-jet printing is a versatile freeform fabrication technique with a high spatial resolution. By suspending ceramic particles in low melting point organic materials and printing above the melting point, rapid cooling on impact after printing results in rapid layer growth. Current results from a collaborative programme studying the hot wax ink-jet printing of structural ceramic components will be reported. The influence of key fluid properties on the ink-jet deposition process are discussed.

### **INTRODUCTION**

Ink-jet printing is a mature technology with many applications. Originally developed for graphics applications it is now routinely used for personal printing, commercial printing, marking, micro-dosing, rapid prototyping and rapid manufacturing. It has been used for a number of years as a tool for ceramic green body fabrication by the deposition of a binder onto a powder bed [1-3]. Direct ink-jet printing of ceramic slurries is potentially a very versatile method for the manufacture of ceramic parts. There has been substantial work on the ink-jet deposition of ceramic powders in aqueous or alcohol suspensions by Evans and co-workers [4-7], chiefly on the deposition of ZrO<sub>2</sub> suspensions. PZT suspensions have also been printed [8]. In all these cases the printer used has been a commercial printer developed for printing on paper. These currently have lateral resolutions up to about 1200 dpi (approximately 20 µm). Ink-jet printing of ceramics using these printers requires the development a ceramic ink with similar fluid properties to the dye or pigment based inks used for graphics applications. These inks dry by evaporation and typically contain only about 5% solids by volume.

A second ink-jet printing technology, also originally developed for the graphic arts, is hot-melt or phase change printing. This uses a dye or pigmented suspension, which solidifies on impact cooling. This technology was developed to eliminate the drying cycle with its risk of smudging during printing. The ink-jet deposit forms a splat of much higher aspect ratio than the conventional fluid inks and thus over-printing can be used to build up significant thickness of deposit. It is possible to purchase hot-melt printers for pattern making and object visualisation. These commercial machines are ideally suited for rapid manufacturing research, as they are capable of building solid objects from STL format CAD files. In earlier work [9,10] we successfully demonstrated the feasibility of passing ceramic slurries up to about 20% by volume solids through one of these commercial machines (Modelmaker 6, Sanders Prototype, Wilton, NH, USA).

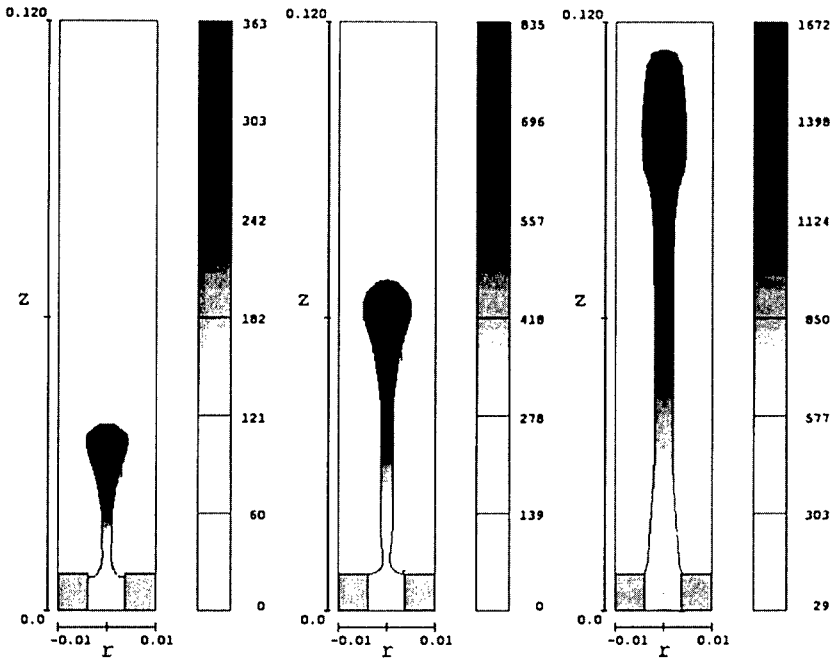


**Figure 1** Fluid dynamics simulation of droplet ejection from an ink-jet printer, calculations performed using the same initial and boundary conditions (including the pressure pulse); time =  $10^{-4}$  s; velocity field is shown by the grey scale (units  $\times 10^{-2}$  m); linear dimensions are given in units of  $10^{-2}$  m. From left to right  $Re/We = 2.5, 3.0$  and  $10$  respectively.

## PROPERTIES OF INK-JET FLUIDS

The fluid dynamics of ink-jet printing has been studied for some time. Drop formation occurs by an instability forming in a column of fluid. By studying the *Navier-Stokes* equation for the case of droplet ejection, Fromm obtained an approximate model of the process [11]. From this he determined a dimensionless characteristic grouping of physical constants, the ratio of the Reynolds number to the Weber number,  $Re/We$ , which can be used to characterise the fluids used for ink-jet printing

$$\frac{Re}{We} = \frac{(\gamma \rho l)^{1/2}}{\eta} \quad (1)$$

where  $l$  is a characteristic length,  $\rho$ ,  $\gamma$  and  $\eta$  are the fluid's density, surface tension and viscosity. Note that  $Re = v l \rho / \eta$  and  $We = v(l \rho / \gamma)^{1/2}$ , and hence are dependent on fluid velocity,  $v$ , while the ratio  $Re/We$  is independent of velocity. In most commercial drop-on-demand printing platforms this dimensionless grouping has a value somewhere between 1 and 10. The influence of this ratio on ink-jet behaviour can be explored by fluid dynamic simulation (figure 1). If this ratio is too small, the viscous term is dominant and large pressure pulses are required to eject a droplet. A high value of the ratio leads to very large liquid column

formation behind the main drop. Low values of  $Re/We$  lead to low droplet velocity and shorter column extensions before droplet ejection.

Another important fluid controlled parameter in ink-jet printing is the extent of spreading that occurs during impact. There exist a number of algorithmic approximations to predict this parameter. All are based on an energy balance of the surface and kinetic energy of the drop in flight against the surface energy of a deformed drop and the viscous work done during drop deformation on impact. Here we use the expression derived by Bhole and Chandra [12] used in an experimental study of the impact cooling of paraffin wax drops. This determines the maximum extent of droplet spreading in the absence of solidification as

$$\xi = \frac{r_{max}}{r} = \sqrt{\frac{We^2 + 12}{3(1 - \cos\theta) + 4We^2/\sqrt{Re}}} \quad (2)$$

where  $r_{max}$  and  $r$  are the maximum splat radius and initial drop radius respectively, and  $\theta$  is the contact angle the droplet makes with the substrate.

In order to ensure dimensional stability, and in the case of multiple material jetting, deposit homogeneity, impacting droplets should not splash. The splashing of liquid drops has been studied by Mundo *et al.* [13] and by Stow and Hadfield [14]. They both found splashing occurring when the parameter,  $K$ , exceeded a critical value  $K_c$ ,

$$K = WeRe^{1/4} \quad (3)$$

For water and methanol  $K_c = 57.7$  [13], for paraffin wax  $K_c = 102$  for a cold surface (23 ...C) and 137 for a hotter surface (73 ...C) [12].

Thus we can see that the ink-jet printing of ceramic slurries is strongly controlled by the fluid properties of the material to be printed as well as the velocity of the liquid drops and their size. Of the fluid properties, viscosity is expected to show the strongest dependence on the volume fraction of particles present. Fluid surface tension may also be influenced by the surfactant properties of additives used to stabilise the ceramic suspensions. Most importantly we can now clearly see that the quality and definition of a ceramic body produced by ink-jet printing should depend on the Weber and Reynolds numbers of the printing fluid.

## MATERIALS

We have used a model system consisting of  $\alpha$ -alumina powder with a mean particle size of 440 nm (RA45E, Alcan Chemicals) dispersed in a commercial grade alkane (paraffin) wax (Mobilwax 135, Mobil Special Products). This system was chosen because of our previous experience in using it for ceramic processing applications [15]. To enhance the dispersion of powders in the wax we have used a system recommended by ICI Surfactants (Middlesborough, UK) using a combination of a short chain fatty acid or derivative (stearic acid) and a commercial polymeric dispersant (Hypermer FP1). Full details of the material preparation and conditions used to measure the slurry viscosity were reported in an earlier paper [9].

**Table 1** Fluid properties of the proprietary Protosupport , Protobuild , paraffin wax and paraffin wax loaded with different volume fractions of alumina particles. Temperature of measurement is indicated in the first data column. Viscosity measurements were made at a shear rate of  $80 \text{ s}^{-1}$ .  $Re$  and  $We$  are determined assuming a velocity of  $3 \text{ ms}^{-1}$  and the characteristic length equal to the radius of the ink-jet orifice,  $l = 35 \text{ }\mu\text{m}$ .

Material	$T$ .C	$\rho$ $\text{kgm}^{-3}$	$\eta$ $\text{mPa.s}$	$\gamma$ $\text{Jm}^{-2}$	$Re$	$We$	$Re/We$	$K$	$\xi$
Protosupport	110	820	9.3	0.0265	9.57	3.32	2.88	5.85	1.15
Protobuild	120	1150	15.4	0.038	7.84	3.09	2.54	5.17	1.14
Wax (0%)	100	900	2.9	0.025	32.59	3.37	9.68	8.05	1.46
Wax (20%)	100	1500	6.5	0.025*	24.23	4.35	5.57	9.65	1.30
Wax (30%)	100	1800	14.5	0.025*	13.03	4.76	2.74	9.05	1.11
Wax (40%)	100	2100	38.0	0.025*	5.80	5.14	1.13	7.98	0.91

\* Value for paraffin wax only

The appropriate fluid properties of the paraffin wax, with and without a range of ceramic particles in suspension, are given in Table 1 along with the data determined for the standard proprietary Protobuild and Protosupport materials used in the Sanders Modelmaker 6. Unfortunately it was not possible to make good surface tension measurements of the filled waxes and so the datum measured for the unfilled wax was used. It is noticeable how the addition of the ceramic powder leads to a significant reduction in Reynolds number. This is because of the strong dependence of viscosity on the volume fraction of alumina powder. However, in all cases, the critical ratio  $Re/We$  remains within the window for ink-jet droplet formation. The value of  $K$ , the splashing parameter, is also far from the critical value for splashing and finally, the predicted radius of splat is similar to that found using the conventional proprietary Protobuild and Protosupport materials used with the Modelmaker 6.

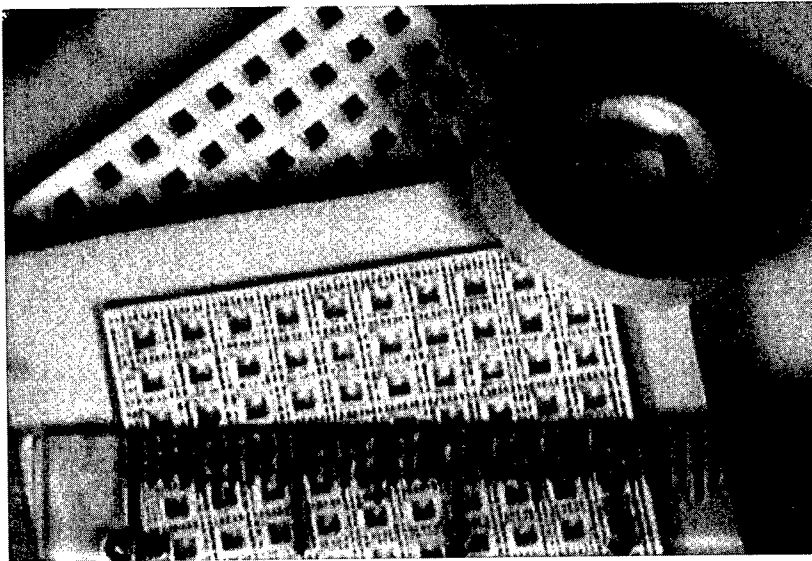
## PRINTING TRIALS

The Modelmaker 6 is a drop-on-demand piezoelectric ceramic driven ink-jet printer. Such printers work by exciting a fluid filled chamber at an acoustic frequency. At one end of the chamber is a small orifice through which a liquid column is ejected. At the other end is a connection to a fluid reservoir. The amplitude of the acoustic excitation pressure pulse is controlled by the amplitude imposed by a transducer and also by the resonance characteristics of the chamber. Thus, the fluid properties affect both the destabilisation of the fluid column into droplets and the amplitude of the exciting pressure pulse. In order to characterise the behaviour of different fluids during ink-jet printing, an instrumented ink-jet test station has been constructed, where the jetting parameters of pulse voltage, pulse shape and frequency

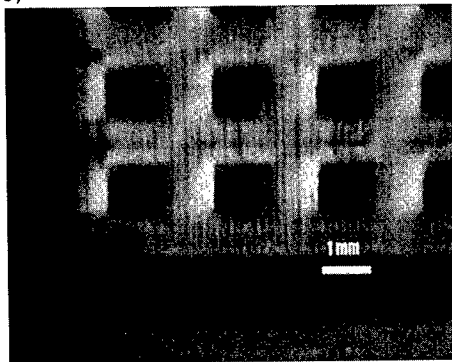
**Table 2** Operating conditions for the Modelmaker 6.

Material	Frequency kHz	Pulse Width $\mu$ s	Driving Voltage V	Temperature $^{\circ}$ C
Protobuild	6	30	50	120
Protosupport	6	30	60	110
20% Al <sub>2</sub> O <sub>3</sub>	6	30	60	110
30% Al <sub>2</sub> O <sub>3</sub>	6	30	70	110

a)



b)



c)

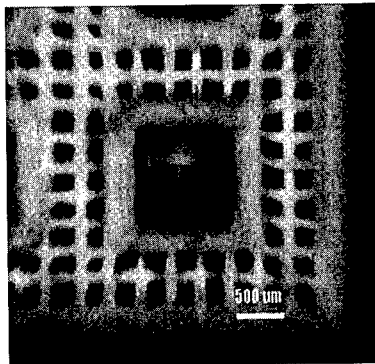


**Figure 2** a) Examples of ceramic green bodies printed from the 30% volume fraction alumina slurries. b) Good resolution of straight edges visible after printing. c) Minimum wall thickness



can be varied and the behaviour of emerging droplets observed. Details of this jet test station have been provided in an earlier publication [10]. A more focussed study on the dynamics of droplet ejection from ink-jet printers using highly filled suspensions is the topic of a companion paper in this volume [16].

In our study of droplet dynamics [16] we found that well formed droplets could be made with slurries up to 30% volume loading. The 30% volume fraction material showed well formed droplets separating from the liquid column about 1mm from the ink-jet orifice. However with the 40% volume loading suspensions, the droplets appeared to be less symmetrical with respect to the ejected column and the characteristic tails appeared to one side. In order to achieve stable droplet formation with the 40% volume fraction alumina suspensions (figure 2b) a small pressure of < 60 Pa was applied to the feeding reservoir. This may be required to allow sufficiently rapid flow to replenish the printing chamber with these higher viscosity fluids and also to transport the printing fluid at low shear rates from the reservoir to the chamber.

In an earlier report [9] we demonstrated that objects could be printed with 20% volume fraction alumina slurries using the Modelmaker 6 with the Protosupport ink-jet head. The driving conditions for this are shown in Table 2. On examining Table 1 we note that the  $Re/We$  ratio for both the unfilled paraffin wax and 20% alumina slurries are significantly different from that of the commercial Protosupport material even though these materials could be easily printed [9]. However, our investigations using the jet test station show that very different driving conditions are needed for optimum printing of the 30% slurries. This is because of the different acoustic properties of the highly filled suspensions in the printing chamber. Unfortunately, it was not possible to alter the majority of the printing process variables within the Modelmaker 6 and hence printing trials were carried out under non-optimum conditions at the frequencies and pulse widths used to print the Protobuild material. The two variables, which can be easily controlled, are the fluid temperature and the driving voltage, both of which can be accessed without using the machine control software code. The greater viscosity of the filled suspensions requires higher driving voltages for the piezoelectric tubes used to excite the ink jet chamber. The voltages used in the printing trials are indicated in Table 2.

Ceramic green bodies have been printed containing 30% by volume alumina particles as shown in figure 2. Figures 2b and 2c show the high resolution obtained with these suspensions with a feature accuracy of better than 100  $\mu\text{m}$ . Figure 3 shows that the printer is capable of producing ceramic green bodies with excellent resolution in the  $x$ - $y$  plane. Accurate rendition in the  $z$ -direction is also required for the freeform fabrication of objects. Figure 3 shows a selection of rectangular section blocks printed using the 30% loaded ceramic slurry. These demonstrate excellent straight edge rendition after deposition of numerous layers through over printing.



## CONCLUSIONS

Hot-melt ink-jet printing, using a commercial piezoelectric drop-on-demand printer, has been successfully demonstrated as a viable method of producing solid bodies containing ceramic particles dispersed in low melting point waxes. Modelling and simulation of the process indicates that printing should be possible using volume loadings in excess of 40% if sufficient power can be transmitted to the ink-jet chamber. Excellent spatial resolution and feature rendition has been demonstrated with a suspension containing 30% by volume ceramic particles. Higher volume loadings of particles to reduce shrinkage during sintering (in excess of 50%) are possible in principle. However, these will require further optimisation of the suspension rheology or possibly by using a carrier wax with a shorter chain length and hence lower inherent viscosity.

## ACKNOWLEDGEMENTS

This project was funded by the EPSRC through grant GR/L42537. We would like to thank Professor John Halloran for many helpful discussions during the early stages of this work. We would also like to thank Sanders Design International for assisting in the design and construction of the jet-test station and providing much information about the Modelmaker printing platform.

## REFERENCES

1. E. Sachs, M. Cima, P. Williams, D. Brancazio, J. Cornie, *ASME J. Eng. Ind.* **114**, 481 (1992).
2. J. Yoo, M. Cima, E. Sachs, and S. Suresh, *Ceram. Eng. Sci. Proc.* **16** [5], 755 (1995).
3. J. Yoo, K. Cho, W. Bae, M. Cima and S. Suresh, *J. Amer. Ceram. Soc.* **81**, 21 (1998).
4. W.D. Teng, M.J. Edirisinghe, J.R.G. Evans, *J. Amer. Ceram. Soc.*, **80**, 486 (1997).
5. Q.F. Xiang, J.R.G. Evans, M.J. Edirisinghe, P.F. Blazdell, *Proc. Inst. Mech Eng. B-J. Eng. Manuf.* **211**, 211 (1997).
6. C.E. Slade, J.R.G. Evans, *J. Mater. Sci. Lett.* **17**, 1669 (1998).
7. M. Mott, J.H. Song, J.R.G. Evans, *J. Amer. Ceram. Soc.* **82**, 1653 (1999).
8. J. Windle and B. Derby, *J. Mater. Sci. Lett.* **18**, 87 (1999).
9. K.A.M. Seerden, N. Reis, B. Derby, P.S. Grant, J.W. Halloran and J.R.G. Evans, *MRS Symp. Proc.* **542**, 141 (1999).
10. N. Reis, K.A.M. Seerden, B. Derby, P.S. Grant, J.W. Halloran and J.R.G. Evans, *MRS Symp. Proc.* **542**, 147 (1999).
11. J.E. Fromm, *IBM J. Res. Dev.* **28** p. 322 (1984).
12. R. Bholra and S. Chandra, *J. Mater. Sci.* **34**, 4883 (1999).
13. C. Mundo, M. Sommerfeld and C. Tropea, *Inter. J. Multiphase Flow*, **21**, 151 (1995).
14. C.D. Stow and M.G. Hadfield, *Proc. Royal Soc. Lon. A* **373**, 419 (1981).
15. J.H. Song and J.R.G. Evans, *J. Rheol.* **40**, p. 131-152 (1996).
16. N. Reis and B. Derby, in this issue.

---

## PROCESS-PROPERTY-PERFORMANCE RELATIONSHIP FOR FUSED DEPOSITION OF CERAMICS (FDC) FEEDSTOCK MATERIALS

N. Venkataraman, S. Rangarajan, B. Harper, M.J. Matthewson, A. Safari and S.C. Danforth  
Department of Ceramic and Materials Engineering, Rutgers University, Piscataway, NJ, 08854-8065.

### ABSTRACT

Fused deposition of ceramics (FDC) is an extrusion based layered manufacturing process. It uses a high solids loaded (>50 vol. % ceramic or metal powder) thermoplastic binder in filament form as the feedstock material. The filament acts as both the piston driving the extrusion process and the feedstock material being deposited in the X-Y direction onto a Z-stage platform. The primary mode of failure of the filament during the FDC process is via buckling. Earlier work has shown that the filament compressive modulus and the feedstock viscosity control the buckling behavior of the filament material in FDC. A study was conducted to investigate the effect of particle/polymer interface on the viscosity and compressive modulus of the PZT filled ECG9 system. The relative viscosity of the untreated and the surface treated particle filled systems increases with solids loading. It is found that both of the surface treated materials (stearic acid and titanate coupling agent) exhibit a lower relative viscosity than the untreated material. A rheological model (Krieger-Dougherty model) was used to investigate the possible reasons for the decrease in relative viscosity due to the surface treatment of particles. The investigation showed that the coupling agent acted as a dispersant (increasing value of  $\phi_m$ ) and thereby decreased the viscosity. The stearic acid may act as a dispersant (increasing value of  $\phi_m$ ) and as a lubricant (decreasing value of  $K_E$ ). The compressive modulus of all the different systems studied showed an increase with solids loading. A generalized Nielsen model was used to describe the relative modulus vs. solids loading behavior for all the different systems studied. Also, the measured compressive modulus of the filled system was found to be insensitive to the modifications in the particle surface treatment.

### INTRODUCTION

Solid freeform fabrication involves fabrication of parts directly from CAD files through sequential addition of material. The various SFF processes are distinguished according to the manner in which they accomplish the sequential addition of material. SFF processes can be classified into deposition based processes and directed energy based processes. Some examples of deposition based processes are 3-D Printing [1], Fused Deposition of Ceramics [2], and Sanders Prototyping [3]. Some examples of the directed energy processes are Stereolithography [4] and Selective Laser Sintering [5].

In fused deposition of ceramics (FDC), the sequential addition of material is accomplished via extrusion of a high solids loaded thermoplastic material. A highly (> 50 Vol.%) solids loaded thermoplastic material, in filament form, is fed into a liquefier which, melts the thermoplastic material. The filament acts as the piston driving the extrusion of the molten material through a nozzle. The extruded material is deposited onto a platform in the X-Y plane. Following the completion of a layer, the platform indexes down for further deposition of material. The FDC process is currently being used to fabricate functional components of a variety of ceramic and metallic materials such as:  $\text{Si}_3\text{N}_4$ , lead zirconate titanate (PZT),  $\text{Al}_2\text{O}_3$ , hydroxyapatite and stainless steel for a variety of structural, electroceramic and bioceramic applications [6-8].

In FDC, the filaments act as both the piston driving the extrusion process and the molten feedstock material being extruded. During the FDC build process, if the extrusion pressure ( $\Delta P$ ) exceeds a certain critical value, the filaments tend to buckle. A schematic of the buckling of filaments during FDC is shown in Figure 1.

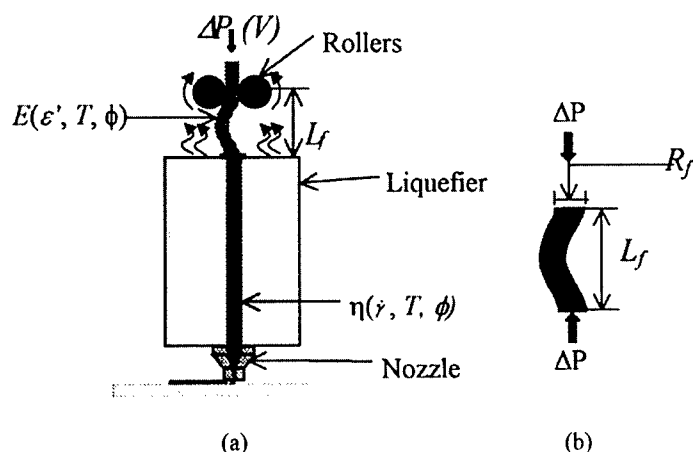


Figure 1: (a) Schematic showing the buckling of a filament during FDC. The schematic also shows the important process and material parameters involved in buckling ( $\Delta P$ : extrusion pressure,  $V$ : volumetric feed rate,  $T$ : temperature,  $\phi$ : solids loading,  $\gamma$ : shear rate,  $\eta$ : viscosity,  $E$ : compressive stiffness of filament,  $\epsilon'$ : strain rate), (b) schematic showing the section of filament between the rollers and liquefier (of radius,  $R_f$  and length  $L_f$ ), which buckles under a compressive stress,  $\Delta P$ .

It has been shown that for a given FDC nozzle geometry, orifice size of the nozzle, volumetric flow rate and liquefier and roller design, a material with a higher ratio of compressive modulus/viscosity ( $E/\eta$ ) is less likely to buckle during FDC [9]. A cooling jet was used to maintain the filament near room temperature (25°C). As a result the compressive modulus used in the modulus/viscosity ratio was measured at room temperature (25°C). Also the viscosity in the modulus to viscosity ratio was measured at the liquefier temperature of the filament material. It was found that feedstock materials with a ratio ( $E/\eta_a$ ) greater than a critical value ( $3 \times 10^5$  to  $5 \times 10^5 \text{ s}^{-1}$ ) do not buckle during FDC, while those with a ratio less than this range buckle [9]. This establishes that one needs to control the mechanical (compressive modulus) and rheological (viscosity) properties of the filament feedstock material to prevent buckling. Also, in order to enable fast development of filaments of new materials, it is necessary to control the critical filament properties (such as modulus and viscosity) and understand the factors affecting them.

In FDC, the filament feedstock material is a particulate filled thermoplastic composite. The mechanical and rheological properties of these composite materials depend on a variety of parameters, such as: processing conditions, solids loading, the nature of the thermoplastic binder, the particle characteristics (size, size distribution, shape, agglomeration level) and the interface chemistry between the particle and the polymer [10, 11].

The nature of the particle/polymer interface can have a significant influence on the mechanical and rheological properties of particle filled polymer systems [10-14]. For a given particle/polymer system, the nature of the interface can be altered through treatment of the

particle surface with surface agents. The different surface agents can be classified based on their effect on the mechanical and rheological properties of the filled systems [10]. The different types of surface agents are: coupling agents, lubricants and dispersants [10]. The coupling agent is a hybrid inorganic/organic molecule that chemically bonds with both the particles and the polymer to form a particle-polymer bridge [10, 14]. A “true” coupling agent usually increases the viscosity and modulus of filled polymers [10, 13-14]. A dispersant usually modifies the particle surface to make it more compatible with the polymer and thereby enables uniform dispersion [10]. The lubricants can either plasticize the polymer or create slippage at the particle/polymer interface (stress discontinuity) [10]. Both the dispersants and lubricants decrease the viscosity and modulus of filled polymers [10, 15].

In this study, the effect of three different particle surface conditions (untreated, stearic acid and a titanate coupling agent) on the compressive modulus and viscosity of the PZT filled ECG9 system was investigated.

## EXPERIMENT

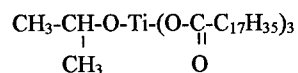
### Materials

The polymer used in this study is a multi-component thermoplastic termed ECG 9. It consists of: an amorphous polyolefin as the backbone, a semi-crystalline wax that modulates the viscosity and adds stiffness, a hydrocarbon resin that acts as a tackifier and finally a crystalline polyolefin that acts as a plasticizer imparting flexibility. The details of the binder composition and fabrication procedure have been presented elsewhere [16]. The density of ECG9 as determined by Helium pycnometry was  $0.91 \text{ g/cm}^3$ .

Lead zirconate titanate particles were used as the filler particles. The lead zirconate titanate powder was obtained from TRS, Inc., State College, PA. The particles are equiaxed, with a median particle size of  $1.2 \text{ }\mu\text{m}$ . The specific surface area of the powder, as determined by single point BET method, was  $1.1 \pm 0.2 \text{ m}^2/\text{g}$ . The density, as determined using helium pycnometry, was  $7.83 \pm 0.03 \text{ g/cm}^3$ .

Two different surface agents were used to modify the nature of the particle surface. One of them was stearic acid ( $\text{CH}_3(\text{CH}_2)_{16}\text{COOH}$ ) which, was obtained from Fisher Scientific, Inc. The stearic acid has a density of  $0.94 \text{ g/cm}^3$ . The other was a titanate coupling agent, KRTTST<sup>TM</sup> (Isopropyl, triisostearyl titanate), which was obtained from Kenrich petrochemicals, Bayonne,

NJ, USA. The chemical formula of KRTTTS is as follows [14]:



The density of KRTTST<sup>TM</sup> according to the supplier's specifications is  $0.95 \text{ g/cm}^3$ .

### Filament Fabrication

The details of the FDC filament fabrication procedure for the stearic acid coated PZT-ECG9 system has been presented elsewhere [9]. In brief, the filament fabrication consists of three important steps: powder coating, compounding and screw extrusion (for extruding filaments). The optimum concentration of KRTTST<sup>TM</sup> in toluene needed for coating the PZT particles was determined (from adsorption isotherm studies) to be 0.3 wt % (powder weight

basis). The PZT powder was then coated with the 0.3 wt % KRTTS™ solution in toluene. The KRTTS™ coated powder was then compounded with ECG9 and screw extruded into filaments. The compounding and extrusion conditions used were identical to that used for the stearic acid coated PZT-ECG9 system.

### **FDC Feedstock Property Characterization**

The steady state viscosity of the different filaments was determined at 140°C (the FDC liquefier temperature for PZT) using an Instron™ capillary rheometer. The experimental procedure employed for the measurement of viscosity has been detailed elsewhere [9].

The compressive modulus of the different filaments was measured using a miniature materials tester (Rheometrics, Inc., Piscataway, NJ). The procedure used to measure the compressive modulus has also been presented in an earlier work [9].

The viscosity of the unfilled ECG9 binder was measured at 140°C, using a steady state cone and plate arrangement on an ARES™ controlled strain rheometer (Rheometrics, Inc., Piscataway, NJ). The compressive modulus of the ECG9 binder was measured using the miniature materials tester (Rheometrics, Inc., NJ).

## **RESULTS AND DISCUSSION**

### **Viscosity Results**

The apparent viscosity of the different filled systems was measured using a capillary rheometer at 140°C. In the literature concerning filled polymer systems, the viscosity of the filled system is usually represented by the relative viscosity [10, 17]. The relative viscosity is defined as the ratio of the viscosity of the filled polymer to the viscosity of the neat polymer. In most classical studies, the relative viscosity (viscosity of filled system/viscosity of unfilled polymer) of filled suspensions is defined using the viscosity at high shear limits [17]. This is so as to minimize the effect of the particle network structure and to obtain a shear rate insensitive relative viscosity value [10, 17]. It was determined, that in the case of PZT (stearic acid coated) ECG9 systems the measured viscosity reaches a plateau by a shear rate value of 1000 1/s (upper Newtonian limit). Therefore, the relative viscosity values in the present work (for all the different solids loadings and surface treatments) are calculated using the viscosity values at the highest shear rate used (1000 1/s). The neat binder was found to be shear thinning (with a power law index of  $n =$  and has a viscosity of  $7.01 \pm 0.2$  Pa.s (at 1000 1/s). The relative viscosity of the untreated, stearic acid treated and KRTTS™ treated PZT filled ECG9 systems is plotted as a function of solids loading in Figure 2. As expected, the relative viscosity of all the different filled systems increases with the solids loading. The relative viscosity of the untreated PZT filled ECG9 system is higher than the surface treated cases. The stearic acid coated PZT filled ECG9 system exhibits the lowest relative viscosity values.

The surface treatment of PZT with KRTTS™ and stearic acid both lead to a reduction in the relative viscosity of the filled system. It was mentioned in the introduction that dispersants and lubricants tend to decrease the viscosity of filled systems [10]. Also, if a coupling agent (such as KRTTS™) reduces the viscosity of the system, it may be functioning as a wetting agent or as a lubricant instead of as a coupling agent [10, 18]. It is important from a scientific point of view to try to understand the possible mechanism by which the surface agents (in this study) reduce the viscosity of the filled system. It was decided to try to see whether a model such as the Krieger-Dougherty model could help understand the mechanism of viscosity reduction. The Krieger-Dougherty model is one of the popular models used to describe the behavior of the relative viscosity of filled suspensions. The model is as follows [19, 20]:

$$\eta_r = (1 - \phi / \phi_m)^{-K_E \phi_m} \quad (2)$$

where,  $\eta_r$ , is the relative viscosity,  $\phi$  is the solids loading,  $\phi_m$  is an empirical constant known as

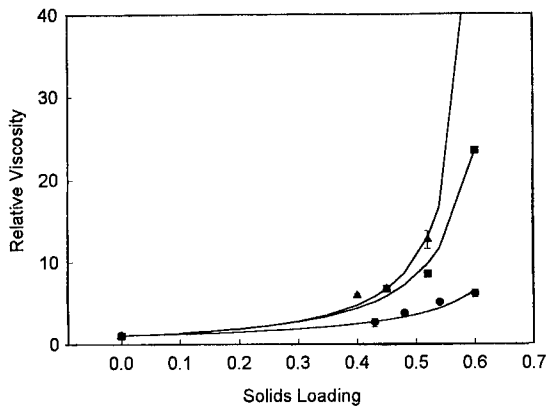


Figure 2: The relative viscosity of untreated PZT (▲), KRTTS™ coated PZT (■) and stearic acid coated PZT (●) filled ECG9 systems as a function of solids loading measured at 140°C. The solid lines represent the fit to the Krieger-Dougherty models [19, 20].

the maximum packing factor and  $K_E$  is an empirical constant called the generalized Einstein coefficient. The value of  $\phi_m$  indicates the packing efficiency of the particles in the suspension [11, 17]. A higher value of  $\phi_m$  indicates a better packing efficiency and thereby lower relative viscosity [11, 17]. In general, the value of  $\phi_m$  will decrease with increasing amount of agglomeration [11, 17]. The value of  $\phi_m$  can also be affected by the particle size and size distribution [11, 17]. For most particle (spheres) filled suspensions the value of  $K_E$  is  $\approx 2.5$  [20, 21]. The typical values for  $\phi_m$  are between 0.52 and 0.74 [19, 20].

The solid lines in Figure 2 represent the best fit curves to the Krieger-Dougherty model. The best fit parameters ( $R^2=0.98$ ) for each of the different surface treatment conditions are presented in Table I. It can be seen from Table I that the treatment of PZT particles with KRTTS™ leads to an increase in the value of  $\phi_m$  from its value for the untreated case. An increase in the value of  $\phi_m$  implies that the inter-particle interactions have decreased, and therefore the tendency to agglomerate has also decreased [11, 17]. One can conclude from the values of  $\phi_m$  for the untreated and KRTTS™ treated cases, that as expected, the untreated particles tend to agglomerate more than the KRTTS™ treated particles. The KRTTS™ is decreasing the level of attractive inter-particle interactions and thereby reducing the tendency to agglomerate, *i.e.* it acts as a dispersant. One can also see from Table I that the value of  $K_E$  is the same for the case of the untreated and KRTTS™ treated particles filled ECG9 systems (2.5). The value of  $K_E$  for most filled thermoplastics is usually 2.5. The value of  $K_E$  can increase if the particles are non-equiaxed and decrease to a value of 1.0 in case of complete slippage at the particle/polymer interface [11, 17].

Table I. The Best Fit Values ( $R^2=0.98$ ) for the Krieger-Dougherty Model (Relative Viscosity) Parameters Corresponding to the Different Surface Treated PZT Filled ECG9 Systems [19, 20].

Surface Condition	$K_E$ (Generalized Einstein Coefficient)	$\phi_m$ (Maximum Packing Fraction)
Untreated PZT	$2.50 \pm 0.01$	$0.66 \pm 0.01$
Stearic Acid Coated PZT	$1.49 \pm 0.04$	$0.73 \pm 0.01$
KRTTS™ Coated PZT	$2.50 \pm 0.01$	$0.73 \pm 0.01$

The PZT particles used in this study are equiaxed, therefore a value of  $K_E$  greater than 2.5 is not expected. As the best fit value of  $K_E$  for the untreated and KRTTS™ treated case is 2.5, one can expect that there is no slippage at the particle/polymer interface.

In the case of the stearic acid treated PZT filled ECG9, the value of  $\phi_m$  is the same as that of the KRTTS™ treated case. This suggests that stearic acid enables more uniform dispersion of the PZT particles in the polymer as compared to the untreated case. Also, the value of  $K_E$  is lower than for the untreated and KRTTS™ treated cases. The lower value of  $K_E$  (1.49 as opposed to 2.5) suggests that the stearic acid may be introducing some slippage at the particle/polymer interface as compared to the untreated and KRTTS™ treated cases. The exact molecular mechanism by which the stearic acid may cause slippage at the particle/polymer interface is unclear. One possible hypothesis, is that the stearic acid may be plasticizing the ECG9 polymer locally at the particle/polymer interface. This plasticized layer at the particle/polymer interface will have lower viscosity than the bulk ECG9. The presence of this lower viscosity layer at the particle/polymer interface can then manifest as slippage (*i.e.* stress discontinuity). Therefore, the stearic acid may be acting as a dispersant (wetting agent) and also as a lubricant.

### Modulus Results

The elastic compressive modulus of the various filled and unfilled systems was measured using the miniature materials tester (at a displacement rate of 1mm/min). The modulus of the

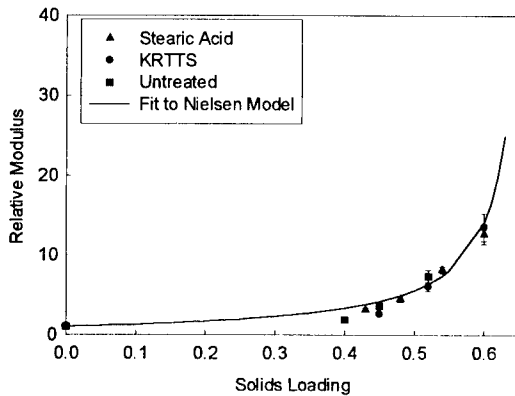


Figure 3 The relative modulus of the various surface treated and untreated PZT filled ECG9 systems vs. solids loading. The solid line corresponds to the fit to the generalized Nielsen model [11]. The modulus was measured at 1 mm/min displacement rate and at 25°C.



unfilled ECG9 as measured using the miniature materials tester (at 1mm/min) is  $7.35 \pm 0.21$  at  $25^\circ\text{C}$ . The relative modulus of the untreated, stearic acid coated and KRTTS™ coated powders is plotted as a function of solids loading in Figure 3.

One can see from Figure 3 that the relative modulus of all the systems increase with solids loading as expected. Also, one can see from the figure that there is no significant effect of surface treatment (or lack of it) on the relative compressive modulus of the filled system. The individual data points corresponding to the different surface treatment conditions were fit to the generalized Nielsen model. The generalized Nielsen model is used to describe the behavior of the relative modulus (compressive, shear or tensile) of filled polymer systems as a function of solids loading [11]. The model is as follows:

$$M/M_0 = \frac{1 + AB\phi}{1 - B\psi\phi} \quad (3)$$

where,  $M$  and  $M_0$  are the modulus of the filled and unfilled systems respectively. The factor  $A$  is related to the Einstein coefficient ( $A=K_E-1$ ),  $B$  usually has a value of 1 for rigid filler particles and  $\psi$  is a function of the maximum packing factor  $\phi_m$  [11].

There was no statistically significant difference between the best fit parameters ( $R^2 = 0.97$ ) for the various surface treatment conditions ( $K_E = 2.5 \pm 0.01$ ,  $\phi_m = 0.67 \pm 0.01$ ). Therefore, the current study shows that the measured compressive modulus (using the current technique) is not sensitive to the changes in the state of dispersion (no change in the value of  $\phi_m$ ) or the particle/polymer interface condition (no change in the value of  $K_E$ ) for the stearic acid and KRTTS™.

In order to decrease the chances of a filament buckling in FDC, a high value of the ratio of the compressive modulus to apparent viscosity is desirable. The experiments conducted in this study suggest that the apparent viscosity of the filaments can be modified (decreased) through the use of surface agents. The compressive modulus however, is not sensitive to changes in the dispersion state or interface conditions for stearic acid and KRTTS™. Therefore, the compressive modulus is not as readily modifiable as the apparent viscosity. As a result, it seems that decreasing the apparent viscosity of the filled system (filament) may be the only way to increase the modulus/viscosity ratio of a given filament. However, the use of a different coupling agent (with a different molecular structure and chemistry than KRTTS™) might act as a "true" coupling agent and raise the modulus of the filled system (filament).

## SUMMARY AND CONCLUSIONS

A study was conducted to investigate the effect of particle/polymer interface on the relative viscosity and relative modulus of the PZT filled ECG9 system. The relative viscosity of the untreated and the surface treated particle filled systems increases with solids loading. It is found that both the surface treated cases (stearic acid and titanate coupling agent) exhibit a lower relative viscosity than the untreated cases. A rheological model (Krieger-Dougherty model) was used to investigate the possible reasons for the decrease in relative viscosity due to the surface treatment of particles. The investigation showed that the coupling agent acted as a dispersant (increasing value of  $\phi_m$ ) thereby decreasing the viscosity. The stearic acid appears to act as both a dispersant (increasing value of  $\phi_m$ ) and as a lubricant (decreasing value of  $K_E$ ). The compressive modulus of all the different systems studied showed an increase with solids loading. The measured compressive modulus of the filled system was found to be insensitive to the changes in the state of dispersion (no change in the value of  $\phi_m$ ) or the particle/polymer interface condition (no change in the value of  $K_E$ ). As a result, it seems that decreasing the apparent viscosity of the

---

filled system (filament) may be the only way to increase the modulus/viscosity ratio of a given filament, and thereby decrease the chances of filament buckling during FDC.

#### ACKNOWLEDGEMENTS

This work was sponsored by the Office of Naval Research under ONR MURI contract number N00014-96-1-1175. The authors also acknowledge the significant assistance provided by Eric Passman, Rhea Jaico, Ryan McCuiston and Brian Harper in this work. The miniature materials tester was obtained with financial support of Allied Signal under DARPA/ONR contract # N00014-94-C-0115.

#### REFERENCES

1. M. Cima, E. Sachs, T. Fan, J.F. Brecht, S.P. Michaels, S. Khanuja, A. Lauder, S.J. Lee, D. Brancazio, A. Curodeau and H. Tureck, U.S. Patent No. 5,387,380 (1995).
2. S.C. Danforth, M. Agarwala, A. Bandyopadhyay, N. Langrana, V. Jamalabad, A. Safari, and R. van Weeren, U.S. Patent No. 5,738,817 (1998).
3. R.C. Sanders, J.L. Forsyth, K.F. Philbrook, U.S. Patent No. 5,506,607 (1996).
4. M.L. Griffith and J.W. Halloran, J. Amer. Cer. Soc. 79 (11), 2601 (1996).
5. D.L. Bourell, H.L. Marcus, J.W. Barlow, and J.J. Beamen, Int. J. Powder Metall. Technol. 28 (4), 369 (1992).
6. M.K. Agarwala, A. Bandyopadhyay, R. van Weeren, A. Safari, and S.C. Danforth, American Ceramic Society Bulletin 75 (11), 60 (1996).
7. A. Bandyopadhyay, R.K. Panda, V.F. Janas, S.C. Danforth, A. Safari, J. Amer. Cer. Soc. 80 (6), 1366 (1997).
8. A. Safari, V.F. Janas, A. Bandyopadhyay, R.K. Panda, M. Agarwala, S.C. Danforth, U.S. Patent No. 5, 818, 149 (1998).
9. N. Venkataraman, S. Rangarajan, B. Harper, M.J. Matthewson, A. Safari, G.Wu, N. Langrana, A. Yardimci, S. Guceru and S.C. Danforth, Accepted for Publication in Rapid Prototyping Journal, April 2000.
10. S.A. Khan and R.K. Prud'Homme, Reviews in Chemical Engineering 4 (3), 205 (1987).
11. L.E. Nielsen and R.F. Landel, *Mechanical Properties of Polymers and Composites*, 2<sup>nd</sup> ed., (Marcel Dekker, Inc., New York, 1994).
12. C.D. Han, T. Van Den Weghe, P. Shete and J.R. Haw, Polym. Engg. and Sci. 21 (4), 196.
13. H.L. Luo, C.D. Han and J. Mijovic, J. Appl. Polym. Sci. 28, 3387 (1983).
14. S.J. Monte and G. Sugerman, Polym. Engg. and Sci. 24 (18), 1369 (1984).
15. C.D. Han, C. Sandford and H.J. Yoo, Polym. Engg. and Sci. 18 (11), 849 (1978).
16. T. McNulty, F. Mohammadi, A. Bandyopadhyay, D.J. Shanefield, S.C. Danforth, and A. Safari, Rapid Prototyping Journal 4 (4), 144 (1998).
17. I. Tsao, PhD Thesis, Rutgers University, May 1990.
18. K.N. Hunt, J.R.G. Evans and J. Woodthorpe, Polym. Engg. and Sci. 28 (23), 1572 (1988).
19. R.J. Hunter, *Foundations of Colloid Science*, Vol.2, (Oxford Science, Oxford, UK, 1987).
20. S. Rangarajan, G. Qi, N. Venkataraman, A. Safari, and S.C. Danforth, Accepted for Publication in the Journal of American Ceramic Society, January 2000.

---

## GAS PHASE SOLID FREEFORM FABRICATION OF SALDVI of SiC CERMETS

J.E. Crocker, L. Shaw, H.L. Marcus  
Institute of Materials Science, Department of Metallurgy and Materials Engineering, University  
of Connecticut, Storrs, CT 06268

### ABSTRACT

In this work, the solid freeform fabrication of cermets was explored. Using a laser-based approach, SiC was deposited by chemical vapor deposition from tetramethylsilane gas into powder layers of Cu, Mo, or Ni. The resulting structures were examined to observe the extent of reaction between the metal powders and the vapor deposited SiC. Silicide formation was observed, most readily with the Ni powder. The thermal expansion of the metals compared to that of the vapor deposited SiC affected the interfacial stresses generated in the cermets during fabrication.

### INTRODUCTION

Solid freeform fabrication, SFF, using laser writing from gaseous precursors has been studied for some time<sup>1-6</sup>. Selective area laser deposition, SALD, is the process of direct localized chemical vapor deposition, LCVD, of a gas phase thermal/photochemical decomposition product into a predefined layer by layer shape to create a part. Selective area laser deposition vapor infiltration, SALDVI, deposits the gas phase decomposition product into a defined shape by infiltration into sequential layers of powder. This paper will describe some early results of the SALDVI process whereby SiC is locally deposited from a gas phase precursor into layered metal powders of Cu, Mo, and Ni.

### EXPERIMENT

#### Equipment

Figure 1 is a schematic of the SALD/SALDVI system used in the study. The system is comprised of a vacuum chamber with a variety of gas ports to introduce the gases to be decomposed. A laser is mounted on the system and focused at the working surface and scanned under computer control either by moving mirrors or mechanically moving the substrate. The lasers used in this study were a 50 Watt CO<sub>2</sub> at 10.6 μm wavelength, and a 150 Watt Nd:YAG at 1.06 μm wavelength. In both cases, the laser beam is nominally Gaussian in shape with a 1/e diameter of 1 mm at the working surface. The displacement of the focused laser beam is computer controlled to get the LCVD deposition onto the desired layer by layer shape. The laser beam scan rates were varied between 1 and 10 μm/s in this work. The surface temperature in the laser heated process zone is measured with an optical pyrometer with a probe diameter of 2 mm. This temperature is used as the feedback signal in a closed loop system to adjust the laser power to maintain a desired surface temperature. Due to the finer size of the focused beam compared to the pyrometer probe, the temperature distribution in the laser-heated hot spot is not uniform within the sampling area of the pyrometer probe. The pyrometer temperature is therefore averaged over the hot spot and is considered an apparent, rather than an absolute, temperature. The apparent surface temperature used in the reported work was 1000°C, a

temperature that prior work has shown to produce good SiC deposition<sup>6</sup>. A video camera allows constant observation of the process as it proceeds.

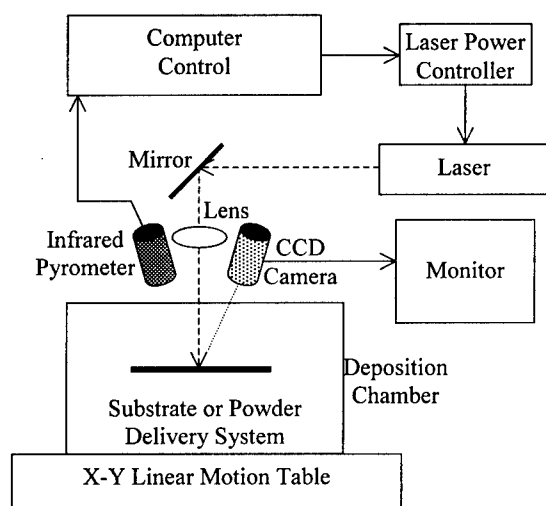


Figure 1. SALD/SALDVI System Schematic.

## Materials

The gas precursor used in this study was tetramethylsilane  $\text{Si}(\text{CH}_3)_4$  that decomposes into SiC. Hydrogen gas is added to some of the runs to minimize the excess carbon that accompanies the decomposition process. Tetramethylsilane is liquid at room temperature but has a vapor pressure of 600 Torr at 20°C. A static pressure less than the room temperature vapor pressure, specifically 10 torr in this work, is then introduced into the deposition chamber.

The metal powders used in the study were Cu, Mo and Ni. The powders are primarily spherical, range in size from a few microns to about 40  $\mu\text{m}$  in diameter, and have an average diameter of about 25  $\mu\text{m}$ . The thermal expansion for each metal, the SALDVI SiC, and two of the nickel silicides are compared in Figure 2 for the range of temperatures typical to the SALDVI process<sup>7-8</sup>. Thermal expansion is presented as the percent change in length from room temperature. The high reflectivity of the Cu limited laser coupling at both wavelengths, making heating of the metal to the decomposition temperature of the gas difficult. To improve laser coupling, it was necessary to introduce some SiC powder to the Cu powder. In this preliminary work, the addition of 50 volume percent SiC powder to the Cu powder drastically reduced the laser power needed to reach the decomposition temperature.

Copper and nickel both have a large number of silicides and a very low temperature eutectic reaction, while molybdenum is a higher temperature material with silicides that could be formed at high temperature<sup>9</sup>. The nature of the binaries and the relative coefficients of expansion were the primary reason for the choice of these metals for the initial SALDVI of cermets.

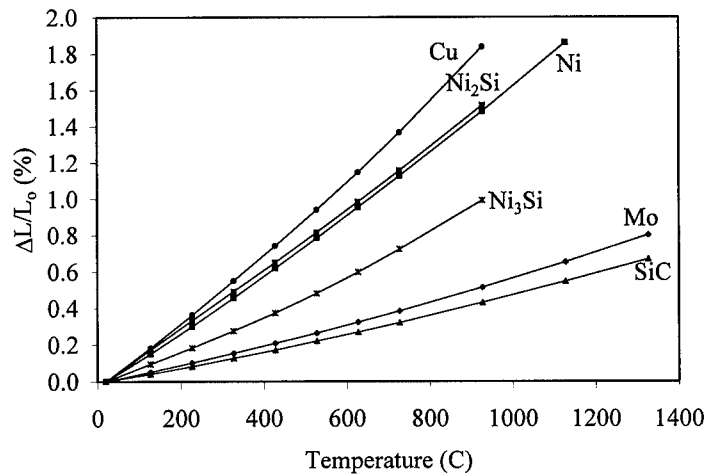


Figure 2. Thermal expansion (% linear change) of metals, SALDVI SiC, and selected silicides<sup>7-8</sup>.

## RESULTS

Three distinctly different results were obtained for the three cermet systems and they will be described separately.

The Cu/SiC cermet formed using the CO<sub>2</sub> laser and a scanning rate of 10 μm/s is shown for a three layered single line pass structure in Figure 3. Present in the metallographic cross section are the Cu powders, the SiC powders used to enhance the laser coupling, and the SALDVI infiltrated SiC. The large amount of SALD growth of SiC at the surface of each layer indicates that the actual surface temperature may have been higher than the desired temperature. Since the SALD layer extends into the region of the following powder layer, the distribution of Cu powder through the layers becomes discontinuous. We have observed the presence of a reaction zone in the matrix region around the Cu particles as a result of reaction between the Cu and the Si from the SALDVI infiltrated material. The distribution of Cu silicide in this reaction zone is not uniform however, possibly due to slow mass transport kinetics in this system.

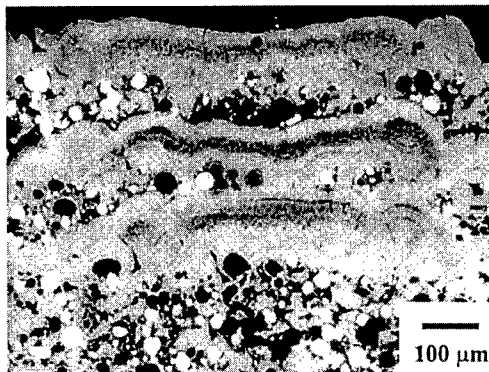


Figure 3. Cross section of Cu/SiC SALDVI three layer single line pass structure.

The other observation is that the Cu powder particles are shown to readily pull out of the cermet during metallographic preparation. This is attributed to the large mismatch in thermal contraction between the Cu and the SALDVI infiltrated SiC that occurs upon cooling from the LCVD processing temperature, resulting in considerable tensile stresses across the particle/matrix interface. Further work is underway to more fully understand this behavior, in particular, to estimate the interface strength that does exist and the interface chemistry that may control it.

The Ni/SiC cermet behaves somewhat differently. Figure 4a shows a cross-section of a SALDVI three layer single line pass structure obtained using the CO<sub>2</sub> laser at 2.5 μm/s scanning rate. What is observed is the severe interaction between the infiltrated SiC and the Ni to form Ni silicides, which is shown in more detail in Figure 4b. The identification of the silicides formed has not been completed but their existence is easily observed. It is apparent that at the surface where more of the thermal energy is absorbed a low temperature eutectic was formed which then resolidified upon cooling. The lowest temperature in the Ni/Si binary is at 964°C, which is less than the apparent surface temperature of 1000°C using during SALDVI processing of the Ni/SiC cermet. In reality we are dealing with the Ni/Si/C ternary system, but these diagrams are not fully available. Therefore, for this paper we will only discuss the results in terms of being silicides. Deeper into the layer, the reaction zone between the Ni and SiC is readily observed. Further work to define the chemistry of the interface phases is in progress.

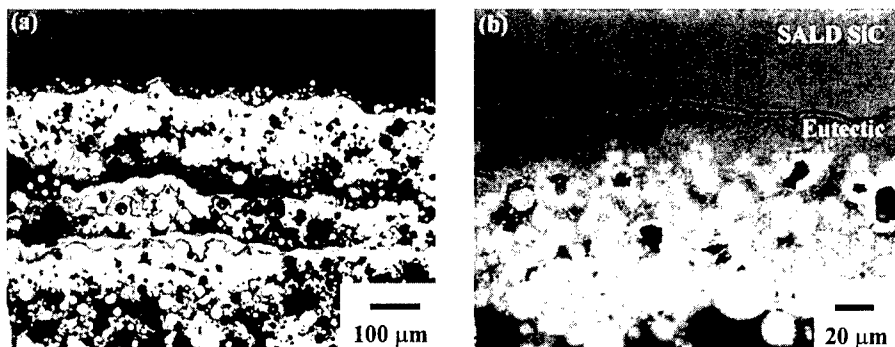


Figure 4. (a) Cross section of Ni/SiC SALDVI three layer single line pass structure and (b) expanded view at SALD/Ni powder layer interface.

The Mo/SiC results are shown in Figure 5 which again shows a cross section of a SALDVI three layer single line pass structure processed with the Nd:YAG laser at a scanning rate of 2.5 μm/s. What is observed from the metallographic cross section is that good infiltration was obtained with greater than 90% density. It is also apparent that there is no interface reaction between the Mo and the SiC. Since the deposition temperature is low compared to the melting temperature of both the Mo powder and its silicides this is not a surprising result. In addition there is little indication of pullout of the Mo particles. The very close match of the coefficient of thermal expansion of the Mo and the SiC would lead to minimal interface stresses consistent with this result. Here again a small amount of SALD SiC on the top surface of each of the three layers is observed.

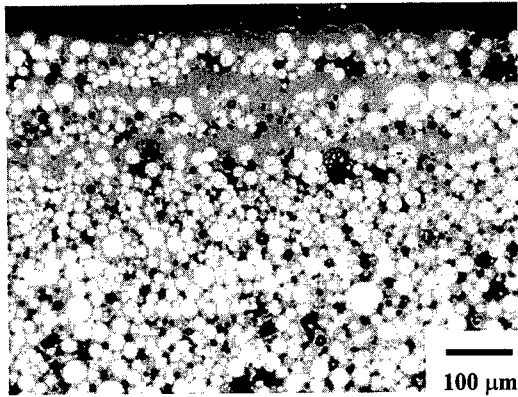


Figure 5. Cross-section of Mo/SiC SALDVI three layer single line pass structure.

## CONCLUSIONS

The ability to form metal cermets using the SALDVI SFF process has been demonstrated. The microstructures observed strongly depend on the system used and on the relationship between the temperature of deposition and the phase equilibria. Cu/SiC shows moderate interface reaction, but interface debonding occurs due to the thermal expansion mismatch. Ni/SiC shows excessive formation of silicide interfaces and surface regions of eutectic silicides. The Mo/SiC system shows no indication of silicides. A good match in thermal expansion between the two components resulting in limited interface stresses.

## ACKNOWLEDGMENTS

The authors gratefully acknowledge the support of the Office of Naval Research (grant #N00014-95-1-0978).

## REFERENCES

1. J.L. Maxwell, J. Pegna, D. Messia, and D. DeAngelis, Proceedings of the Solid Freeform Fabrication Symposium, The University of Texas, pp.227-237, (1996).
2. K.J. Jakubenas, J.M. Sanchez, and H.L. Marcus, Materials and Design, **19**, 11-18, (1998).
3. J.E. Crocker, S. Harrison, L. Sun, L.L. Shaw, and H.L. Marcus, JOM, **50**, 21-23, (1998).
4. M. Wanke, O. Lehmann, K. Muller, Q. Wen, and M. Stuke, Science, **275**, 1284-1286 (1997).
5. S. Harrison and H.L. Marcus, Materials and Design, **20**, 147-152 (1999).
6. L. Sun, K.J. Jakubenas, J.E. Crocker, S. Harrison, L. Shaw, and H.L. Marcus, Materials and Manufacturing Processes, **13**, 883-907, (1998).
7. Y.S. Touloukian, R.K. Kirby, R.E. Taylor, and P.D. Desai, "Thermophysical Properties of Matter, Volume 12, THERMAL EXPANSION Metallic Elements and Alloys", IFI/Plenum, New York, New York, 1975.
8. B.F. Gilp and P.D. Desai, *Properties of Intermetallic Alloys, Volume II. Silicides*, Metals Information Analysis Center, Purdue University, pp 15.1 and 16.1, (1994).
9. H. Baker, et al., *Alloy Phase Diagrams*, ASM Handbook, Volume 3, ASM International, (1992).

## AUTHOR INDEX

- Aksay, I.A., 165  
Amancherla, S., 31  
Auyeung, R.C.Y., 99
- Bak, Joseph V., 51  
Beaman, Jr., Joseph J., 67  
Bell, Nelson, 129  
Bird, Connie E., 51  
Bourell, David, 67  
Brice, C.A., 31  
Brinker, C. Jeffrey, 141  
Brooks, John A., 9, 21  
Bulthaup, Colin, 135
- Cheeseman, B.A., 159  
Chou, T.W., 159  
Chrissey, D.B., 99  
Chung, R., 99  
Cohen, E., 81  
Crocker, J.E., 211  
Crowe, C.R., 3
- Danforth, S.C., 159, 179, 203  
Derby, B., 117, 195  
Detig, Robert H., 151  
Dimos, Duane, 129
- Ensz, M.T., 9  
Evans, J.R.G., 195
- Fan, Hongyou, 141  
Fish, R., 81  
Fitz-Gerald, J.M., 99  
Fraser, H.L., 31
- Gao, Hongjun, 111  
Gasdaska, C., 179  
Grant, P.S., 195  
Griffith, M.L., 9  
Guerit, P., 81
- Harlan, Nicole R., 67  
Harper, B., 179, 203  
Headley, Thomas J., 21  
Hebner, Thomas R., 123  
Hofmeister, W.H., 9  
Hubert, Brian, 135
- Jacobson, Joe, 135  
Jang, J.H., 173
- Kalman, Z., 179  
Kamimura, A., 91
- Kampe, S.L., 3  
Kander, R.G., 75  
Kang, S., 187  
Kelly, S.M., 3  
Khandelwal, P., 81  
Kotila, Juha, 45
- Lakeou, S., 99  
Lee, J.H., 165  
Leu, Ming C., 57  
Lind, Jan-Erik, 45  
Liu, H.C., 187  
Liu, S., 81  
López, Gabriel P., 141
- Madigan, Conor F., 123  
Manos, Dennis M., 111  
Marcus, H.L., 211  
Martin, J.P., 75  
Matthewson, M.J., 203  
Mayo, W., 179  
McCuiston, R., 179  
Mohdi, R., 99  
Murakami, T., 91
- Nakajima, N., 91  
Nam, S.W., 187  
Narang, S., 81  
Nyrhilä, Olli, 45
- Park, Sehyung, 37  
Park, Seok-Min, 67  
Philliber, J.A., 9  
Piqu, A., 99  
Prinz, F.B., 187  
Prud'homme, R.K., 165  
Puskar, J.D., 9
- Rangarajan, S., 179, 203  
Register, Richard A., 123  
Reis, N., 117, 195  
Rice, R.W., 173  
Ridley, Brent, 135  
Robino, Charles V., 9, 21  
Ruan, X.P., 159
- Safari, A., 159, 179, 203  
Schmidt, Wayne R., 51  
Schultz, J.P., 75  
Schulze, W., 173  
Schwendner, K.I., 31  
Seerden, K.A.M., 195  
Shaw, L., 211



---

Smugeresky, J.E., 9  
Song, Yong-Ak, 37  
Stampfl, J., 187  
Sturm, J.C., 123  
Suchicital, C.T.A., 75  
Syvänen, Tatu, 45

Troian, Sandra, 123  
Twait, D., 81

Venkataraman, N., 203  
Ventura, S., 81

White, Ronald D., 51  
Wilhelm, Eric, 135  
Wu, H.D., 99  
Wu, Lingling, 111

Yang, Bo, 57  
Young, H.D., 99

Zhang, X.D., 31  
Zimbeck, W.R., 173

## SUBJECT INDEX

- actuator, 159
- all-printing, 135
- as-formed microstructure, 3
  
- biomaterial, 165
- Bis-GMA, 165
  
- case studies, 45
- ceramic(s), 195
  - alumina, 165
  - metal systems, 211
  - packaging, 173
  - piezoceramic, 159
  - silicides, 31
  - silicon
    - carbide, 211
    - nitride, 179, 187
  - suspensions, 195
  - zirconia, 67
- composite, 165
- compressive modulus, 203
- conformal cooling, 51
  
- design of experiments (DOE), 51
- digital light projection, 81
- direct
  - masking, 91
  - metal laser sintering (DMLS), 45
  - photo shaping, 81
  - writing, 99
- drop-on-demand, 117
  
- elastomer, 135
- electroforming, 57
- electronic components, 99, 151
- electrostatic printing, 151
- extrusion, 203
- evaporation-induced self assembly (EISA), 141
  
- finite element analysis, 159
- flat panel displays, 151
- flex circuits, 151
- fluid(s), 129
  - dynamics, 117
- fused deposition of ceramics (FDC), 179, 203
  
- gel-casting, 187
  
- Hamaker constants, 129
  
- injection molding, 51
- ink jet, 117
  - printing, 123, 141, 195
  
- lamp exposure, 91
- laser
  - additive manufacturing (LAM), 3
  - deposition, 99
  - engineered net shaping (LENS), 9, 21, 31
  - lateral dye distribution, 123
  - layer bands, 3
  - Lifshitz theory, 129
  - liquid embossing, 135
  
- mask-based surface conversion patterning, 111
- matrix assisted pulsed laser evaporation (MAPLE), 99
  - direct write (MAPLE DW), 91
- mechanical alloying, 75
- metals
  - copper-nickel-molybdenum, 211
  - metal components, 45
  - molybdenum, 31
  - niobium, 31
  - silver toner, 151
  - stainless steel, 9, 21
  - titanium(-), 67
    - aluminum-vanadium, 3
- microelectronics, 173
- microstructures, 21
  - microstructural evolution, 9
- modeling, 9, 117
- mold, 67
  - casting, 67
  - inserts, 45
  - SDM, 187
- multi-chip module, 173
- multi-material part, 37
  
- nanocrystal, 135
- net-shape, 45
- nonaqueous, 129
  
- organic light emitting diodes, 123
  
- particle/polymer composites, 203
- patterned multifunctional nanostructures, 141
- pen lithography, 141
- photocurable ceramic dispersion, 81
- photolithography, 173
- plasma source immersion ion implantation (PSII), 111
  
- rapid tooling, 57
- rheology, 203
  
- seeds, 179

selective  
  area laser deposition (SALD), 211  
  vapor infiltration (SALDVI), 211  
  laser sintering (SLS), 75  
silicon nitride, 81  
sol-gel, 141  
  transformable photopolymer resin, 91  
solid freeform fabrication (SFF), 37, 57, 67, 75,  
  91, 159, 187, 195  
solidification, 21  
stereolithography, 165, 173  
  refrigerative stereolithography, 91  
suspensions, 117  
texture, 179  
thermal expansion, 179  
thin films, 99  
  transistor, 135  
3D welding and milling, 37  
tooling, 51  
transformation mechanisms, 21